ALMA MATER STUDIORUM - UNIVERSITA' DI BOLOGNA

FACOLTÀ DI INGEGNERIA

CORSO DI LAUREA MAGISTRALE IN INGEGNERIA CIVILE

Dipartimento di Ingegneria Civile, Ambientale e dei Materiali

D.I.C.A.M.

TESI DI LAUREA

in

Tecnica delle Costruzioni M

DYNAMIC AND SEISMIC BEHAVIOUR OF MULTIPLE ROCKING ELEMENTS AND APPLICATION TO POST-TENSIONED BRIDGES

CANDIDATO:

Rodolfo Mazza

RELATORE:

Chiar.mo Prof. Ing. **Marco Savoia**

CORRELATORI:

Dr. **Alessandro Palermo**

Dr. Ing. **Stefanie Gutschmidt**

Anno Accademico 2011/2012

Sessione II

"Twenty years from now you will be more disappointed by the things you didn't do than by the ones you did do. So throw off the bowlines, sales away from the safe harbour. Catch the trade winds in your sails. Explore, Dream, Discover."

-Mark Twain-

ACKNOWLEDGEMENTS

There are a large number of people who I have to thanks to, who have supported me during my time at university.

First and foremost, I would like to thank my supervisors of Canterbury University: Dr. Eng. Alessandro Palermo and Dr. Eng. Stefanie Gutschmidt for their support and encouragement during my thesis studies. I would like also to thank my Italian supervisor Prof. Ing. Marco Savoia to had allow me to do this magnificent experience.

I would also acknowledge my many friends who supported me extensively throughout my studies and with who I spent, probably, the best period of my life, in particular: Diego, Gianmarco, Lorenzo, Simone Mattia, Alessio, Enrico, Claudia, Sara, Valentina and Anna. I do not want to forget my new friends in Cristchurch with who I spent unforgettable moment, in particular: Patrick, Ben, Francesco, Daniel, Tim, Louise, Maria, Polina, Flore and Tanya.

Finally, I am immensely appreciative of the support provided by my father, mother and brothers during my entire time at university.

Abstract

Nella società moderna è molto importante che ingegneri progettisti riescano a costruire strutture con livelli di performance superiori in grado di resistere anche ai terremoti più rari. Agli ingegneri è richiesto di progettare strutture che non solo rimangano operative anche dopo un evento sismico straordinario, ma anche di limitare i costi diretti di riparazione e i costi indiretti dovuti alla di affari o l'interruzione prolungata di questi ultimi.

Non è economico né pratico, costruire edifici che rimangano nel campo elastico anche durante sismi di rara entità. Per tanto, lo stato dell'arte tradizionale è di dimensionare gli elementi della struttura in modo che rispondano con deformazioni plastiche alle sollecitazioni non comuni. Conciò vengono progettate delle zone degli elementi in cui vengono concentrate le deformazioni plastiche. Queste zone sono definite come "cerniere plastiche". Questo diffuso standard di costruzione nel monto dell'ingegneria sismica è definito come "Capacity Design", un concetto sviluppato Nuova Zelanda circa 30 anni fa. Il principale scopo del capacity design è di preservare la vita. Questo obbiettivo si raggiunge, come sopracitato, nel localizzare i danni strutturali in parti specifiche della struttura fornendo ad essa un comportamento duttile. Inoltre, garantendo allo stesso momento una "via" sicura per lo scarico dei carichi gravitazionali al suolo.

Negli ultimi due decenni, con lo scopo di far crescere le performance strutturali, la maggior parte degli sviluppi nel campo dell'ingegneria sismica utilizzano connessioni duttili con elementi prefabbricati. Le connessioni prefabbricate sono assemblate mediante l'utilizzo di trefoli/trecce/fili post-tesi non confinati. L'utilizzo di questi elementi permette di ottenere nelle sezioni in cui sono previste le deformazioni plastiche il meccanismo definito come Controlled Rocking. Questo tipo di meccanismo confina tutte le deformazioni in un numero di aperture progettate tra i diversi elementi che compongono la struttura. Questo meccanismo permette alla struttura di ricevere pochi danni a seguito di un terremoto e conseguentemente di abbattere drasticamente i costi di riparazione e i costi indiretti per l'interruzione del commercio.

In passato, nell'ambito della costruzione di ponti gli elementi prefabbricati comprendevano solamente impalcati di medie o corte campate e la costruzione in situ degli altri elementi incideva notevolmente sul costo dell'opera, causando per di più notevoli disagi, in termini di viabilità, alla comunità. Per tanto negli ultimi 20 anni si è cercato di promuovere notevolmente la costruzione di ponti totalmente prefabbricati, sia la sovrastruttura sia la sottostruttura. Questa notevole spinta, per cercare di cambiare radicalmente lo stato dell’arte, è stata effettuata dal dipartimento dei trasporti statunitense. Ma nonostante il progetto, denominato Accelerate Bridge Construction and Design, stia ricoprendo una sempre maggior parte del mercato nelle regioni a basso pericolo sismico esiste ancora un forte scetticismo e una forte mancanza di confidenza nella costruzioni di ponti in regioni ad alto rischio sismico; influenzato prevalentemente da una mancanza di una normativa specifica per queste tipologie di costruzioni.

Per queste ragioni lo scopo di questa ricerca è quello di cercare di far luce sul comportamento dinamico delle pile composte da elementi separati e poi assemblate. Per di più un ulteriore intento di questo lavoro è di capire se è possibile implementare nelle diverse sezioni tra un segmento della pila e l’altro la tecnologia controlled rocking con dispositivi per la dissipazione dell’energia.

Lo studio è stato portato a termino attraverso una serie di test dinamici. La prima investigazione comprende l’analisi del comportamento dinamico di una serie di tre parallelepipedi in legno impilati. Le analisi riguardano il range delle oscillazioni libere e lo studio dello stesso elemento sotto forzante quasi armonica. Particolare attenzione è stato posta sulla variazione del comportamento dinamico e delle aperture dei gap tra un elemento e l’altro al cambiare della geometria dei blocchi e alla superficie di contatto tra di essi. Le tipologie di contatto comprendono il contatto legno-legno e la seconda gomma-legno. La seconda opzione è stata utilizzata sia per prevenire lo sliding tra gli elementi sia per valutare le variazioni dinamiche apportate al sistema da una superfice con maggiore damping.

Il secondo test propone uno studio sul comportamento dinamico su tavola vibrante di un ponte semplificato in scala 1:30. Questo è composto da due campate e da un'unica pila centrale. Il ponte costruito è completamente post-teso sia la pila sia l’impalcato. A causa delle ridotte dimensioni è risultato impossibile armare la pila e per questo per fornire un adeguata resistenza all’elemento si sono utilizzate delle sezioni cave in acciaio (SHS) all’interno delle quali è stato gettato il calcestruzzo. Anche in questo secondo test lo scopo è stato focalizzato sulla misurazione delle aperture del gap tra i segmenti del pilastro e nella sezione di contatto tra gli impalcati delle due campate. Il modello è stato testato utilizzando un input sinusoidale con un picco massimo di accelerazione di 0.85g

I dati sono stati utilizzati mediante l’utilizzo di due High-Speed Camera. Le quali furono impostate per registrare 300 fps (fotogrammi per secondo) durante il primo test e 600 fps per la seconda investigazione. Successivamente le immagini registrate sono state processate utilizzando un programma scritto in MatLab chiamato Digital Image Correlation and Tracking. Il programma è in grado di seguire lo spostamento di una griglia di pixel selezionati inizialmente in tutta la sequenza di foto registrate. In questo modo è possibile conoscere lo spostamento relativo o assoluto dei punti della griglia al tempo t=0 e conoscendo il time-step tra un fotogramma e il suo successivo è possibile ricavare le altre grandezze fisiche come la velocità la variazione angolare e la velocità di variazione angolare e per di più l’energia cinetica e potenziale del sistema

INDEX

INTRODUCTION

The importance for design engineers to provide modern societies with structures that have a superior level of performance for resisting a major earthquake event has became widely accepted. Engineers are required to design structures, which will not only remain operational after a major earthquake event, but should also limit direct costs associated with repair and indirect financial loss associated with business operation and downtime.

It is not economical, nor practical, to design structures to remain in elastic range following a major earthquake event. Therefore, traditional seismic design methodologies require structures to respond inelastically by detailing members to accommodate significant plasticity ("plastic hinge zones"). This widespread construction standard in the world of seismic structural design is " Capacity Design", a concept developed in New Zealand around 30 years ago. The main purpose of capacity design is preserving life safety. It is achieved by controlling the location of damage to specific part of the structure in the event of a large earthquake by ductile structural response. Furthermore, guarantying at the same time a secure way for the gravity load to reach the ground.

In the light of growing demand for high-performing structures, major developments to the construction of seismic resisting systems utilizing dry, joined, ductile connections within precast concrete structures have heavily researched over the last two decades. Precast joined system are constructed with unbounded post-tensioned tendons to induce a controlled rocking mechanism in place of a region of significant plasticity. This controlled rocking confines all the deformation to a number of "gap openings" throughout the structure, as opposed to the inelastic response of multiple plastic hinge zones in traditional monolithic concrete construction, precast concrete emulation of monolithic concrete construction . This significantly reduces direct costs associated with structural repair and indirect costs associated with downtime and business disruption.

Cast-in-place substructures for bridges are the most commonly used technology regardless of the bridge dimensions (span lengths, pier heights). The use of cast-in-place formwork for standard column shapes (circular or rectangular) is very cost effective. The precasting of bridge components in the past has been intended primarly for superstructure elements for bridges with short and moderate spans. However, construction time, and un-skilled labour can drastically impact on construction timeframe, causing further disruption and alteration to the business and the asset management of clients respectively. Therefore, in the past 20 years a total prefabrication of bridges (substructure and superstructure) has been promoted specially by the Department Of Transportations (DOTs) in the U.S.. Although Accelerated Bridge Construction and Design (ABCD) for bridge piers is becoming more popular in the region with low seismicity, high criticism and lack of confidence still appears if the technology applies in the earthquake prone areas.

For this reason the aim of this research is shed light on the dynamic behavior of the multiple segmented bridge pier. Moreover the goal of this work is try to understand if is possible combine ABC implementing the system with a multiple rocking dissipative section. This study was carried out throw dynamic test.

The first investigation presents the study of the behavior of free multiple rocking rigid timber blocks under free oscillation decay and quasi sinusoidal input. Subsequently a controlled rocking system was tested. Particular focus is placed on the variation of the dynamic behavior and gap opening between the multi rocking interfaces due to both changing of the blocks dimension ratio and by the changing of friction coefficient.

The second test propose a dynamic test on shake-table of a scaled two span bridge with single pier in scale 1:30. The bridge analyzed is completely post-tensioned both pier and deck. Even in this testing the aim is to study the dynamic behavior of the bridge and measure the gap opening both in pier rocking sections and deck under sinusoidal input with a maximum acceleration value of 0.85g.

The data were collected by using an High-Speed Camera. The camera was set to capture 300 fps (frame per second) during the first test and 600 fps during the second experiment. Subsequently the images were processed with a program wrote in MatLab called Digital Image Correlation and Tracking. The program is able to follow the initial position of pixels marked in the first picture and compare the same pixel with all the other picture. In this way is possible know the relative/absolute displacement of the body. Furthermore knowing the displacement and the time-step between two frames is possible derivate all the other physical quantities like angular displacement and velocity, potential and kinetic energy of the system.

1

Literature Review

1.1 Introduction

Currently the widespread construction standard in the world seismic structural design is “Capacity Design”, a concept developed in New Zealand around 30 years ago [1]. The main purpose of capacity design is preserving life safety, and this is achieved by controlling the location of damage to specific parts of the structure in the event of a large earthquake, guaranteeing at the same time a secure way for gravity load to reach the ground by ductile structural response. However, with this approach, the localized damages in the buildings are often difficult to repair. As a result recent research has focused on the development of solutions to ensure isolated and repairable damage or solution with zero residual damage. Therefore engineers, predominantly in the last decade, began to take a greater interest in the mechanics of rocking motion. This approach when applied correctly acts as an effective isolation mechanism for structures against severe ground motion [2].

Modern researchers have suggested that the ancient Greek and Romans may have deliberately design their columns to rock in strong ground motions contributing to the survival of many ancient structures [3, 4]. It was not until 1980 that New

Zealand engineers constructed the first modern structures specifically designed to rock for seismic protection. The South Rangitikei Viaduct in Mangaweka (Figure 1-1) and a reinforced concrete chimney at Christchurch International Airport are two of the few structures in the world, which are deliberately designed to rock [5].

a) *b)*

1.1 *Figure : a) The South Rangitikei Viaduct, b) A close up of rocking connection at the pier base*

1.2 Housner Model: Rigid Block on Rigid Foundation

The modern studies of the dynamics of a rocking rigid block are typically attributed to Housner [6], who was the first to analyze the dynamic response of a rigid block rocking on a rigid foundation. Housner started to analyze this phenomenon after the devastating 1960 Chilean earthquake, where a number of tall, slender structures survived the ground shaking while other more appearing stable structures were overturned and severely damaged.

Housner first develop a piecewise differential equation 1.1 of motion for a rigid rectangular block placed on a rigid foundation as show in figure 1-2.

$$\begin{cases} I_0 \dfrac{\partial^2\theta}{\partial t^2} = -MgR\sin(\alpha-\theta) & \text{For } \theta > 0 \\ I_0 \dfrac{\partial^2\theta}{\partial t^2} = MgR\sin(\alpha+\theta) & \text{For } \theta < 0 \end{cases} \tag{1.1}$$

Where M is the total mass, $R=\sqrt{H^2+B^2}$, $\alpha=\tan^{-1}(H/B)$ is the index of the slenderness of the block, $I_0=(4/3)MR^2$, the corresponding moment of inertia which is defined respect to O or O', g is the acceleration of gravity, and θ is representing the opening of the gap or rotation.

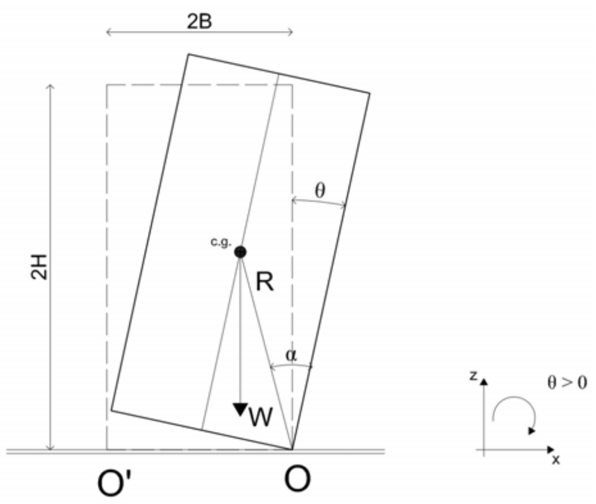

1.2 – *Schematic of a Free-Standing Block Rocking Motion*

The rigid block will oscillate around the pivot of rotation O and O' when it is set to rocking. It is assumed that the coefficient of friction is sufficiently large to prevent sliding between the block and the base.

For tall and slender blocks, which have an angle α less than 20° the previous equation (Eq. 1.1) can be approximated as:

$$I_0\ddot{\theta}-MgR\theta=-MgR\alpha \qquad \text{For } \theta>0 \qquad (1.2)$$

Assuming initial condition $\theta=\theta_0<\alpha$ and $\dot{\theta}=0$ at t=0, which represent the block released from the rest position with an initial displacement θ_0, the equation 1.2 has the solution:

$$\theta(t)=\alpha-(\alpha-\theta_0)\cosh(pt) \qquad (1.3)$$

This equation is a closed-form expression describing the rotation of the block around the point O as it falls back to the vertical position and is valid until the moment of impact. Therefore the formula describe the period of vibration for a quarter of a rocking cycles. Housner's expression for the quarter rocking period, it is obtained entering in the equation 1.3 $\theta(t)=0$ and time $t=T/4$ as show in equation 1.4. The response of a rigid block under free vibrating is strongly non-linear; and the period of the system is highly influenced by the initial rotation amplitude θ_0 (Figure 1.3) [7], where the period is zero when the release position is θ_0=0 and it tends towards infinity before overturning, that is when θ_0 > α. In figure 1.3 is depicted the relation between the lateral response in terms of overturning moment versus base rotation referred to the pivot O.

$$T = \frac{4}{p}\cosh^{-1}\left(\frac{1}{1-\theta_0/\alpha}\right) \qquad p = \sqrt{\frac{MgR}{I_0}} \tag{1.4}$$

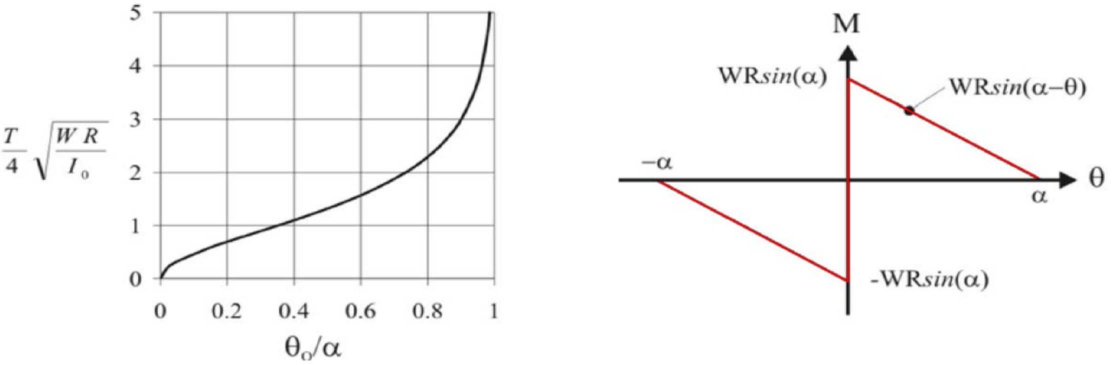

a) *b)*

1.3 *Figure - (a) Period of rocking with amplitude* θ_0 *; (b) Moment rotation response of rocking block*

Furthermore using the assumption of the conservation of angular momentum it was developed an expression for the coefficient of restitution, which represent the ratio between the kinetic energy at the instant just after the impact and immediately before, as show in equation 1.5. In the years subsequent, this formula was extensively used to measure the energy lost after each impact.

$$r = \left(\frac{1}{2}I_0\dot{\theta}_2^2\right) / \left(\frac{1}{2}I_0\dot{\theta}_1^2\right) = \frac{\dot{\theta}_2}{\dot{\theta}_1} \tag{1.5}$$

Housner pursued his study analyzing the overturning of a block rested on a base which was suddenly given a constant acceleration “a” and a sinusoidal acceleration enduring for a time “t” . The studies showed that if the ratio between a/g is major than α and the acceleration acts for a sufficient length of time, the block will overturn. This research led to discover how the vulnerability of slender freestanding blocks to overturn is linked with their physical dimension. Moreover Housner showed how, an apparently intuitive behaviour, is in point of act a non-linear complex process, nevertheless a simplify and idealistic approach was used.

1.3 Other Rocking Models

1.3.1 Two spring foundation and Winkler foundation

After the theory of the rigid block on rigid foundations, the next step in complexity is to assume the contact between the block and the foundation no longer rigid but deformable. A simple way to describe the behaviour of a deformable rocking interface is by inserting two springs and dampers in a prescribed fixed location [8] (Figure 1.3 (a-b)).

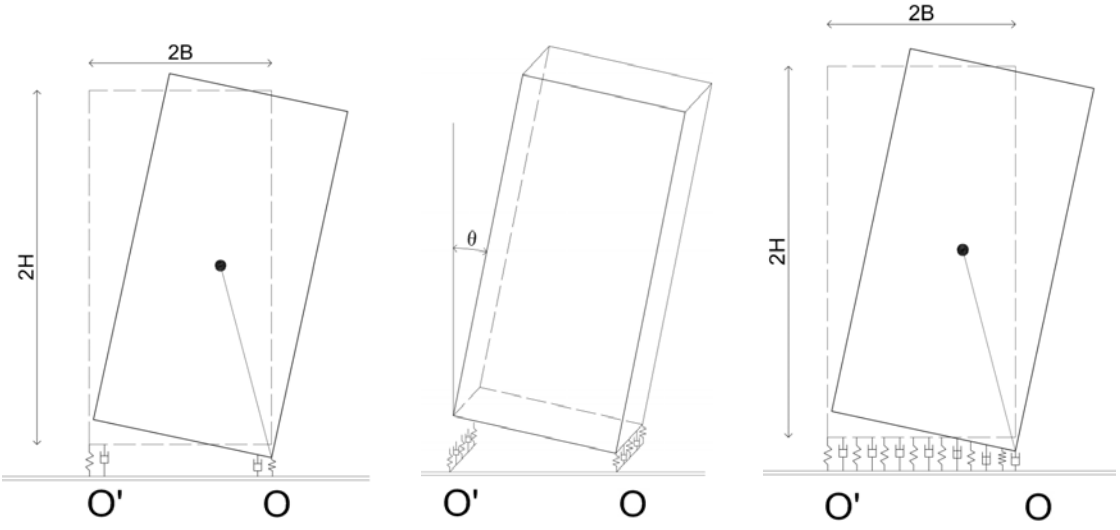

(a) *(b)* *(c)*

1.4 *Figure - (a-b) Free-Standing Block Rocking Motion on two spring foundation and (c) on a Winkler foundation*

Where the spring represents the deformable contact and the damper the dissipation of energy after each impact. The model with the two spring foundation is simple to analyze and covers many of the dynamic characteristics of rocking bodies. Nevertheless, the foundation is over simplify for more accurate application. To improve the precision of the model, researchers implemented an elastic tensionless Winkler foundation [9, 10].(Figure 1.4). The Winkler foundation eliminated the necessity to specify the location of rocking pivots and the distribution of the local pressure. This provides an improved representation of the supporting condition. With the intent to model the inability of the soil to carry tensile stresses, it is assumed that the block is just resting on the spring, with an unbounded connection. In this way, whenever the block starts to rock and the displacement of one of the two edges is bigger than the elastic deflection of the soil, the block will separate from the springs.

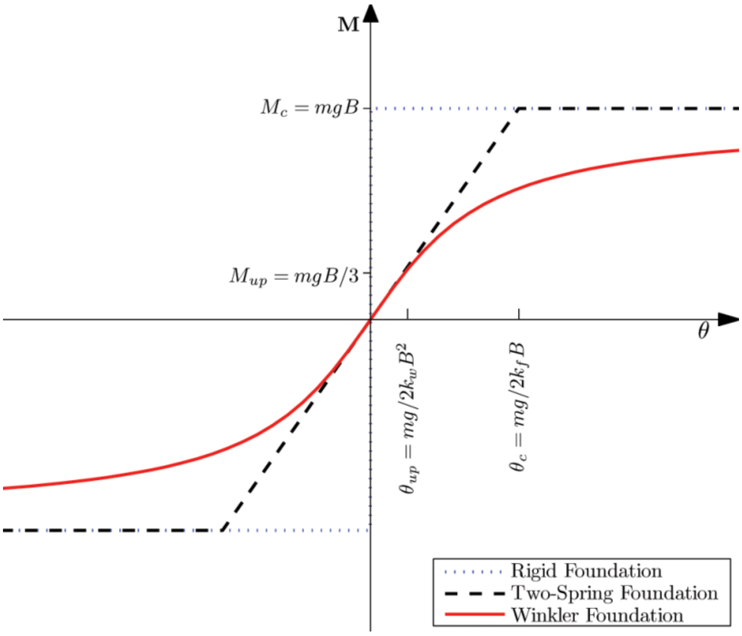

1.5 *Figure – Comparison between the three rocking surface assumption*

Even in those models is assumed that slipping between the block and the foundation is not allow. Therefore the system has only two degree of freedom: vertical motion, given by the vertical displacement, y, of the centre of the mass measured from the position of rest, and the rotation, obtained by the angle of tilting, θ . One of the most important parameter to obtain an accurate prediction in both methods of analysis is the selection of stiffness of the spring and the value of the damping coefficient. For the Winkler foundation the stiffness is calculate per unit length. The stiffness is assumed constant and independent of the displacement amplitude or excitation frequency in both formulations. Since the block has only two degrees of freedom, its response depends only on the vertical force and on the moment referred to the centre of mass.

After the first publications of these models, the Winkler foundation response was considered more accurate but at the same time required a more complicate procedures and a longer computation times that using an a equivalent two spring model. Therefore some researchers applied the two spring foundation model in their case studies and works [11] or developed advanced formulations to predict better a seismic response [12]. Starting from twenty years ago, with more analysis capacity given by more power computer the Winkler foundation formulation is used widely in the research [13-15].

1.3.2 Impulsive Dirac-δ Forces in the Representation of a Rocking Block

A Dirac-delta forces method is a development in the mathematical treatment of a rocking motion in the construction of the governing differential equation of motion. This treatment is an alternative for the traditional model. In the field of rocking rigid blocks, Prieto [16] used this function to represent the discontinuity effect between the rocking of a rigid block from one point of rotation to the other. In his work the formulation is presented without the need to calibrate the coefficient of restitution. The Dirac-delta function has the effect of an impulsive force and simulates the energy lost in function of the work done by the force.

This approach was tested to set the behaviour of a rigid rocking block under free vibration and harmonic forcing. The main parameter is the impulse force F_δ which is introduced in the generalized equation of motion (Equation 1.6).

$$\frac{\partial^2 x}{\partial t^2} - x + sign(x) = F_\delta \tag{1.6}$$

Three basic conditions are required for satisfy the impulse F_δ to be:

- The force is concentrate in the space and in time.
- The force produced a sudden change in direction and value of the velocity corresponding to r-value.
- The force reduces the velocity in both directions of motion.

The Dirac- δ function is defined by:

$$\delta(x) = \begin{cases} +\infty, & x = 0 \\ 0, & x \neq 0 \end{cases} \tag{1.7}$$

The Dirac-δ can be loosely described as a function on the real line which is zero everywhere except at the origin, where it is infinite.

$$\int_{-\infty}^{\infty} f(x)\delta(x)dx = f(0) \tag{1.8}$$

As a special case of equation 1.8 is the formula beneath (Eq. 1.9), where x_1 and $-x_1$ are two real number which could be infinite. The Dirac delta is not a function in the traditional sense as no function defined on the real numbers has these properties [17]. The Dirac-δ function can be rigorously defined either as a distribution or as a measure.

$$\int_{-x_1}^{x_1} \delta(x)dx = 1 \tag{1.9}$$

The Dirac-δ can be built by a limiting process of sequences of continuous functions; where one of the most common way is to consider it as a limit of Gaussian:

$$\delta_n(x) = \lim_{\delta n \to 0} \frac{1}{n\sqrt{\pi}} e^{-\frac{x^2}{n^2}} \tag{1.10}$$

To define F_δ we can start from Newton's second law and rewrite it using the properties of Delta function, after that taking the Laplace transform and imposing the limit of the equation, followed by the Inverse Laplace transform and some steps, the explicit form of the F_δ can be:

$$F_\delta = \frac{-A}{n\sqrt{\pi}} \tanh(\frac{v}{n}) v^2 e^{-\frac{x^2}{n^2}} \tag{1.11}$$

Which substituted into Equation 1.6 results:

$$\ddot{x} - x + sign(x) = \frac{-A}{n\sqrt{\pi}} \tanh(\frac{\dot{x}}{n}) \dot{x}^2 e^{-\frac{x^2}{n^2}} \tag{1.12}$$

Where A is damping nature of the force and n, which represented the abruptness of the contact force, is approach to 0.

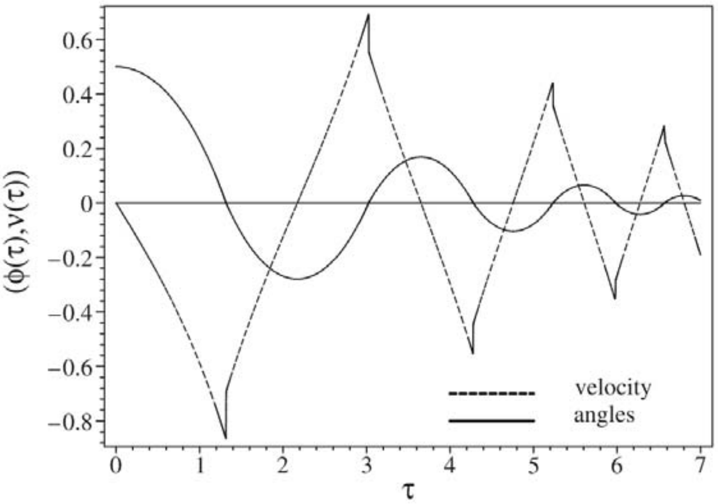

1.6 *Figure - Velocity and angle variation with r=0.8, n=10^{-3} and initial condition x_0=0.5,v_0=0.0. ([16])*

The numerical integration of Equation 1.12 allows the demonstration that the typical features of rocking motion for a slender block. In figure 1.5 is empathize the suddenly chancing of velocity after each impact.

The approach presented by this formulation provides a significant step towards a rocking motion formulation , which can be extended to more complex problems than the solely single block rocking dynamics.

1.3.3 Analytical modelling of flexible rocking structures

Since the research on rocking block on a rigid foundation start, the rocking response of flexible rocking structures received less attention. Most of the experiments carried out, treated the dynamics of the block with a simplified equivalent oscillator without directly introducing in to the analysis the interaction between the elasticity and rocking[18, 19]. One of the last developments in this field was carried out by researchers at University of Cambridge [20], with the aim to identify the effect of the interaction on the collapse of a flexible rocking structure. The non linear equation of motion was derived using the Lagrangian formulation for large rotation and was presented for an idealized structural model.

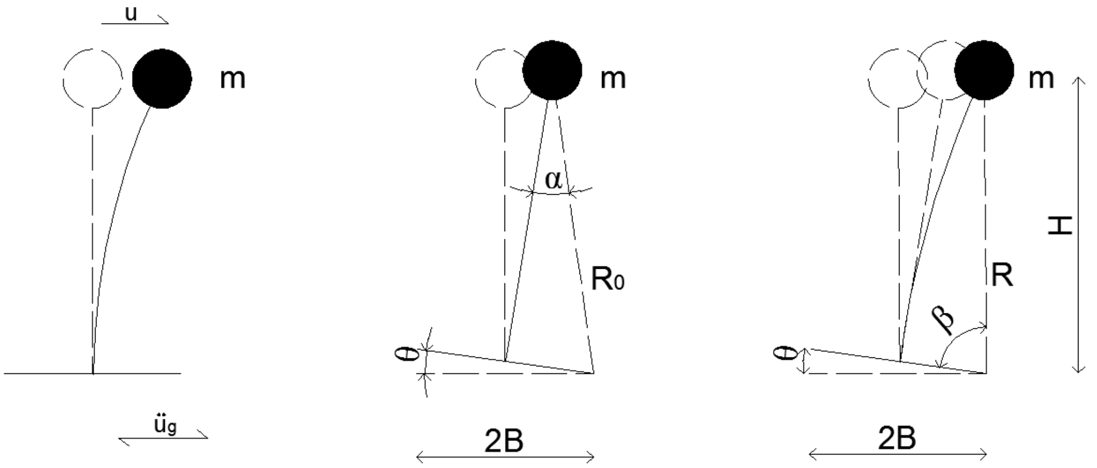

(a) *(b)* *(c)*

1.7 *Figure - Schematic of idealized analytical models: (a) linear elastic oscillator, (b) rigid rocking structure, (c) flexible rocking structure*

Instead, the equation of motion assuming small displacement for the linear elastic SDOF (Figure 1.6 (a)) is given by:

$$\ddot{u}_g + 2\xi_n \dot{u} + \omega_n{}^2 u = -\ddot{u}_g \tag{1.13}$$

Where $\ddot{u}_g$ is the horizontal ground acceleration, $\omega_n = \sqrt{k/m}$ is the natural frequency of the system and $\xi_n = c/(2\sqrt{km})$ is the damping factor. It is very important to notice that the behaviour of the linear elastic oscillator is independent from the geometry of the system [21] While the equation of motion for a rigid rocking structure is described above. The idealized analytical model depicted in Figure 1.6 (c) was developed for first time in the field of small displacement with the aim to investigate the deformation at the flexible structure subjected to uplift. It was later derived for the large rotation to analyze the overturning instability [22].

In this treatment the kinematics of the model depends on two Lagrangian parameters which are assumed to be β and R, where unlike of the rigid body theory are still scalar but no more constant. These parameters substitute the classical parameters u, θ at the rigid block theory. Different phases and the piecewise continuous equations of motion often necessitate the transition from the rigid model to the flexible one. For this reason the following equations (1.14) exist to allow easily the switch between the two sets of parameters.

$$\begin{gathered} \theta = \beta \pm \sin^{-1}(H/R) \\ u = \pm B \mp \sqrt{R^2 - H^2} \end{gathered} \tag{1.14}$$

The model can present alternatively two phases: the full contact phase and the rocking phase. At the initial condition of rest, the system is ruled by the equation of the full contact stage, behaving like a linear elastic oscillator. As soon as the rocking of the structure starts the equations describe was the dynamics of the system change. The equation for the full contact phase is given by equation 1.13 and utilized the classical set of parameter u, θ, where in the rest position u= θ= 0. At the onset of the rocking the parameters are converted in β and R.

The equations of motion of the system in the uplift phase are derived using le Lagrangian approach, in which large rotations and small elastic displacement are assumed.

$$\begin{cases} \ddot{R} = \omega_n{}^2 R\left(\dfrac{B}{\sqrt{R^2 - H^2}} - 1\right) - 2\xi\omega_n R^2 + R\dot{\beta}^2 \pm \ddot{u}_g \cos\beta \mp g\sin\beta \\ \ddot{\beta} = \dfrac{-2\dot{R}\dot{\beta}}{R} \mp \dfrac{g}{R}\cos\beta \mp \dfrac{\ddot{u}_g}{R}\sin\beta \end{cases} \tag{1.15}$$

Where the plus/minus refers to the uplift of the right edge or the left respectively. The first line of Equation (1.15) represents the equilibrium of all forces acting on the system along the radial vector from the pivot point. The second line is the moment equilibrium condition along the direction tangential to rotation of the mass. It obvious that the equations are highly non-linear. The equation of motion for the rigid system depends on the Lagrangian parameters β and may be obtained as a limit case of second of Equations (1.15) by setting $R=R_0$. Equation 1.15 can be expressed in terms of the classical parameters u, θ. Assuming neglected the quadratic Lagrangian displacement and velocity and the elastic displacement are assumed small compared with the model width and by deriving the Equations 1.14 twice to obtain respectively $\dot{u}$, $\dot{\theta}$; ü, $\ddot{\theta}$ and after a substitution of this new values into the Equation 1.15 the results is:

$$\ddot{\theta}+\frac{H}{R^{2}}\ddot{u}\mp\frac{2B}{R_{0}{}^{2}}(\dot{\theta}+\frac{H\ddot{u}}{R_{0}{}^{2}})\dot{u}=-\frac{1}{R_{0}}(\ddot{u}_{g}\cos(\pm\alpha-\theta)+g\sin(\pm\alpha-\theta)) \tag{1.16}$$

Where the natural frequency of the system and the dumping factor are respectively:

$$\omega\ \omega_{n,u}=\frac{R_{0}}{B}\omega_{n} \qquad ; \qquad \xi_{u}=\frac{R_{0}}{B}\xi \tag{1.17}$$

The structure start begins to rock when the overturning moment due to the external loads reaches the available resting moment due to gravity and the ground acceleration; therefore, the equation is defined as show below, where the upper sign is defining the uplifting in the right edge:

$$\mp mH(\ddot{u}+\ddot{u}_{g})>mg(B\mp u) \tag{1.18}$$

The definition of the phase is particularly delicate because after impact the system may proceed with a new rocking phase or remain in a full contact phase. With the aim to determine in which phase the model could be, an energetic approach was proposed. The fictitious full contact phase happens when, upon impact, the deformation of the body continues only in the field of pure elastic deformation. Assuming the conservation of the angular momentum, it is possible achieve the Equation 1.19 for the post impact velocity after a fake full contact phase.

$$\dot{u}_{2}=\mp\left(\frac{2B}{R_{1}}\right)\dot{R}_{1}+\left(1-\frac{B^{2}-u^{2}}{H^{2}}\right)H\dot{\beta}_{1} \tag{1.19}$$

Where the subscript 1 and 2 are respectively referred to the measures just before and just after the impact phase. After the impact phase $u_{2}=u_{1}$ and $\theta_{2}=\dot{\theta}_{2}=0$, hence the kinetic energy in the transition full contact phase is given by:

$$E_{fc}=\frac{1}{2}m\dot{u}_{2}^{2} \tag{1.20}$$

The post-impact parameters of the rocking phase are also derived assuming the conservation of the angular momentum on the impact corner; where are also considered the effect of the elastic behaviour of the model in the following formulation (Equation 1.21) and assuming that the elastic translational velocity remains the same before and after the impact. It is possible write the second equation for the post-impact velocities as:

$$\dot{\beta}_2 = (\frac{H^2 - B^2 + u^2}{R^2{}_2})\dot{\beta}_1 \mp (\frac{2HB}{R_1 R^2{}_2})\dot{R}_1 \tag{1.21}$$

$$\dot{R}_2 = -\dot{R}_1 (\frac{R_1}{R_2})(\frac{B \pm u}{B \mp u}) \tag{1.22}$$

It is important to underline that the elastic effect are neglected in Equation 1.20, this equation becomes the same as Equation (1.5). The kinetic energy is given by the following equation:

$$E_r = \frac{1}{2} m(R^2{}_2 \dot{\beta}_2^2 + \dot{R}_2{}^2) \tag{1.23}$$

To determine when the system is in a new rocking phase or in a full contact phase the two values of the Equations 1.20 and 1.23 are compared. If the energy in the rocking phase is bigger than in the phase of full contact ($E_r > E_{fc}$) the system rocks by a rotating in the edge where all the previous conditions are satisfied, otherwise if the rocking energy is less than the full contact energy ($E_r < E_{fc}$) the model enter in the phase of full contact.

These equations are different from the ones already presented in literature and the results achieved from the simulations and parametric study confirm the superior stability of flexible rocking structures, initially questioned by Housner [6]. Nevertheless was demonstrated how the flexible structures are harder to uplift and easier to overturn than more stiff structures.

Previously some research was published with the aim to introduce the flexibility behaviour in the analysis. In particular Spyrakos at al. [23] develop a simple design criteria including the flexibility effects of slender structures to their overturning stability under instantaneous impulse. The develop was based on expressing the system deformation in terms of generalized coordinates. Their conclusion, after numerical examples, parametric studies and comparison was that flexibility reduces the magnitude of the spectral pseudo velocity which is the cause for overturning and how significant the lack of the flexibility is in the analysis where it is ignored in the develop of the overturning criteria.

The fundamental dynamics properties of the linear elastic oscillators, rigid rocking structures and flexible rocking structure are summarized and compared in the table below.

Parameters/ characteristics	***Linear elastic oscillator***	***Rigid rocking structures***	***Flexible rocking structures***
Restoring mechanism	Elasticity	Gravity	Gravity and elasticity
Restoring Force/Moment	$F_r = ku$	$M_r = -mgR_0 \sin(\pm\alpha - \theta)$	$M_r = -mgR_0 \sin(\pm\alpha - \theta) - m(\ddot{u})H$
Stable equilibrium	$u = 0$	$\theta = 0$	$u = 0$
Stiffness and stable equilibrium	Finite	Infinite	Finite
Stiffness away from stable equilibrium	Positive	Negative	Depend upon the phase of motion
Frequency parameter(s)	ω_n	P	ω_n ; P
Uplift amplitude and rocking phase angles	Uplift is not allowed	$\phi = f(\frac{A}{g\tan(\alpha)})$	$f(\frac{\omega}{\omega_n};\xi;\frac{A}{g\tan(\alpha)})$
Damping	Continuos,ξ	At impacts only, coefficient of restitution	Continuos and at impact

2.1 Table -Fundamental dynamics properties of the linear elastic oscillators, rigid rocking structures and flexible rocking structure[20, 24, 25]

1.4 Controlled Rocking and Hybrid Rocking Concept

Another important area of recent research in the rocking field is the emergence of controlled rocking and the hybrid rocking concept. The impact of the consequence of damage caused by earthquakes during the past decades have raised serious question about how the current building seismic design approach are satisfying the needs of the modern society. Usually the standard design is widely focused and based on the life prevention approach were structural and non-structural damage are accepted beyond the elastic limit and eventually with the develop of a mechanism that allows the formation of a number of flexural plastic inches. No other economic parameters, like the cost of damage and the cost associated followed by a loss of workability after a moderate-strong earthquake, are currently accounted inside the design project. The cost associated with the loss of business operation, structural damage and damage to equipment often, particularly in those centres of advanced technology, are comparable with the cost of the same building [26]. Due to the greater interest in the last decade a high–performance seismic resisting system based on post-tensioned, jointed ductile connections, with the aim to satisfy the currently increasing requirement of seismic design performance criteria is being developed. The common trend in emerging performance criteria is to reduce the level of damage and therefore the direct and indirect cost associated to the structural repair and business interruption.

The controlled rocking as a development of the of the pure rocking block by locating prestressed tendon(s) inside the block to increase the stability of the system (figure 1.8) ; where the first investigation was carried out by Aslam et al. in 1980 [27].

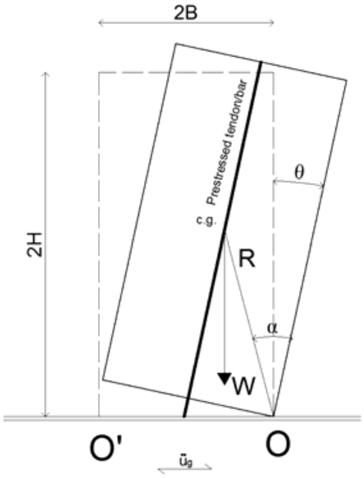

1.8 *Figure – Schematic block with controlled rocking*

The introduction of the post-tensioned tendon widely improve the stability of the block. Figure 1.9 compares the lateral response of a pure rocking block with an element designed with control rocking; where d_i is the distance between the position of the tendon and the pivot of rocking, T_{pt} is the initial prestressing force while K is the stiffness of the tendon(s) or bar(s).

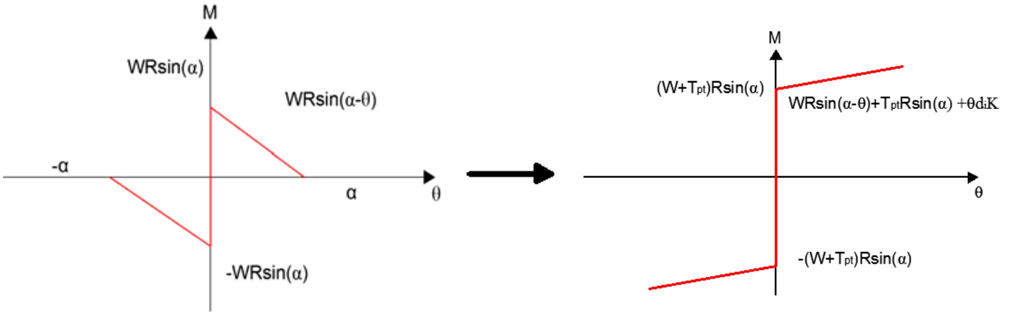

(a) *(b)*

1.9 *Figure – Comparison between pure rocking Moment Curvature (a) with Controlled Rocking (b)*

From the picture is easy to understand the two biggest advantages of the controlled rocking element, the first one is the significant increasing of the bilinear stiffness. The second one is that the overturning of the block is prevented. The system still remains non linear but the dynamic characteristics are now closer to the traditional ductile system [28]. With this next step in the theory of rocking motion, it is now possible adopt the traditional response spectra for the design.

In 1999 Makris and Zhang [29] performed the second last level development in the field of rocking element by adding a ductile anchorage, with a bilinear behaviour, at the pivot of rocking section. The researchers come to the conclusion that the restrainers are more efficient in prevent the overturning of small slender blocks subjected to low frequency ground excitations. Moreover stronger is the level of the restrain, smaller is the acceleration amplitude needed to overturn a rigid block from its rest position.

In the last decades some studies, conduced on jointed precast concrete frames [30], allowed to understand and predict the behaviour of deformable concrete bodies equipped with the controlled rocking system. The last level of performance in terms of controlled rocking is combining the self-centring capacity, provided by tendons or bars, with the energy dissipation obtained by installing dissipative devices or mild steel bars. This new concept of rocking element his called hybrid controlled rocking (Figure 1.10).

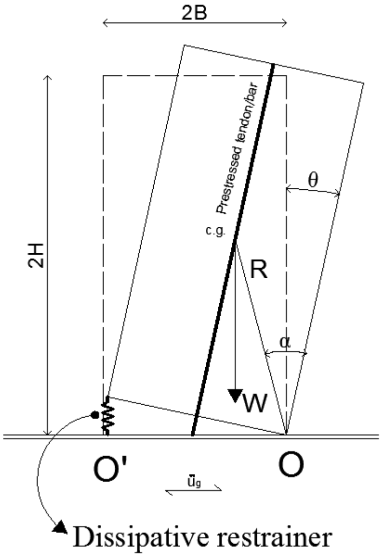

1.10 *Figure – Schematic of block with hybrid controlled rocking*

The adopting of hybrid rocking concept to rigid deformable bodies can achieved a considerable performance in terms of cycling motion behaviour. If the ratio between the self-centering capacity and the dissipation contribute are adequately balanced, the system is characterized by an hysteretic behaviour typically called "flag-shape" as showed in figure 1.11.

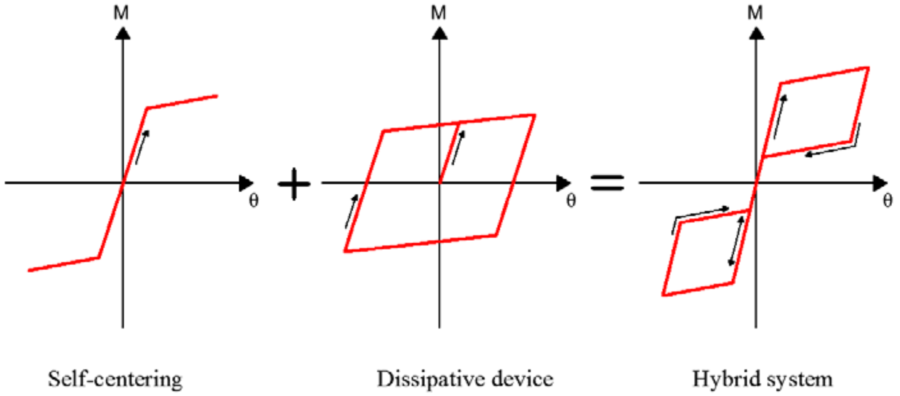

1.11 *Figure – Flag shape hysteresis rule for deformable concrete member designed with hybrid rocking.*

1.4.1 Section analysis method for concrete member with prestressed rocking connection

The section analysis theory for the concrete member with prestressed rocking connection loses one of the most important hypothesis in the standard design for normal concrete element: the Bernoulli theory. Thus it is not possible to consider anymore that the plane of the section remains plane, hence the section compatibility between steel and concrete is not more applicable ($\varepsilon_c \neq \varepsilon_s$). Therefore the moment-curvature analysis is no more appropriate; instead the moment-rotation analysis is performed. Due to this new behaviour of the section, a new alternative compatibility condition for the equilibrium at the global level is required.

The full step-by-step analysis to elaborate the moment-rotation response of a hybrid rocking connection (post-tensioning, rocking and dissipating device) was developed as part of the PRESSS program (PREcast Seismic Structural System) by Pampanin et al.[30] and published under the name of PRESS Design Handbook [31]. This method is called Monolithic Beam Analogy (MBA), as depicted in Figure 1.12, and it is assume that the lateral displacement of a post-tensioned rocking connection Δ_{pt} is identical to an Equivalent Reinforced Monolithic (EM) connection Δ_{mono} for the same lateral load, (Equation(1.21)). Moreover if the geometric and the reinforcement typology of the two different elements are considered equivalent, the rigid-plastic displacement contributes to a post-tensioned (PT) and the monolithic (MONO) element could be considered equated in Equation (1.22).

$$\Delta_{pt} = \Delta_{mono} \tag{1.21}$$

$$\theta_{imp} L_{cant} = (\phi_{mono} - \phi_y) L (L_{cant} - \frac{1}{2} L_p) \tag{1.22}$$

Where θ_{imp} is the rotation at the rocking section, L_{cant} is the cantilever length of the element and L_p is the length of the plastic hinge in the monolithic element. The concrete strain ε_c, of the equivalent element, can be evaluated within the PT connection starting from Equation (1.22) by considering $\phi = \varepsilon_c / c$. Where ε_c is the theoretical concrete strain and c is the depth of the neutral axes at the rocking section.

$$\varepsilon_c = \left[\frac{\theta_{imp} L_{cant}}{(L_{cant} - \frac{1}{2} L_p} + \phi_y \right] c \tag{1.22}$$

The length of the plastic hinge can be calculated using the Equation (1.23) below designed by Priestley et al., in which k is the measure of the spread of plasticity, $k = 0.2(f_u / f_y - 1) \leq 0.08$; L_{sp} is the length of the strain penetration, $L_{sp} = 0.002 f_y d_b$ (d_b is the diameter of longitudinal bars); f_y and f_u are the yielding and ultimate stress of the longitudinal reinforcement respectively.

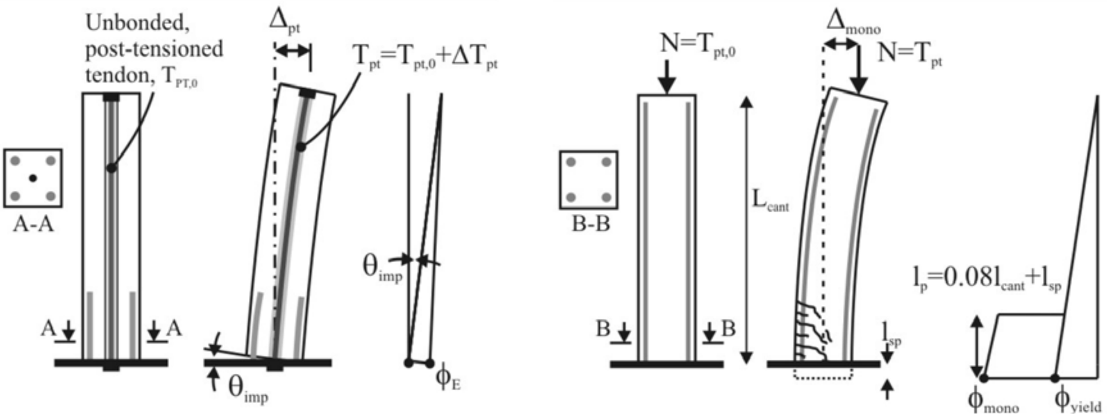

(a) Displacement components of a monolithic connection

(b) Displacement components of a post-tensioned connection

1.12 - *The Monolithic Beam Analogy (MBA) [28]*

After the first publication, the Member Beam Analogy was revised in 2004 by Palermo [32] and substituted with *revised*MBA. He verified that the elastic displacement for both elements will be the same, if the physical and reinforcing geometry are the same, nevertheless the post-tension solution has more flexibility consequently to the gap opening at the rocking interface. In his research Palermo subdivided the Equivalent Beam Analysis in three regions of applicability in terms of displacement:

1) $0 \leq \Delta \leq \Delta_{dec}$
2) $\Delta_{dec} \leq \Delta \leq \Delta_y$

3) $\Delta_y \le \Delta \le \Delta_u$

Where Δ_{dec} is the displacement at the decompression point, Δ_y is the displacement at the yielding point and Δ_u is the displacement at the failure point.

The first region is characterized by the same behaviour of the both beam. In this range the maximum concrete strain in the monolithic element, $\varepsilon_{c,mono}$, and at the border of the rocking interface $\varepsilon_{c,pt}$ are the same and described by the following equation:

$$\varepsilon_{c,pt} = \varepsilon_{c,mono} = \varepsilon_0 + \phi_{mono} \cdot \frac{1}{2} D \tag{1.23}$$

Where ε_0 is the initial compression strain in the section due to the presence of the axial load or initial prestressing force; D is the depth of the section and Φ_{mono} is the curvature at the bottom section of the monolithic cantilever with an applied lateral force F. The equivalence between the two elements keep going until the action of the decompression force. Before this point only a single calculation for both columns is required, therefore the value of the displacement, of the force and the concrete strain are evaluated with the Equations mentioned below:

$$F_{dec} = \frac{M_{dec}}{L_{cant}} = \frac{(N + T_{pt,0}) \cdot D}{6L_{cant}} \tag{1.24}$$

$$\Delta_{dec} = \frac{\Phi_{dec} \cdot L^2_{cant}}{3} = \frac{2(N + T_{pt,0}) \cdot L^2_{cant}}{3E_c BD^2} \tag{1.25}$$

$$\varepsilon_{c,dec} = 2\varepsilon_0 = \frac{2(N + T_{pt,0})}{E_c BD} \tag{1.26}$$

Where M_{dec} is the decompression moment; N the applied axial load; $T_{pt,0}$ is the initial post-tension force of the bar/tendon; Φ_{dec} is the decompression curvature; B the with of the section and E_c is the elastic modulus of the concrete.

The second rage put in relation the strain of the Equivalent Monolithic member with the Post-tensioned between the decompression to the yielding displacement. The lateral displacement is given by a rigid rotation of the element on the rocking interface and the elastic deformation:

$$\Delta_{pt} = \theta_{imp} \cdot L_{cant} + \Delta_e \tag{1.27}$$

Where Δ_e is the elastic displacement of the cantilever element and θ_{imp} is the rotation of the rocking interface. Instead the monolithic displacement is given by:

$$\Delta_{mono} = \frac{\phi_{mono} L^2{}_{cant}}{3} \tag{1.28}$$

It easy to evaluate that the difference in terms of lateral displacement in this region between the two different system due to a lateral force is exactly the rigid displacement rotation of the post-tensioned element, as show in Equation(1.29)

$$\theta_{imp} \cdot L_{cant} = \Delta_{mono} - \Delta_{dec} = \frac{\phi_{mono} L^2{}_{cant}}{3} - \frac{\phi_{dec} L^2{}_{cant}}{3} \tag{1.29}$$

Where rearranging the Equation (1.29) it is possible find the hypothetical concrete strain at the pivot of rotation in the rocking section.

$$\varepsilon_c = \left(\frac{3\theta_{imp}}{L_{cant}} \cdot \Phi_{dec} \right) \cdot c \tag{1.30}$$

In the third region the displacement of the post-tensioned element doesn’t change from the equation (1.27) above; while the displacement of the monolithic element becomes:

$$\Delta_{mono} = \frac{\phi_y L^2{}_{cant}}{3} + (\Phi_{mono} - \Phi_y) \cdot L_p \cdot \left(L_{cant} - \frac{L_p}{2} \right) \tag{1.31}$$

As in the second region above, after a rearrangement of the Equation (1.31) it is possible obtain the theoretical concrete strain at the pivot of rotation in the rocking section as depicted below.

$$\varepsilon_c = \left[\frac{\frac{3\theta_{imp}}{L_{cant}} - \left(\phi_y - \phi_{dec} \right)}{\frac{3L_p}{L_{cant}} (1 - \frac{L_p}{2L_{cant}})} + \phi_y \right] \cdot c \tag{1.32}$$

As declared at the beginning of this paragraph, the hypothesis of strain compatibility between concrete and steel is no more utilizable, hence the steel strain is valuated separately, by considering an imposed displacement along the rocking interface. If the steel strain remains in the elastic range, it can be calculated with the following the Equation(1.33). Where $\varepsilon_{ms,i}$ is the strain at the i-th layer of the mild steel; $d_{ms,i}$ is the distance from the pivot of compression for the i-th mild steel layer and $l_{ub,ms}$ is the unbounded length of the mild steel bars. While if the strain of mild steel exceeds the elastic range into the plastic behaviour, it can be evaluated with the Equation (1.34).

$$\varepsilon_{ms,i} = \frac{\theta_{imp}(d_{ms,i} - c)}{l_{ub,ms} + \frac{4}{3} l_{sp}} \tag{1.33}$$

$$\varepsilon_{ms,i} = \frac{\theta_{imp}\left(d_{ms,i} - c\right) + \frac{2}{3} l_{sp} \alpha_i \varepsilon_y}{l_{ub,ms} + 2 l_{sp}} \tag{1.34}$$

Where α_i is an elastic strain ratio defined in Equation (1.35) and the Equation (1.36) allow to compute the strain value in the post-tensioned tendons as:

$$\alpha_i = \left(\frac{f_{ms,i}}{E_s \cdot \varepsilon_y} \right) \tag{1.35}$$

$$\varepsilon_{pt,i} = \varepsilon_{pt,0} + \frac{n \cdot \theta_{imp}\left(d_{pt,i} - c\right)}{l_{ub,pt}} \tag{1.36}$$

Where $\varepsilon_{pt,0}$ is the initial strain in the post-tensioned tendons; n is the number of gap opening along the unbounded tendons length; $d_{pt,i}$ is the distance from the pivot of compression for the i-th tendons and $l_{ub,pt}$ is the unbounded length of the tendon. With this equations it is now possible to compute the resultans and satisfy the translational equilibrium (force equilibrium) and design the moment-curvature of the section for each increment of θ_{imp} to define the entire loading envelopment for the section. Usually the terms λ needs to be define at the start of the analysis.

$$\lambda = \frac{M_{pt} + M_n}{M_{ms}} \tag{1.37}$$

This equation define the ratio between the re-centring capacity with the dissipative energy characteristic of the system. Increasing λ due to having a big re-centring capacity and as a consequence guaranteing a small residual displacement; vice versa small values of a λ due to have more energy dissipation under the force applied but to the detriment of larger maximum residual displacement. In the figure below is showing how the area of the flag hysteresis change for the value of λ and how using different type of behaviour dissipating devices (yielding, friction, viscoelastic) the shape change; Figure (1.13).

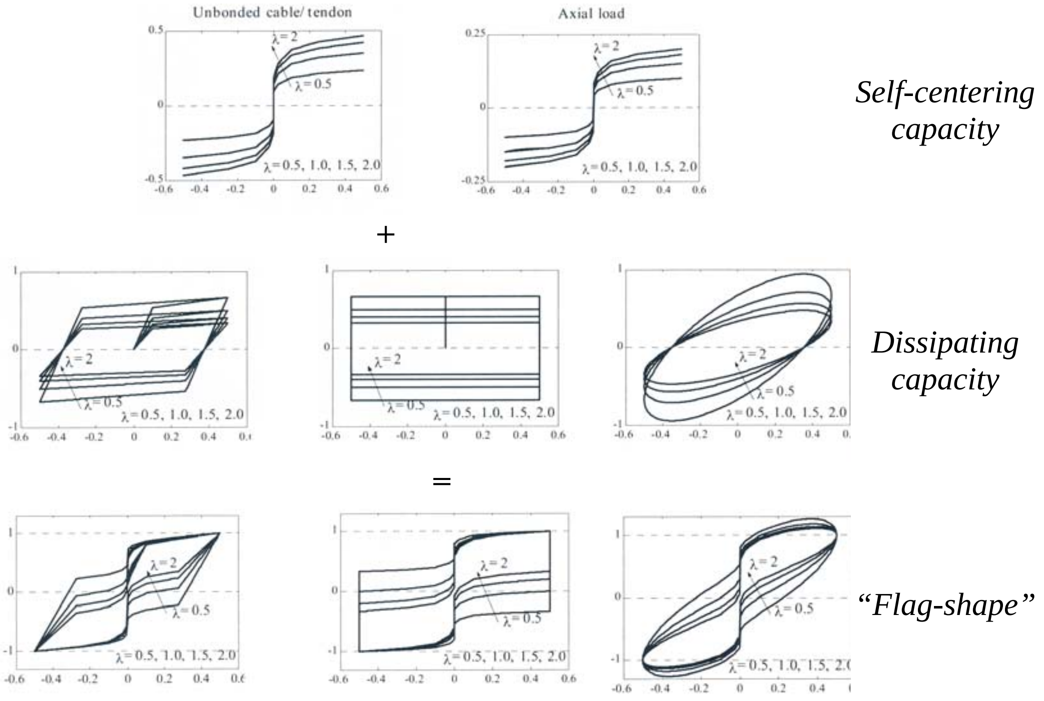

1.13 *Figure – Flag-shape hysteresis behaviour for different dissipation devices : elasto-plastic, friction, viscous-elastic[33]*

1.4.2 Lateral behaviour at a hybrid connection

In Figure(1.14) all the steps which describing the behaviour of an hybrid connection under horizontal load are showed.

(a) The point of decompression is reached when the moment given by lateral load reaches until the level of the moment of the post-tensioned tendon and the contribute given by the weight of the structure. This phase is characterized by a strain state where the fibres, diametrically opposite from the edge of rotation, approaching zero. The neutral axis depth, when the uplift starts, is located at the edge of the section and is characterized by a sudden reduction of stiffness when this is compared to the initial stiffness.

(b) The geometrically non-linearity point occurs when the neutral axis depth approaches the mid height of the total rocking section and consequently characterized by a additional reduction of stiffness.

(c) The point of yielding of the mild steel reinforcement can happen before or after the geometrically non-linearity point, because depending on how the section was designed and which is the dimension of the mild steel bars. At this point the section steals loosing his of stiffness but the total system starts to dissipate energy and the stability is still guaranteed by the fully workability of the tendons.

(d) The yielding of the prestressed reinforcement will have like a result the total loss of stiffness. The post-tensioned element, both tendons and bars, are characterized by an high elastic limit but meanwhile are inherently brittle with a minimal strain ductility. Once this point is reached the full centring behaviour of the system is compromised, at this stage some residual displacement is tolerated.

(e) The failing of mild steel reinforcement can be located in specific sections (unbounded length) and it is not, in general, equated to a total loss of stability. For this reason, during some rare events, the rupture of the mild steel may be tolerated; especially if the dissipation of the energy is charged to on external device, which can be replaced immediately after the event.

(f) The failing of confinement or the failing of prestressed reinforcement means that the ultimate limit of the structure is reached and causes a sudden loss of lateral stability.

(g) Loss of stability or overturning.

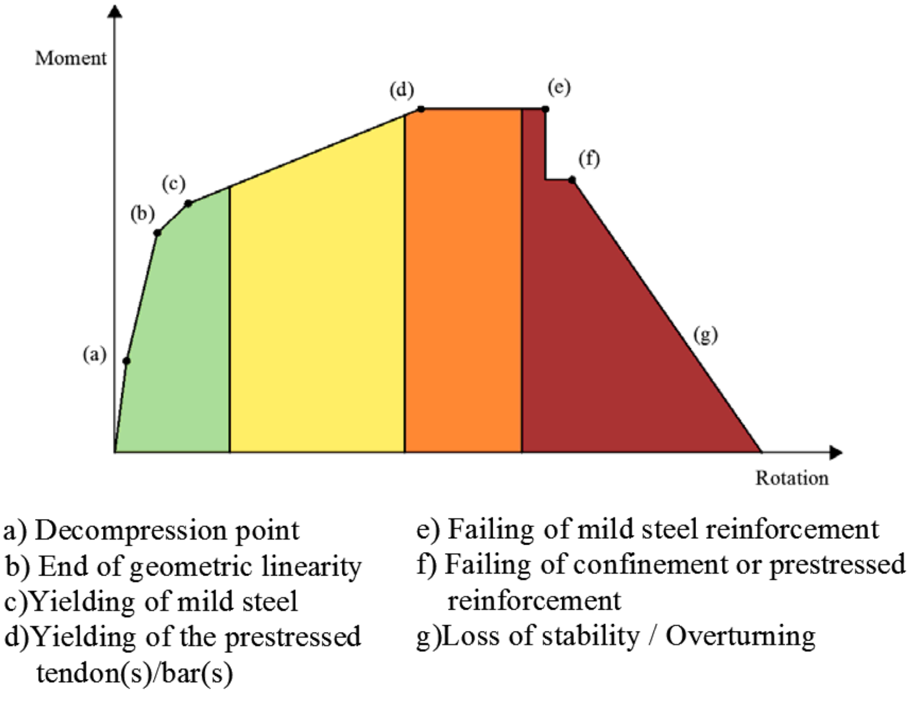

1.14 *Figure – Structural limit state of a post-tensioned rocking element.*

1.4.3 Practical development

The development of alternative solutions for precast concrete structures, based on ductile connection, began in the 1990s as part of the PRESSS program. The major intent was to improve the inelastic response, the design recommendation and provide an alternative solution to the emulation of the cast in place approach [34]. The US.PRESSS program was divided in three phases: the first one with the aim to develop and evaluate the concept of newly proposed structural system specifically concerned the practically the economic and seismic performance. The second phase involved the experimental and analytical studies about precast component and the last phase implicated the testing of a 60% scale, multi-storey precast building having structural moment resisting frames and shear wall elements.

Building designer are already moving towards low-damage and precast system technology (e.g. the 39-storey apartment building in San Francisco [35], Figure 1.9) for both structural and non structural components. Bridge engineering has to inherit those enhanced concepts and technologies. In fact in order to save lives and protect the economy, new social target which aim to limit business disruption to a minimum, it is vital that the bridges remain drivable after a natural disaster, such an earthquake [36].

1.15*Figure – From theory to practice. 39-storey apartment building in San Francisco, Paramount Building, equipped with rocking frame connection [35, 37]*

Currently in the United States, there is a strong momentum to develop Accelerated Bridge Construction techniques (ABC). In 2002 the American

Association of State Highway Transportation Officials (AASHTO) started a strong collaboration with several research institutes and universities with the aim to develop a strategic bridge plan, for the next years, to improve the bridge performance under different aspects [38-41]. At this time the most common practice is to have a prefabricated deck but a robust accelerated progress, in terms of construction, could be given by using precast columns and bend.

1.16 *Figure – Lake Belton Bridge, Texas-U.S.A.*

Examples of bridges constructed with segmental columns include the Louetta Road Overpass (SH-249, Texas), Linn Cove Viaduct (Grand-father Mountain, North Carolina), Sunshine Skyway Bridge (I-275, Florida), Varina-Enon Bridge (I-295, Virginia), John T.Collinson Rail Bridge Pensacola, Florida, Seven Mile Bridge (Tallahassee, Florida), Lake Belton Broidge (Texas, Figure 1.16) and the Chesapeake,Delaware CanalBridge (St. Georges, Delaware). However, the application of ABC for bridge pier is becoming more popular in the regions in non active seismic regions and are still limited in the regions with high seismicity due to the concerns about their seismic response [42].

Due to this scepticism and consequently to the success obtained with precast building researches and applications, in the last decades precast segmental concrete bridge construction has done substantial improvements [42, 43]. One of the first application end extension of controlled rocking or hybrid response was presented by Hewes and Priestley [44]. They first tested an unbounded post tensioned precast concrete segmental bridge columns under simulated lateral earthquake loading. It was found that the analytical model, created to predict the force displacement behaviour, was reasonable appreciable. Afterwards other finite-elements analyses were proposed on a monotonic unbounded concrete pier with the aim to study monotonic and cyclic behaviour [45, 46]. Palermo and Pampanin [47] [48], at the University of Canterbury, modelled and tested in quasi-static cyclic test in 2007, 1:3 scaled hybrid concrete bridge pier and one benchmark specimen representing a typical cast-in-place solution to enhanced the differ behaviour between the two different solution. In the hybrid solution the energy dissipation capacity was provided by internal mild steel dissipaters. The experimental results confirmed the advantages in terms of performance of jointed ductile connections compared to the traditional monolithic solutions. The main advantages underlined by the hybrid solution were: the lack of damage in the structural elements, the self-centering capacity provided by the unbounded tendon and the stable hysteretic behaviour up to high ductility levels. This results was confirmed with high satisfactory accuracy by the lumped plasticity model adopted. The civil structural department of University of Buffalo has a great interest in the field to develop and understand the behaviour of pre-cast segmental bridge pier. In 2008 Jui-Chen Wang et al. [49] tested four type of tall bridge pier in large scale distinguished by the different geometry of the segment, different high of the post-tensioned anchor, position of the internal dissipaters and different connecting section with the foundation. The results at the end of the test, confirmed by the finite element method, was that the piers an higher and anchored block on the bottom promising a better solution to the applications of tall concrete bridge columns with precast segmental construction in seismic region. Another significant experiment is the half scale fully precast segmental bridge subjected to an earthquake of magnitude 7.0 Richter [50] (Figure 1.17). The bridge remained functional with no structural damage after three shake table test in both vertical and horizontal direction. The bridge was not equipped with any kind of dissipaters devices but multi-rocking and sliding friction between the segments was allowed.

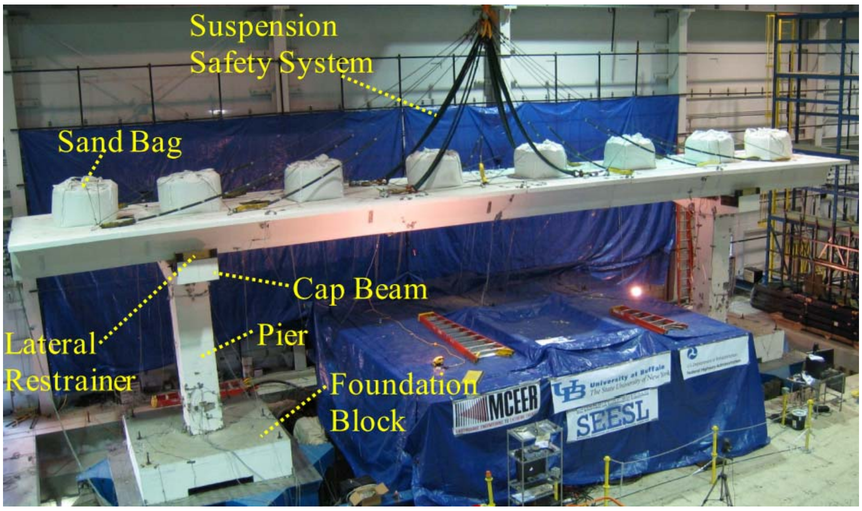

1.17 *Figure – Half-Scale post tensioned, segmented bridge system, after testing.*

Other researchers are focused on the seismic behaviour of Fiber-Reinforced-Polymer (FRP) and Concrete-Filled-Tube (CFT) [51-53] where the confinement given by the fiber can simulate a system of retrofitting for damaged pier.

Despite ABC becoming more popular in regions with low seismicity and in the last ten years a lot of research and tests was carried out on the field of ABC for bridge piers to understand the behaviour in high seismicity area. However the unfounded criticism and most of all the lack of a proper guidelines are delaying the spread of this technologies.

2

Dynamics of Multiple Rocking Rigid Block Columns

2.1 Introduction

Previously most of the research done in the field of multi segmental column was carried out by Manos [54-56] on the understanding behaviour of the ancient Greek and Roman ancient columns and colonnades. The columns are connected at the top with the epistyle, also composed of monolithic orthogonal blocks, spanning the distance between two columns. The seismic response mechanism that develop on this solid block structural system during strong ground motions can include sliding and rocking, thus dissipating the seismic energy in a different way from that of conventional contemporary structures (Figure 2.1).

This chapter presents an investigation of the behaviour of free multiple rocking rigid timber blocks under free oscillation decay and quasi sinusoidal input. Subsequently a controlled rocking system was tested with the same procedure. The intent of the study is to shed light on the dynamic process that occur when the multi segmented column is in free rocking motions or treated under quasi sinusoidal input. Particular focus is placed on the variation of the dynamic behaviour and gap opening between the multi rocking interfaces due to both the changing of the blocks dimension ratio and by the changing of friction coefficient.

2.1 *Figure – The real origin of rocking systems self centering and limited damage response under earthquake loading [57]*

2.2 Experimental Setup

The raw material used for this experiment is Laminated Veneer Lumber (LVL), which is an engineered wood product that provides a consistent high-performance alternative to solid lumber and steel structural uses. The mechanical characteristics are resumed in the table below [58]. The LVL timber was mainly chosen for simplifying the fabrication of the specimen.

Mechanical Property LVL		
Modulus of elasticity	*(MoE)*	11.0 [GPa]
Bending	*(f'b)*	48.0 [MPa]
Tension parallel to grain	*(f't)*	30.0 [Mpa]
Compression perpendicular to grain	*(f'p)*	12.0 [Mpa]
Compression parallel to grain	*(f'c)*	45.0 [Mpa]
Shear in beam	*(f's)*	6.0 [Mpa]

2.1 Table - Mechanical Property LVL

For this experiment were created eight different type of specimens, where two of those are monolithic blocks and the others six are composed by three independent blocks. The specimens, as show in the Figure 2.2, are composed by: Three Cubes (3Cu), Three Cubes with Rubber interface (3CuR), Monolithic block for 3Cu comparison (MCu), Three Rectangular Parallelepiped (3Rect), Three Rectangular Parallelepiped with Rubber interface (3RR), the Monolithic solution for the 3Rect comparison (MR) and a combination with one cube block at the bottom with two rectangular parallelepiped in both configurations, with and without rubber connection (1+2) (1+2R). The monolithic specimens are used to compare the experimental and mathematical results with the segmented solution. The prototypes cover three differ type of aspect ratio 1:3, 1:4, 1:5 and two type of contact between the interface of the blocks : timber-timber and rubber-timber. The second types of contact will assume three important meanings: first, the rubber between the segments and at the bottom interface has the function to prevent the sliding; second it increases the coefficient of restitution *r* and third it change radically the behaviour of the segmented rocking columns. The spring and the steel elements are used to simulate the controlled rocking system. Where the spring simulates the tendon\bar in the controlled rocking mechanism, the steel plates simulate a lumped mass at the top of the pier and the others four devices have the function to restrain the spring after the post-tension load.

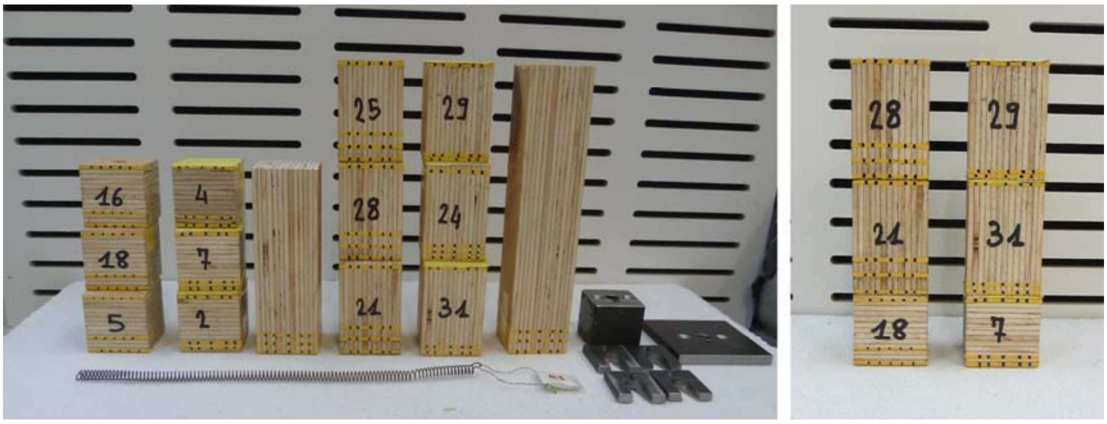

a) *b)*

2.2 *Figure – Specimens used in the tests: a)3Cu,3CuR,MCu,3Rect,3RR and MRect, b)1+2 and 1+2R*

Geometrical characteristic of the blocks and load plate

N. Block	*Base [mm]*	*Width [mm]*	*Height [mm]*	*Weight [g]*
2	*45.35*	*44.89*	*45.20*	*50.30*
4	*44.90*	*45.15*	*45.52*	*49.30*
5	*45.31*	*44.80*	*45.50*	*49.70*
7	*45.65*	*44.97*	*45.26*	*51.03*
16	*45.45*	*44.71*	*45.41*	*50.20*
18	*45.32*	*44.77*	*45.49*	*51.00*
21	*45.58*	*44.87*	*70.14*	*82.20*
24	*45.58*	*44.70*	*70.69*	*80.90*
25	*45.66*	*44.80*	*70.67*	*81.30*
28	*45.67*	*44.80*	*70.73*	*81.50*
29	*45.63*	*44.98*	*70.09*	*81.5*
31	*45.50*	*44.83*	*70.44*	*80.59*
Monolithic C.	*45.13*	*44.97*	*135.24*	*119.70*
Monolithic R.	*45.07*	*44.86*	*210.11*	*243.70*
Steel Plate 1	*80.00*	*80.00*	*10.00*	*409.86*
Steel Plate 2	*40.00*	*40.00*	*37.00*	*419.30*

2.2 *Table - Geometrical characteristic of the blocks and load plate*

The elastic constant of the spring was calculated using the formula below (formula 2.1). In mechanics and physics, Hooke's law of elasticity is an approximation that states that the extension of a spring is in direct proportion with the load applied to it. Many materials obey this law as long as the load does not exceed the material's elastic limit. Materials for which Hooke's law is a useful approximation are known as linear-elastic or "Hookean" materials. Where Δl is the displacement of the spring's end from its equilibrium position, F is the restoring force exerted by the spring on that end and k is is a constant called the rate or spring constant.

$$F = k \cdot \Delta l \tag{2.1}$$

Spring constant

F[N]	*L[m]*	*L'[m]*	*ΔL[m]*	*kg*	*K[N/m]*
0.00	*0.00*	*0.000*	*0.00*	*0.00*	*0.00*
9.81	*0.265*	*0.320*	*0.055*	*1.00*	*178.36*
13.73	*0.265*	*0.345*	*0.080*	*1.40*	*171.67*
15.73	*0.265*	*0.355*	*0.09*	*1.6*	*174.84*

2.3 *Table – Spring constant*

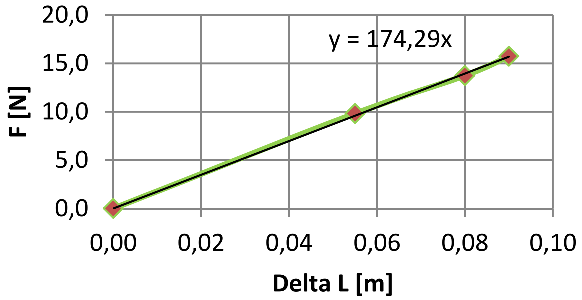

2.3 *Figure – Spring constant*

The post-tension forces used during the test are quantified in: 3.5N, 6N, 13N. Those values correspond at 20% fy, 40% fy, 75% fy of the spring.

For the Free Oscillation (FO) investigation the specimens, for each test run, were hold by hand in an apparently inclined rest position at the angle of 0.15 ± 0.01 rad , 8.60 ± 0.5 degree corresponding, and then released. Each test run was repeated at least three times. In total, over 240 test runs were completed.

The dynamic tests cover a range of frequency of motion from 2Hz to 6Hz in step of 1Hz and one more test run was done for 3.5Hz because is the frequency value in which most of the specimens start the rocking motion.

2.2.1 Shaking table and Accelerometer

The same specimens are used for the dynamic analysis on a small shaking table (Figure 2.4) to provide a quasi-sinusoidal input. The shaking table is 750 mm x 500mm and height 200 mm, its operational frequency is between 0Hz and 15Hz, the maximum fixed lateral displacement is 3.8mm in both direction and the max load capacity is more than 7kg. This shaking table works thanks to an elliptical bull wheel connected by a connection rod to a ram. The ram slides on rails and it is welded to the upper steel plate. Due to this type of connection is possible transfer the rotational motion of the wheel in to a sliding motion for the steel plate. The stroke of the steel plate is controlled by the geometry of the bull wheel. Therefore changing the dimension and the shape of the wheel it is possible obtain a differ shape of the wave and different stroke. Smaller displacement means small bull wheel, vice versa bigger wheel due to have a bigger displacement. Notwithstanding the shaking table was designed to have a sinusoidal wave of displacement in a 2D plane, due to the friction, the damping between the mechanical parts and the impossibility to transfer constantly the forces generated, the displacement\acceleration shape is not properly a sinusoidal wave. The shaking table is equipped with a very basic master controller box with only a rotational knob with which is possible varying the frequencies. However this device does not have any kind of display to show the input and output values. Therefore is essential equips the shaking table with an accelerometer (figure 2.5) or others devices.

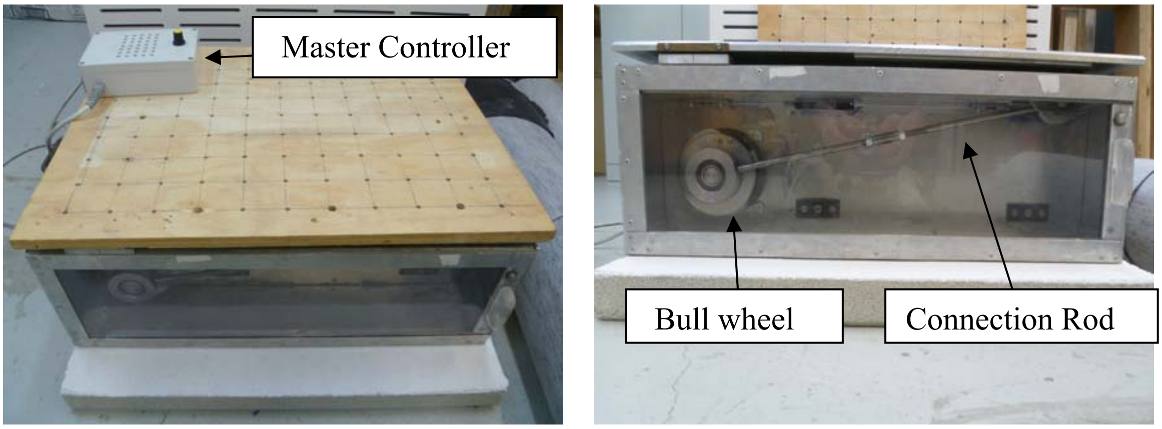

2.4 *Figure – Shaking Table*

On the market exist different kinds of accelerometers: piezoelectric accelerometers divided in mono axial accelerometers and tri axial accelerometers, ICPT and MEMS accelerometer. Usually to the set-up for to know the accelerations is composed by the accelerometer, standard coaxial high impendence cables, accelerometer power amplifier and a readout [59-61]. The high impendence cables from the accelerometer to the power amplifier constitute a crucial element for the acceleration measures. It must be a high isolation, a low noise and its could not exceed

2.5 *Figure – Accelerometer, accelerometer power amplifier, standard coaxial low impendence cable.*

a few meters. In this investigation it was used a piezoelectric tri axial accelerometer. It offer multiple advantages:

- It has High sensibility frequency range 1-30000 Hz.
- It is Strong and reliable.
- It can resist to high shock input.
- It is not composed by mobile part which can demote.

Nevertheless this accelerometer typology presents some limitation of use:

- It is not able to measure static accelerations
- It has some difficulty to measure frequency less than 1Hz.
- In the conventional devices the cables are a weak part of the system.

Piezoelectricity is a property possessed by certain crystals, e.g. quartz, it meaning that they have differing potential difference when subjected to mechanical deformation. This is a reversible effect and occurs with very small (nanometer) deformations. When to the face of the crystal are applied compression forces, tension forces or shear forces, due to the deformation generated, on the two faces born positive and negative charge. This difference in charge creates a potential gradient like in an electric condenser. The charges are proportional to the force (F) applied:

$$Q = d_{ij} \cdot F \tag{2.2}$$

$$Q = CV \tag{2.3}$$

Where Q is the charge, d_{ij} is the piezoelectric constant of the material, F is the force applied, C is the condenser capacity, V is the potential difference.

If the condenser is connected in to a electric circuit the differential of potential is proportional to the force applied, hence to the acceleration (Equation 2.4).

$$V = d_{ij}\frac{F}{C} = d_{ij}\frac{d}{\varepsilon_0\varepsilon_r S}F = d_{ij}\frac{d}{\varepsilon_0\varepsilon_r S}m\ddot{y} \tag{2.4}$$

Where ε are the dielectric constant, S is the area of the faces and d is the distance between the two faces.

The inputs transmitted by the shaking table to the specimens are showed in figure 2.6.

Frequency 2Hz

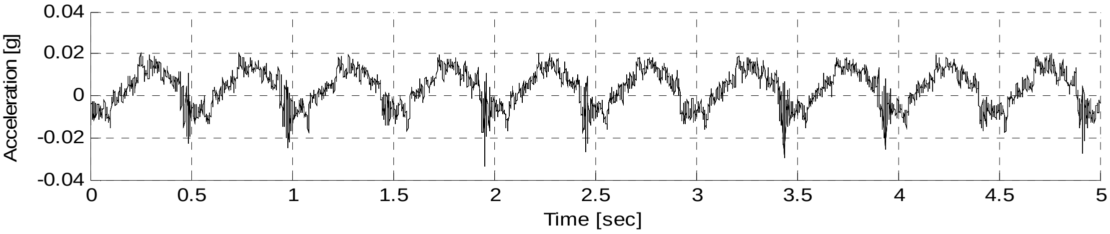

Frequency 3Hz

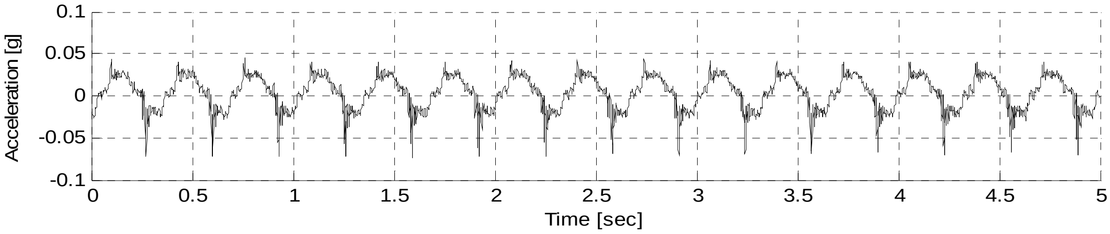

Frequency 3.5Hz

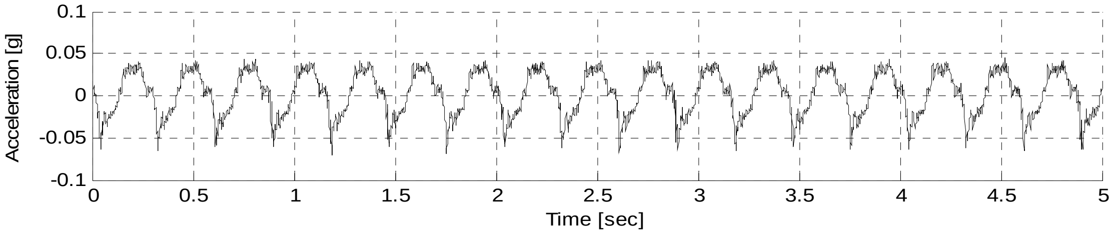

Frequency 4Hz

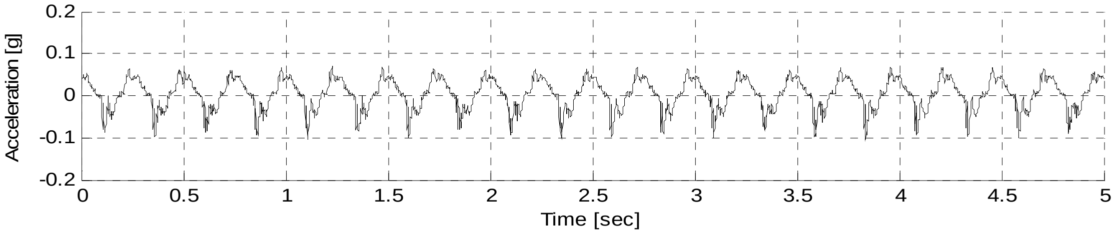

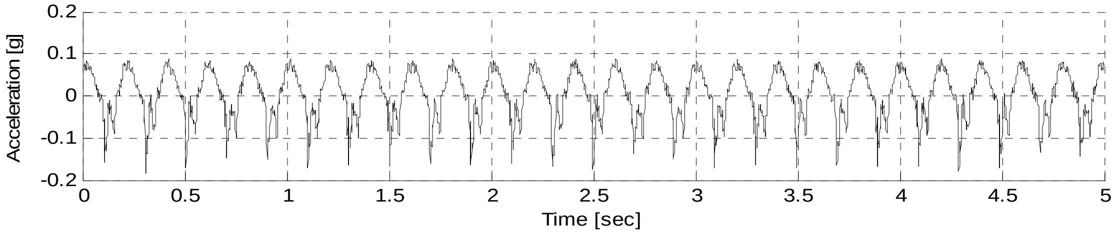
Frequency 5Hz

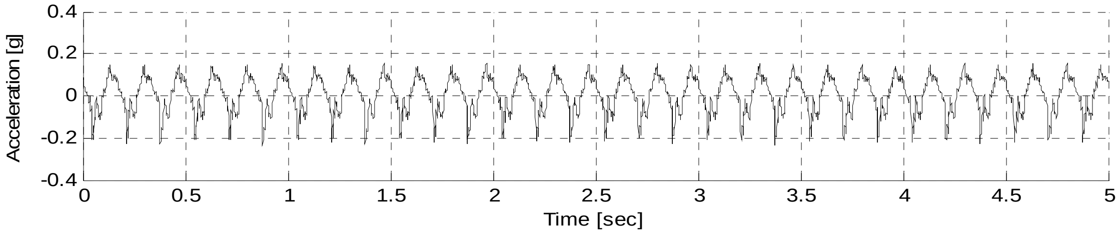
Frequency 6Hz

2.6 *Figure – Shaking table inputs*

2.3 Instrumentation and Data Acquisition

2.3.1 High-Speed Camera

The data were acquired by the use of a Casio EX-F1 (Figure 2.7). This model of High-Speed camera is equipped with a CMOS sensor and it has two mains settings mode to record the motion of the object: the high-speed Continuous Shutter (CS) and the High-Speed Movie (HSM) [62].

With the CS it is possible set the numbers of frame per second (fps) which are recorded from the camera from 1 fps to 60 images and even change speed image while the recording is in progress. Using this type of setting the images continue to be shot as long as the operator keeps the shutter button depressed and the quality of the images can be set to the highest resolution 1920x1080 pixel.

Use the HSM allow to the operators to record a High-speed movie at up to 1200 frame per second. The aspect ratio of movies recorded with this mode depends on the movie recording speed: more are the fps recorded more the images are in low quality; e.g. for 300 fps correspond an images quality of 512x384 px or for 1200 fps the images quality is 336x96. So it is compulsory find a compromise between the speed of the cam-record and the quality of the images. During HSM recording, Auto Focus (AF) and exposure remain fixed at the level they were when the user started recording. Moreover zoom back lighting correction, monitor screen content switching and AE Lock/AF lock are all disabled. When recording a HSM, light source flicker can cause horizontal band to appear in the image. This does not indicate malfunction of the camera but is one of the distortion effects that the acquiring system has. In the paragraph below are described the different kind of distortion that an High-Speed Camera can show during the image acquisition process.

For this experiment was used High-Speed Movie setting; 300 fps was chosen because the CS mode was not fast enough.

2.7 *Figure - Casio Exilim EX-1*

2.3.1.1 Sensor Artefact

On the market there are two types of sensors which can equip the camera: Charge-Coupled Device Image Sensor (CCD) and Complementary Metal Oxide Semiconductor Image Sensor (CMOS). While most of the camcorders on the market have traditionally used CCD sensors, many new camcorders are coming on the market are now using CMOS sensors. While CMOS and CCD both have unique properties that make each one suitable for one type of job or another, there are unique characteristics to each that need to be understood in order for a user to know whether a CMOS or CCD camera is more appropriate for the type of shooting they'll be doing. Choosing a CCD or CMOS system can have a very real impact on the type of footage you can gather, as well as ancillary impact such as the battery life of your camcorder (CMOS sensors are typically quite a bit more energy efficient, needing less electricity to power them and generating less heat than a comparable CCD.) CMOS sensors can scan and offload their footage quicker, making CMOS a more appropriate choice for high-speed cameras, for example. While CMOS and CCD sensors do the same basic job (gathering light and turning it into a video image), they go about it in different ways, how is showed in Figure 2.8, and the differences can have very significant impact on your footage [63].

There are four main characteristics sensors may exhibit. CCDs can suffer from vertical smearing on bright light sources, while CMOS sensors are immune to that artifact. But CMOS sensors (equipped with "rolling shutters") can exhibit skew, wobble, and partial exposure; CCD sensors are immune to those effects. And a CMOS sensor with a "global shutter" would also be immune to them, but since no current CMOS camcorders are equipped with global shutters.

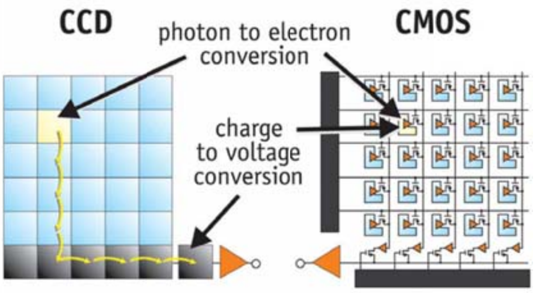

2.8 *Figure – How CCD and CMOS sensor work, [64]*

A *Global Shutter* exposes the entire imager simultaneously. The entire frame is exposed and begins gathering light; when the predetermined "shutter speed" has elapsed, the sensor stops gathering light and turns its current exposure into an electronic image. There is no physical "shutter" that covers and uncovers the sensor; it's all done with timing. At the start of exposure the entire sensor starts gathering light; at the end of exposure the light-gathering circuitry is turned off and the contents of the sensor are then "read out" to become an image.

A *Rolling Shutter* is very different. The rolling shutter actually exposes different portions of the frame at different points in time, "rolling" through the frame. Again, it's not an actual physical moving shutter that's doing this (as opposed to a movie camera, which actually has a moving physical shutter). Instead, the sensor is telling different portions to become light-sensitive at different moments in time, and as this process proceeds down the course of the full frame, until the entire frame is exposed. If the subject or the camera were to move during the exposure, the result would be reflected in the frame as one of the three Rolling Shutter Artifacts (Skew, Wobble, or Partial Exposure).

Skew is one of the more prevalent Rolling Shutter effects. With horizontal camera motion, vertical objects can look like they are "leaning". Skew and other rolling shutter artefacts are not affected by shutter speed, they are affected by the frame rate. Faster is the frame rate, less is the skew that you can see in the figure 2.9.

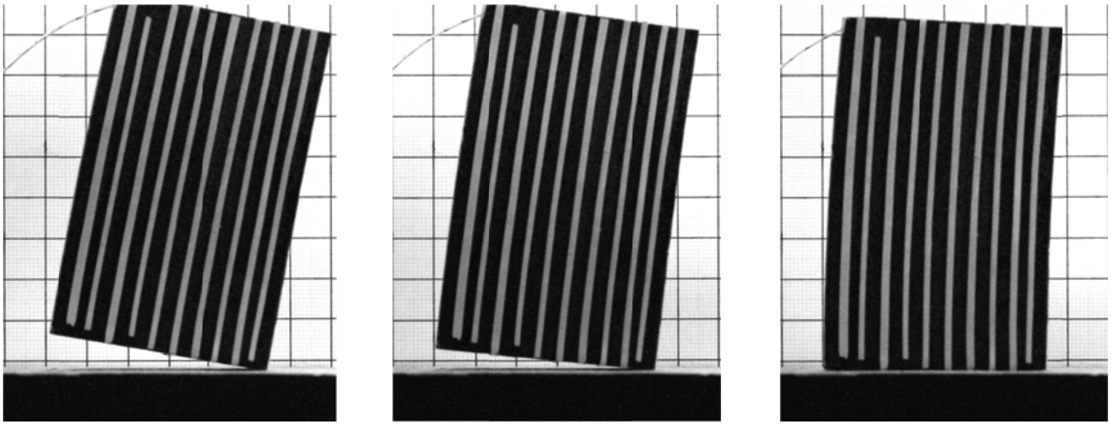

2.9 *Figure – Skew artefact*

Smear occurs when a very bright portion of an image causes an entire column of pixels to overload and bloom to white (Figure 2.10). Any bright point of light can potentially cause smear; common offenders include street lights and car headlights; it can also happen if the camera is shooting footage of a camera flash, or even the sun. Avoiding smear involves lowering the exposure enough that the bright lights don't bloom and trigger a column of smearing

2.10 *Figure – Smear effect*

Wobble is related to skew, and is caused by the same root causes. Whereas skew represent the leaning of vertical objects, wobble is a stretchy/rubbery look that happens to the video. Wobble is more likely to occur in handheld footage, or in situations where the camcorder is subject to vibration or sudden motion.

2.4 Data Analyzing

With the High-Speed camera was possible record until 2000 picture to describe the motion of the block. Now to pass from the images to the number was used a program wrote in MatLab called "Digital Image Correlation and Tracking with MatLab" ,which allow to characterized the entity and kind of the displacement.

Digital Image Correlation and Tracking (DIC/DDIT) is an optical method that employs tracking & image registration techniques for accurate 2D and 3D measurements. This is often used to measure deformation, displacement, and strain. Therefore with this technique strain, displacement and the others can be calculated from a series of consecutive images with sub pixel resolution.

Digital Image Correlation technique has been increase in popularity, especially in micro- and nano-scale mechanical testing applications due to its relative ease of implementation and use. Advances in computer technology and digital cameras have been the enabling technologies for this method. Early development in DIC field was led by researchers starting from early 1980s [65-67] and has been optimized and improved in the recent years [68-71]. DIC is predicated on the maximization of a correlation coefficient that is determined by examining pixel intensity array subsets on two or more corresponding images and extracting the deformation mapping function that relates the images (Figure 2.11)

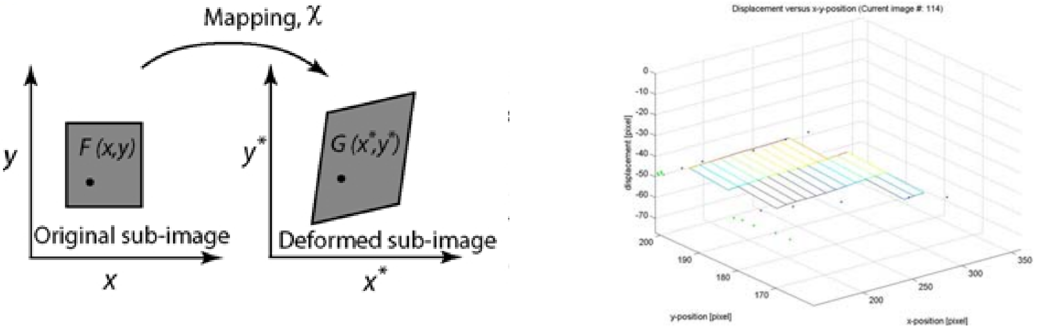

2.11 *Figure – Basic concept of Digital Image Correlation*

An iterative approach is used to minimize the 2D correlation coefficient by using nonlinear optimization techniques. The cross correlation coefficient r_{ij} is define as show below:

$$r_{ij}(u,v,\frac{\partial u}{\partial x},\frac{\partial u}{\partial y},\frac{\partial v}{\partial x},\frac{\partial v}{\partial y})=1-\frac{\sum_i\sum_j\left[F(x_i,y_j)-\bar{F}\right]\left[G(x_i*,y_j*)-\bar{G}\right]}{\sqrt{\sum_i\sum_j\left[F(x_i,y_j)-\bar{F}\right]^2\left[G(x_i*,y_j*)-\bar{G}\right]^2}} \quad (2.4)$$

Where $F(x_i, y_j)$ is the pixel intensity or the gray scale value at a point (x_i, y_j) in the undeformed image. $G(x_i* ,y_j*)$ is the gray scale value at a point (x_i*, y_j*) in the deformed image. $\bar{F}$ and $\bar{G}$ are mean values of the intensity matrices F and G, respectively. The coordinates or grid points (x_i, y_j) and (x_i*, y_j*) are related by the deformation that occurs between the two images. If the motion is perpendicular to the optical axis of the camera, then the relation between (x_i, y_j) and (xi*, yj*) can be approximated by a 2D affine transformation such as:

$$x* = x + u + \frac{\partial u}{\partial x}\Delta x + \frac{\partial u}{\partial y}\Delta y \quad (2.5)$$

$$y* = y + v + \frac{\partial v}{\partial x}\Delta x + \frac{\partial v}{\partial y}\Delta y \quad (2.6)$$

Where u and v are translations of the center of the pixel in the X and Y directions, respectively. The distance from the center of the pixel to the point (x,y) is denoted by Δx and Δy. Thus, the correlation coefficient r_{ij} is a function of the displacement component (u, v) and displacement gradients $\frac{\partial u}{\partial x},\frac{\partial u}{\partial y},\frac{\partial v}{\partial x},\frac{\partial v}{\partial y}$.

It is explained above how the program detects the difference between two or more pixels marked in to a row of consecutive images. The pixels are defined by different parameters and information given by saturation, shade, intensity and luminosity. With the aim to have a good and clean tracking, without the risk to lose the pixel marked during the analysis, it is recommended that there is a high contrast difference between the marks and the background. Color images are recommended because the pixels in the color image are defined by two more information: the color in black and white pictures is defined by a number, instead it need three coordinates (e.g. RGB color format) to be define, as show in the Figure 2.12 below.

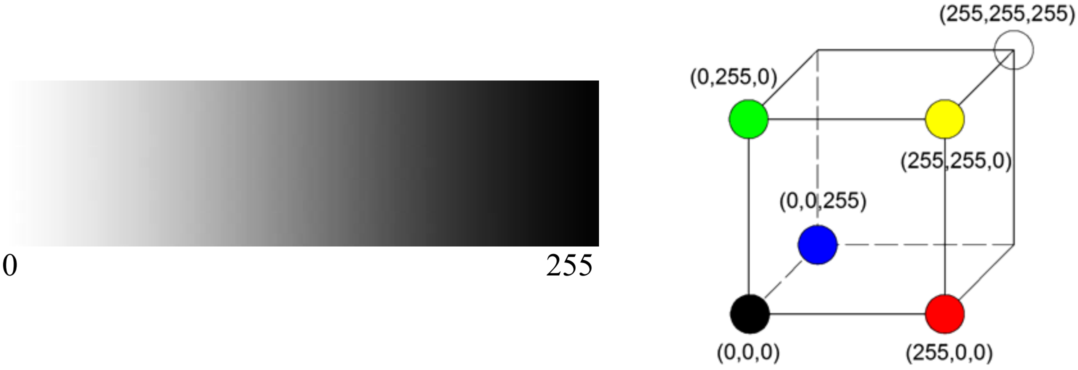

2.12 *Figure – Black & White array and RGB format*

The choice of the point to analyze depends on the purpose of your research. If the strain is the topic of the analysis, a surface grid is required. Instead if the aim is only to track the displacement of a rigid body, only a few points are need. The main purpose in this research is to analyze the displacements, so a simple grid was chosen, as show in Figure 2.13. The picture explains even how the track of the dots works. On the specimen were drawn some black dots in precise position with the aim to create an high contrast and define the position were the marks have to be chose. The green crosses characterize the position of the tracked pixel in the initial rest position at time t=0 [72]. The red crosses identify the movement of the pixel marked from picture to picture.

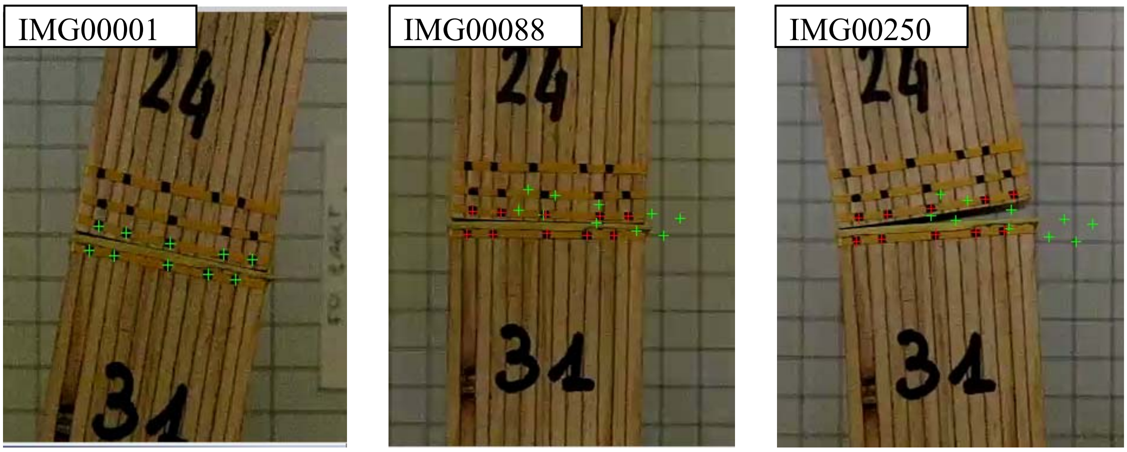

2.13 *Figure – The tracking of the marked dots/pixels*

The program at the end of the analysis gives in terms of results the values of the absolute displacement. It is refer to the relative reference system centred in each dots. The displacements obtained are in pixels and to transform the pixels in millimetres the user need to know how many pixels are present in known length. In this investigation the resolution of the camera permit to has 33px every 10mm, it means that every displacement of one pixel correspond 0.33 mm in the reality. Thanks to this easy conversion the users are able to know the real displacement obtained from the pictures. In this way knowing the relative displacement of each dot is possible identify and quantify the value of the gap opened between the two blocks throw an easy subtraction.

In these kinds of experiments it is important know the variation of the angle in the time with the purpose to know the entire kinematics of the blocks. To know the angle value it is necessary to connect two points in the same row throw the basic mathematical equation of the line passing to two points. Subsequently it is necessary to calculate the angular coefficient respect the horizontal line.

$$\theta(t) = \frac{y_2(t) - y_1(t)}{x_2(t) - x_1(t)} \tag{2.7}$$

Where x_2, y_2 and x_1, y_1 are the spatial coordinate of the two dots analyzed. Moreover the time value is also easy to calculate. It depends in how many frames per second the camera is set. In this first experiment the camera was set to record 300 fps, hence the time step between two frames is 0.0033 sec.

The next step is to calculate the angular velocity and the energy content during a rocking cycle. Those values are calculate throw the classical formulation of mechanics physics. Before in the previous steps, the angle and the time was determined and with this is possible calculate the velocity with a simple derivative in time as show in the formula 2.8 below.

$$\dot{\theta}(t) = \lim_{t\to 0} \frac{(\theta_{i+1} - \theta_i)}{(t_{i+1} - t_i)} \tag{2.8}$$

A rigid block with initial rotation begins to rock with a fixed gravitational potential energy, U^0. The energy is exchanged into kinetic energy, E_k, as the block start rotates and accelerates. When the block reaches the upright position, an infinitesimal moment before an impact, it is said to have zero gravitation potential energy and maximum kinetic energy equalling to the potential energy it began with. Immediately after an impact, the kinetic energy is reduced to $r \times U^0$ and the rocking motion begins again about a new rocking pivot, at a slightly reduced angular speed corresponding to the new energy content of the system, $r \times U^0$. The block then loses speed as it rocks further to the opposing peak, exchanging its kinetic energy with gravitational potential energy. When it reaches the peak rotation, the block again has maximum potential energy, U^1, and zero kinetic energy. Half of a rocking cycle is now complete at this point and the motion begins again as before but in the opposite direction. This is illustrated diagrammatically in Figure 2.14 [73].

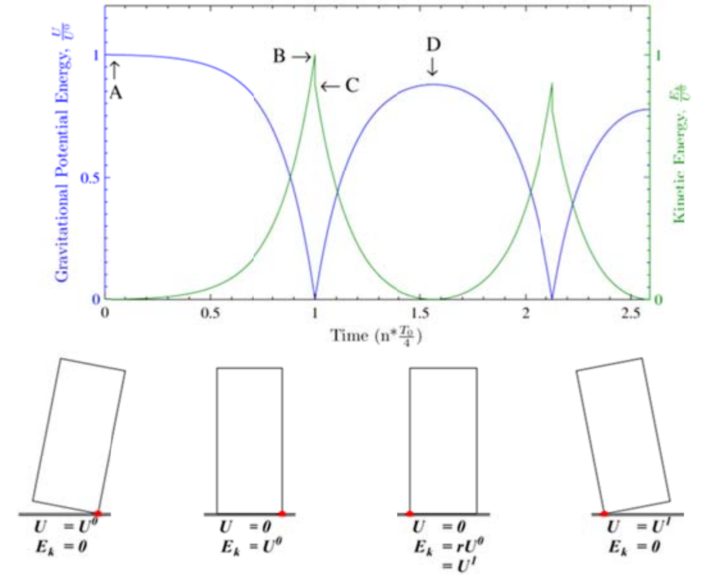

A) The block is released and it begins to rotate counter clockwise.

B) The block returns to the upright position. It has zero potential energy and is travelling at maximum speed.

C) The block switches to a new rocking pivot smoothly, but the impact causes the block to lose speed and hence kinetic energy.

D) The block comes to a stop at the opposing peak rotation. It has zero kinetic energy and maximum potential energy. The cycle repeats in the opposite direction.

2.14 *Figure – Idealised energy content during a rocking cycle*

Mathematically, the energy content of a rocking block can be evaluated by Equations 2.9 and 2.10 below.

$$E_k(t) = \frac{1}{2} I_0 \dot{\theta}^2 \tag{2.9}$$

$$U(t) = mgR(\cos(\alpha - |\theta|) - \cos(\alpha)) \tag{2.10}$$

Moreover, if energy is conserved during the smooth phases of a rocking cycle, as assumed in Housner's simple rocking motion theory, the energy lost through an impact can be estimated by considering the energy of the system at the peak rotation of the cycle before and after the impact.

$$r = \frac{E_k^{i+1}}{E_k^{i}} = \frac{U^{i+1}}{U^1}$$

$$r = \frac{mgR(\cos(\alpha - |\theta_{peak}^{i+1}|) - \cos(\alpha))}{mgR(\cos(\alpha - |\theta_{peak}^{i}|) - \cos(\alpha))} \tag{2.11}$$

$$r = \frac{\cos(\alpha - |\theta^{i+1}_{peak}|) - \cos(\alpha)}{\cos(\alpha - |\theta^{i}_{peak}|) - \cos(\alpha)}$$

Where U^i potential energy content at the time of peak rotation before impact i (θ^i_{peak}) (A in Figure 2.14), E_k^i is kinetic energy content just before impact i (B in Figure 2.14), U^{i+1} Potential energy content at the time of peak rotation attained after impact i (D in Figure 2.14) and E_k^{i+1} Kinetic energy content just after impact i (C in Figure 2.14).

2.5 Preliminary Numerical Simulation

A preliminary numerical simulation was done even to predict the response in advance, even to compare the results obtained by the experiments. The simulation was carried out only for both monolithic solutions: specimens Mcu and MR. The equation of the motion was solved by MatLab using a Newmark-β integration algorithm, more specify the Constant Avarage Acceleration Method; Figure 2.15.

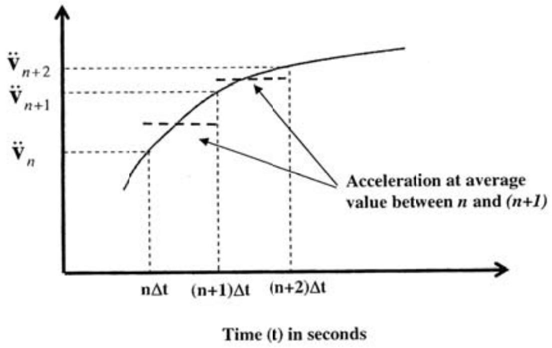

2.15 *Figure - Newmark-β, Constant Avarage Acceleration Method*

The Newmark-beta method is a method of numerical integration used to solve differential equations. It is widely used in numerical evaluation of the dynamic response of the structures and solids such as in finite element analysis to model dynamics systems. The method is named after Nathan M. Newmark, former Professor of Civil Engineering at the University of Illinois, who developed it in 1959 for use in structural dynamics. It is verified that the constant average acceleration method (CAAM) is spectrally stable for nonlinear system in a whole integration procedure based on a linearized stability analysis [74]. The first step is start from the equation of motion for a single degree of freedom, where the initial value problem is to find a solution v=v(t) to satisfy the given initial condition v(0)=d_0 and $\dot{v}(0) = v_0$. CAAM can be used to obtain the approximate solution and its general formulation is:

$$m\ddot{v}_{i+1} + c\dot{v} + kv = f \tag{2.12}$$

$$
\begin{aligned}
m\ddot{v}_{i+1} + c\dot{v}_{i+1} + kv_{i+1} &= f_{i+1} \\
v_{i+1} &= v_i + (\Delta t)v_i + \beta(\Delta t)^2(\ddot{v}_i + \ddot{v}_{i+1}) \\
v_{i+1} &= v_i + \gamma(\Delta t)(\ddot{v}_i + \ddot{v}_{i+1})
\end{aligned}
\tag{2.13}
$$

Where v_{i+1}, $\dot{v}_{i+1}$, $\ddot{v}_{i+1}$ are approximations to the displacement, velocity and acceleration at the (i+1) –th time step, respectively; and f_{i+1} is the external force at the (i+1) –th time step. β and γ are two parameters which determine the type of the Newmark-β integration tha the program will use. With β=1/4 and γ=1/2 will use the Constant Average Acceleration Method, with β=1/6 and γ=1/2 will use the Linear Acceleration method. To apply the proposed evaluation technique to asses numerical properties of an integration method in the solution of non linear system the changes of the structural properties in the computing sequence for each time step must be realistically reflected. After substituted the terms β and γ and after some step and re-arrangement the Equations 2.13 became:

$$
\begin{aligned}
\left(\frac{4m}{\Delta t^2} + \frac{2c}{\Delta t} + k\right)v_{n+1} &= f_{n+1} + m\left(\frac{4}{\Delta t^2}v_n + \frac{4}{\Delta t}\dot{v}_n + \ddot{v}_n\right) + c\left(\frac{2}{\Delta t}v_n + \dot{v}_n\right) \\
\dot{v}_{n+1} &= -\dot{v}_n + \frac{2}{\Delta t}(v_{n+1} - v_n) \\
\ddot{v}_{n+1} &= \frac{4}{\Delta t^2}(v_{n+1} - v_n - \dot{v}_n\Delta t) - \ddot{v}_n
\end{aligned}
\tag{2.14}
$$

In the case of free oscillation f is equal to zero and the initial conditions to set are v=θ equal to the starting inclination angle, velocity and acceleration equal to zero. The damping term c is even equal to zero. Apparently imposing c=0 there is not dissipation of energy, but in the code have to be set coefficient of restitution r, which is activate every time the block impact the ground surface. To explain the rocking behaviour of a rigid block one more condition must to be sets. It has the aim to switch the equations 2.14 from the positive angle to the negative angle when the block change the pivot of rotation.

Usually this equation is solved iteratively. Hence, θ is replaced by $\theta_{i+1}^{(n)}$ in an iteration procedure and $\theta_{i+1}^{(n)}$ represent the angle after n iterations at the (i+1) steps for which given convergence tolerance is satisfy. It is worth nothing that the angle at the end of the i-th time step is usually used to start the iteration and thus $\theta_{i+1}^{(0)}=\theta_i$. Hence, after sub-stituting $\theta_{i+1}^{(0)}$ into Eq. (2.14), the resulting angle is found to be the $\theta_{i+1}^{(1)}$ for the first iteration. This iteration procedure can be repeated until the difference between the two consecutive iteration less than or equal to a fixed tolerance limit. As a result, a convergent solution can be achieved if the specified convergence criteria is satisfy.

2.5.1 Comparing Experimental Results against Housner's model

A typical displacement time-history of a test-run is presented in Figure 2.16. in this figure, the block with an initial rotation appeared to come to rest as a typical viscously damped linear elastic system. On a closer inspection the system does not have a constant natural period, but instead the period of vibration decreases as the peak amplitude of each quarter cycle is decreased, this is a characteristic sign of a nonlinear rocking system.

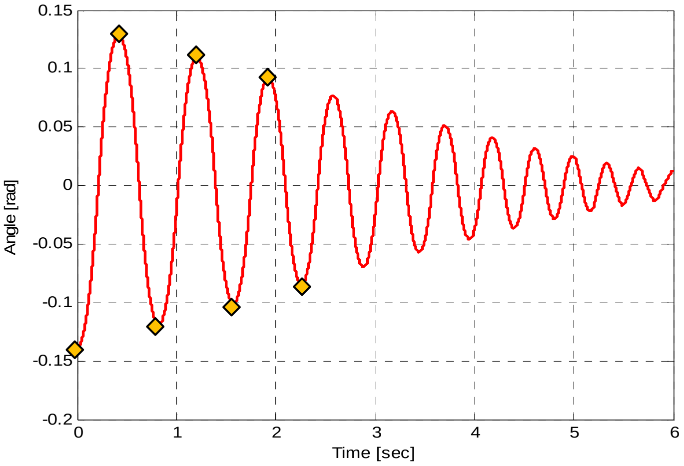

Time [sec]	***θ [Rad]***	***Period [sec]***
0	*-0.14*	*0.821*
0.213	*0*	
0.425	*0.129*	
0.625	*0*	
0.821	*-0.119*	
1.019	*0*	*0.749*
1.206	*0.110*	
1.395	*0*	
1.570	*-0.10*	
1.755	*0*	*0.689*
1.900	*0.090*	
2.097	*0*	
2.259	*0.084*	

2.16 *Figure – Typical rocking time history*

Comparing the test run for the mono-block solution against the numerically simulated results based on the Housner's simple rocking model (SMR) revealed some inconsistencies. Figures below show the time history comparison of the numerically simulated result against the experimental results obtained by a typical test run for the Mcu and MR solutions. These plot highlights that the standard SRM only adequately simulates the motion. The matching is improved for the firs few cycle of the motion in the time domain.

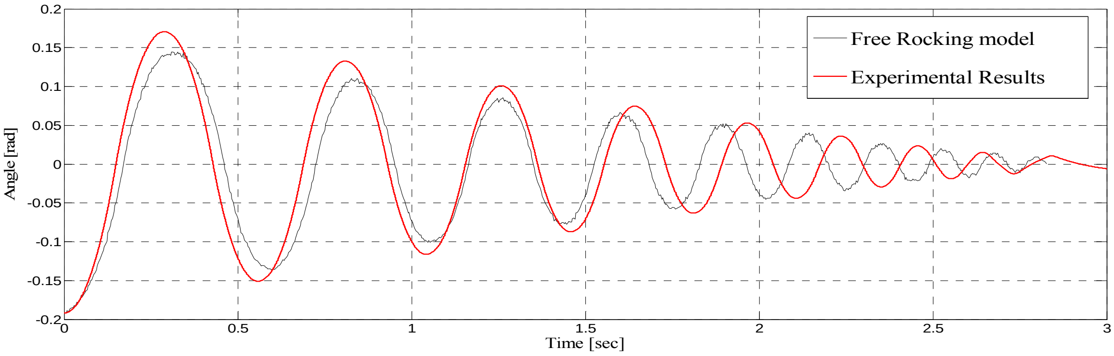

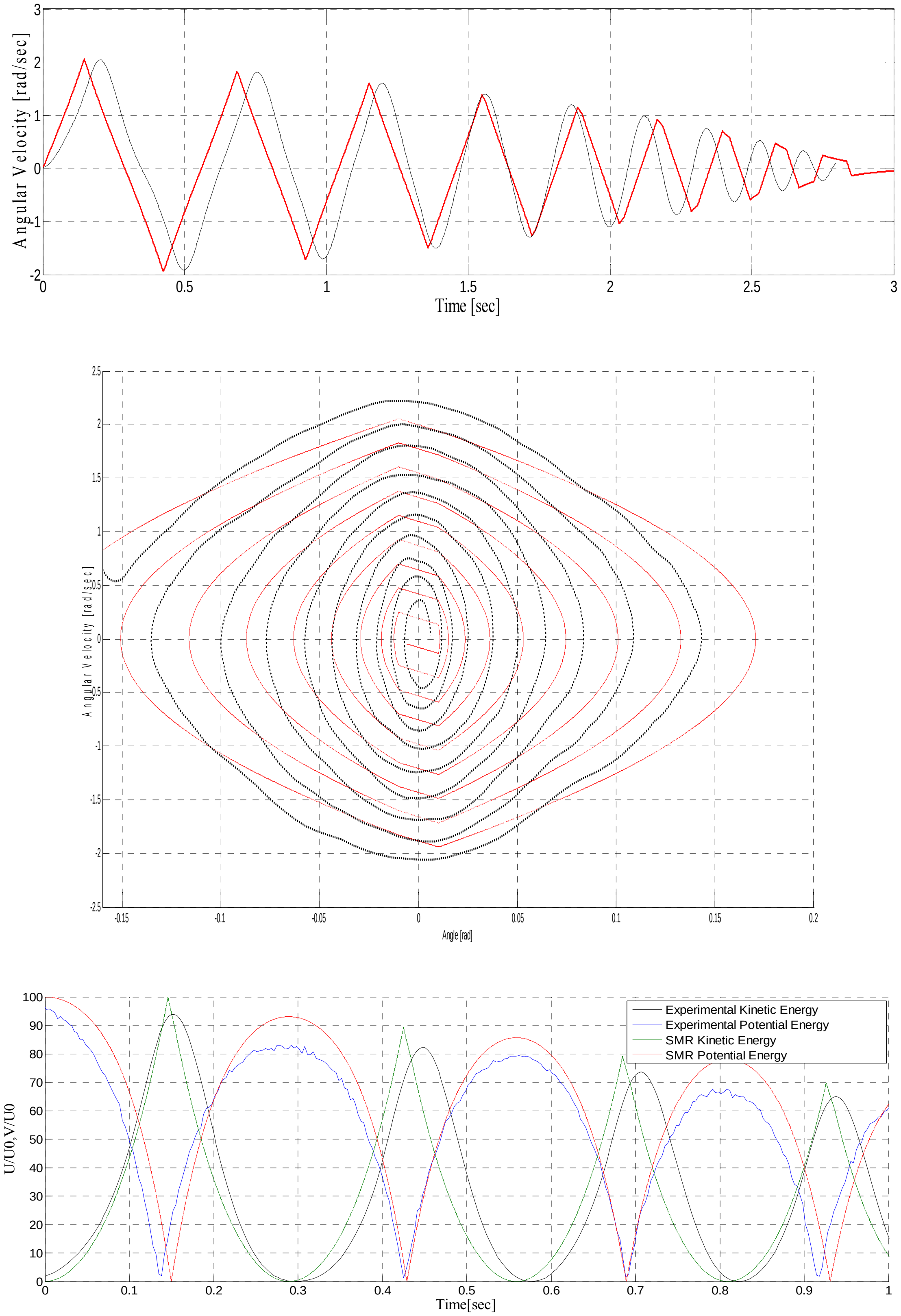

2.17 *Figure – Typical experimental and simulated results for a MCu block*

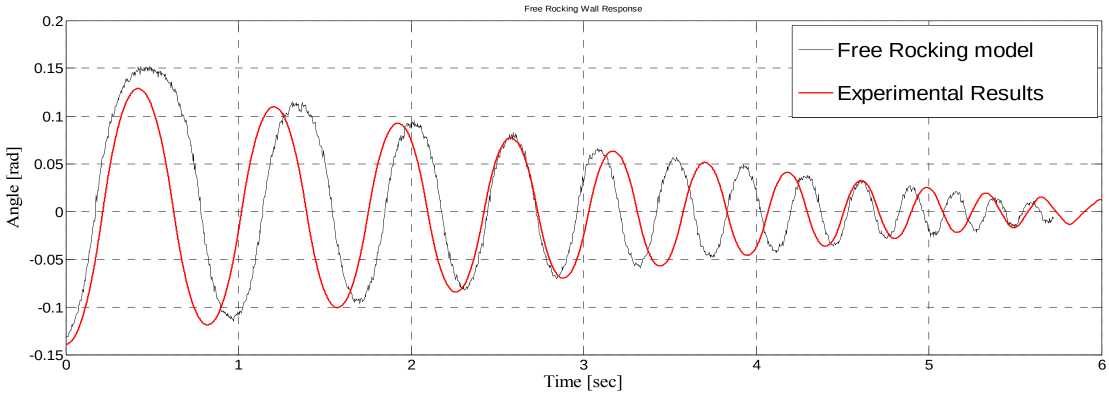
Free Rocking Wall Response
Free Rocking model
Experimental Results
Angle [rad]
0.2
0.15
0.1
0.05
0
-0.05
-0.1
-0.15
0
1
2
3
4
5
6
Time [sec]

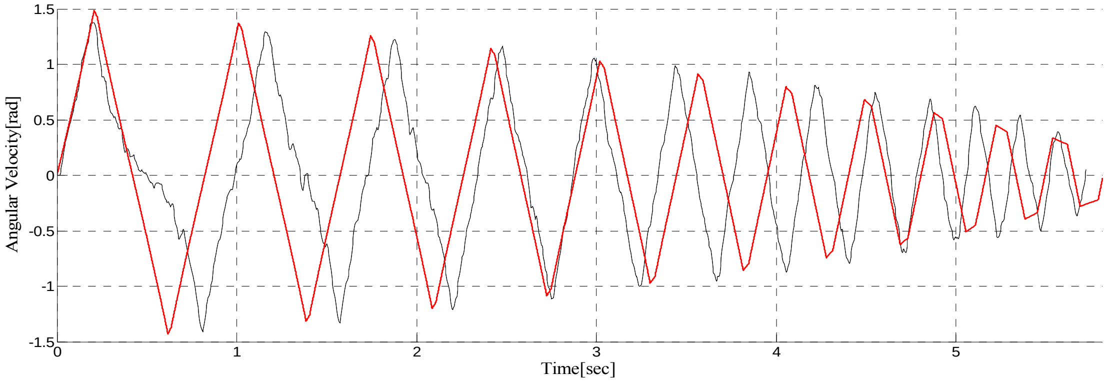
Angular Velocity[rad]
1.5
1
0.5
0
-0.5
-1
-1.5
0
1
2
3
4
5
Time[sec]

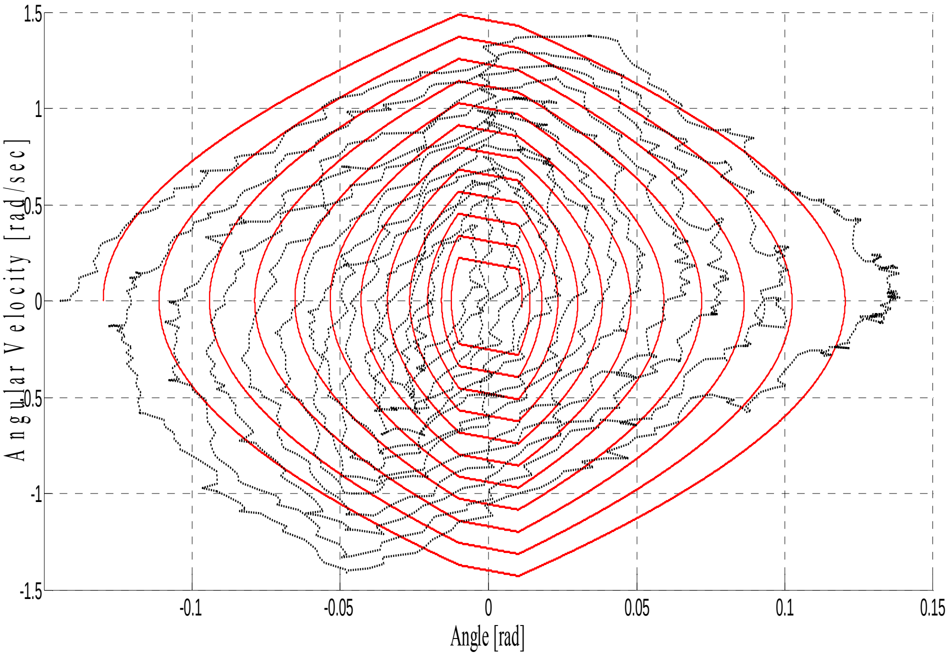
Angular Velocity [rad/sec]
1.5
1
0.5
0
-0.5
-1
-1.5
-0.1
-0.05
0
0.05
0.1
0.15
Angle [rad]

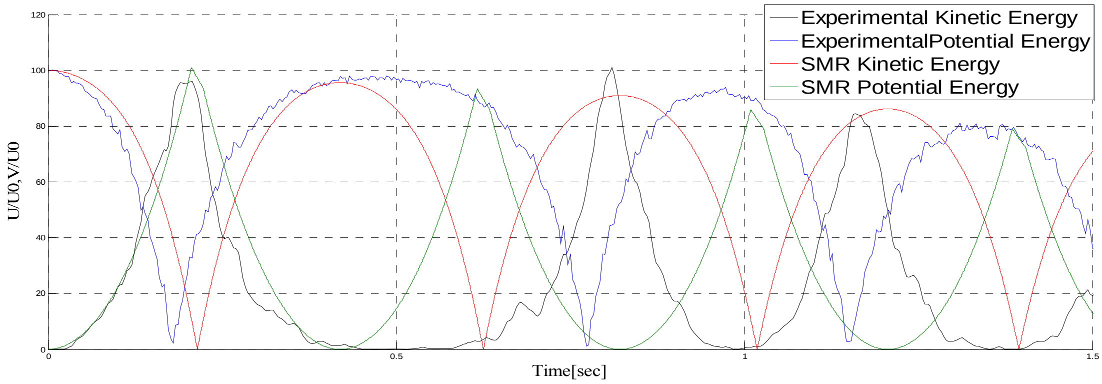

2.18 *Figure - Typical experimental and simulated results for a MR block*

The third chart, presents the temporal evolution of the angle speeds against the angle variation in the time domain. The phase portrait is useful in identifying system behaviour as it consolidates the system response and remove the distracting effect of time. This chart show a range of orbits corresponding to the time-history results where the traces representing the passage of time, the block travels counter clockwise as it did in the conservative case until the block reaches its up left position, the y axis. Here the angular speed of the block is reduced by the impact to the ground. Although it is not specifically depicted in the chart, the trace will eventually spiral towards the origin, illustrating that in a long term, the block will come to rest in its upright position with rotation and speed (x, y) equal to zero. This illustrates the use of a graphical technique in the prediction of long term behaviour of a system.

2.6 Experimental results

In this paragraph only a few experimental setting will be show. Nevertheless all the considerations will be do on the entire case study investigated. All the charts omitted are showed in the appendices.

In this session the specimens will be show in the field of the Free Oscillation (FO) and in the dynamic field with a frequency of 4Hz. The choice of the frequency is a consequence of the clearness of the results obtained. The specimens showed are:

- Three Rectangular parallelepiped (3Rect),
- 3Rect with a thin rubber pad,
- 3Rect with quasi-sinusoidal input 4Hz and the equivalent MDOF with the spring and the mass on top.
- 3Rect with spring with post-tensioned force equal at 6

Based on careful observation and in according with the experimental results, dynamic responses of a multi-segmental rocking system on a rigid foundation are classified. Figure 2.19 show the schematic classification of response states. Initially, the body as the possibility to behaving either under liftoff or slip motions, when subjected to base excitations. The subsequent response is either liftoff, slip or liftoff-slip interaction motions. Since further response come under either of them, this classification covers all response states that inevitably occur. These response states and transition conditions are influenced both geometrically configuration and boundary condition. The geometry and boundary condition determine when the motion of interest commences or terminates. This figure considers only the bi-dimensional behaviour. During the experiment the rotation at the base of the blocks was not an isolate episode. The rotation occurs because of the anisotropy of the material used and it is more accentuate by the small dimension of the specimens where the unavoidable imperfections are not unimportant. During the tests on the shaking table the rotation phenomenon occurs prevalently with the high level of frequency.

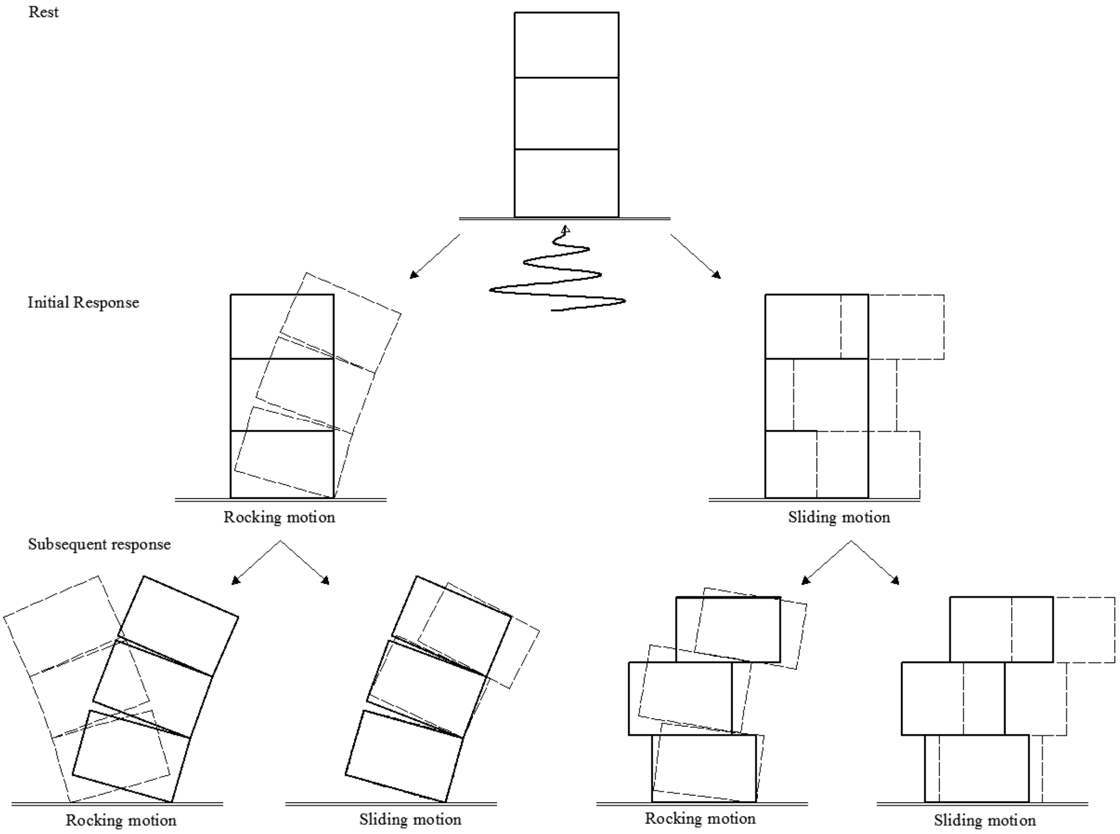

2.19 *Figure – Classification of responses*

2.6.1 Three Rectangular Parallelepiped in Free Oscillation

2.6.1.1 Bottom block

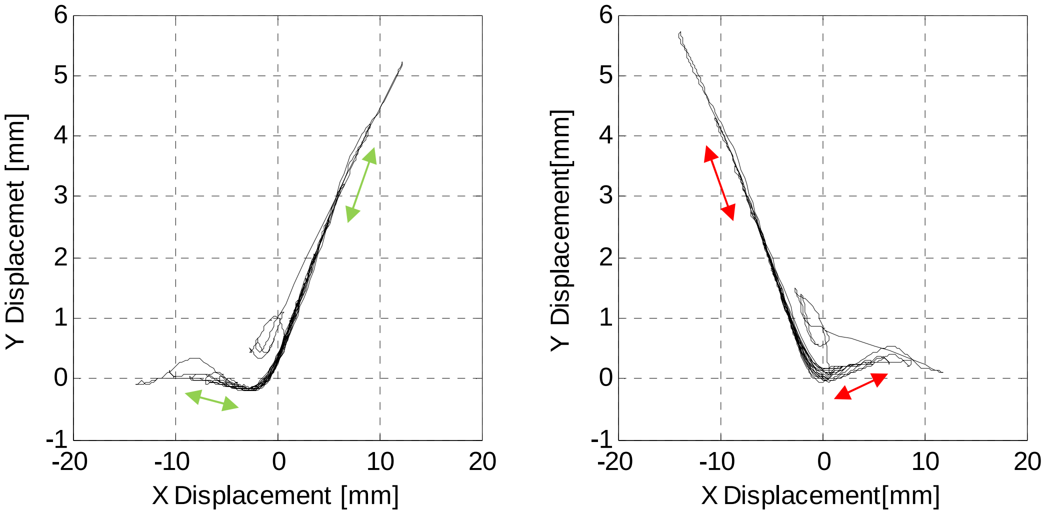

2.20 *Figure – 3Rect, bottom block x, y displacements in the time domain*

The charts above represent the temporal evolution of the displacements in the plane X-Y in the time domain. Where the traces representing the passage of time while the blocks are moving from one pivot of rotation to the other. The x displacements depicted in the charts are not calculated on the base but at the top of the block considered. Hence the shorter traces are so horizontal compared with the Figure 2.21 below. Usually in this kind of test all the data is recorded by following the points situated on the border of the block. In this case however because the small and wide rotations of the block during the motion involve the loss of the physic surface of the dot and the creation of shadow which cause a loss of clearness between one pixel and

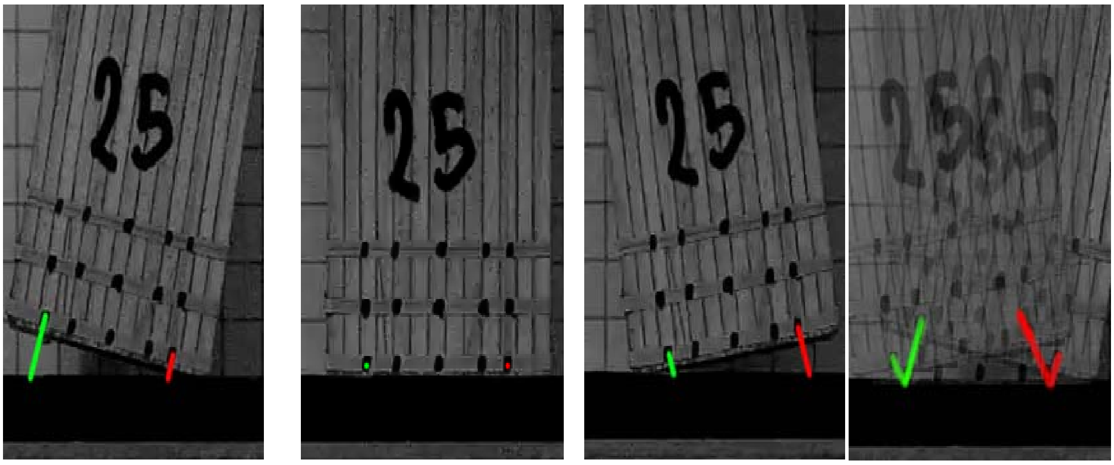

2.21 *Figure – Explanation of block trace in time domain* the other during the tracking analysis. Due to the loss of the dots, intern points were chosen. Moreover the choice of the internal point involves the presence of the shorter traces in the graphs. With border point the only trace should be the longer.

The Figure 2.22 below represents the y displacement of the dots. In the charts each peak represents the maximum y displacement reached by the dots. On closer analysis it is easy to identify how the two charts are complementary. The peaks in the charts are shifted by a half rocking period, when the left point reach the highest position, the right dot is the lowest point and vice-versa. After the fourth second due to the small and fast rotations around the rest position the program in not able to follow univocally the pixel and the consequence is the noise of end analysis. The traces out of place in Figure 2.20 are the same noise detected in the picture below.

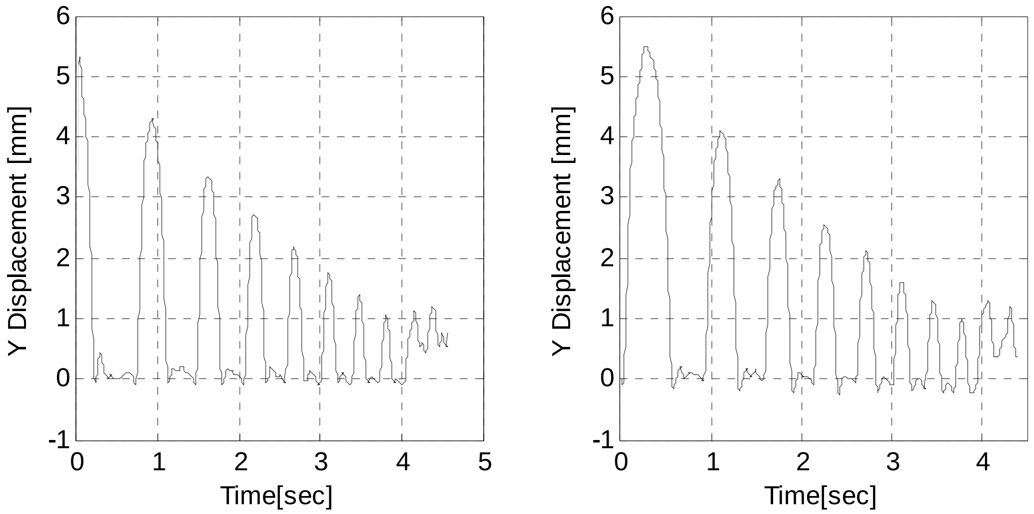

2.22 *Figure – y displacement, 3Rect*

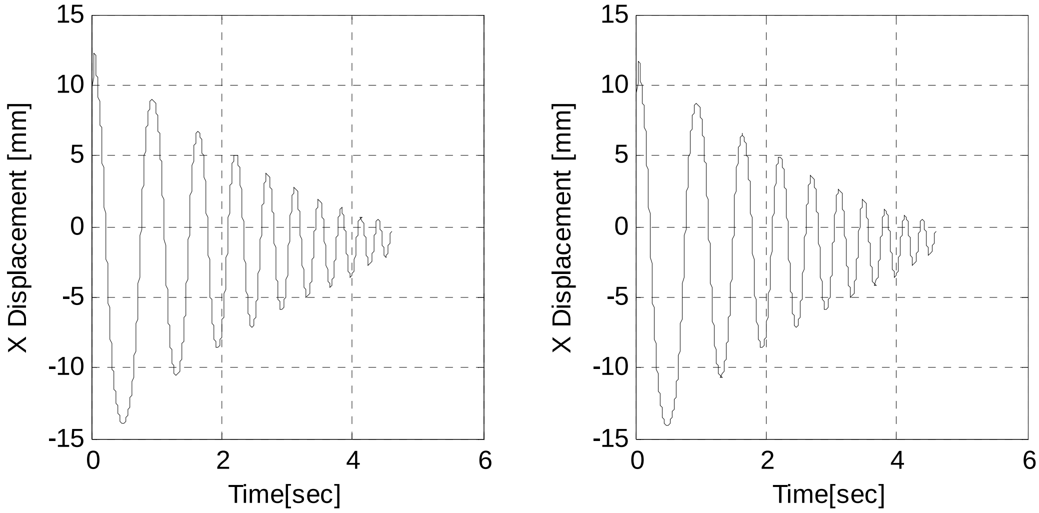

2.23 *Figure – x displacement, 3Rect*

The Figure 2.23 show the block x displacement during the free rocking motion. Even in this chart the position is counted by the top of the block. The block starts with an initial lateral displacement due to the angle induced for determine the free oscillation behaviour and subsequently to the release of the block it starts to oscillate round the final rest position. As is show in the chart it is easy to deduce that the block at the end of the motion maintains a residual sliding displacement.

The charts 2.24 as depicted below show the variation of the angle during the block rocking phase.

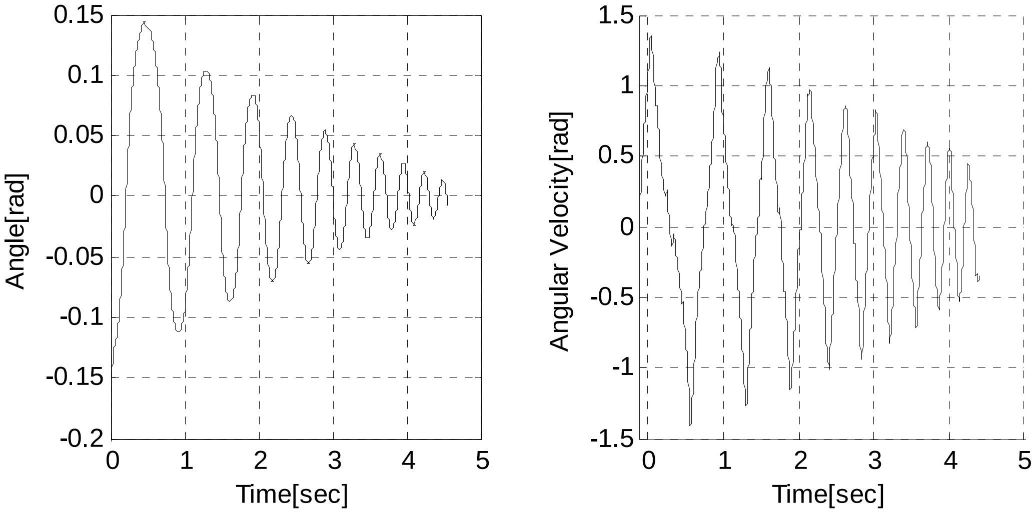

2.24 *Figure – Angle variation and Angular Velocity during the rocking block motion, 3Rect*

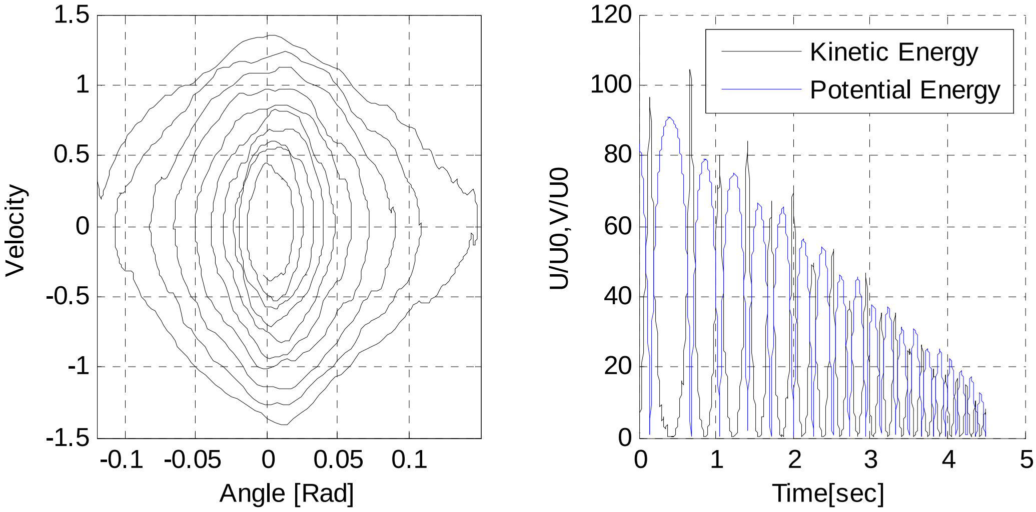

2.25 *Figure – Angle and Velocity trace in the time domain, Kinetic and potential Energy, 3Rect*

The total energy should never be more than the 100%. A plausible explanation for this is the existence of experimental and data processing errors. This could include errors in establishing the properties of the block, sampling errors in the data acquisition and numerical processing errors in obtaining velocities from the displacement.

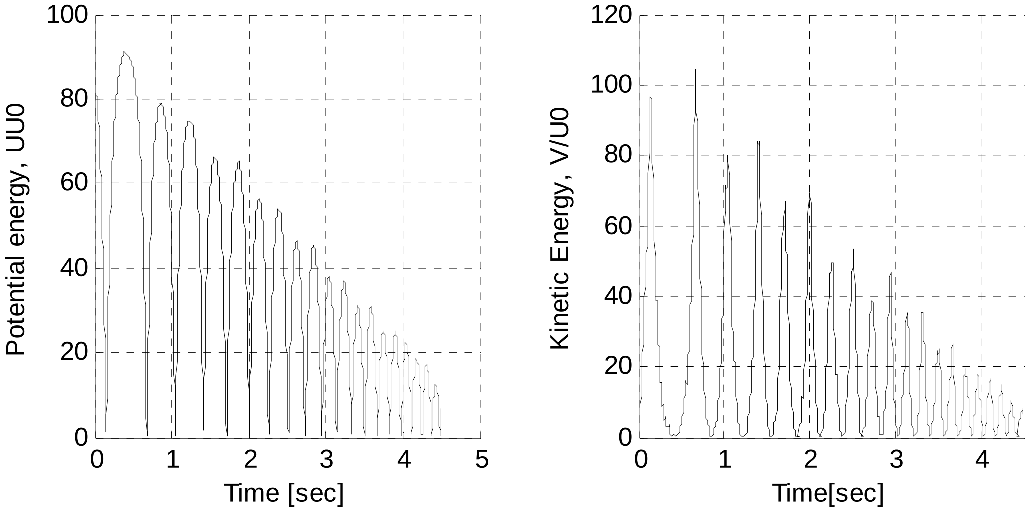

2.26 *Figure – Potential and Kinetic energy, 3Rect*

In this paragraph were explained the typologies of graphs which will be show for the other block and for the other specimen typologies. The last charts, at the end of the middle block part, represent the opening of the gap, in the right and left corner, between the two blocks. The red line means the difference in y displacement during the rocking motion, hence the gap opening. Instead the first two are equivalent with the y displacement chart described before. Therefore in the next paragraphs, by consistency of the chapter, these two graphs and other will be omitted. Nevertheless a completely presentation of all the charts will be do in the appendices.

2.6.1.2 Middle Block

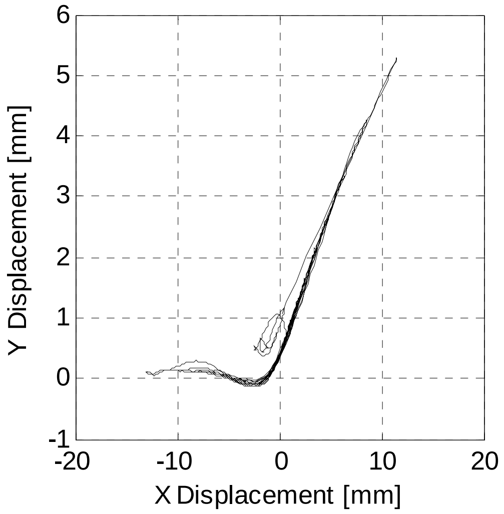

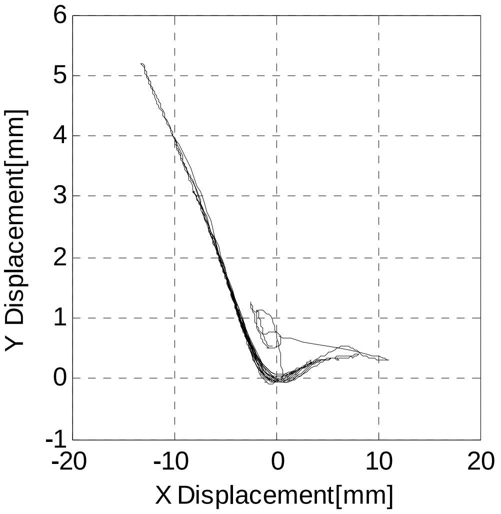

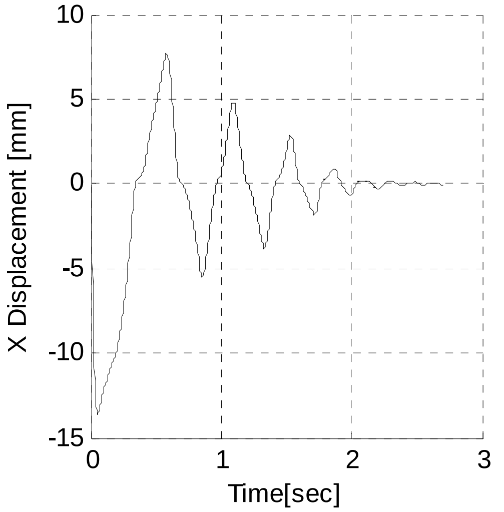

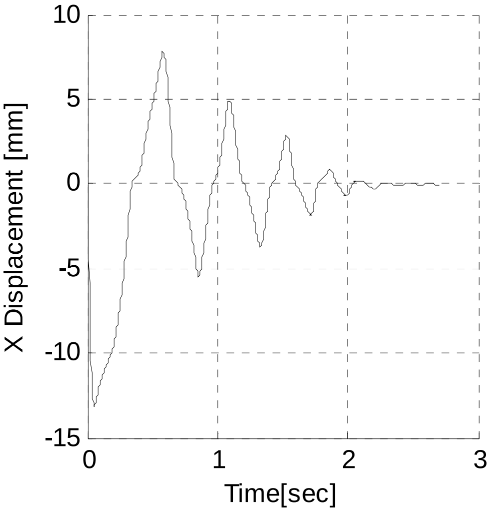

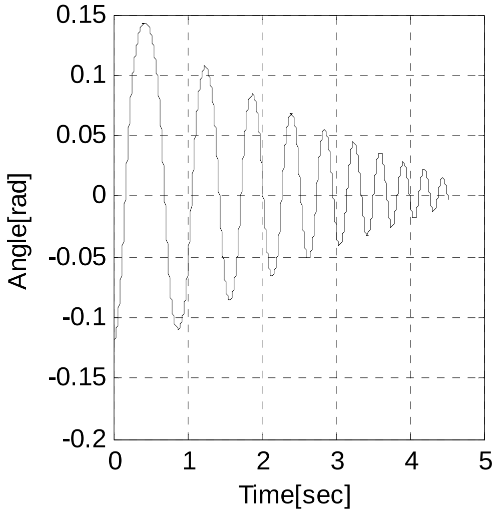

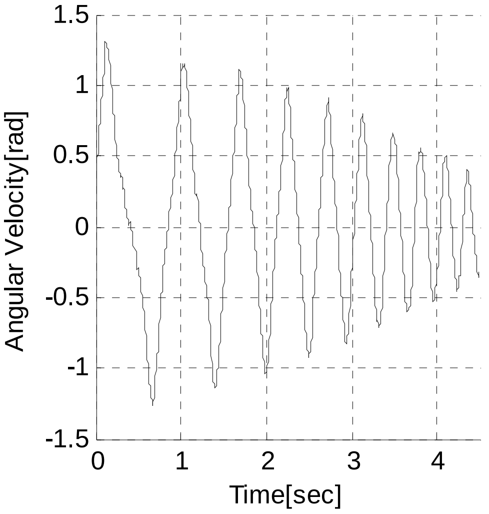

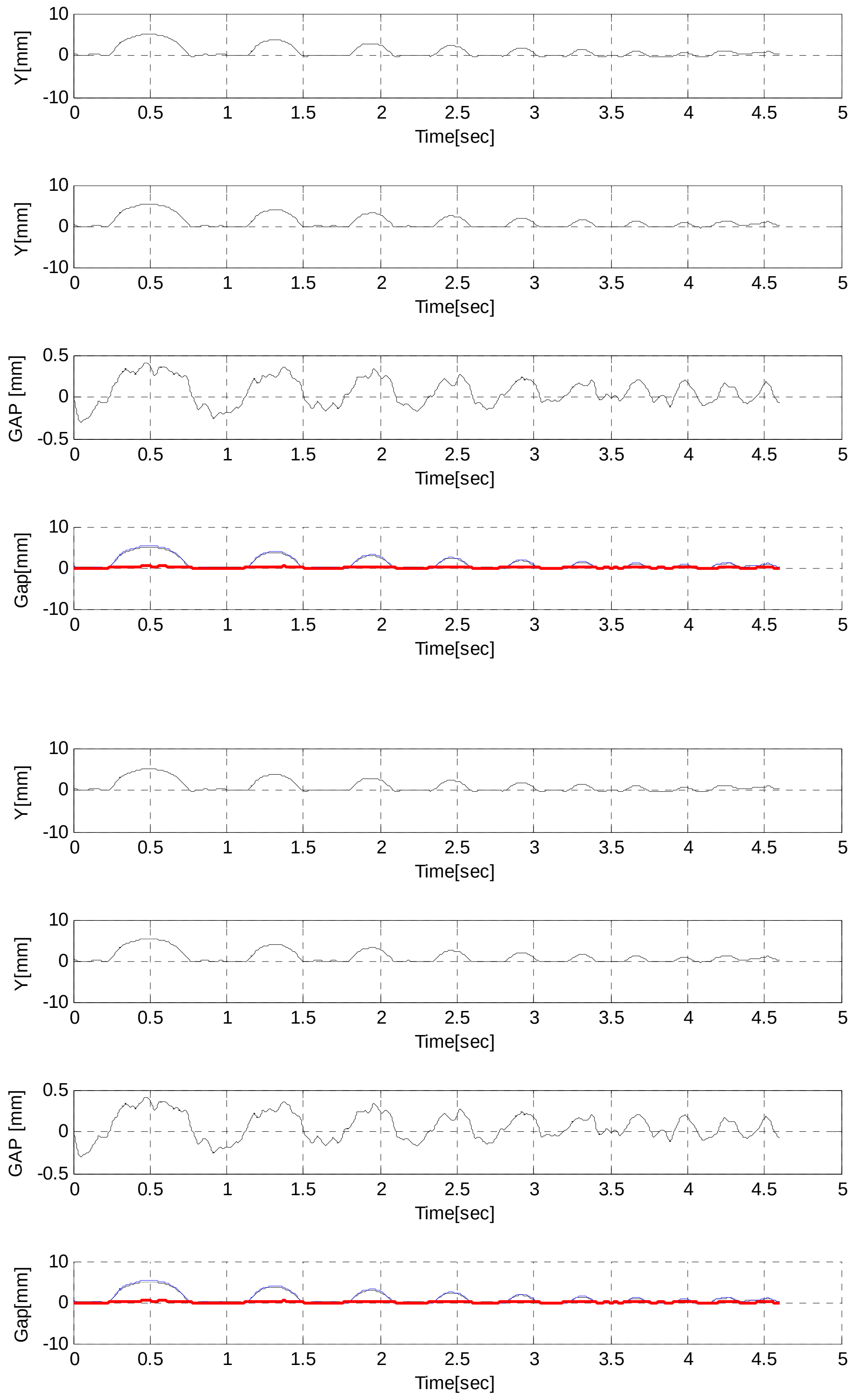

2.27 *Figure - Three Rectangular Parallelepiped in Free Oscillation, middle block, 3Rect*

2.6.1.3 *Top block*

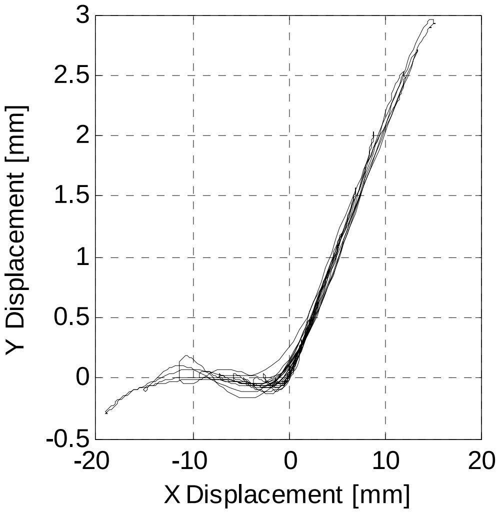

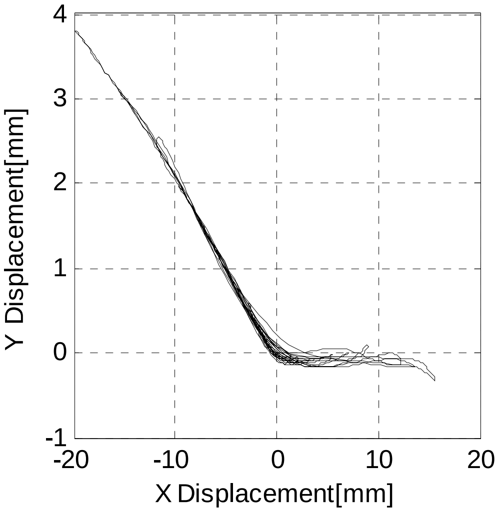

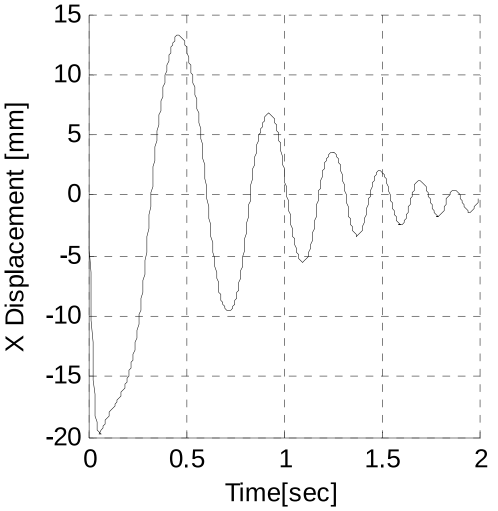

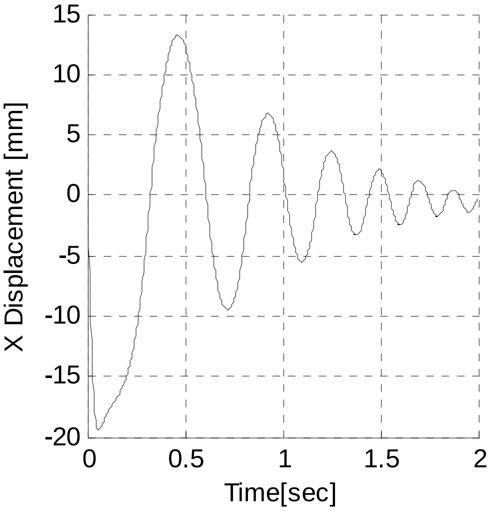

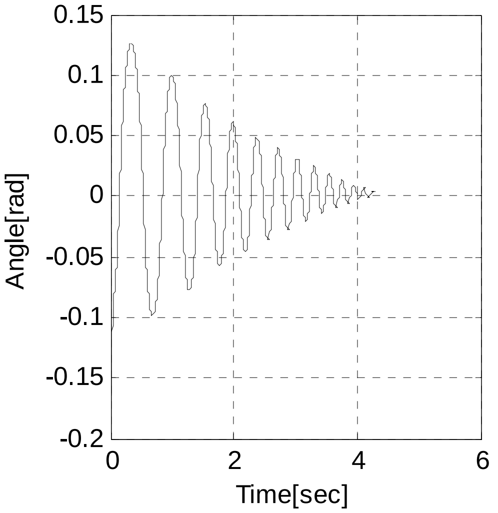

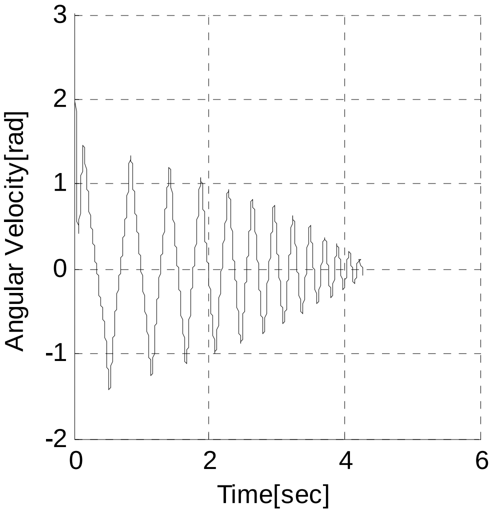

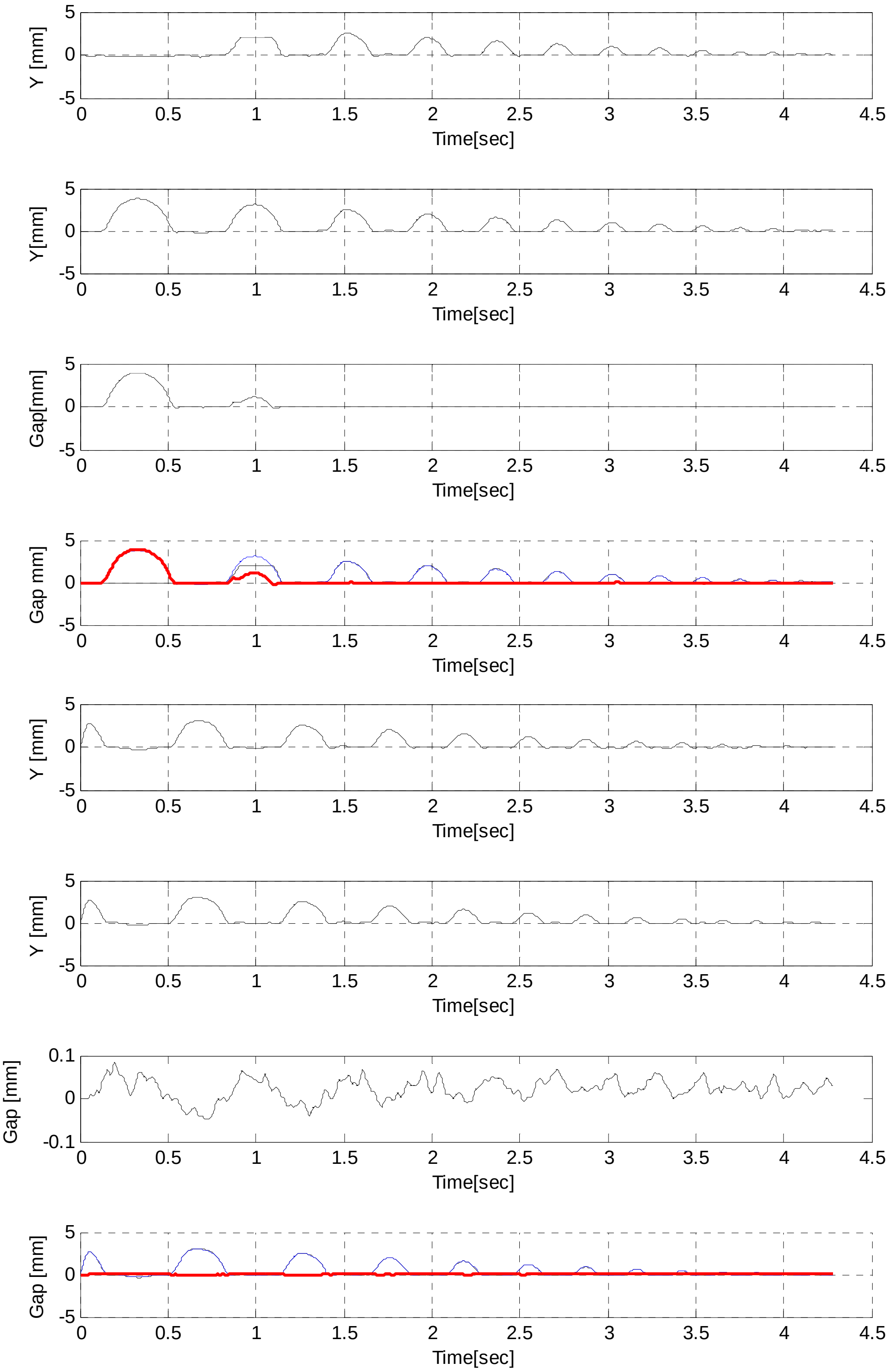

2.28*Figure - Three Rectangular Parallelepiped in Free Oscillation, top block, 3Rect*

2.6.2 Three Rectangular Parallelepiped with Rubber Pad in F.O

2.6.2.1 Bottom Block

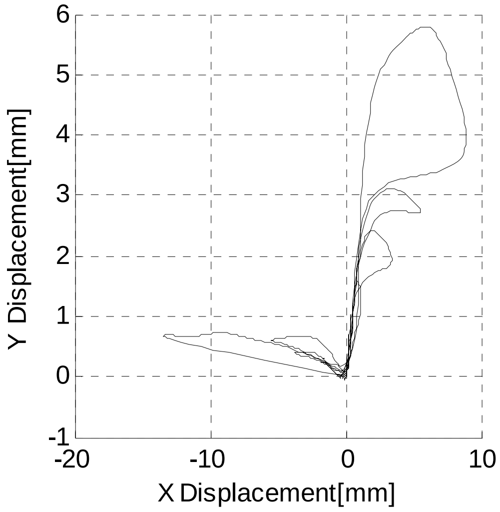

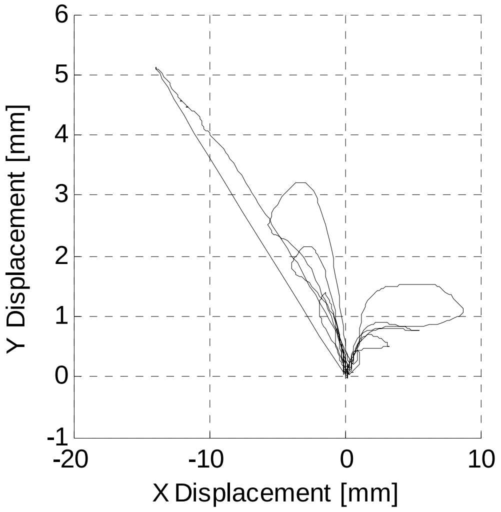

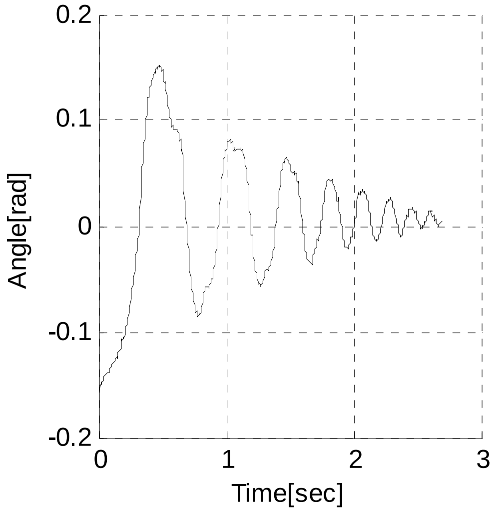

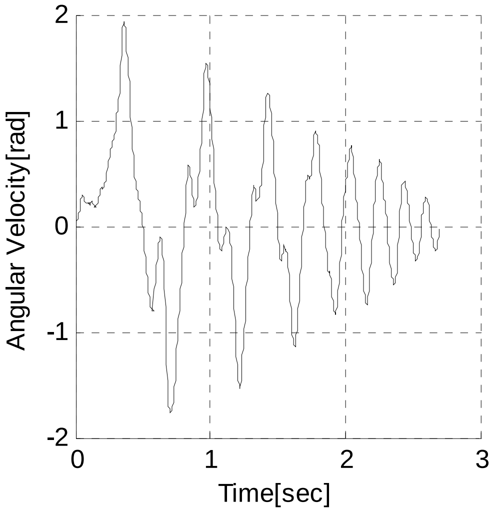

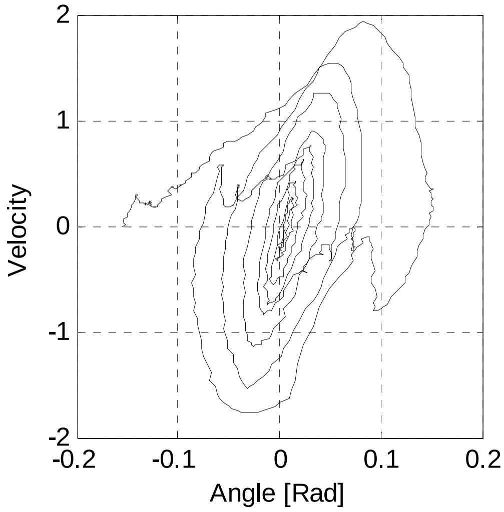

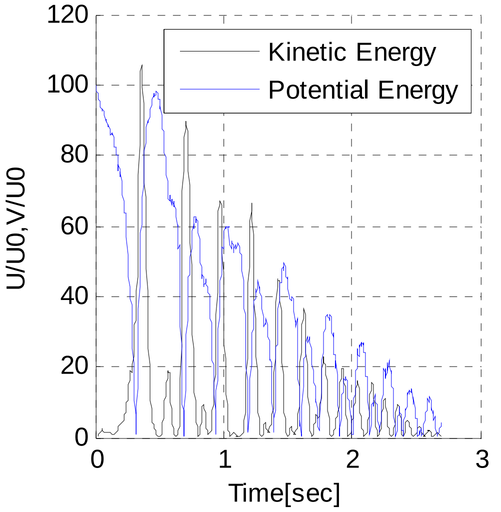

2.6.2.2 Middle block

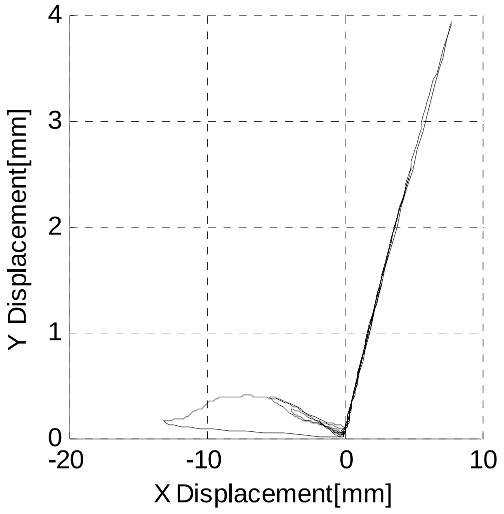

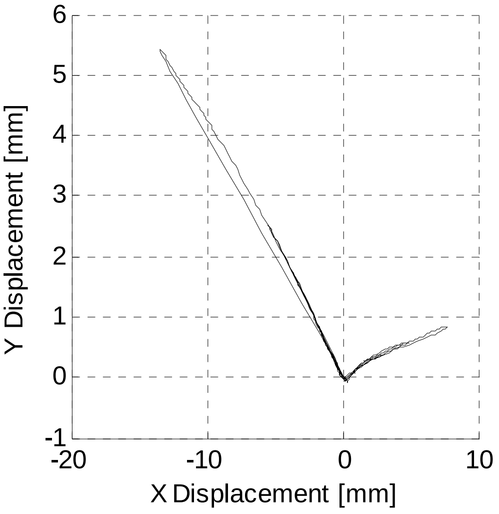

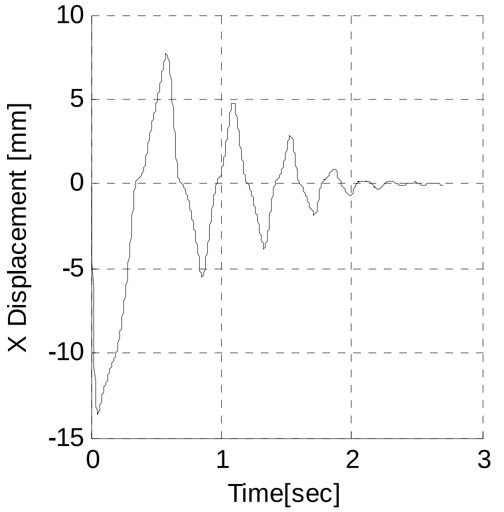

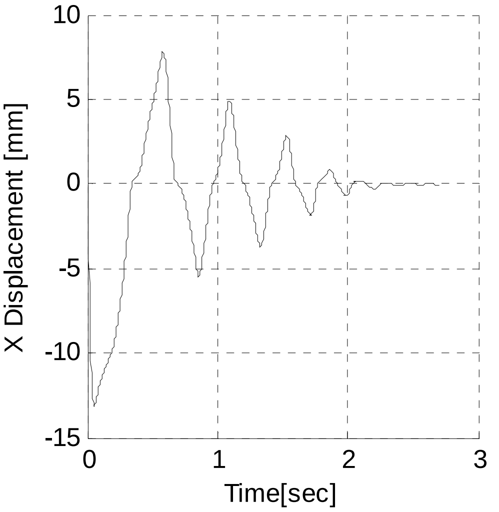

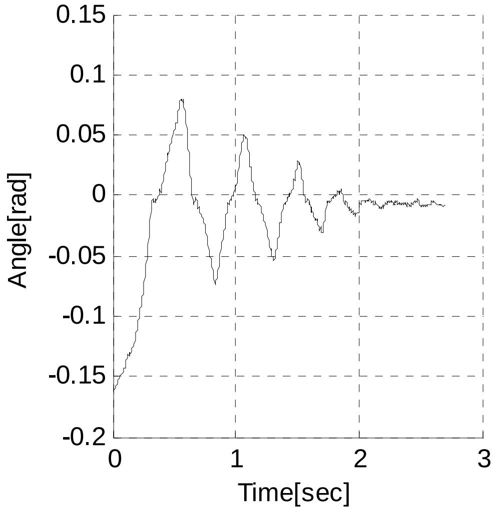

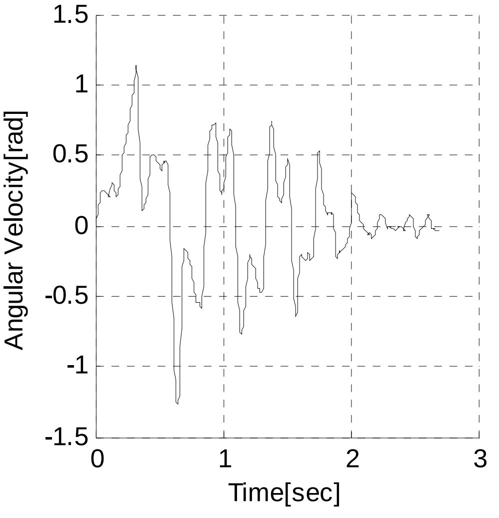

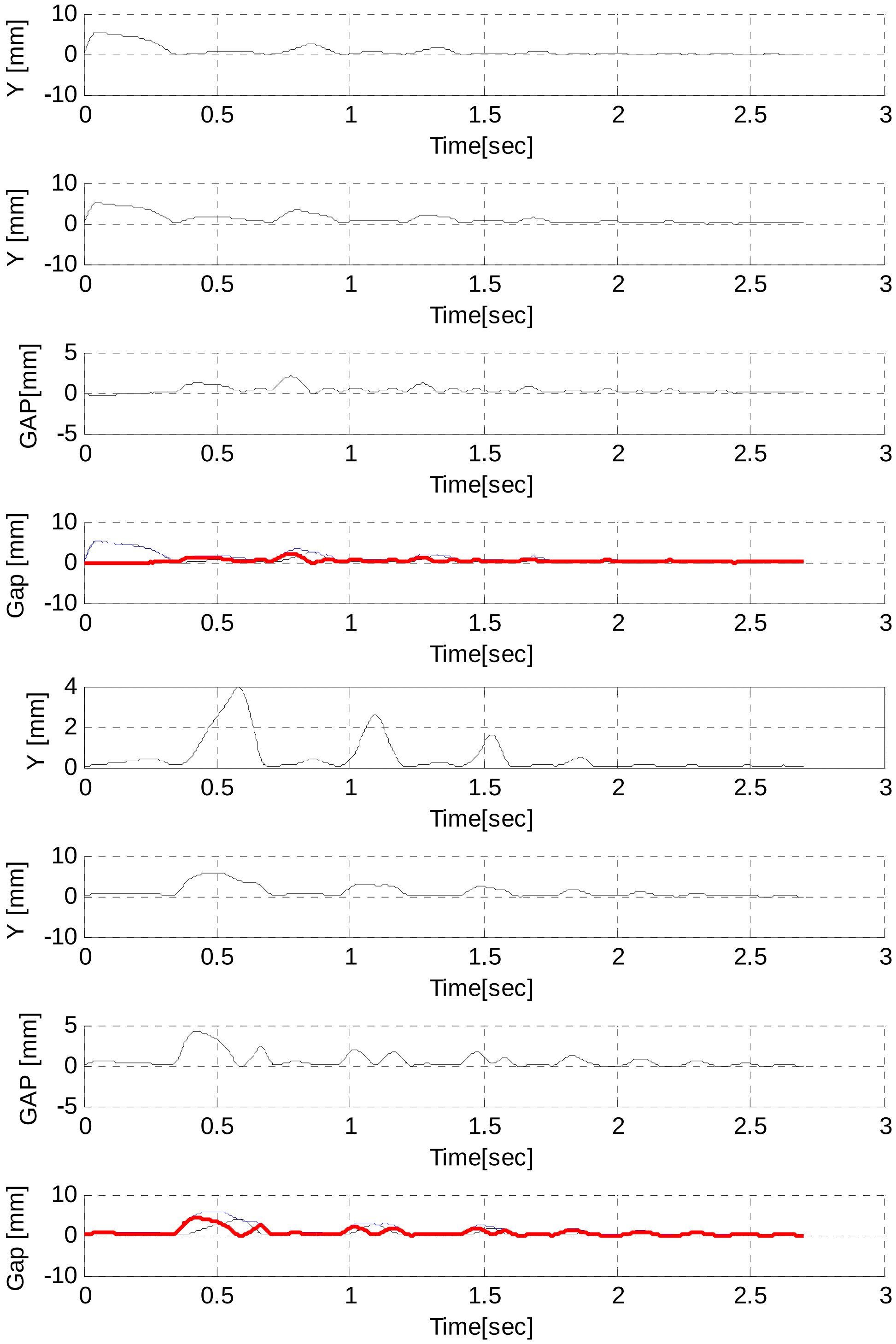

2.29 *Figure - Three Rectangular Parallelepiped in Free Oscillation with rubber pad, middle block*

2.6.2.3 Top Block

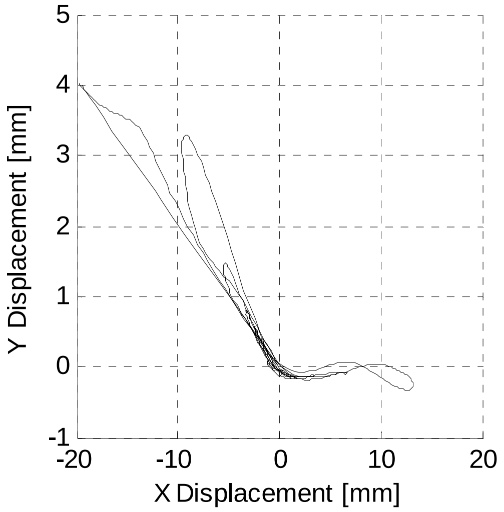

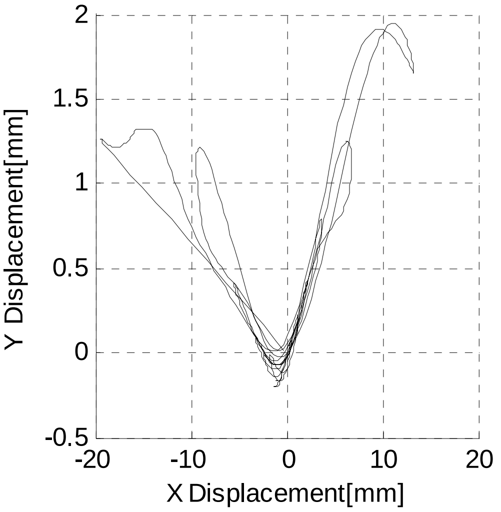

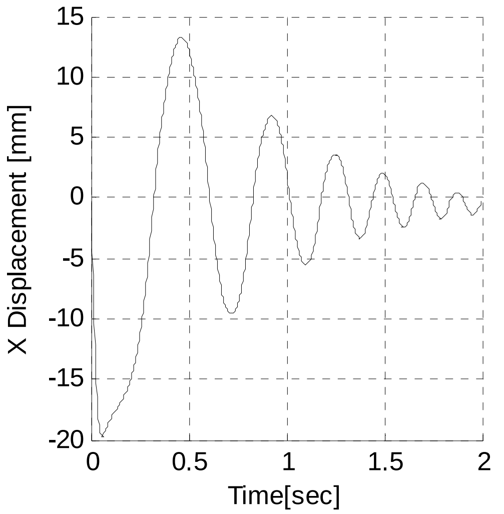

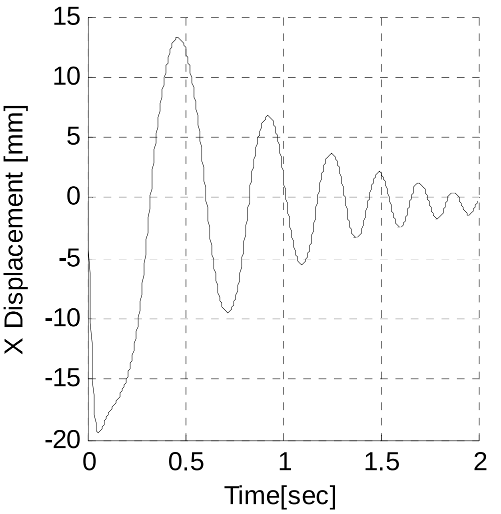

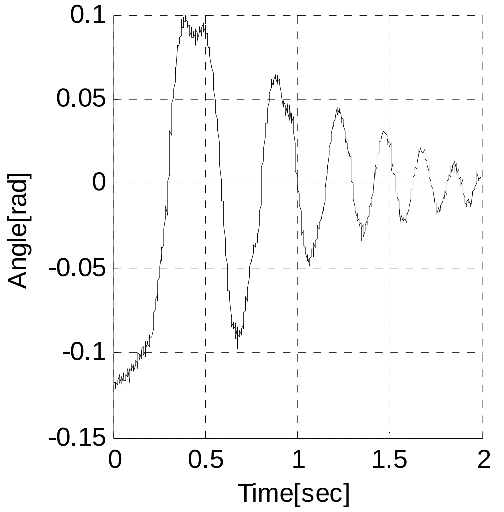

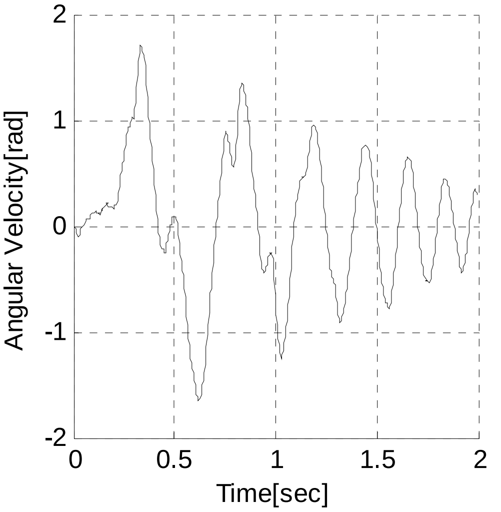

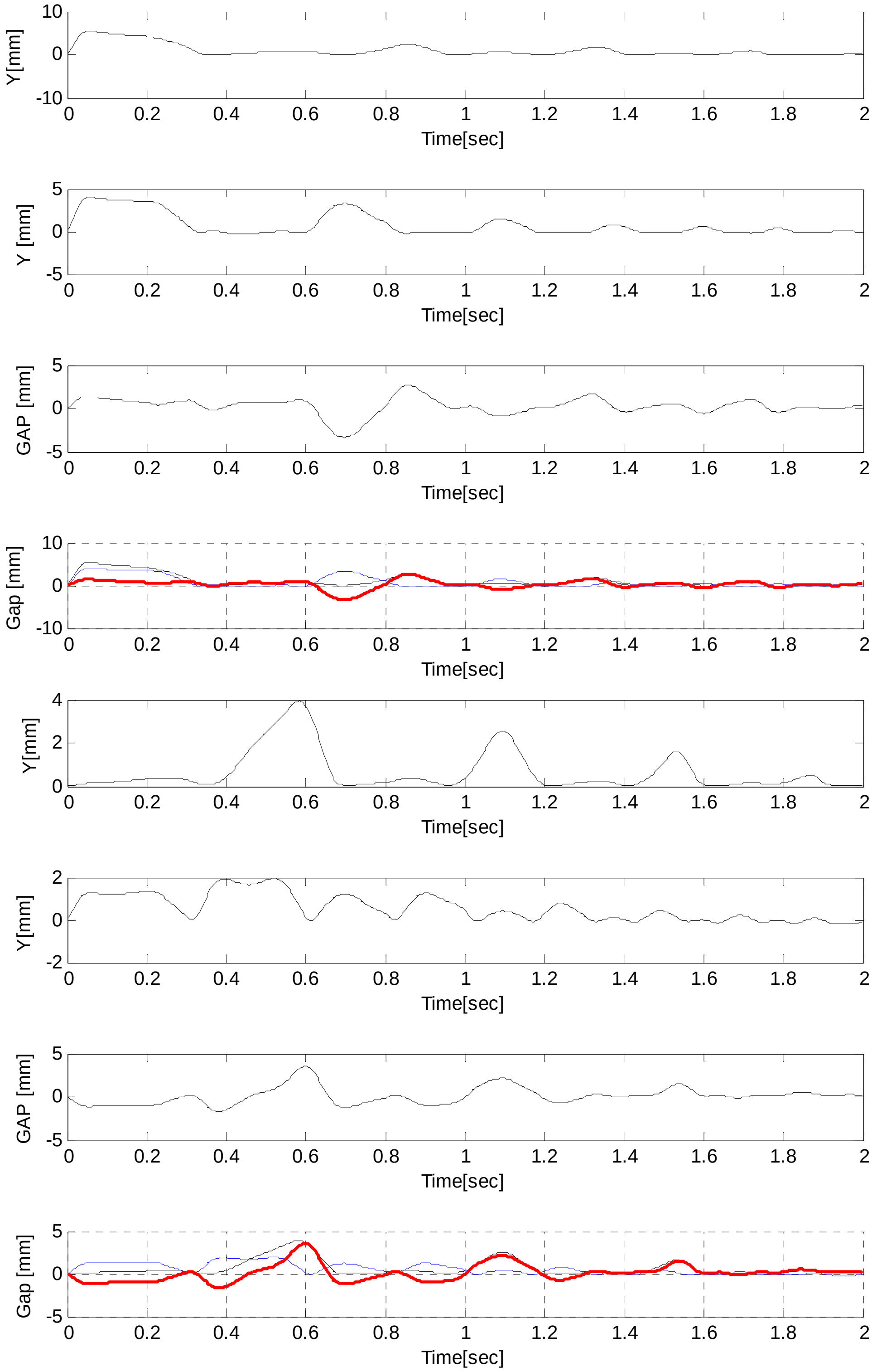

2.30 *Figure - Three Rectangular Parallelepiped in Free Oscillation with rubber pad, top block*

2.6.3 Three Rectangular Parallelepiped with Spring in F.O, Pt. Force = 6N

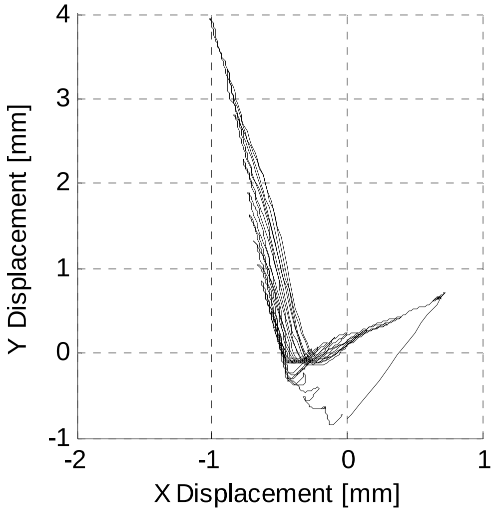

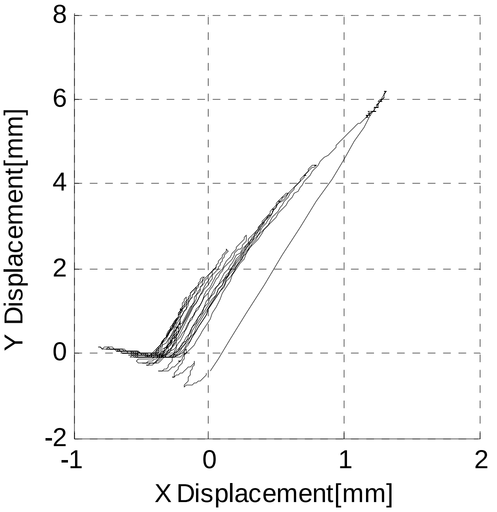

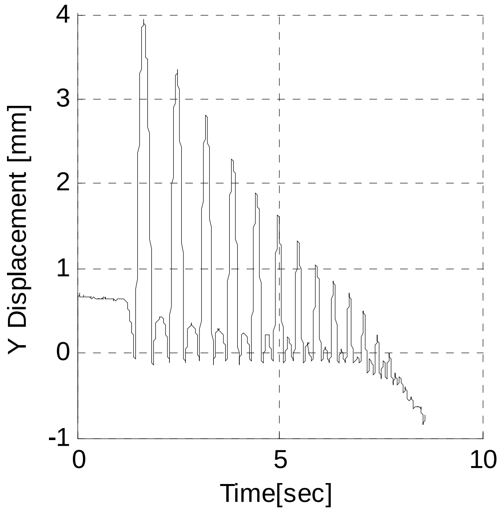

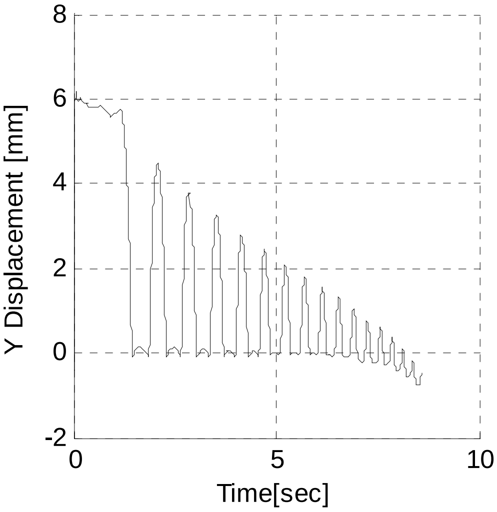

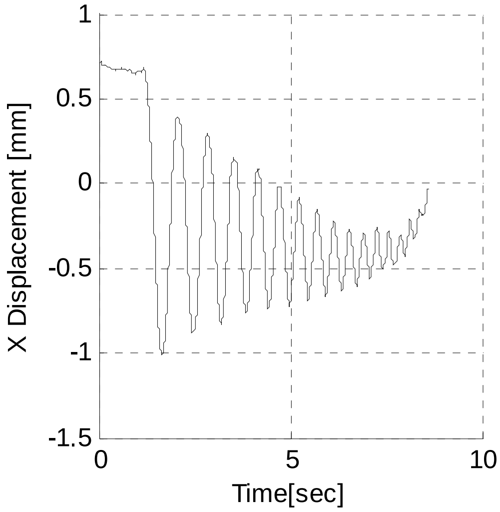

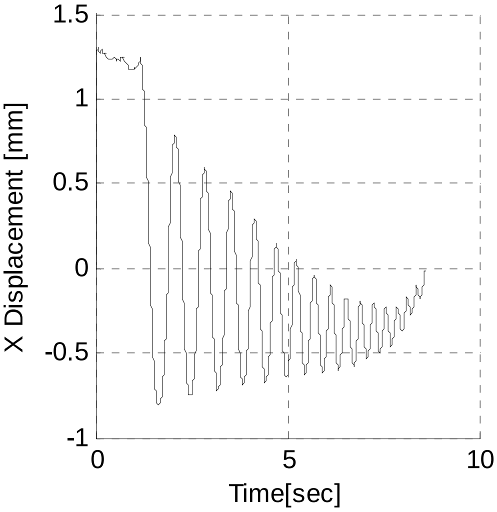

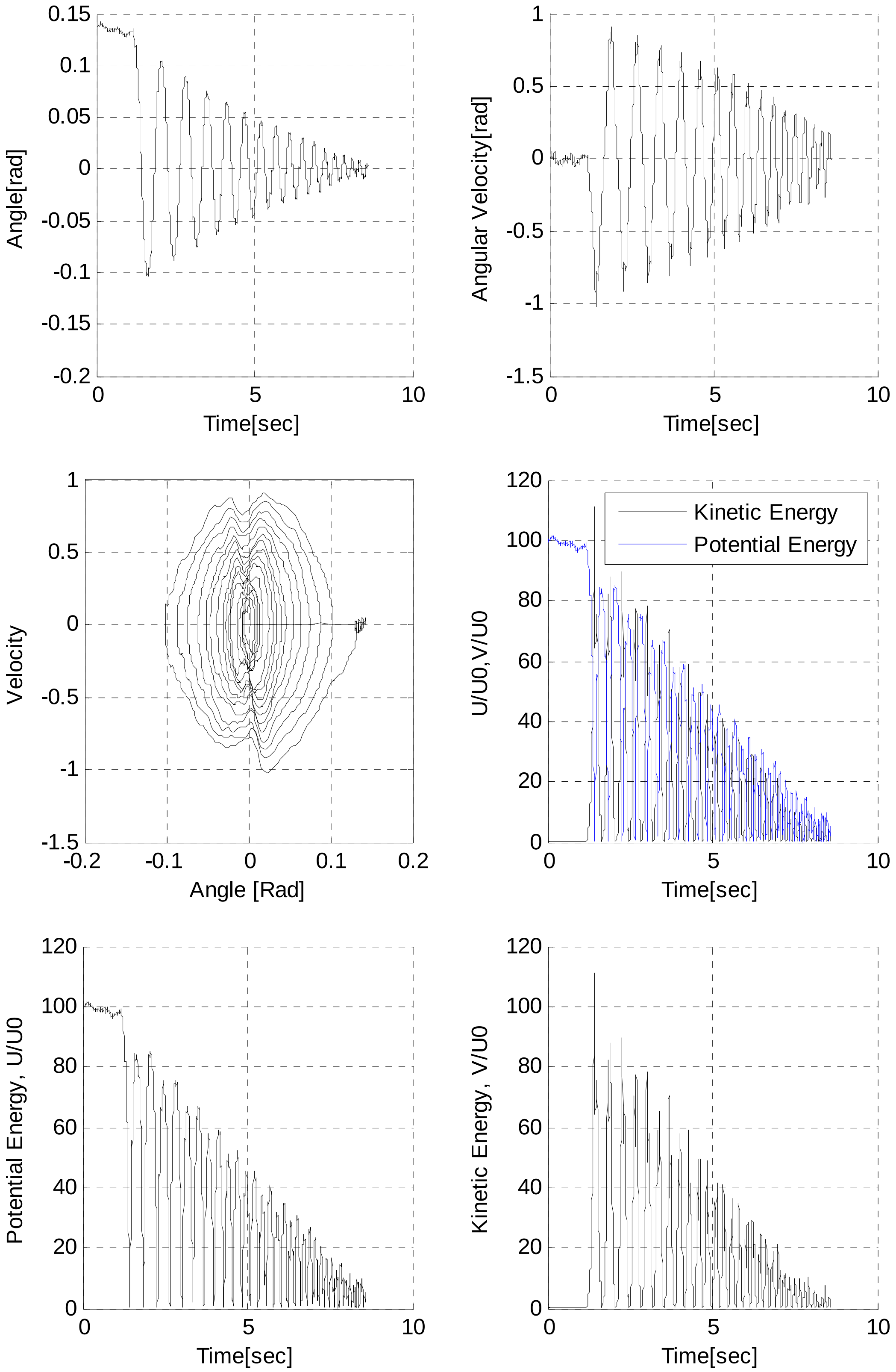
Angle[rad]
0.15
0.1
0.05
0
-0.05
-0.1
-0.15
-0.2
0
5
10
Time[sec]
Angular Velocity[rad]
1
0.5
0
-0.5
-1
-1.5
0
5
10
Time[sec]
Velocity
1
0.5
0
-0.5
-1
-1.5
-0.2
-0.1
0
0.1
0.2
Angle [Rad]
U/U0,V/U0
120
100
80
60
40
20
0
0
5
10
Time[sec]
Kinetic Energy
Potential Energy
Potential Energy, U/U0
120
100
80
60
40
20
0
0
5
10
Time[sec]
Kinetic Energy, V/U0
120
100
80
60
40
20
0
0
5
10
Time[sec]

2.6.4 Three Rectangular Parallelepiped with quasi-sinusoidal input f = 4H

2.6.4.1 Bottom Block

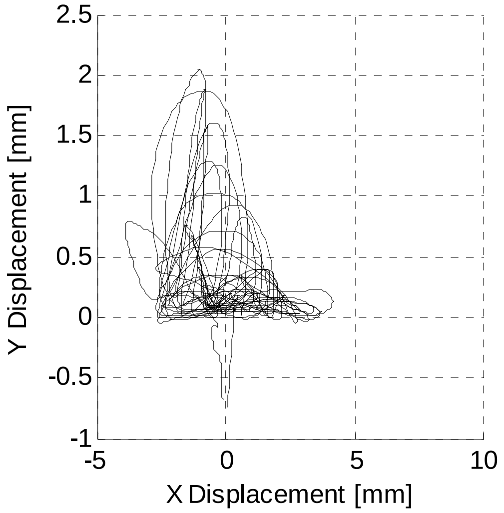

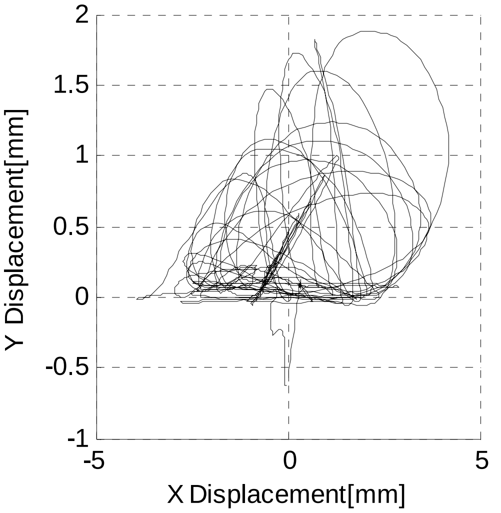

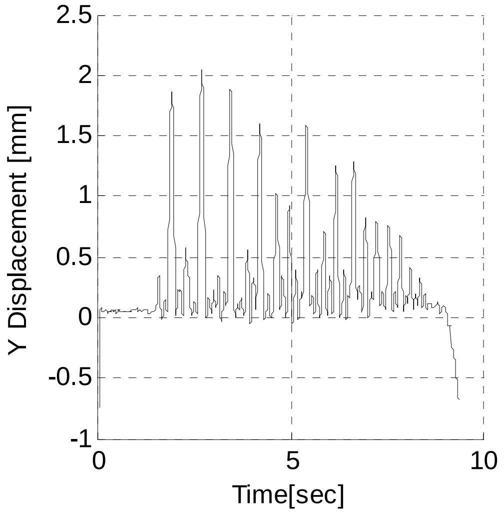

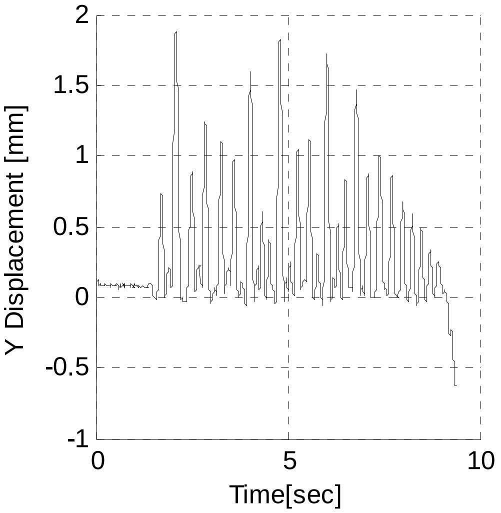

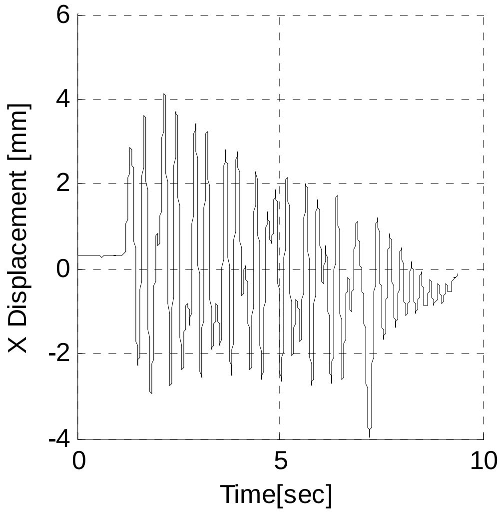

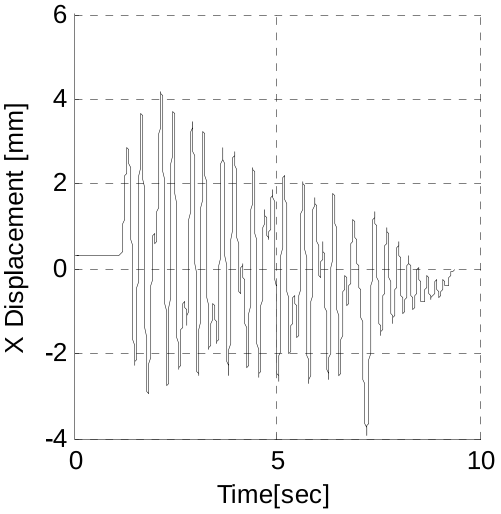

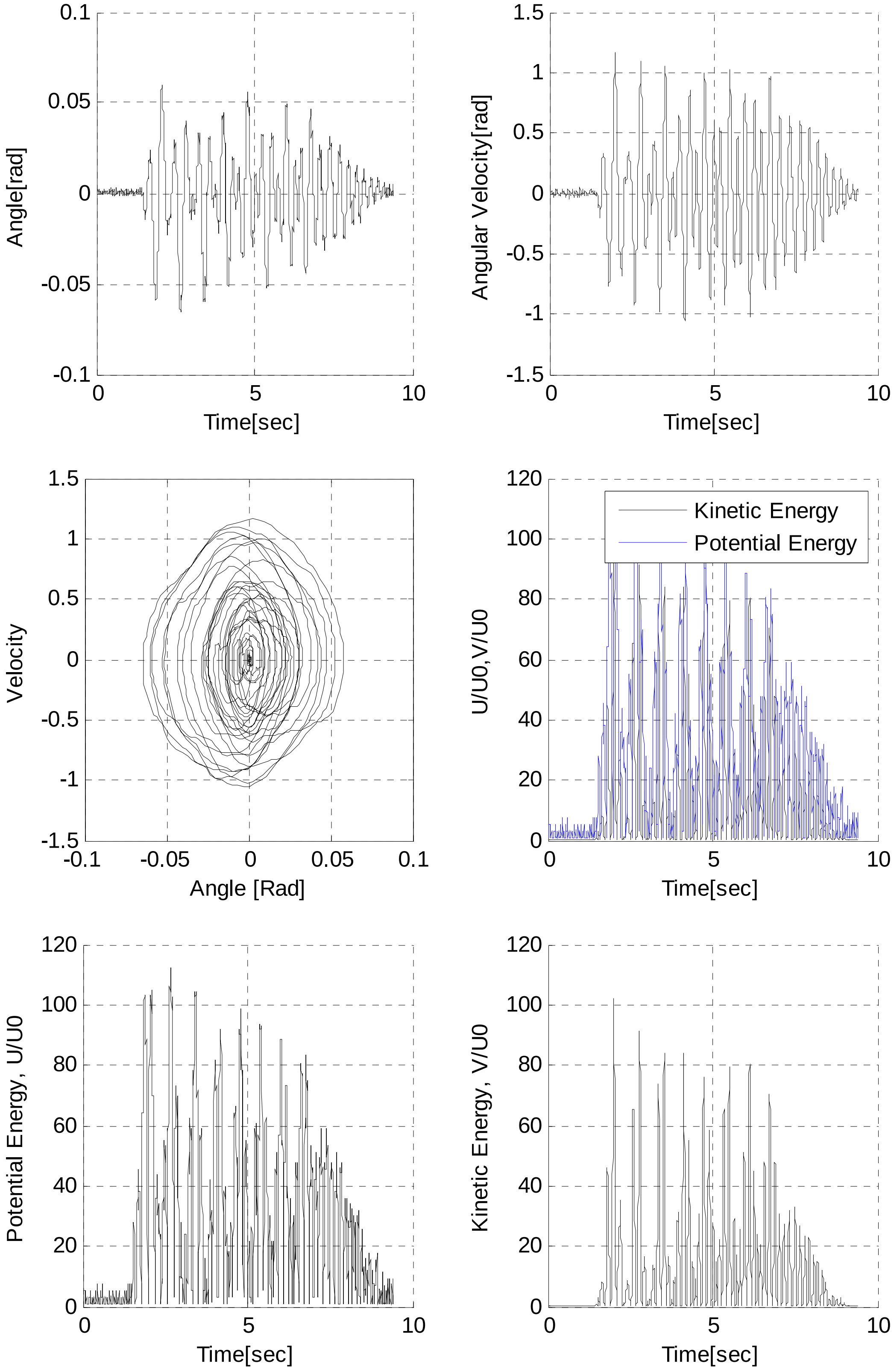
Angle[rad]
0.1
0.05
0
-0.05
-0.1
0
5
10
Time[sec]
Angular Velocity[rad]
1.5
1
0.5
0
-0.5
-1
-1.5
0
5
10
Time[sec]
Velocity
1.5
1
0.5
0
-0.5
-1
-1.5
-0.1
-0.05
0
0.05
0.1
Angle [Rad]
U/U0,V/U0
120
100
80
60
40
20
0
Kinetic Energy
Potential Energy
0
5
10
Time[sec]
Potential Energy, U/U0
120
100
80
60
40
20
0
0
5
10
Time[sec]
Kinetic Energy, V/U0
120
100
80
60
40
20
0
0
5
10
Time[sec]

2.6.4.2 Middle block

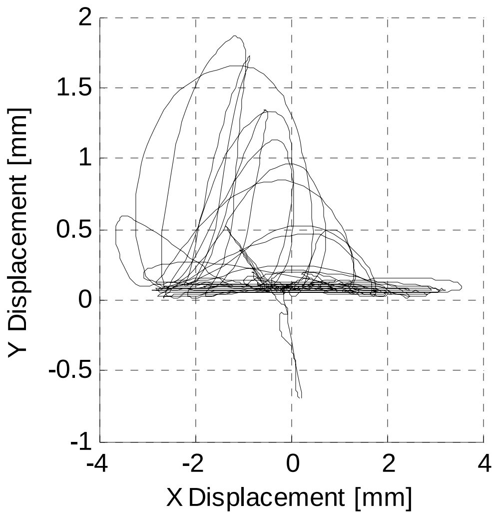

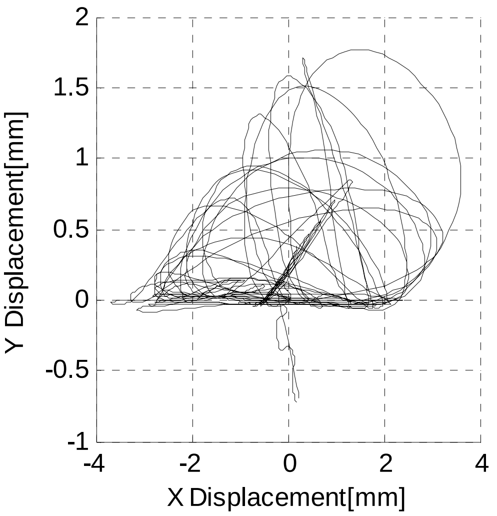

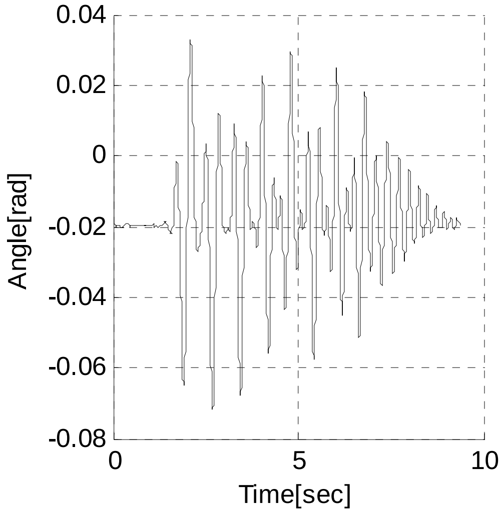

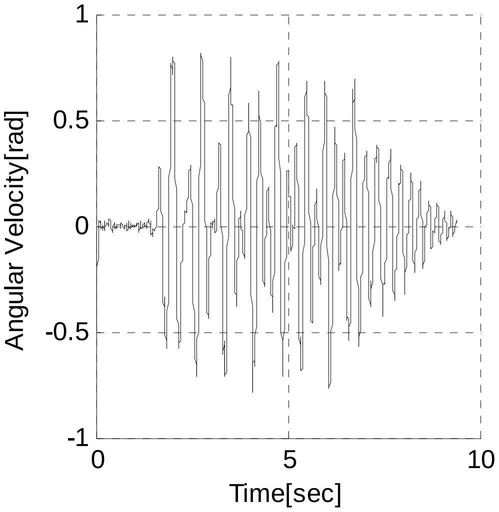

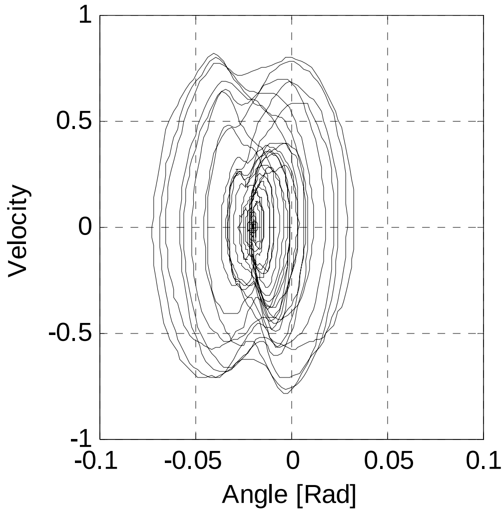

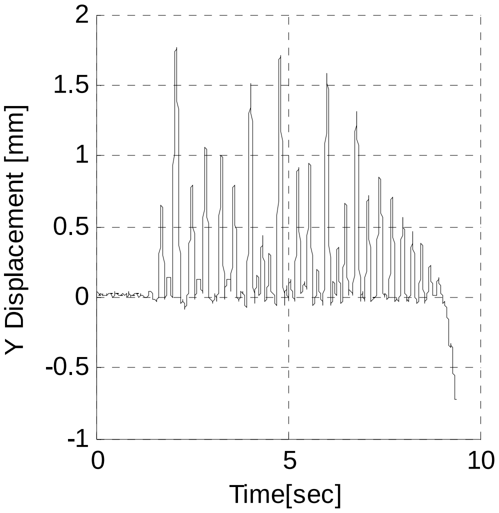

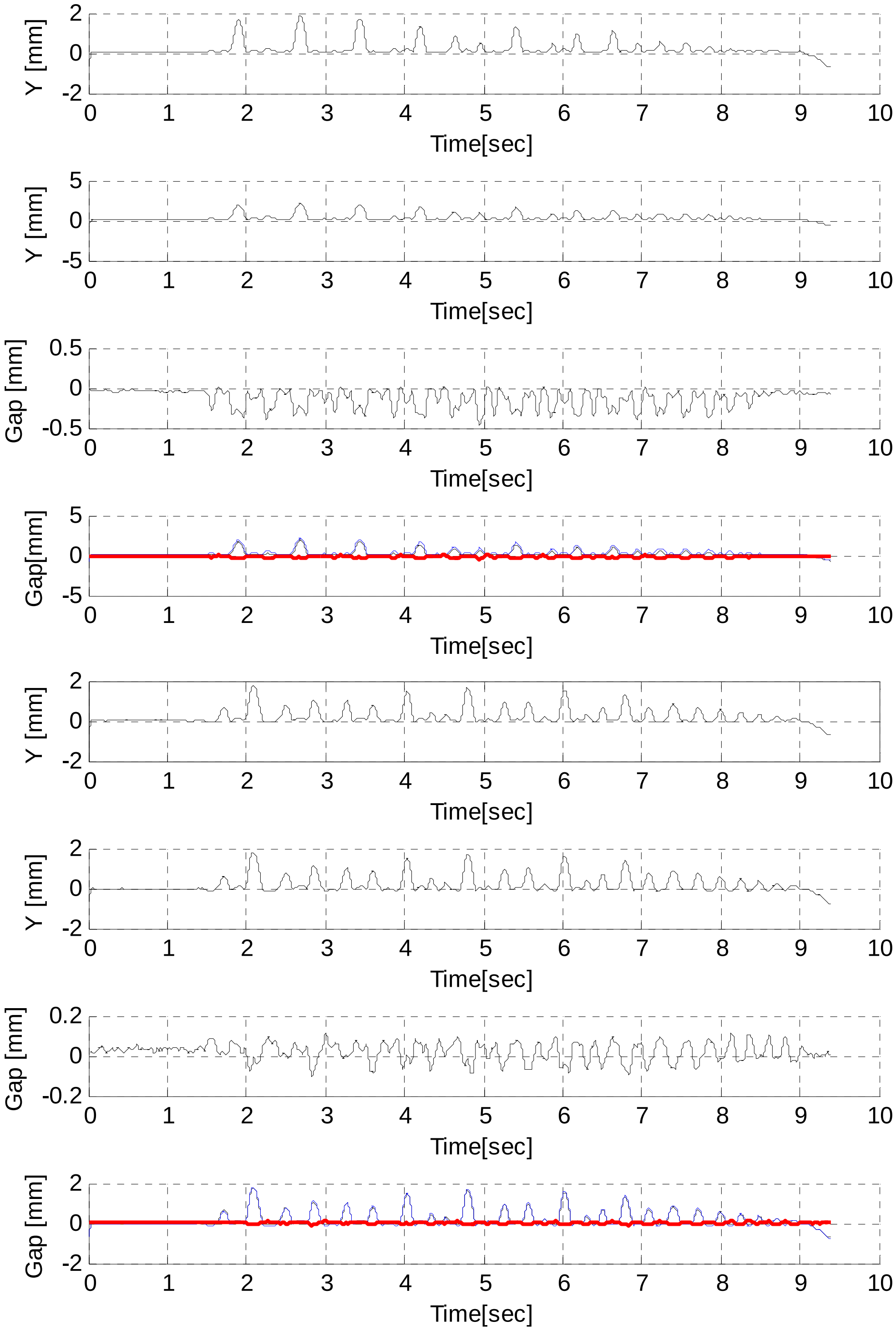

2.31*Figure - Three Rectangular Parallelepiped with quasi sinusoidal input, f=4Hz, middle block*

2.6.2 Summary of all Test Results

The aim of this paragraph is to make a summary of all the results and observation obtained by the test done. Each chart represent the summary of each test run divided by geometrical configuration of the pier an type of contact. In the graphs where one of the colour does not appear means that the dynamic behaviour in not present.

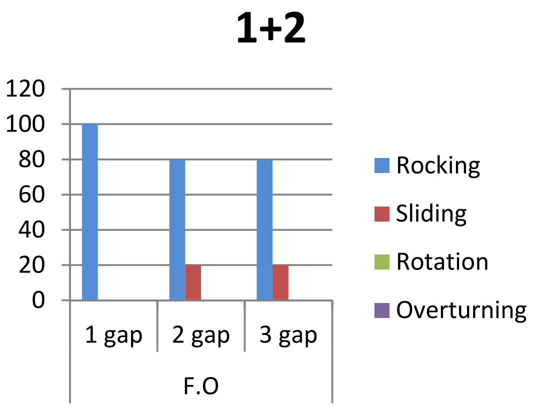

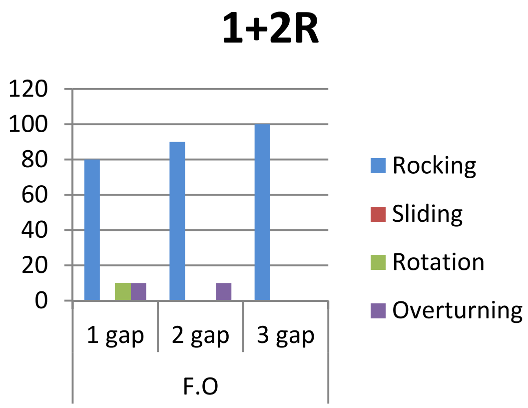

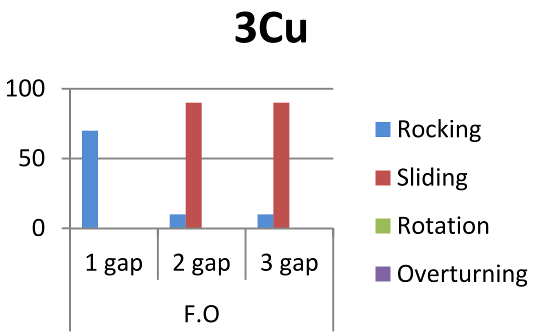

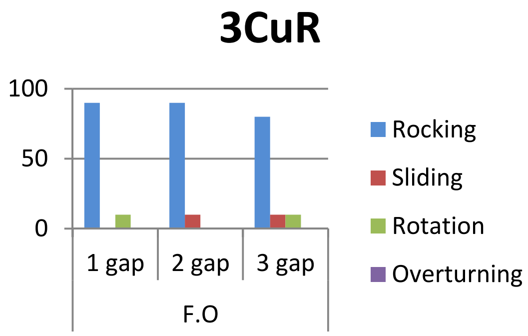

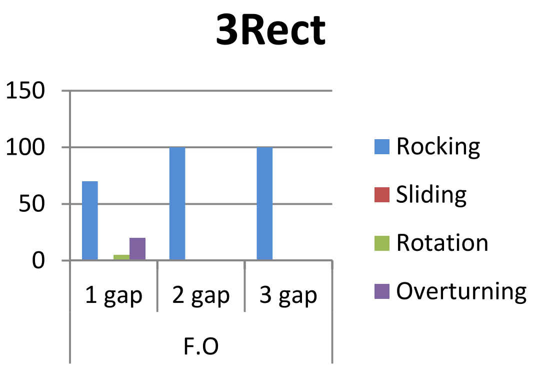

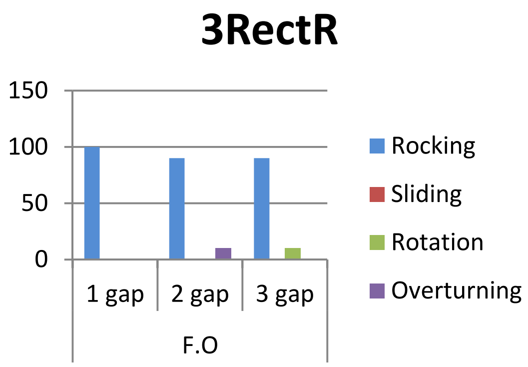

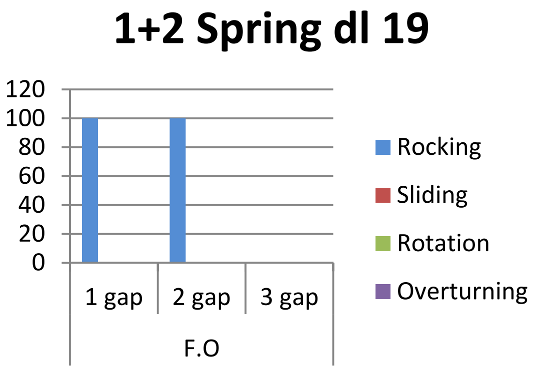
1+2 Spring dl 19
120
100
80
60
40
20
0
1 gap
2 gap
3 gap
F.O
Rocking
Sliding
Rotation
Overturning

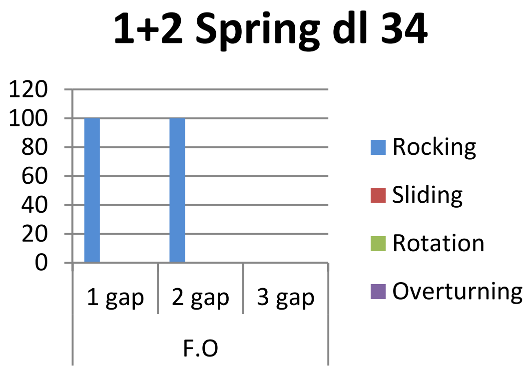
1+2 Spring dl 34
120
100
80
60
40
20
0
1 gap
2 gap
3 gap
F.O
Rocking
Sliding
Rotation
Overturning

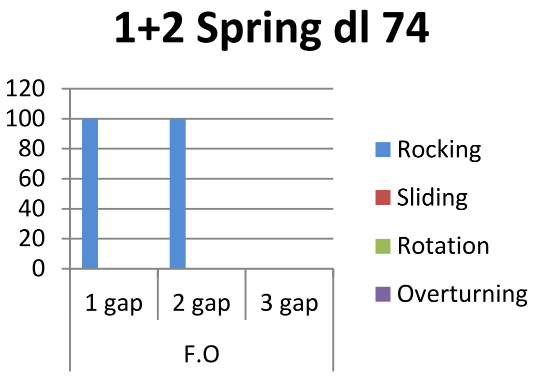
1+2 Spring dl 74
120
100
80
60
40
20
0
1 gap
2 gap
3 gap
F.O
Rocking
Sliding
Rotation
Overturning

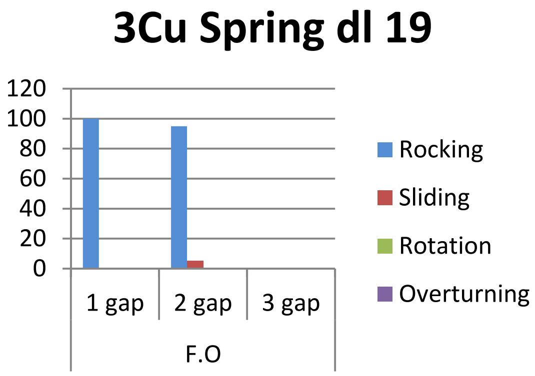
3Cu Spring dl 19
120
100
80
60
40
20
0
1 gap
2 gap
3 gap
F.O
Rocking
Sliding
Rotation
Overturning

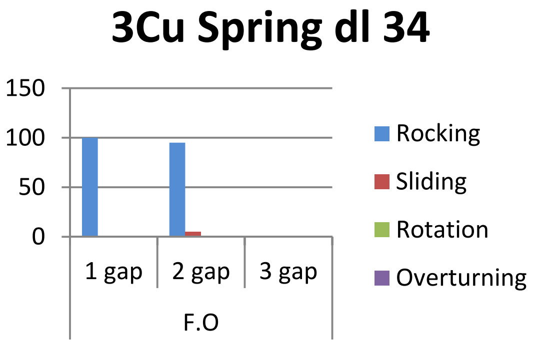
3Cu Spring dl 34
150
100
50
0
1 gap
2 gap
3 gap
F.O
Rocking
Sliding
Rotation
Overturning

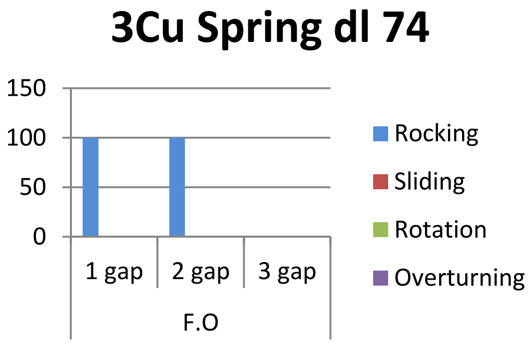
3Cu Spring dl 74
150
100
50
0
1 gap
2 gap
3 gap
F.O
Rocking
Sliding
Rotation
Overturning

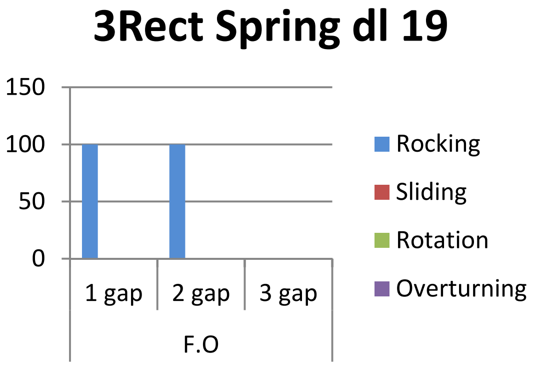
3Rect Spring dl 19
150
100
50
0
1 gap
2 gap
3 gap
F.O
Rocking
Sliding
Rotation
Overturning

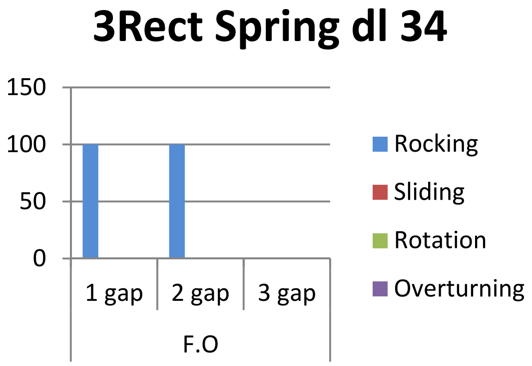
3Rect Spring dl 34
150
100
50
0
1 gap
2 gap
3 gap
F.O
Rocking
Sliding
Rotation
Overturning

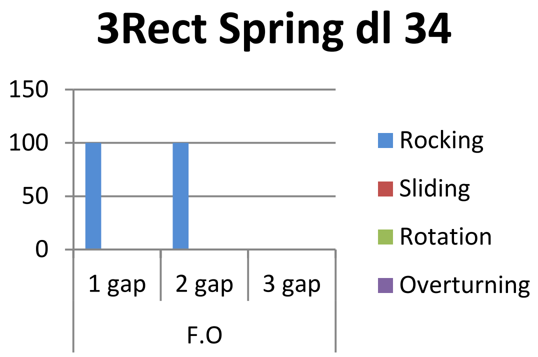
3Rect Spring dl 34
150
100
50
0
1 gap
2 gap
3 gap
F.O
Rocking
Sliding
Rotation
Overturning

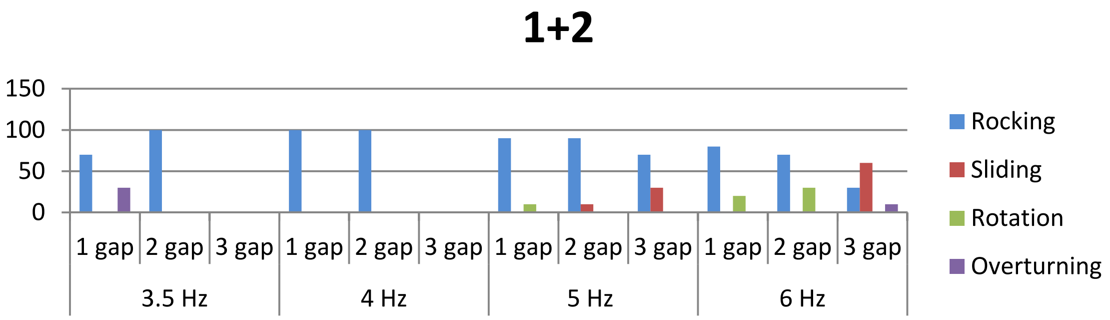
1+2
150
100
50
0
1 gap
2 gap
3 gap
3.5 Hz
4 Hz
5 Hz
6 Hz
Rocking
Sliding
Rotation
Overturning

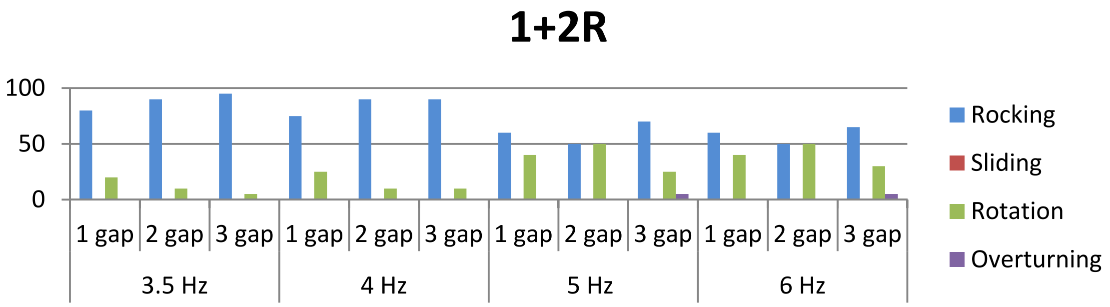
1+2R
100
50
0
1 gap
2 gap
3 gap
3.5 Hz
4 Hz
5 Hz
6 Hz
Rocking
Sliding
Rotation
Overturning

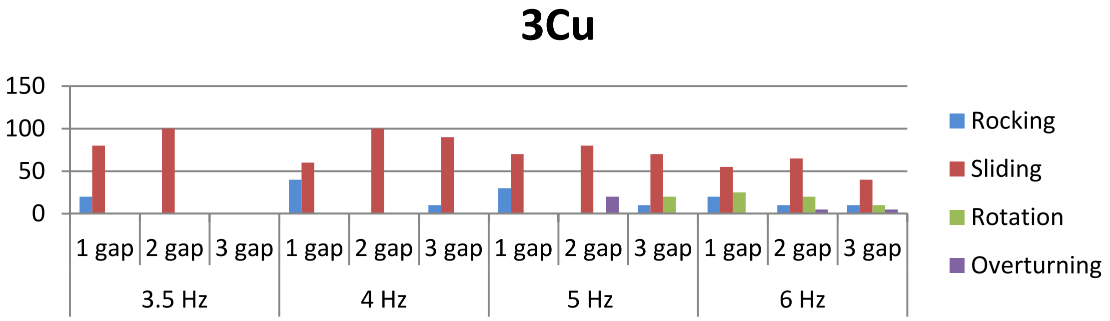
3Cu
150
100
50
0
1 gap
2 gap
3 gap
3.5 Hz
4 Hz
5 Hz
6 Hz
Rocking
Sliding
Rotation
Overturning

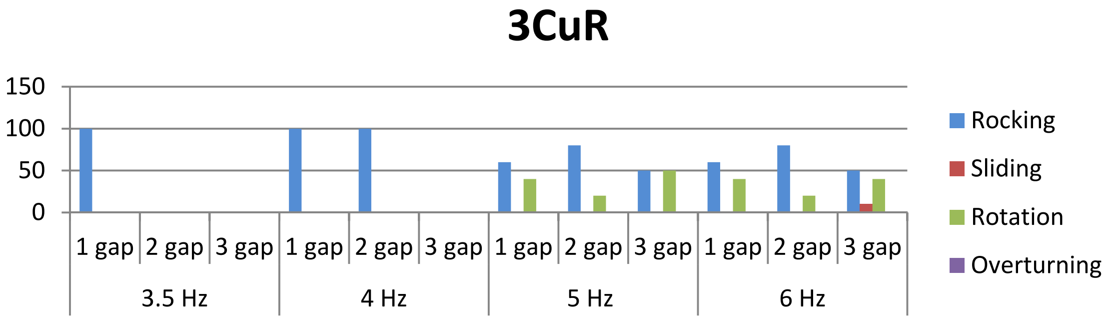
3CuR
150
100
50
0
1 gap
2 gap
3 gap
3.5 Hz
4 Hz
5 Hz
6 Hz
Rocking
Sliding
Rotation
Overturning

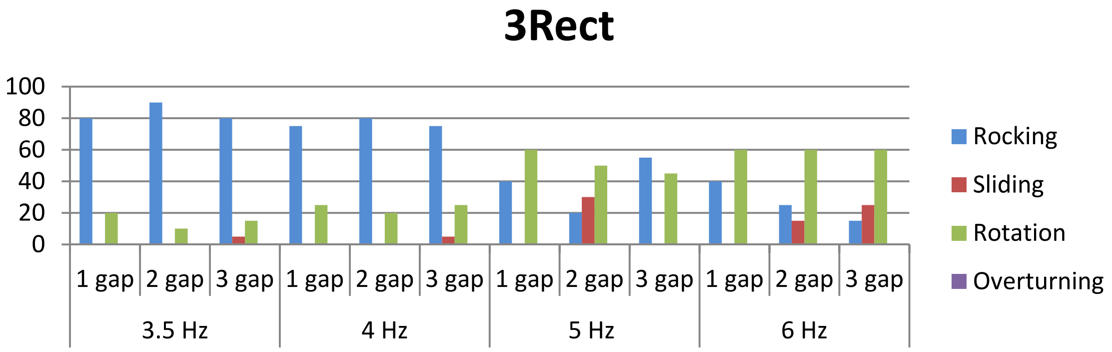
3Rect
100
80
60
40
20
0
1 gap
2 gap
3 gap
3.5 Hz
4 Hz
5 Hz
6 Hz
Rocking
Sliding
Rotation
Overturning

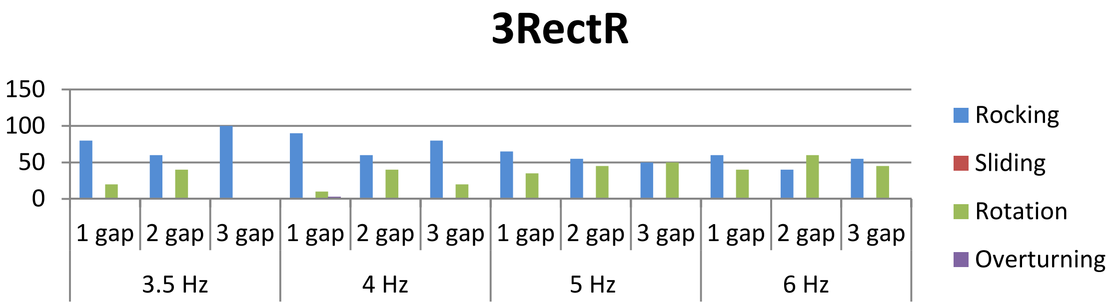
3RectR
150
100
50
0
1 gap
2 gap
3 gap
3.5 Hz
4 Hz
5 Hz
6 Hz
Rocking
Sliding
Rotation
Overturning

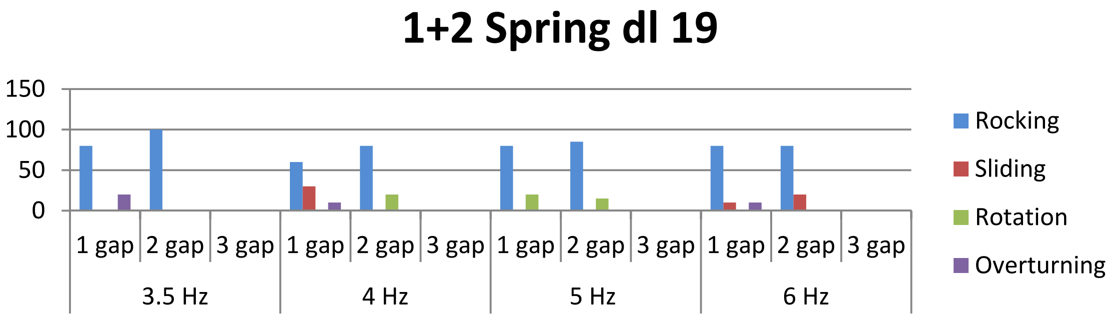
1+2 Spring dl 19
150
100
50
0
1 gap
2 gap
3 gap
3.5 Hz
4 Hz
5 Hz
6 Hz
Rocking
Sliding
Rotation
Overturning

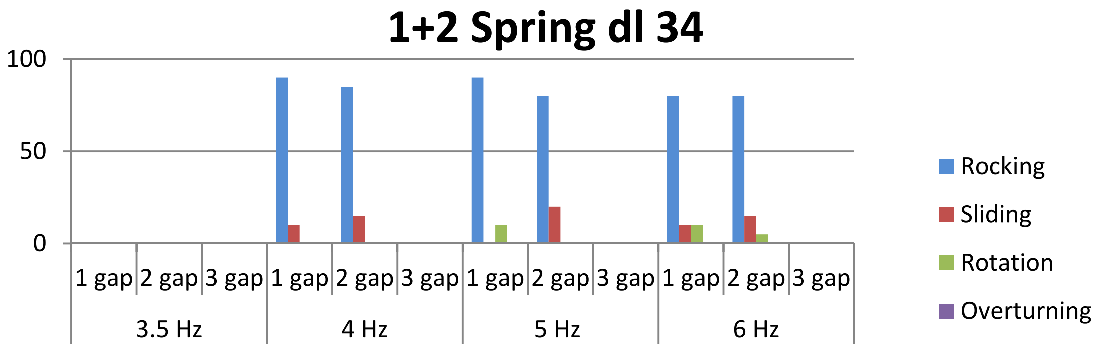
1+2 Spring dl 34
100
50
0
1 gap
2 gap
3 gap
3.5 Hz
4 Hz
5 Hz
6 Hz
Rocking
Sliding
Rotation
Overturning

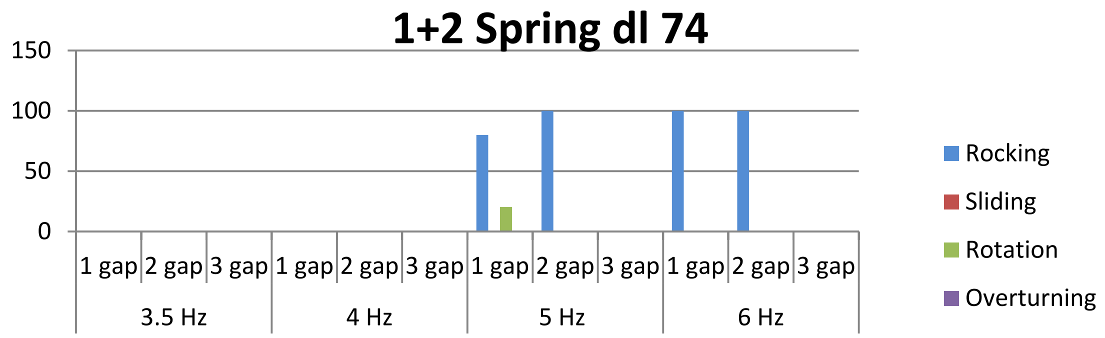
1+2 Spring dl 74
150
100
50
0
1 gap
2 gap
3 gap
3.5 Hz
4 Hz
5 Hz
6 Hz
Rocking
Sliding
Rotation
Overturning

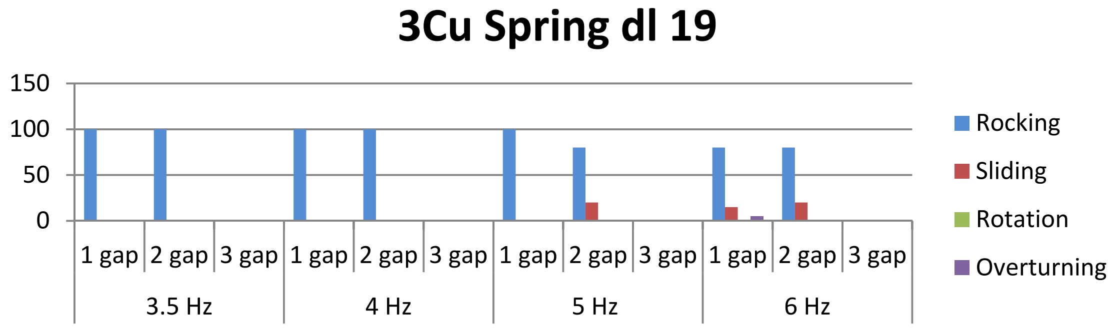
3Cu Spring dl 19
150
100
50
0
1 gap
2 gap
3 gap
3.5 Hz
4 Hz
5 Hz
6 Hz
Rocking
Sliding
Rotation
Overturning

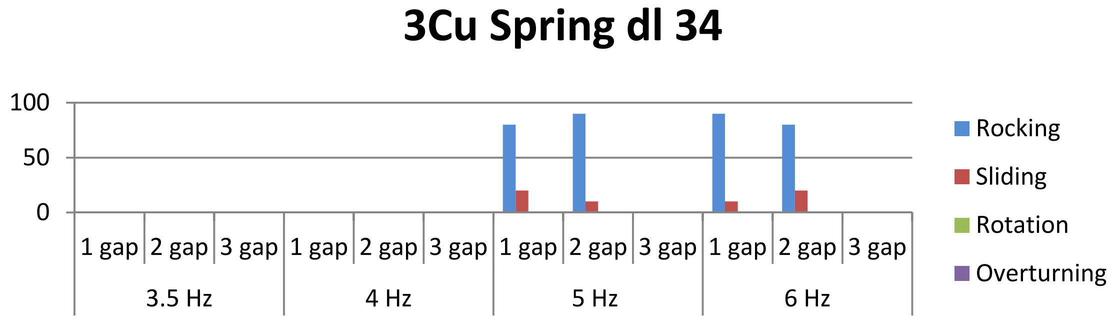
3Cu Spring dl 34
100
50
0
1 gap
2 gap
3 gap
3.5 Hz
4 Hz
5 Hz
6 Hz
Rocking
Sliding
Rotation
Overturning

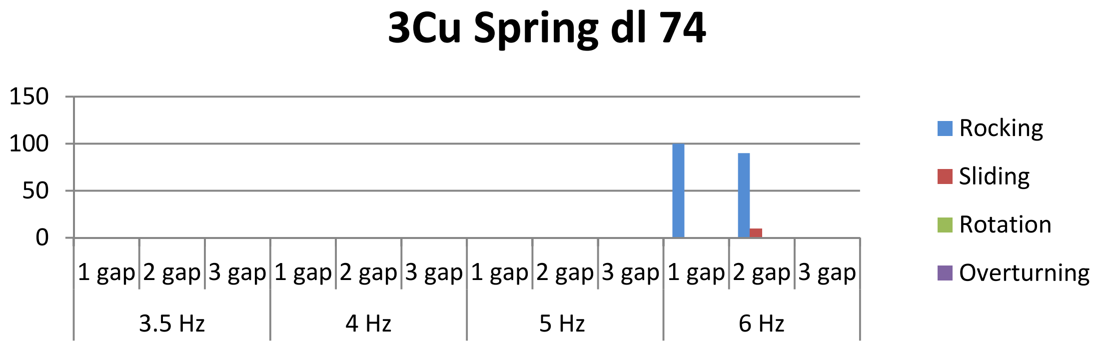
3Cu Spring dl 74
150
100
50
0
1 gap
2 gap
3 gap
3.5 Hz
4 Hz
5 Hz
6 Hz
Rocking
Sliding
Rotation
Overturning

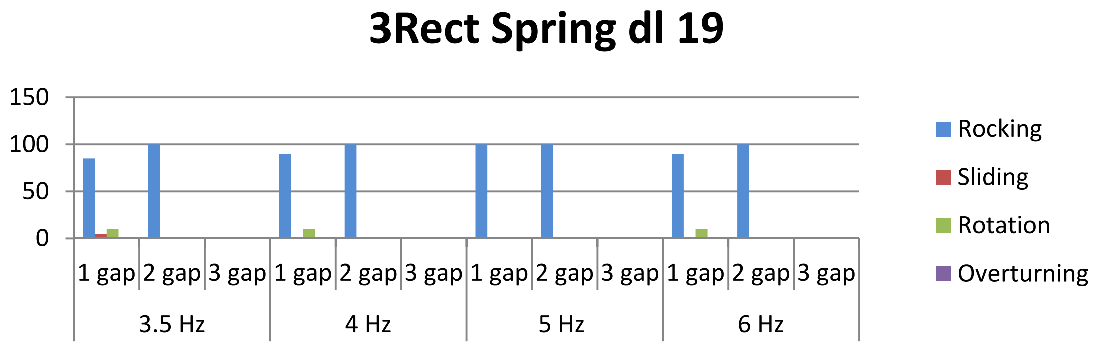
3Rect Spring dl 19
150
100
50
0
1 gap
2 gap
3 gap
3.5 Hz
4 Hz
5 Hz
6 Hz
Rocking
Sliding
Rotation
Overturning

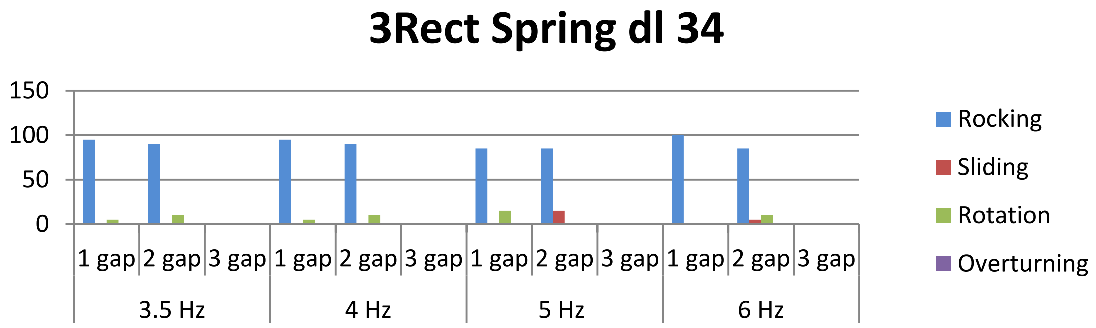
3Rect Spring dl 34
150
100
50
0
1 gap
2 gap
3 gap
3.5 Hz
4 Hz
5 Hz
6 Hz
Rocking
Sliding
Rotation
Overturning

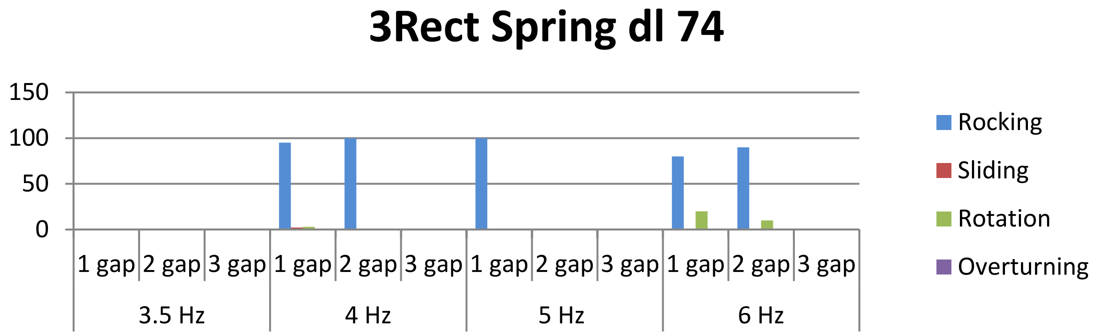
3Rect Spring dl 74
150
100
50
0
1 gap
2 gap
3 gap
3.5 Hz
4 Hz
5 Hz
6 Hz
Rocking
Sliding
Rotation
Overturning

3

Testing of a Multiple Rocking Scaled Bridge

3.1 Introduction

In this chapter is proposed a dynamic test on a shaking table. This experimental part aims to capture the behaviour of a multiple segmented bridge. The bridges are composed by a multi-segmental pier and deck allow to rock. The specimens are a 1:30 scaled bridge. The model covers two different types of bridges: two spans bridge and three spans bridge. The bridges tested are completely post-tensioned both pier and deck. Thanks to the post-tension bar in to the deck was possible study and compare different types of connection between the abutment and the deck. The propose specimens start from a design of two real bridge typologies which are common and practiced in New Zealand. However because the small scale it was impossible installing device to dissipate energy.

In this chapter, how after mentioned, is described the design and the construction of two bridges typologies but only the two spans bridge results are reported.

3.2 Design of the Prototype Bridge Pier

The selection of the types of bridge to adopt was taken with the idea to maximize the dimension of the scaled bridge on the shaking table without loss sight of the bridges reproducibility in real. Consequently the pier dimension adopted is 12m tall for both configuration, 28m span bridge for the configuration with two spans and 20m, 16m, 20m for the three span bridge. The two categories of bridge are showed in the Figure 3.1. In according with New Zealand transport agency and them report published in 2008 [75] two different system of standard precast concrete bridge deck are considered as follows.

- Super T Bridge 1225 Deep – 28m span
- I Beam 1600 Deep – 20m and 15m span

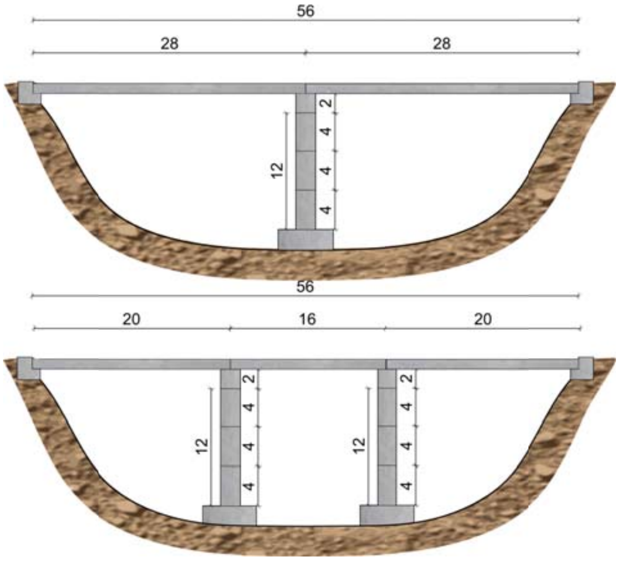

3.1 *Figure – Bridge Typologies*

Figure 3.2 (a) and 3.2 (b) show the deck section for the Super T 1225 and I Beam 1500 bridges respectively, while in Table 3.1 are reported the design load.

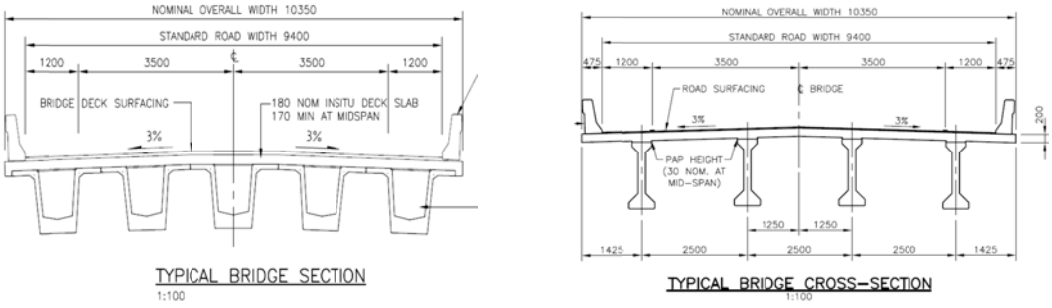

a) *b)*

3.2 *Figure – Bridge deck cross section*

Superstructure System	Bearing Design Loads (kN)			DL+LL (kN)	DL+OV (kN)	No of beams	Total Superstructure weight (W_t) in kN
	DL	LL	OV				
Super T 1225	500	440	515	1020	1095	5	4957
I Beam 1500	452	435	541	887	993	4	3317

3.1 Table – Design Load

Where the design load HN-OH-72 (NZTA bridge manual) is used for design the precast beam. DL is the unfactored Deal Load, LL is the Live Load and referring to the Bridge Manual is equal to 1.35HN·l and OL is the Over Load, it is equal to HO·l. In according to NZ 1170.5 [76] 1000 years return period seismic hazard is considered for each prototype. Table 3.2 summarize the design parameters.

Return period	*Zone factor (Z)*	*Return period factor (R)*	*Type soil*	*Structural performance factor (S_p)*	*N(T,D)*
1000	*0.33*	*1.3*	*Shallow (C)*	*1.0*	*1.0*

3.2 Table – Seismic Hazard Parameters

Using the information in table 3.2 the corresponding acceleration design spectra of NZS 1170.5 for 5% of critical damping is show in the Figure 3.3 below.

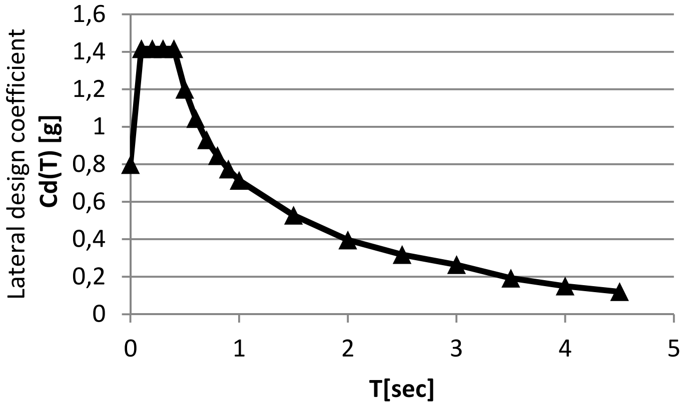

3.3 *Figure – Design spectra for 1000 years return period.*

The purpose of the design of the specimens is to obtain a model which is able to remain into the elastic range. The focus is to study the behaviour of the structure and try to not damage the specimens. Due to this aim the section will be over-designed. The demand capacity is calculate starting from the design spectra as show in Table 3.3.

Period T[SEC]	***Ch(t)***	***C(T)***	***Cv(T)***	***Cd(T)***	***V[KN]***	***F[KN}***	***M[KN*m]***	***M+PΔ [KN*M]***
0	2.36	0.9204	0.64428	1.416	5664	5664	67968	70961
0.1	2.36	0.9204	0.64428	1.416	5664	5664	67968	70961
0.2	2.36	0.9204	0.64428	1.416	5664	5664	67968	70961
0.3	2.36	0.9204	0.64428	1.416	5664	5664	67968	70961
0.4	2.36	0.9204	0.64428	1.416	5664	5664	67968	70961
0.5	2	0.78	0.546	1.2	4800	4800	57600	60136
0.6	1.74	0.6786	0.47502	1.044	4176	4176	50112	52318
0.7	1.55	0.6045	0.42315	0.93	3720	3720	44640	46606
0.8	1.41	0.5499	0.38493	0.846	3384	3384	40608	42396
0.9	1.29	0.5031	0.35217	0.774	3096	3096	37152	38788
1	1.19	0.4641	0.32487	0.714	2856	2856	34272	35781
1.5	0.88	0.3432	0.24024	0.528	2112	2112	25344	26460
2	0.66	0.2574	0.18018	0.396	1584	1584	19008	19845
2.5	0.53	0.2067	0.14469	0.318	1272	1272	15264	15936
3	0.44	0.1716	0.12012	0.264	1056	1056	12672	13230
3.5	0.32	0.1248	0.08736	0.192	768	768	9216	9622
4	0.25	0.0975	0.06825	0.15	600	600	7200	7517
4.5	0.2	0.078	0.0546	0.12	480	480	5760	6014

3.3 Table – Moment and Shear Demand

Where:

$$C(T) = C_h(T)ZRN(T,D) \tag{3.1}$$

$$W_i = G_i + \sum \Psi_E Q_i \tag{3.2}$$

$$C(T) = C_h(T)ZRN(T,D) \tag{3.3}$$

$$C_d(T) = \frac{C(T)S_p}{k_\mu} \tag{3.4}$$

$$V = C_d(T) \cdot W_t \tag{3.5}$$

The aim of this part of analysis was to determine the size of the section, the vertical and dynamic load to scale for the dimension of the specimens. Due to this was use a quick-design approach with CUMBIA program [77]; which gave as a result 1.80 x1.80m base pier sections. No more considerations are referred to the real bridge.

CUMBIA is a program wrote in MatLab to perform monotonic moment-curvature analysis and force displacement response of reinforced concrete members with rectangular or circular section. An axial load–moment interaction analysis is also performed. The member response is obtained from the section moment-curvature results along with an equivalent plastic hinge length, as presented by Priestly at al. [78]. Shear deformations are calculated following the procedure described by Priestly, Calvi and Kowalsky. The shear strength envelope for the member is calculate using the revised UCSD shear model [79]. While the onset of buckling is determined in according with two different models [80, 81].

The program allows the user to specify their constitutive model for the concrete and steel, it also provides a default model that can be used. The default model for the confined and unconfined concrete are both proposed by Mander, Priestley and Park [82]. There are also two different models provided for steel. The code allows the analysis of members subjected to axial load, both in tension and compression, and single double bending.

3.2.1 Scaling Model and Similitude Requirements

The global dimension of the structure is 54m long, 10.35m width and 14m tall. As before mentioned 28m is the length for each deck 12m the tall of the pier and 2m the tall of the cap. During the dynamic test not only the geometry scaling is important but more import is achieving the same dynamic effect. It is possible trying to obtain the same inertial force. Similitude rules comprise a quantitative relationship between the behaviour of the model tested (scaled) and that of the prototype structure [83]. Satisfying all similitude requirements to have a perfect scaled replica would be impossible or extremely costly. The selection of a similitude law needs to based in the parameters that need to remain constant to simplify requirements and to achieve a good representation of the system that is being emulate.

An accurate simulation of the stress-strain relationship of the material is the key point considering the scaled materials needs to demonstrate the same behaviour as the original material. Thus, considering the impossibility to scale stress-strain relationship for the concrete, the best solution is to use a similitude law that keep stress constant. The Cauchy-Froude similitude law, showed in Table 3.4, not only keeps stress-strain constant, but also maintains accelerations, which is an advantage point to be consider during the shaking table test. In this test a scale 1:30 was adopted, so the value to use in the similitude law is λ = 0.033.

Parameter	***Symbol***	***Scale factor***
Modulus of elasticity	E	*1*
Length	L	λ
Area	A	λ^2
Volume	V	λ^3
Mass	m	λ^2

Displacement	*d*	λ
Velocity	*v*	$\lambda^{1/2}$
Acceleration	*a*	*1*
Weight	*w*	λ^{2}
Force	*F*	λ^{2}
Moment	*Mt*	λ^{3}
Stress	σ	*1*
Strain	ε	*1*
Time	*t*	$\lambda^{1/2}$
Frequency	*f*	$\lambda^{1/2}$

3.4 Table – Scale factor to satisfy the Cauchy-Froude similitude laws

3.2.1.1 Similitude Requirements for Scale Model with Subject to Inertia Forces

The flow-chart below represent how obtain the similitude requirements for the scale model with subject to inertia forces. The main requirement to use this method is to assume model and prototype with the same material.

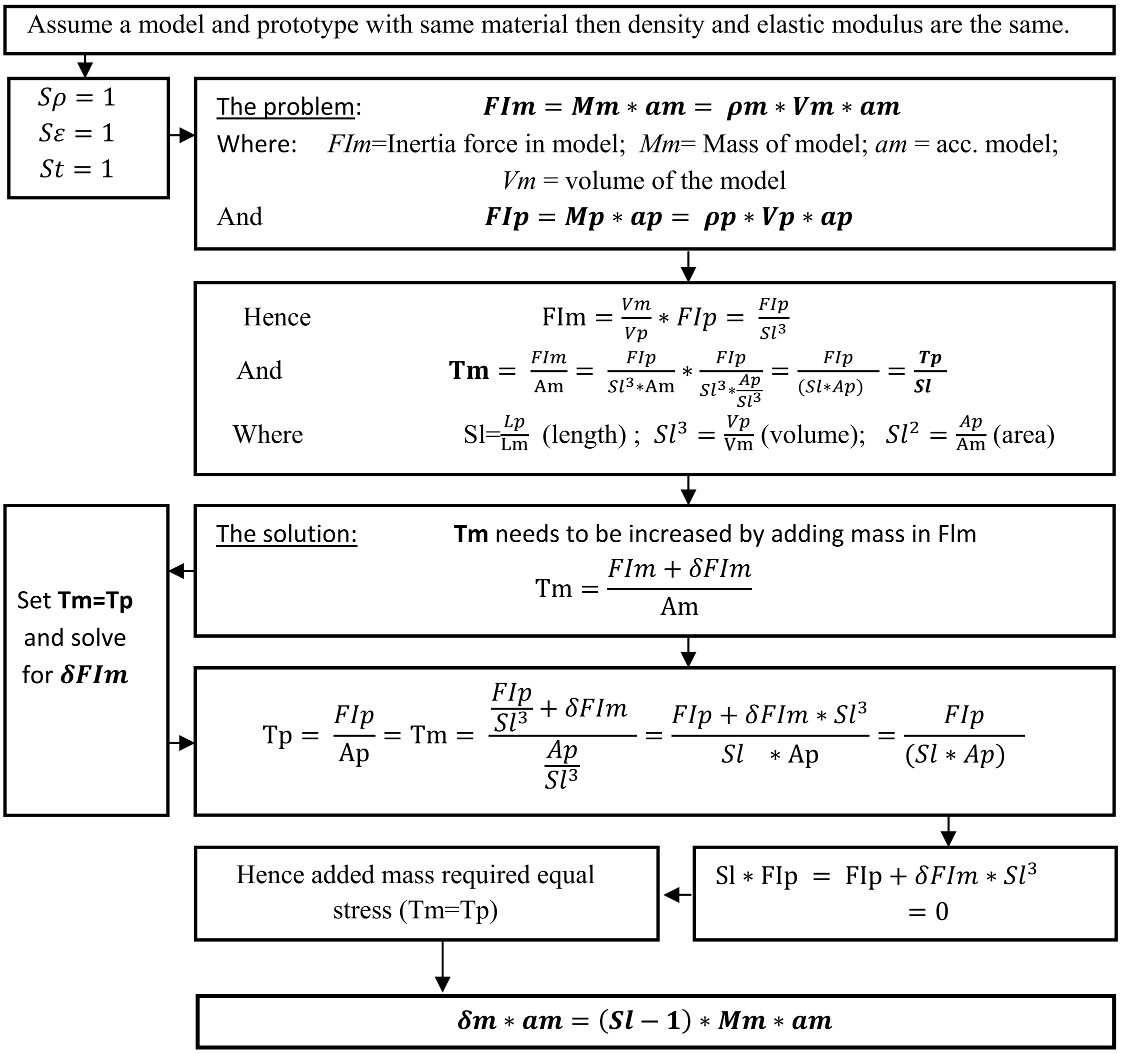

3.2.1.2 Scaling of the Specimens

This paragraph presents how the prototypes are scaled in to a model. The starting prototypes are described in Table 3.5 and Table 3.6. In this phase will be calculate how many weight have to be added to the specimens. The load to add is considered at the bottom of the pier.

In the tables below there is geometry and weight scaling comparison for each component of the specimen. The dimensions are scaled referring to the Table 3.4. The weight of the model is the sum of the real weight of the specimen. Instead the sum of the prototype weight is to refer to the scaled value, moreover the deck weight is selected in according to NZTA bridge manual [75]. As is show below the total weight to add to the specimens is the difference between the two values. Consequently to the results obtained the weight of the specimens will be add using steel plates.

Despite the adding of the weight, it will be impossible achieve the same dynamic inertia forces, because the distribution of the mass in the specimens is not equal compared to the prototype.

2 Spans Bridge			
Scale factor 1:30		***Prototype***	***Model***
Deck	*Base [m]*	*10.35*	*0.35*
	Width [m]	*27*	*0.925*
	Height [m]	*1.3*	*0.055*
	Weight [kg]	*495700*	*45*
	Scaled Weight[kg]	*551*	
Cap	*Base [m]*	*1.9*	*0.065*
	Width [m]	*10.35*	*0.35*
	Height [m]	*1.9*	*0.065*
	Weight [kg]	*89239*	*4*
	Scaled Weight[kg]	*99*	
Pier	*Base [m]*	*1.9*	*0.065*
	Width [m]	*1.9*	*0.065*
	Height [m]	*12*	*0.390*
	Weight [kg]	*103968*	*5*
	Scaled Weight[kg]	*116*	
Total scaled weight [kg]		***766***	***54***
Weight to add [kg]		***711***	
Steel Plate	*Base [mm]*	*178*	
	Width [mm]	*580*	
	Height [mm]	*20*	
	Weight [kg]	*16*	
	N-Steel plate	***44***	
	Total Load [Kq]	***704***	

3.5 Table – Scaling 2 Spans Bridge

	2 Spans Bridge		
Scale factor 1:30		***Prototype***	***Model***
Deck (20 m)	*Base [m]*	*10.35*	*0.35*
	Width [m]	*20*	*0.675*
	Height [m]	*1.3*	*0.055*
	Weight [kg]	*221400*	*33*
	Scaled Weight[kg]	*246*	
Deck (15 m)	*Base [m]*	*10.35*	*0.35*
	Width [m]	*15*	*0.500*
	Height [m]	*1.3*	*0.055*
	Weight [kg]	*110300*	*25*
	Scaled Weight[kg]	*122*	
Cap	*Base [m]*	*1.9*	*0.065*
	Width [m]	*10.35*	*0.35*
	Height [m]	*1.9*	*0.065*
	Weight [kg]	*89239*	*4*
	Scaled Weight[kg]	*99*	
Pier	*Base [m]*	*1.9*	*0.065*
	Width [m]	*1.9*	*0.065*
	Height [m]	*12*	*0.390*
	Weight [kg]	*103968*	*5*
	Scaled Weight[kg]	*116*	
Total scaled weight [kg]		***583***	***38***
Weight to add [kg]		***545***	
Steel Plate (deck 20m)	*Base [mm]*	*178*	
	Width [mm]	*460*	
	Height [mm]	*20*	
	Weight [kg]	*13*	
	N-Steel plate	***27***	
	Total Load [Kq]	***351***	
Steel Plate (deck 15m)	*Base [mm]*	*178*	
	Width [mm]	*400*	
	Height [mm]	*20*	
	Weight [kg]	*11*	
	N-Steel plate	***20***	
	Total Load [Kq]	***220***	

3.6 Table – Scaling 3 Spans Bridge

3.2.2 Level of Post-Tension Design

To calculate the parameter to design the characteristic of the post tension bar, the quick-design procedure was adopted [84]. The two span bridge model was simplified like a SDOF with the same geometrical characteristic.

The design acceleration is equal to 0.85g and starting from this value the base shear and moment were calculated. So the starting parameters are: M=1.22 KN*m and V= 2.21 KN. The next step, is assuming the depth of the neutral axis. Due to the elevate stiffness of the element given by SHS section the neutral axis was considered equal to 0.15*d. In figure 3.4 is schematized how the system works.

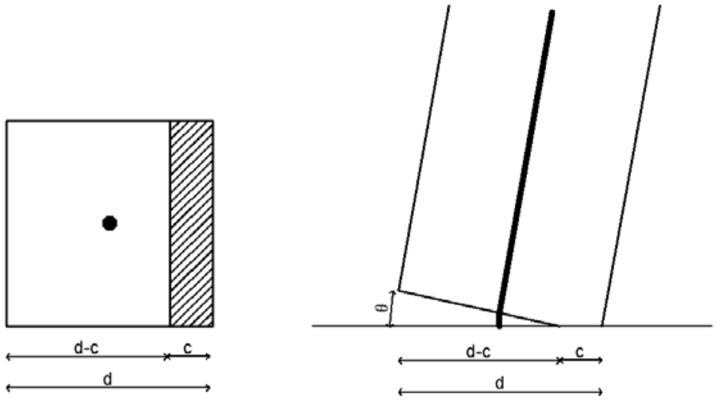

3.4 *Figure –Simplified behaviour of a rocking section*

The design moment is define like 15% less than the moment domain, as show in Equation below, because in this way the element is allows to rocking:

$$M^*_{design} = 0.85 \cdot M_{dem} = M^*_{sc} + M^*_s \tag{3.6}$$

$$M^*_{design} = 0.6M^*_{sc} + 0.4M^*_s \tag{3.7}$$

$$M^*_{sc} = M^*_{pt} + M^*_N \tag{3.8}$$

Where M^*_{sc} is the self-centring moment, M^*_s is the moment given by dissipative device, M^*_{pt} is the moment given by the post-tension contribute and M^*_N is the moment given by the vertical load. At this step the procedure asks to define the λ coefficient which defines the ratio between the re-centring capacity with the dissipative energy characteristic of the system. In this case there is not any device with the aim to dissipate energy, so in this case λ is always major than α_0. Further to le lack of dissipative device M^*_s is equal to zero and consequently $M^*_{design} = M^*_{sc}$.

$$\lambda = \frac{M^*_{pt} + M^*_N}{M^*_s} \geq \alpha_0 \tag{3.9}$$

$$\alpha_0 = \frac{M^*_{pt} + M^*_N}{M^*_{total}} = \frac{\lambda}{\lambda + 1} = 0.56 \qquad (3.10)$$

$$M^*_N = W \cdot (\frac{d}{2} - c) \qquad (3.11)$$

$$M^*_{pt} = M^*_{sc} - M^*_N \qquad (3.12)$$

M^*_{pt} is the unknown quantity, however it possible easily obtain M^*_N value with the Equation 3.11 and hence M^*_{pt} using the Equation 3.12. Consequently knowing the total moment contribution given by the post-tensioned bar is possible calculate the post-tension force with the following formula.

$$F_{pt} = \frac{M^*_{pt}}{(\frac{d}{2} - c)} \qquad (3.13)$$

Therefore the force to give to the post-tension bar is quantified in 40 KN corresponding to the 54% f_{ypt}. The last unknown quantity left is the diameter of the bar and the results given by the following formula is 11.4 mm. On the market there are only standard dimensions, so the choice was to use a 12 mm bar.

$$A_{pt} = \frac{F_{pt}}{80\% f_{ypt}} \qquad (3.14)$$

Consequently of the non-ductile behaviour of the post tension bar and tendon it was used a safety factor expressed considering the 80% of yielding stress of the bar.

The same procedure was used to define the characteristic of the bars to use for the abutment column. While the pier column is allows to rock, the abutment column are not. Hereby considering the same data in input the dimension was extremely over designed. Hence reassuming the quantity found:

Bar	***Grade***	***A[mm^2]***	***D [mm]***	***f_{pt} [KN]***	***f_y [KN]***	***f_u [KN]***
Pier Threaded bar	*8.8*	*104*	*12*	*40*	*72*	*90*
Columns Abutment Threaded bar	*8.8*	*380*	*22*	*80*	*243*	*304*

3.7 Table – Geometrical characteristic of the pier and column abutment treaded bar

In this kind of connection if is not present a shear key, all the shear demand is in charge of the post-tensioned bar/tendon. Hence the check on the pier threaded bar was carried out with the Equation 3.15 below. Where R_n is the shear resistance of the bar A_b is the gross sectional area of the bar and F_u^b is the tensile strength of the bar.

$$R_n = F_u^b (0.75 A_b) \tag{3.15}$$

A prediction of the behaviour of the element was carried out using the program Hybrid. This program gives in output the moment-curvature chart. Due to this is possible try to predict the level of the gap opening during the solicitation given by the shake-table. The blue line on the chart represents the moment curvature shape, while the red one is the opening of the gap. Both quantities are in relation with the rotation of the rocking section. From the chart below is possible to identify where is locate the decompression moment (green dot) and the value of the gap opening moment (orange dot). The flat part of the blue curve means that the bar is yielded. The yielding level in this model is reached fast because the length of the bar is only 550mm.

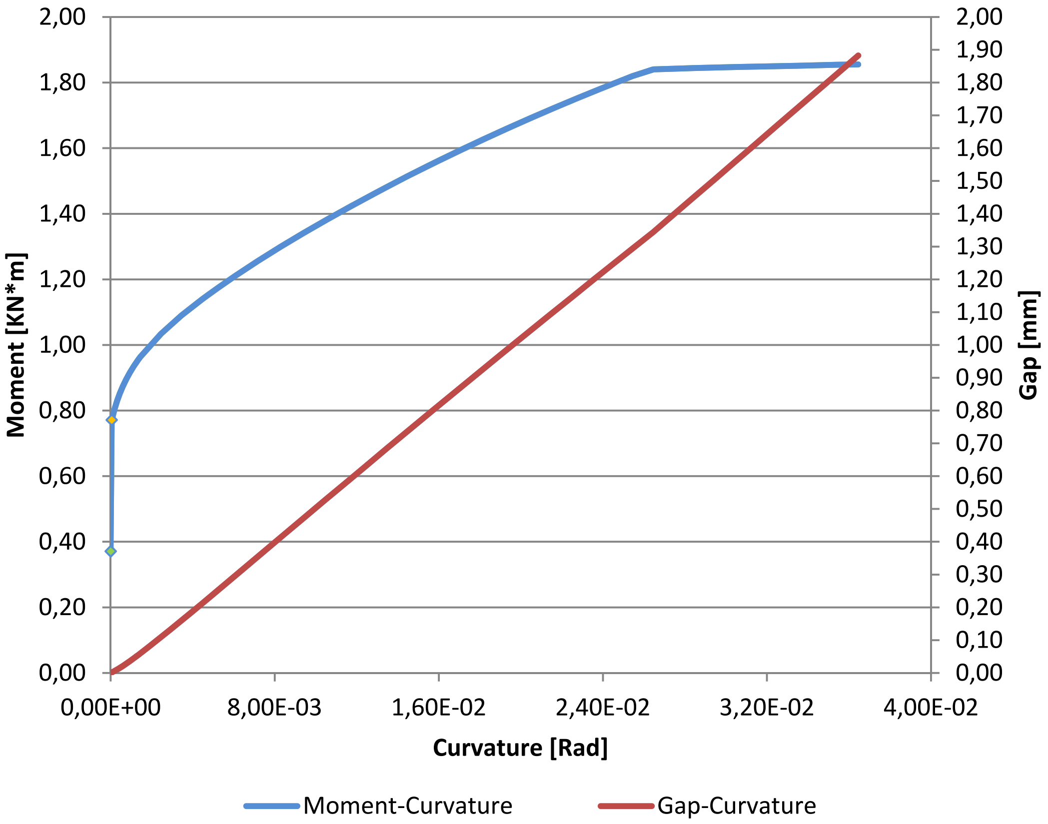

3.5 *Figure – Moment-Rotation and Gap-Rotation predictions*

3.3 Structural Details and Construction of the Bridge Test

The purpose of those types of specimens is to analyze the behaviour of a multiple rocking bridge piers and decks; simulating a construction with precast elements. Consequently of that was decided to divide the pier in three equal segments. The division of the pier in three rectangular parallelepiped parts depends on the results obtained in the previous experiment; where was detected that this configuration is easier subjected to rock compared with the other. Not only for the dynamic characteristic but even for the practical construction procedure this configuration was chosen. The model is allow to rock not only in the pier section but even between the section of contact of the two deck. The concept design of this project is to test the model with different kinds of restrains. This is possible because inside the decks are located four post-tension bars: two in the middle e two external. Both of them are connected and could be fixed with the abutment.

The specimens are composed by many parts and all components are assembled together by a post tensioned rods bar. In the Figure 3.6 below, is explained how the specimens are composed. Both the two spans bridge and the three spans bridge have some part in common with the purpose to have faster construction and assembling and they are conceived with the same concept and the test methodology is the same.

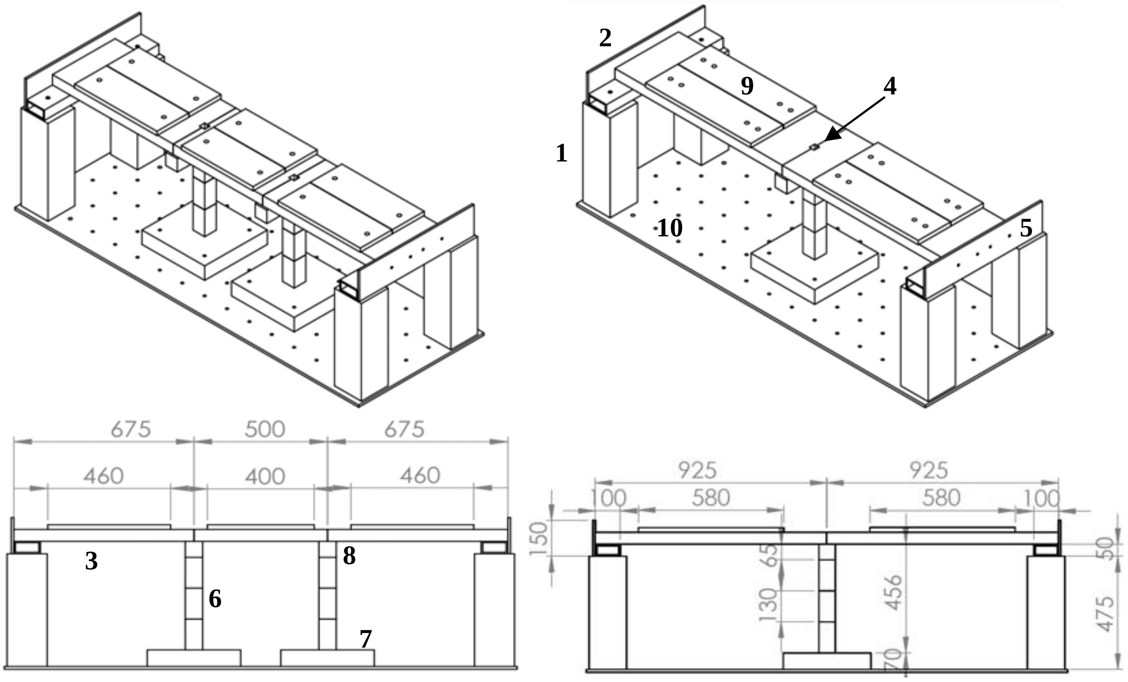

1) Abutment Column; 2) Abutment; 3) Deck; 4) Post tension hole pier; 5) Post tension hole abutment; 6) Segmented pier; 7) Foundation; 8) Cap; 9) Load steel plate; 10) Shake table

3.6 *Figure – Three spans bridge typology*

1) The abutment columns are 150x150x475 mm. The aim of this element is only to provide an adequate rigid support to the abutment. The four abutment columns are designed with the purpose to be fully fixed on the shaking table plane, even under the sinusoidal input. Due to this to increase the stiffness, prevent any damage, prevent the bending of the element and simplify the construction procedures, the external section is composed by a steel Square Hollow Section (SHS) and inside the concrete was cast, as show in Figure 3.7. Those columns are equipped with a D22 Threaded Bar 8.8 Grade, which allow it to be fixed to the element of the shaking table throw post-tensioning forces. Previously the casting duct was centred in the SHS to allow the bar to slip in during the tensioning phase.

3.7 *Figure – Abutment columns*

2) The abutment in this simplified model is composed by a beam and by a steel plate welded with the horizontal element. The beam has geometrical dimensions equal to 50x100x640 mm. It connects the two external columns and it is fixed to them with the same post tension bars used to clamp the abutment columns on the shaking table. This operation is possible due to the holes drilled in the element, as shown in the Figure 3.8 below with the letter B. Equal to the element described above this element is composed of a steel Rectangular Hollow Section (RHS) and inside was cast the concrete. Due to the lack of room to insert longitudinal and transversal bars to provide enough shear and moment resistance to the element RHS was adopted. The steel plate connected to the beam has the purpose to allow the anchoring of the deck post tension bars, through the holes represented in the figure below with the letter A, and provide a stiff deck rocking base. Its dimensions are equal to 640x150x10. The rigid connection between the plate and the beam is given by a 5mm width weld on top and bottom.

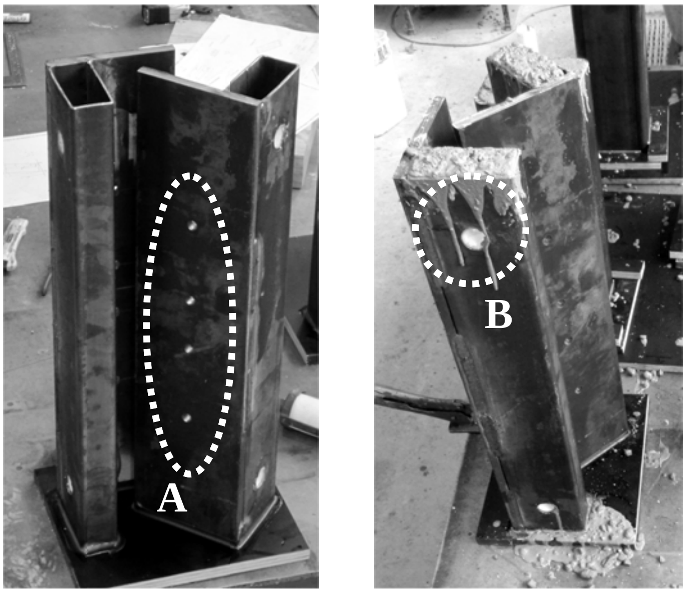

3.8 *Figure – Abutment and connection beam*

3) Three types of decks were built in total: 925x350x50 mm, 675x350x50 mm and 500x350x50 mm. The first construction step was creating the timber mould for the concrete and fix inside the duct for the post-tension rods, as show in Figure 3.9-A. Moreover vertical ducts (B) were added to allow the connection between the load steel plate and the deck using a rods steel bars. Furthermore, as show in the picture and underline by the letter D, was fixed a timber appendage in the timber mould with the aim to create a slot in the concrete slabs. Due to this the post tension pier bar was allowed to crossing throw the deck. Further in this way was easily possible tensioning the threaded bar and fix it with a nut. The longitudinal reinforcement was designed only for the worst case study, in terms of vertical load and then the model was used for the less critical slabs. The critical combination is the two spans bridge (longer span) where more than 350kg of steel plates are clamped on each deck. The result achieved was four D10 mild steel bars on the bottom and three D10 mild steel bars on the top. The threaded bar for the deck post –tension are D10 Threaded Bar 4.6 Grade.

4) As described in the point 3, in Figure 3.10 is presented a close out of the slot before mentioned. It is needed for a more clear explanation about the meanings of the appendage used in the timber mould.

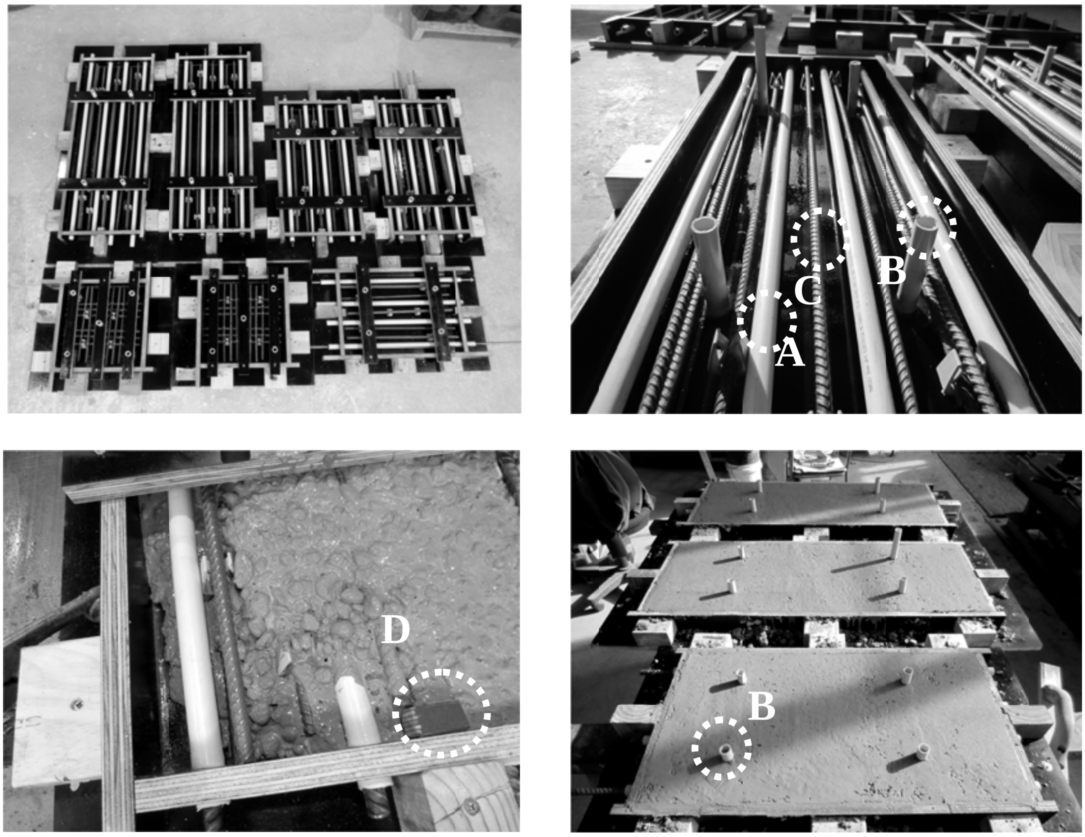

3.9 *Figure – Bridges Decks*

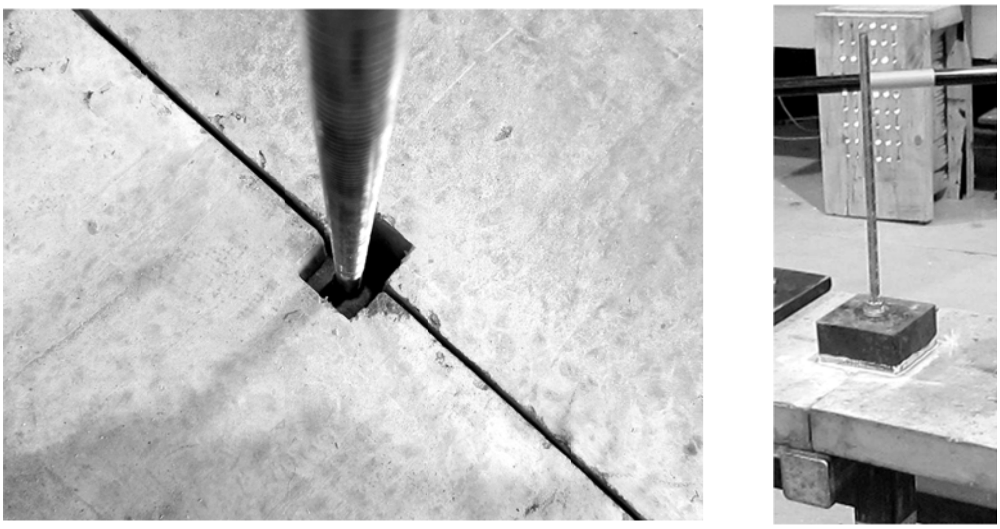

a) *b)*

3.10*Figure – Close out of the deck slot for the post-tension bar (a) and the rod before the post-tension phase (b)*

5) At this point are showed how the holes in the abutment steel plate works. The figure a) present the deck bars before the application of the tension force. After the application of the force the bars will fix with a washers and nuts. The Figure 3.11-b represent an overview of the parts assembled.

a) *b)*

3.11*Figure - Close out of deck post-tension bar (a) and overview of columns abutment and deck post tension bar (b)*

6) In the Figure 3.12 are showed the six pier segments built. Each segment is 65x65x130 mm. Equal to the others structural elements, where not enough room is present for the classical reinforcement, with the aim to prevent the smashing of the edge during the rocking motion and simplify the construction procedures were adopted steel SHS. Subsequently the concrete was cast inside. Previously the cast phase, all the segments are equipped with centred duct (A) in the SHS to allow the bar to slip in during the tensioning and rocking phase. The need to have the duct fixed even during the setting of the concrete and to obtain a smooth surface contact for the rocking phase, timber cap showed in the picture (B) was installed.

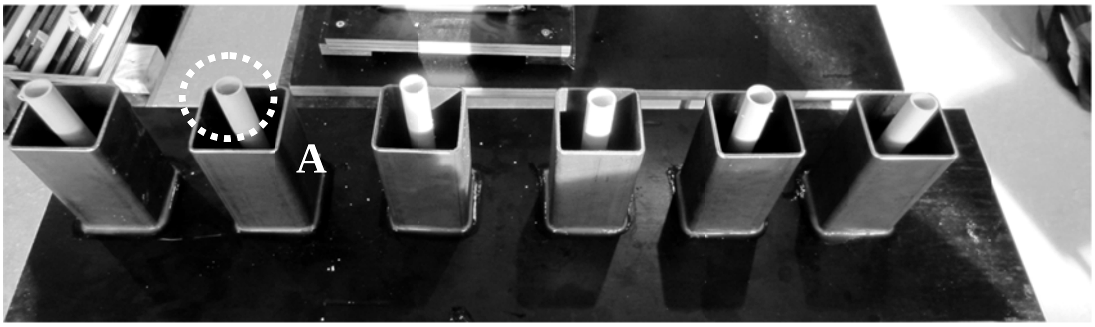

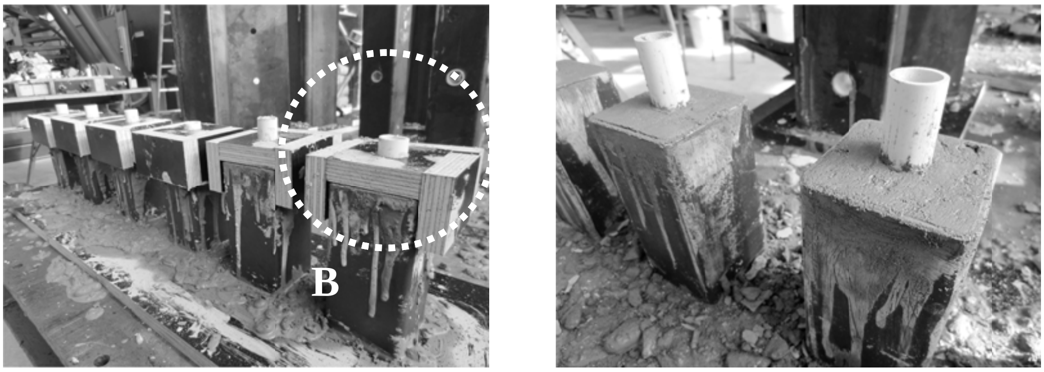

3.12*Figure – Segmented piers*

7) The foundation is 350x350x70 mm. It is not scaled from the prototype because it is not involve in the dynamic motion, but it is only a support for the pier. Its size was chosen due to the aim to fix the element on the shaky table and consequently the pier too. The four angular ducts (A) are insert to allow the bolts to pass through the foundation and be fixed on the shaking table. While the centred duct (A) is for the pier post tension bar. The longitudinal reinforcement are designed to prevent any possible failure of the concrete. The reinforcement are composed six D10 Mild Steel bars in both direction, longitudinal and transversal.

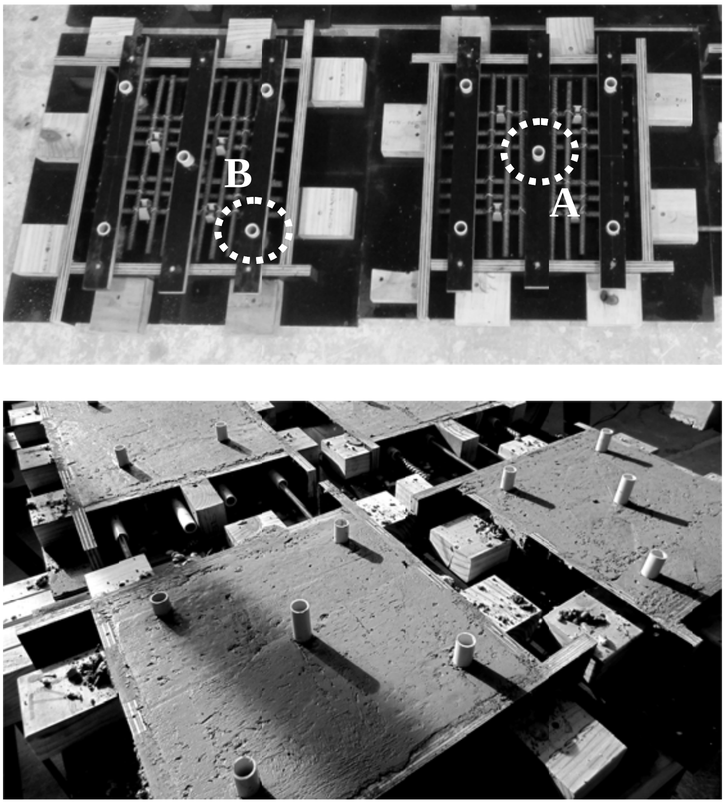

3.13 *Figure – Pier Foundation*

8) The cap is 65x65x370 mm. The construction of this element is done with the same procedures of the other structural element. Due to the lack of room for the classical longitudinal and transversal reinforcement SHS was adopted. The hole left in the section, as show in Figure 3.14-A, has the purpose to allow the pier post tension bar to pass through.

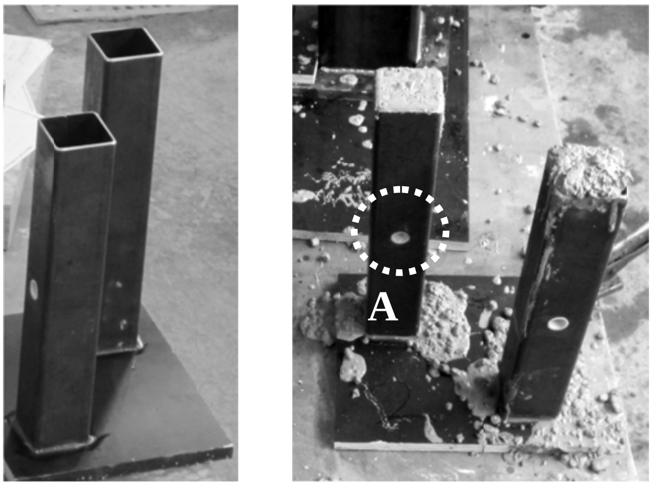

3.14 *Figure – Pier Cap construction phase.*

The Figure 3.15 below represent two span bridge model assembled on the shaking table. The steel plate under the foundation and the four abutment columns were used to lift off the model with the crane after the assembling.

All the technical drawings about the component of both specimens will be presented in the appendix.

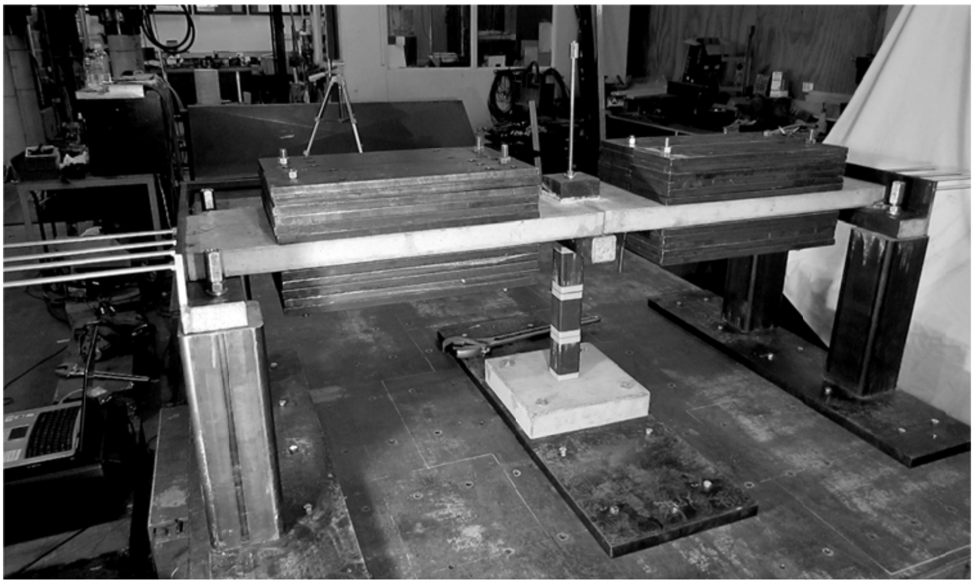

3.15 *Figure – Two span bridge model assembled*

3.3.1 Material Properties

3.3.1.1 *Mild Steel*

The only mild steel in the dynamic test was used for the longitudinal reinforcement in to the deck and in to the foundation elements. The average mechanical properties are reassume in the table below:

E	f_y	f_u	ε_y	ε_{sh}	ε_u
200000Mpa	322Mpa	457Mpa	0.0016	0.0264	0.20

3.8 Table – Mild Steel mechanical properties

3.3.1.2 *Rectangular and Square Hollow Section*

The RHS and SHS was used for the most type of element composing the models. On the market the size of RHS is in the range 50x20x2 mm wall thickness up to 300x200x9.0mm, while SHS is in the range 25x25x1.6 up to 400x400x9.0 mm. All the section used satisfied NZ & Australian Standards AS-1163-C350/450.

3.3.1.3 *Threaded Bars*

Two different type of threaded bars are used in the model. The 8.8 Grade for the pier and for the four abutment columns, instead 4.6 Grade bars were used for the deck post-tension. The average mechanical properties are described in the table below.

	E	f_y	f_u	ε_y	ε_{sh}	ε_u
8.8 Grade	200000Mpa	640	800	0.0072	NA*	NA*
4.6 Grade	200000Mpa	240	400	0.00792	NA*	NA*

*NA=not applicable

3.9 Table – Treaded Bars mechanical properties

3.3.1.4 *Concrete*

For both models, due to the small dimension of the specimens the consequently lack of room between the components inside the timber mould like horizontal and vertical duct, the longitudinal reinforcement and the using of post-tension was necessary adopt a specific design for the concrete mix. The mix designed was calculated specifically for the use of post-tension. The expected range was between 50-58 MPa but after the compression tests the average results was 68Mpa. The concrete mix design used is explained in the Table 3.10 below.

Mix design	
Mix volume [L]	*80*
Gp Cement [Kg]	*35.93*
Water [Kg]	*14.64*
13mm Aggregate [Kg]	*99.75*
Sand [Kg]	*74.7*
Microsilica [Kg]	*3.125*
SP [ml]	*95*

3.10Table – Concrete Mix Design

3.4 High-Acceleration Control Using Shake-Table and Data Acquisition

3.4.1 Shake-Table

3.4.1.1 Description of the Shake- Table

The shake-table at the University of Canterbury is a uniaxial earthquake ground motion simulator. The table has a plan area of 2m wide by 4.5m in length. The table top is constructed from 12mm steel plate connected on top of 4-410UB54 steel sections running the length of the table. In the transverse direction 12mm steel plate stiffeners are welded between all four 410UB sections at intervals of 500mm. Connected to the web of the exterior 410UB sections are 4-100DU115 steel housings which accommodate a series of Teflon bearings. The Teflon bearings slide along a 100mm diameter Bright steel shaft; each shaft sits on top of a 250UB37 steel beam bolted to the laboratory strong floor. The shake-table has an unloaded mass of 2500kg. A 300Hp motor operating at 4000psi powers a 280kN double acting hydraulic actuator which drives the shake-table. A set of Moog E072-054 servovalves control the hydraulic actuator and are capable of supplying 232 lpm.

The servovalves are controlled by a TestStar control system from MTS Systems Corporation. The MTS control is a closed servo loop using proportional, integral and derivative feed-forward adjustment. By altering the amount of proportional and/or integral gain, the tracking of the table can be manipulated. A table command is given to the system as a displacement time history, doubly integrated from the desired acceleration time-history.

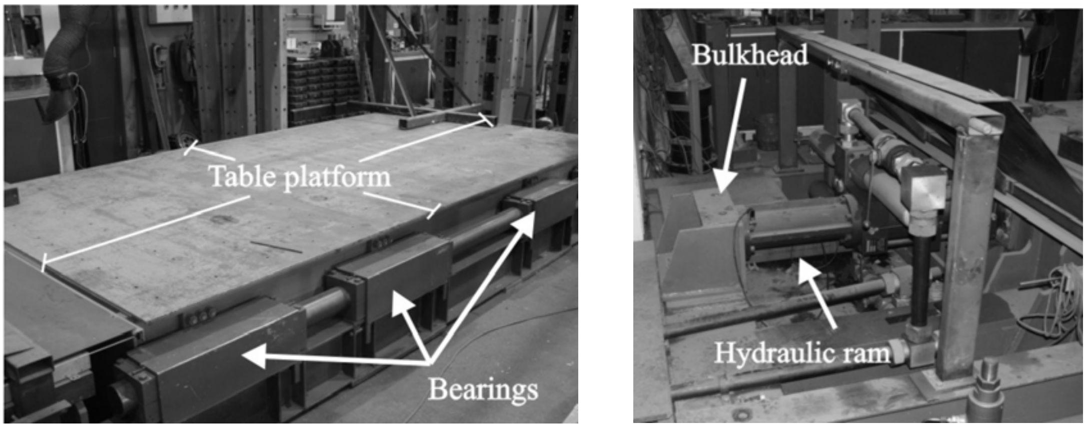

a) *b)*

3.16 *University of Canterbury Shake-Table: Shake-Table platform a); Shake-Table hydraulic ram and bulkhead b); [85]*

3.4.1.2 Shake-Table Capacity

The shake-table has a payload capacity of 20 tonnes and displacement amplitude of 130mm (total stroke of 260mm). The capacity of the servovalves limits the velocity of the table to approximately 242mm/s. This is defined as the saturation velocity of the table, and in all cases, should be avoided. As the table reaches saturation, the velocity gradient suddenly reaches zero, resulting in large table accelerations. These acceleration spikes can be very significant and, in many cases, can be much greater than that expected from the desired acceleration command.

3.4.1.3 Acquisition System

Shake-table data acquisition was collected via a high speed logger and computer arrangement. A total of 64 channels could be logged at any one time. The logger unit had an in-built analogue filter buried within the software. This analogue filter had a pass-band of 200Hz, that is, at 200Hz the normalised pass-band voltage was equal to 0.707 (Figure 3.17).

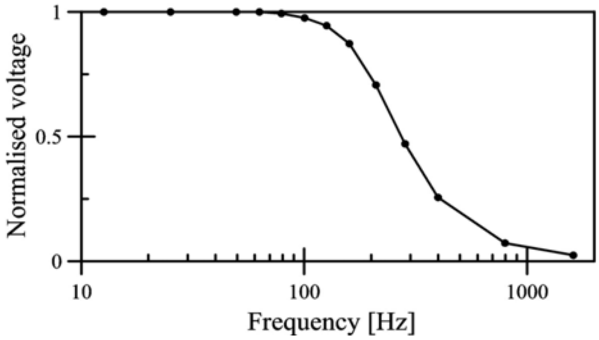

3.17 *Figure – Normalized passband voltag*

Data could be sampled from as low as 1Hz to upwards of 1000Hz. While, the full effect of sampling at 1000Hz would not be felt due to the analogue filter, it was used in order to have a sufficient sample size for filter options during post-processing. The displacement command supplied to the MTS control unit was in time steps of Δt = 0.005 to maximise the resolution: this was the smallest time step that could be recognised by the control unit.

3.4.1.4 Displacement Protocol and Control Algorithm

For this experiment, knowing the design acceleration, it was easy define the displacement input needed by the shaky-table. As is describe below due to a double integration a sinusoidal displacement command and frequency was imposed to the shake-table to achieve the design acceleration. While generating the command signals, consideration was given to the limitations of the shake-table. In particular, the velocity limit of 242mm/s (a safe velocity limit of around 235mm/s was targeted) and the maximum displacement stroke of ±130mm could not be exceeded. The sinusoidal displacement x(t), velocity v(t) and acceleration a(t) time-history is expressed in Equation (3.6), (3.7) and (3.8) respectively.

$$x(t) = A \cdot \sin(\omega \cdot t) \tag{3.16}$$

$$v(t) = A \cdot \omega \cdot \cos(\omega \cdot t) \tag{3.17}$$

$$a(t) = -A \cdot \omega^2 \cdot \sin(\omega \cdot t) \tag{3.18}$$

Where:

A = Maximum displacement amplitude within the cycle
ω = Angular frequency of excitation, where ω=2Πf in units of rad/s
f = Excitation frequency in units of Hz

An easy and fast, but less accurate method to determine the acceleration, the velocity, the displacements and the frequency starting from two of them is to use the diagram showed in Figure 3.18. This diagram is in a logarithmic scale and connects all four dimensions together.

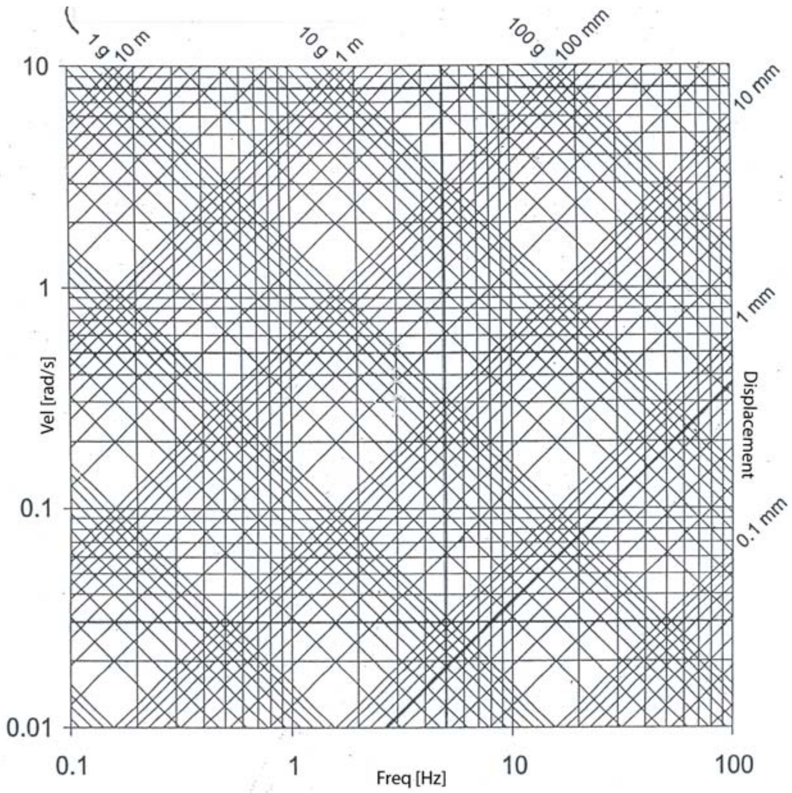

3.18 *Figure – Acceleration, Velocity, Displacements and Frequency diagram interaction*

3.4.2 Image Data Acquisition

The data were acquired by the use of Redlake's MotionPro X3 high-speed motion camera. This camera combine an excellent resolution to frame rate performance, along with the advanced features for accurate high-speed motion analysis [86]. MotionPro X systems has a wide variety of dynamic range options which make them ideal for Design, and Test (RDT) applications, Range, Aerospace, and Ballistics (RAB) and Research, including a unique and proprietary extended dynamic range mode (XDR). It also feature excellent sensitivity and frame rates, including a 1280x1024 resolution at 1000fps for superior resolution at high speeds and a 512x512 resolution at 5000fps for reduced resolution at ultra-high speeds. The camera is equipped with 4GB memory allows more than 3 seconds recording time in the MotionPro X3 (1280x1024 at 1,000 fps), which has a full resolution of 1.3Mpixels, providing a 260K pixel resolution. Also, the recording time can be further increased by selecting a smaller region of interest.

The data was acquired with this different camera because the camera used in the previous experiments, described in the chapter two, was considered inadequate. Instead the data were processed with the same modality and consideration.

3.5 Laboratory Test Set-Up and Experimental Program

The general layout of the laboratory shake-table set-up is illustrated in Figure 3.19, a) and b). The model was positioned perpendicularly to the direction of the shake-table motion. Due to this is possible analyze the transversal response of the bridge. The model was located to one side of the shaking table such that it was possible place the secondary camera (Figure 3.19,a) A) above the deck with the aim to detect the deck gap opening under the sinusoidal input. The primary camera was located on the on the side, as shown by the mark B in the picture. The lens was set with the aim to record the picture focused on the gap between the bottom segment and the middle segment. This option was chosen because the level of the bending moment is higher in the selected section rather than between the middle and top block and consequently the gap is more evident. In the Figure with the letter C are underlined the lamp. They are essential during the test run because the camera needs more light as more are the frame per second recorded. An example is show in the figure c). As is easy understand, notwithstanding there are three bright light the pictures taken are still dark.

During the test only a 3Hz frequency range was investigate with a peak of the acceleration on 0.85g. So the input given to the shaking table was a 3Hz frequency and displacement stroke ±20 mm necessary to achieve the acceleration needed. In the Figure 3.20 is showed the typical time history of the displacement and acceleration recorded during the tests.

The tests are divided in three macro categories. Those categories are differentiated first for the typology of restrains between the deck and the abutment and second for the level of post-tension of the pier. The restrains are obtained post-tensioning or not post-tensioning the rods bar of the deck. All four bars tensioned represent a fully fixed connection; no bars tensioned represent the pin connection and only the two bars locate in the middle represent a hybrid connection between pin and fully fixed connection. The nominal level of the deck tension given in each categories of tests is 15KN. The second sub-category is given by the change of the post tension of the pier bar. The first nominal level, as described in the paragraphs 3.2.2, is 40KN the second level of post tension is equal to 30KN. It is representing the 0.30fy,pt. In the Table 3.11 below is explained the testing program.

	Deck connection					
	Fully fixed		***Pin connection***		***Free connection***	
	Nominal pier post-tensioning level		***Nominal pier post-tensioning level***		***Nominal pier post-tensioning level***	
	30 KN	*40 KN*	*30 KN*	*40 KN*	*30 KN*	*40 KN*
Frequency	*3 Hz*	*3 Hz*	*3 Hz*	*3 Hz*	*3 Hz*	*3 Hz*

3.11 Table – Shake- table testing program

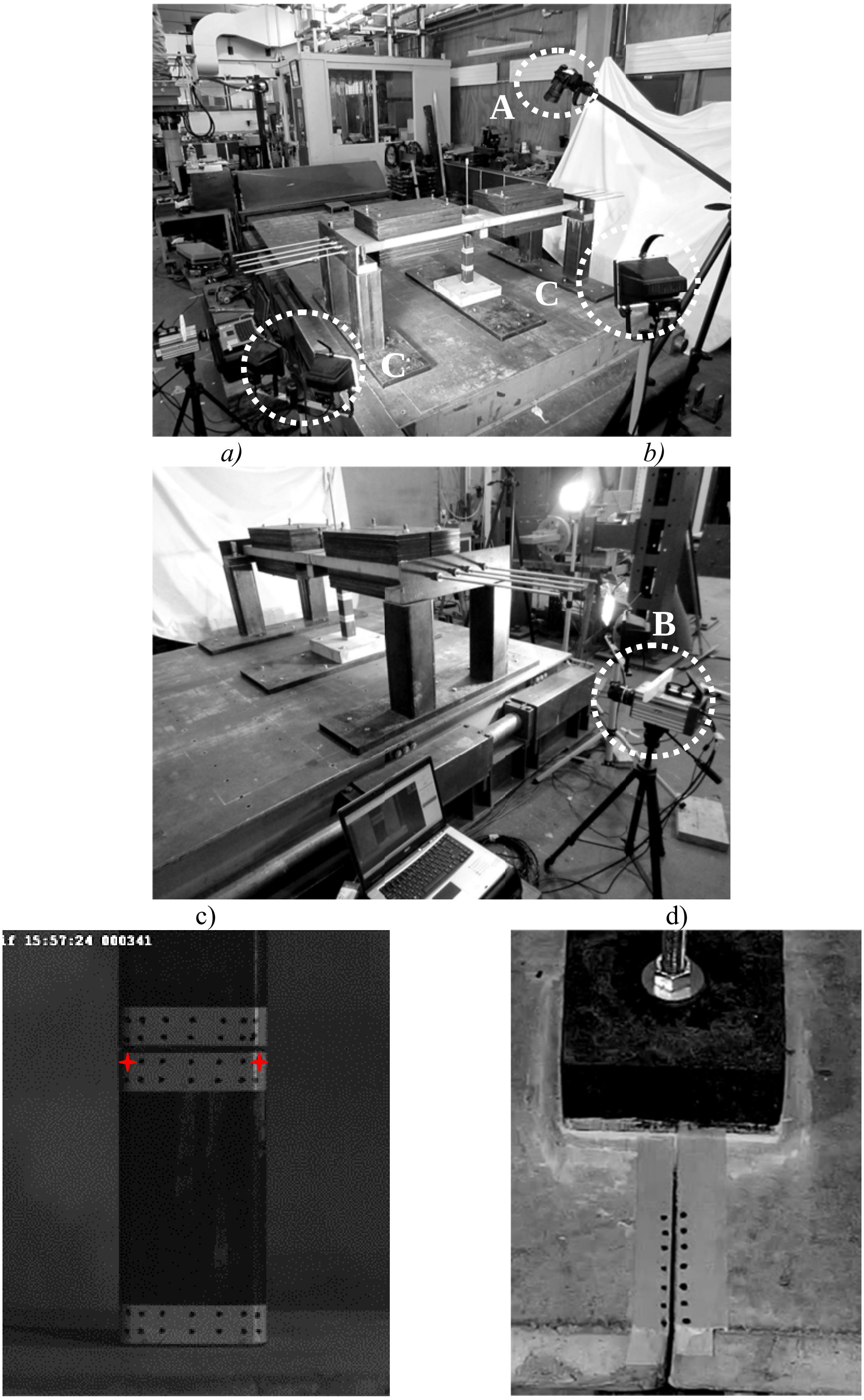

a) *b)*

c) d)

3.19 *Figures - Shake-Table laboratory set-up: a) and b) overview of the model set-up; c) and d)close out of the cameras view*

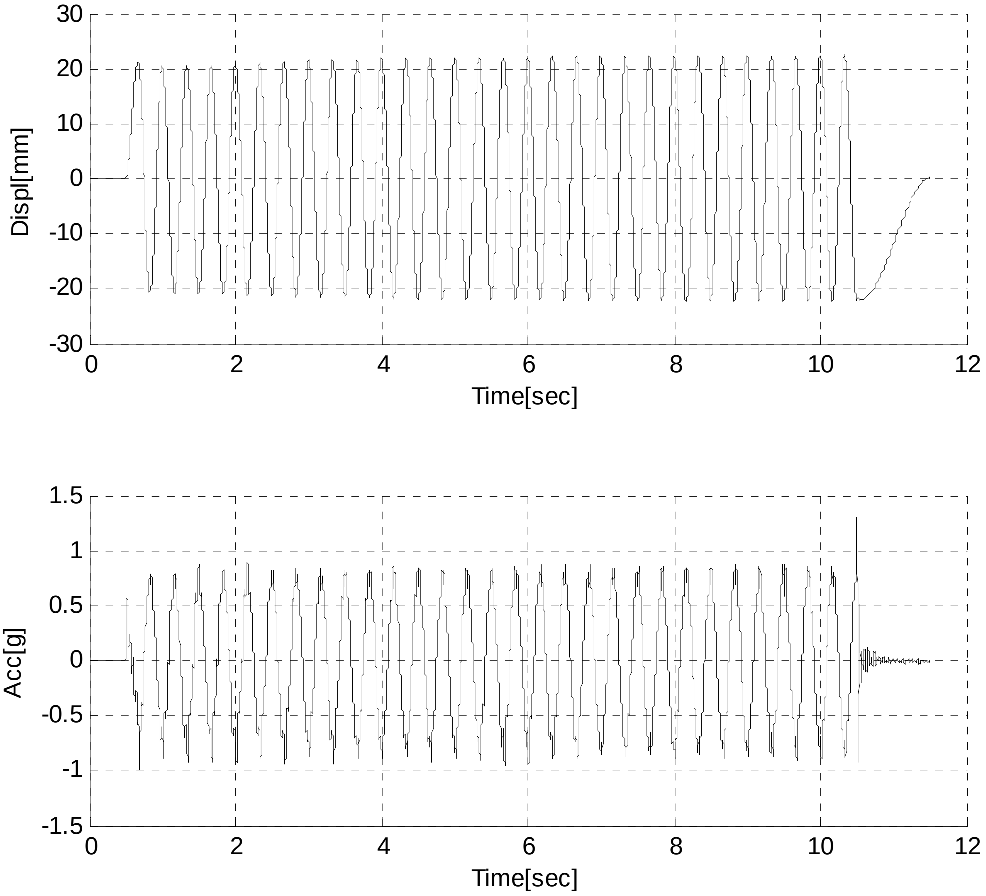

3.20*Figure – Displacement and Acceleration time history, shaky-table output*

3.6 Discussion on the Experimental Results

This paragraph is dedicated to show the results of some of the test done. In detail will be discuss and show the results pertaining to the pier with 40 KN of post-tension level in the three different types of deck connection. The results are focused on the second rocking section. The second rocking section is the interface between the first and the second segment, starting count from the bottom. This choice was done because the highest rocking section (between the last segment and the cap) is covered by the steel plate locate under the deck to try to prevent the torsional moment; the bottom section is the interface widely studied in the monolithic configuration and the section between the second and third pier segment present less gap opening than the others because of the minor presence of bending moment. Moreover even the deck gap opening was detected but for reason of clarity in the results only one test run will be show. The list of the test run published in this paragraph is depict below.

	Deck connection		
	Fully fixed	***Pin connection***	***Free connection***
	Nominal pier post-tensioning level	***Nominal pier post-tensioning level***	***Nominal pier post-tensioning level***
	40 KN	*40 KN*	*40 KN*
Frequency	*3 Hz*	*3 Hz*	*3 Hz*
Acceleration	*0.85g*	*0.85g*	*0.85g*

3.12 Table –List of test-run discussed

The charts below represent the temporal evolution of the x and y displacement. The phase portrait is useful in identifying the system behaviour as it consolidates to remove the distracting effect of the time. Those charts show a range of orbits corresponding to the time-history results, where the traces represent the passage of time. The dots followed in the process results phase are show in the picture 3.19 c market with a red cross shape. The quasi-elliptic traces are given by the simultaneous displacement in x direction given by the shake-table displacement combined with the vertical y displacement due to the gap opening. The charts show as the system behaviour is not symmetric. This non symmetric behaviour is due to both construction imperfections and non-symmetric shake-table displacement. The figure a) represent the time-traces of the left dot while the chart b) show the time-traces of the right dot. The figure c) is proposed to show how the two displacement are complementary. The focus is on the gap opening but it is interesting observe as the segment has a compression phase too, underline by the negative values in y axes. Referring to the chart c) focusing the attention on the far end of the traces it is possible verify as while the left dot is in uplift (blue traces) the right dot (black traces) is in compression phase and vice versa.

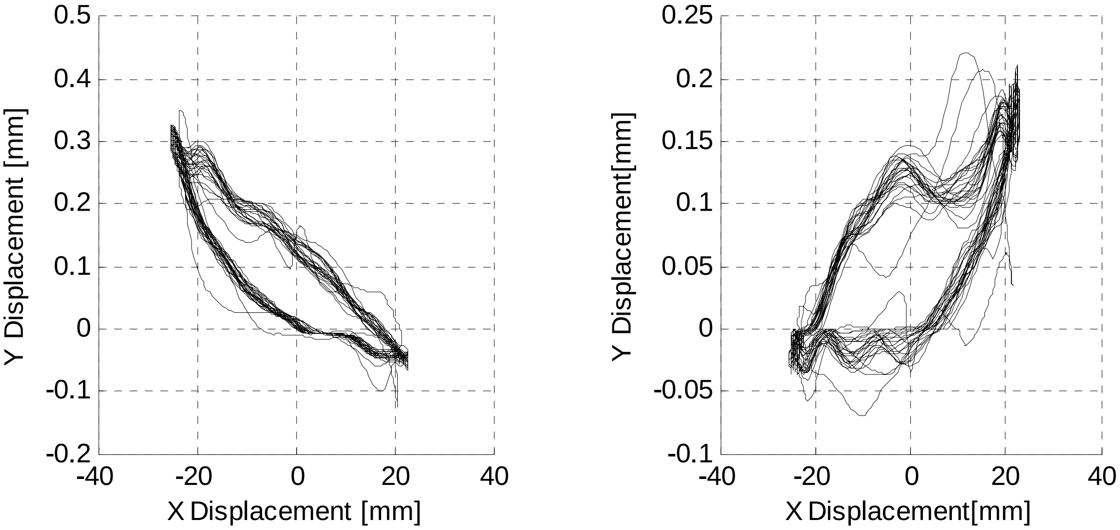

a) b)

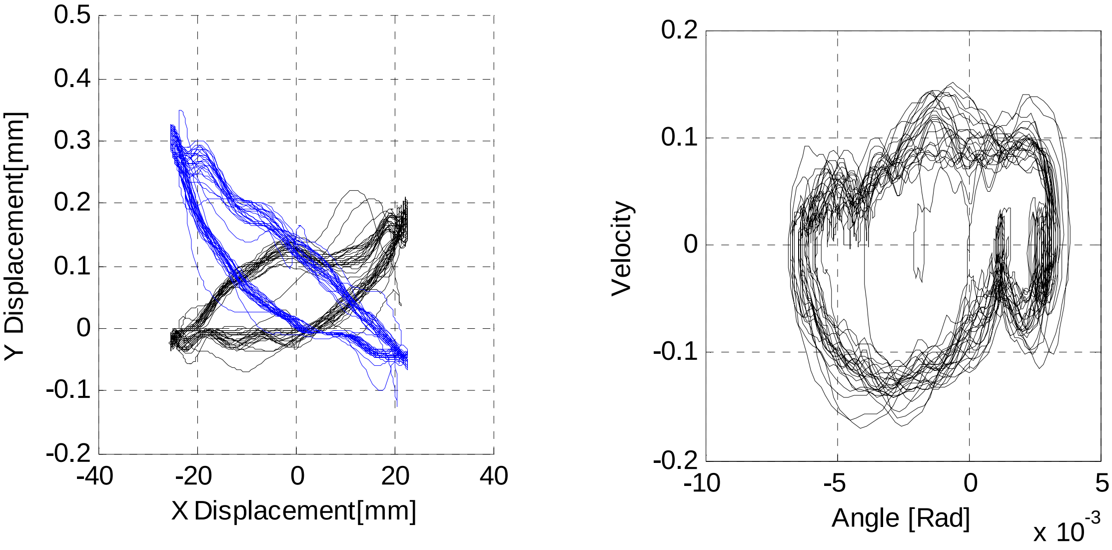

c)

d)

3.21*Figure – Temporal evolution of the x displacement and y displacecement and angular velocity with angular variation in time domain of free deck connection test-run*

The Figure 3.21d is another phase portrait chart indipendent by the time but focused on the angular velocity and the angle due to the rocking phase with the horizontal line. Even in this chart is enphatized as the system behaviour is not symmetric, but it has a preferred rocking dyrection.

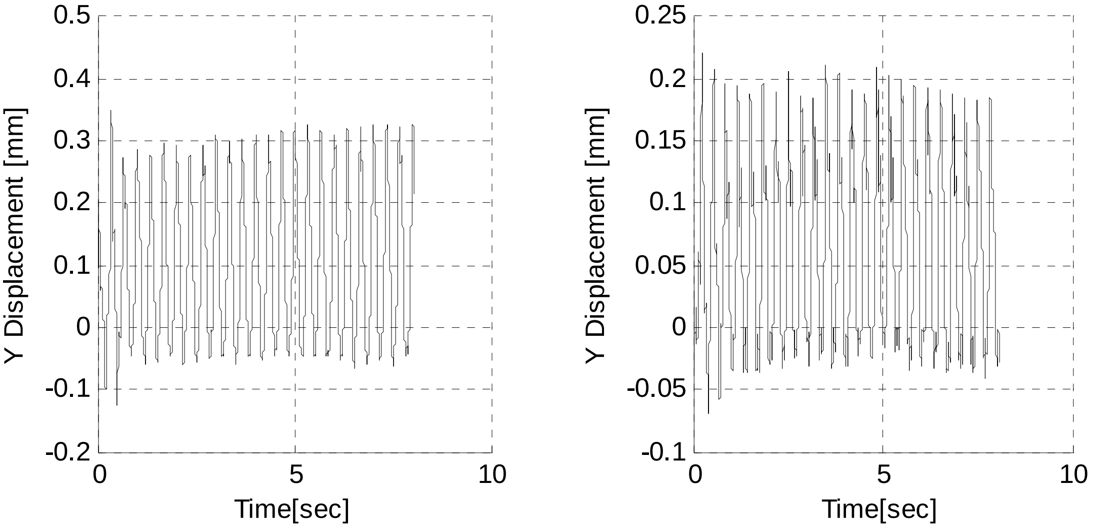

3.22 *Figure – y displacement against time of free deck connection test-run*

In the Figure 3.22 above is showed the displacement of the two dots tracked. In this charts is more clear the displacement range of the two segment. While the left edge has a major uplift compared with the right one, while the compression phase is almost the same for both edge.

The figure below show the variation of the angle in the time domain. This value was achieved connecting the two dots and then it was calculate the angular coefficient referred to the horizontal line. The negative values are obtained when the system rotate on clock-wise direction, vice versa the positive values during a counterclockwise rotations. This chart confirms the preferred rocking direction throw higher values in clockwise rotation.

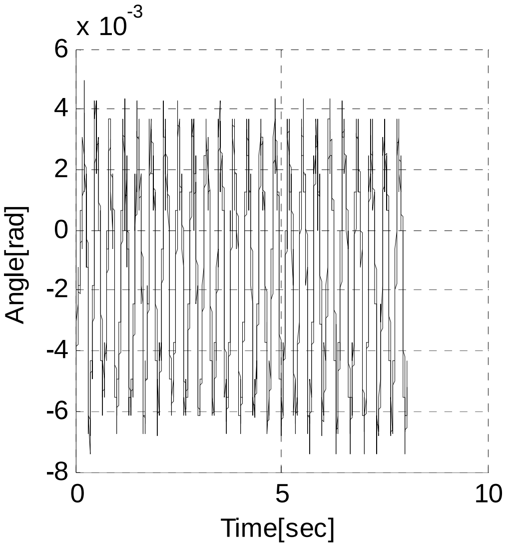

3.23 *Figure – Rocking Angle variation in time domain of free deck connection test-run*

The Figure 3.24 show as the sliding component between the two segments is almost equal to zero. This value is obtained comparing the relative x displacement between the two segment.

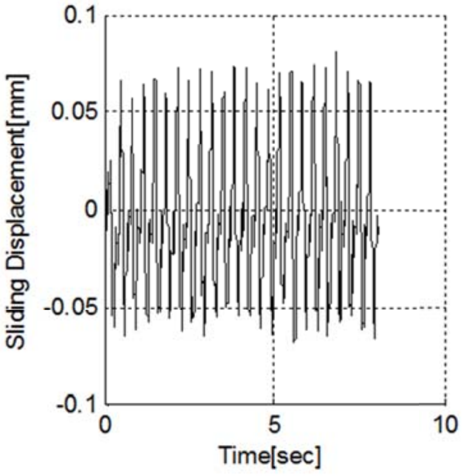

3.24 *Figure – Sliding contribution in time domain of free deck connection test-run*

Instead the chart below represent the gap opening between the two segment. This value was obtained tracking the y displacement in time domain of the dot in the first segment and in the middle segment. The difference in y displacement of the two dots tracked represent the gap opening during the rocking phase.

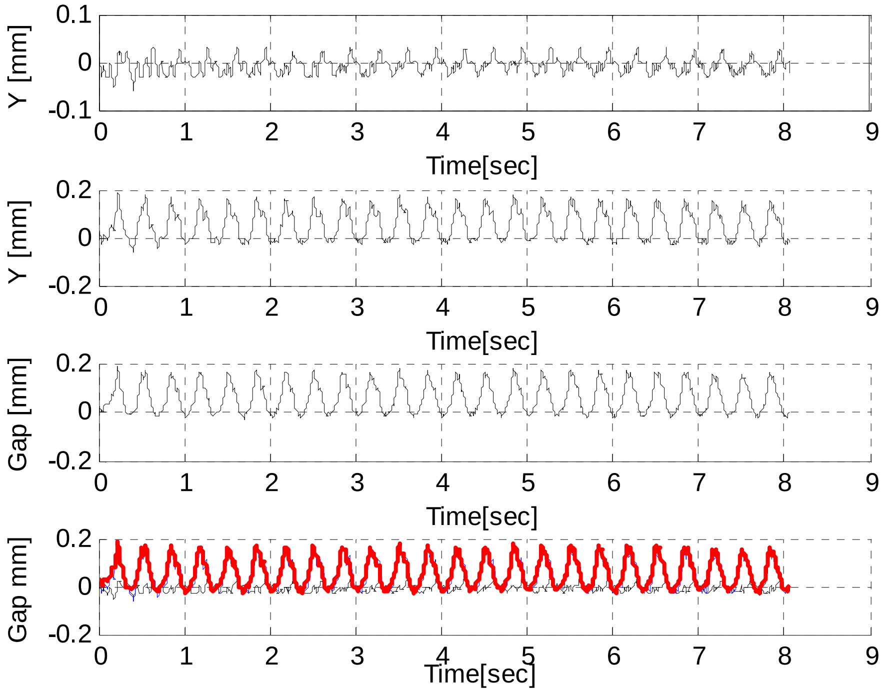

3.25 *Figure – Gap opening between the firs and the second segment of free deck connection test-run*

The figure below is not representing the gap in the rocking pier section but the rocking phase between the two deck segment. The point tracked showed in the Figure 3.27-a. During test-run the deck was allow to rocks. The Figure 3.27-a represent the compression phase instead the Figure 3.27-b the step during the gap-opening phase.

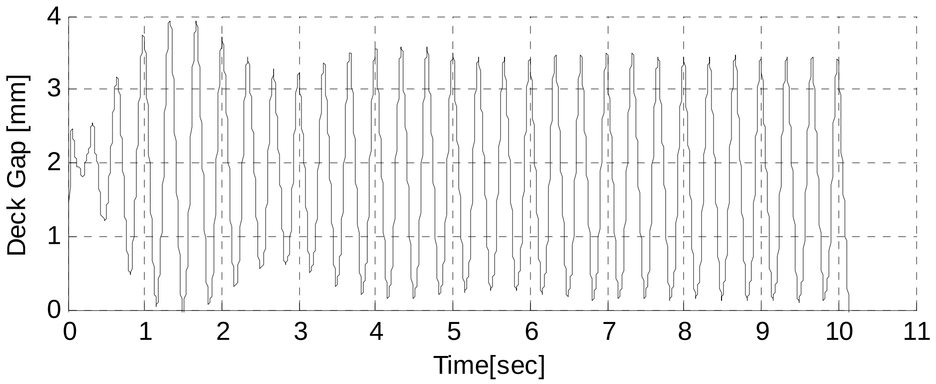

3.26 *Figure – Deck gap opening phase of free deck connection test-run*


a) b)

3.27 *Figure – Two photograms during the deck rocking phase of free deck connection test-run*

The charts below show the results of pin deck connection and fully fixed deck connection test run. Comparing Figure 3.28. with Figure 3.22 is possible observe a reduction of the vertical displacement due to the increase of restrain of the deck and consequently an increase of stiffness of the entire system.

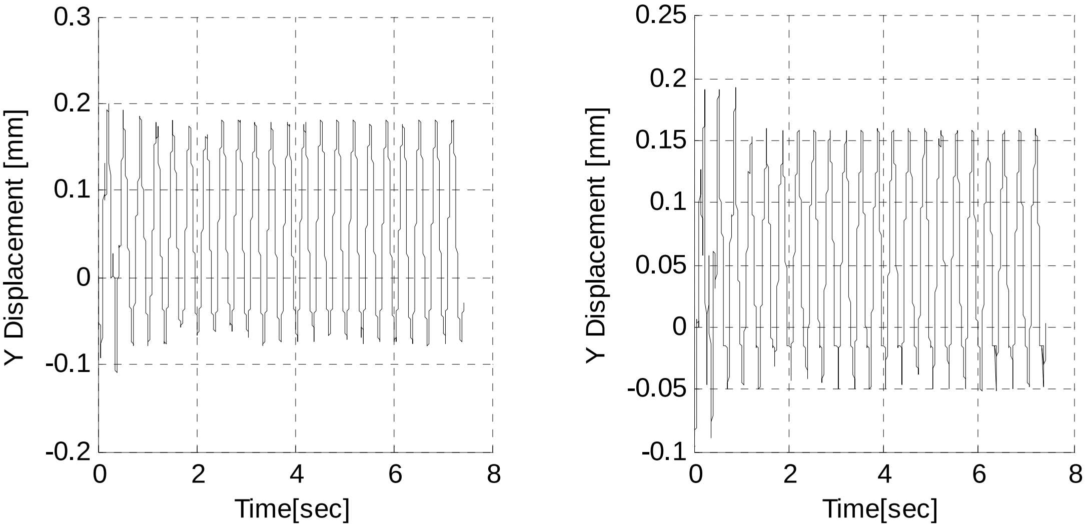

3.28 *Figure – y displacement against time of pin deck connection test-run*

Consequently after change the restrain of the system passing from a pin connection to a fully fixed connection, it is logic thinking in a further reduction of the vertical displacement of the block. Consequently to an increase of stiffness of the system decrease the y displacement and it's mean a decrease of the rocking phase; as show in Figure 3.29.

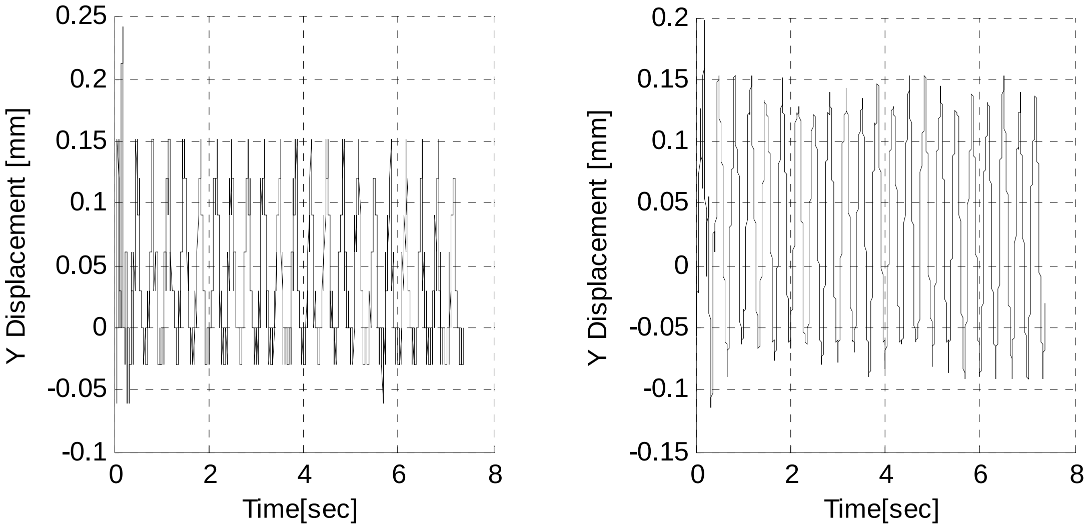

3.29 *Figure– y displacement against time of fully fixed deck connection test-run*

The increase of stiffness can be detected even in the phase diagram of angular and velocity variation. It is possible observe a reduction of t the non-symmetric behaviour of the entire system and the answer of the model to the sinusoidal input became closer to the pure theoretical behaviour.

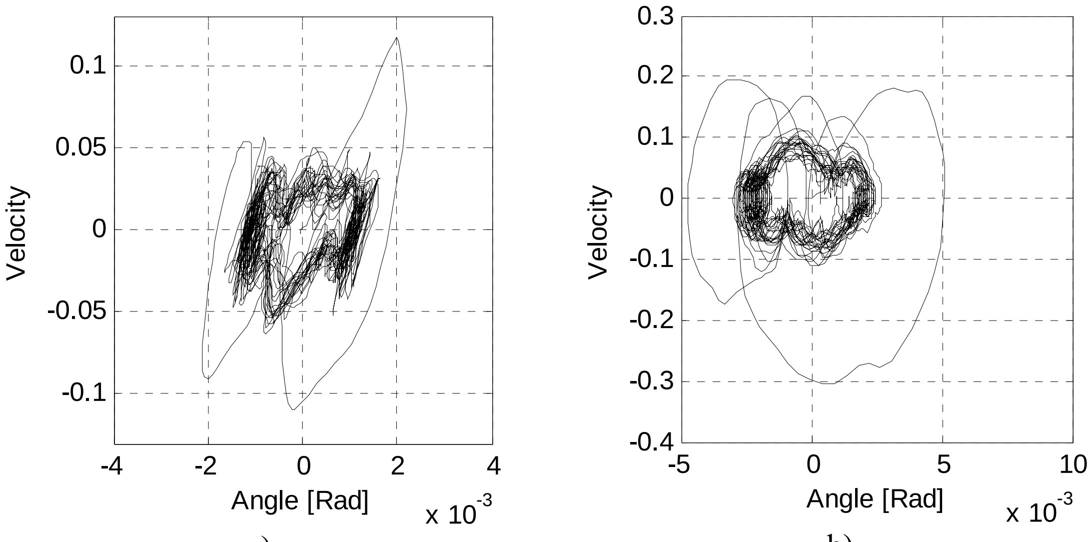

a) b)

3.30 *Figure – Angular variation with angular velocity in time domain of pin deck connection (a) and fully fixed deck connection(b)*

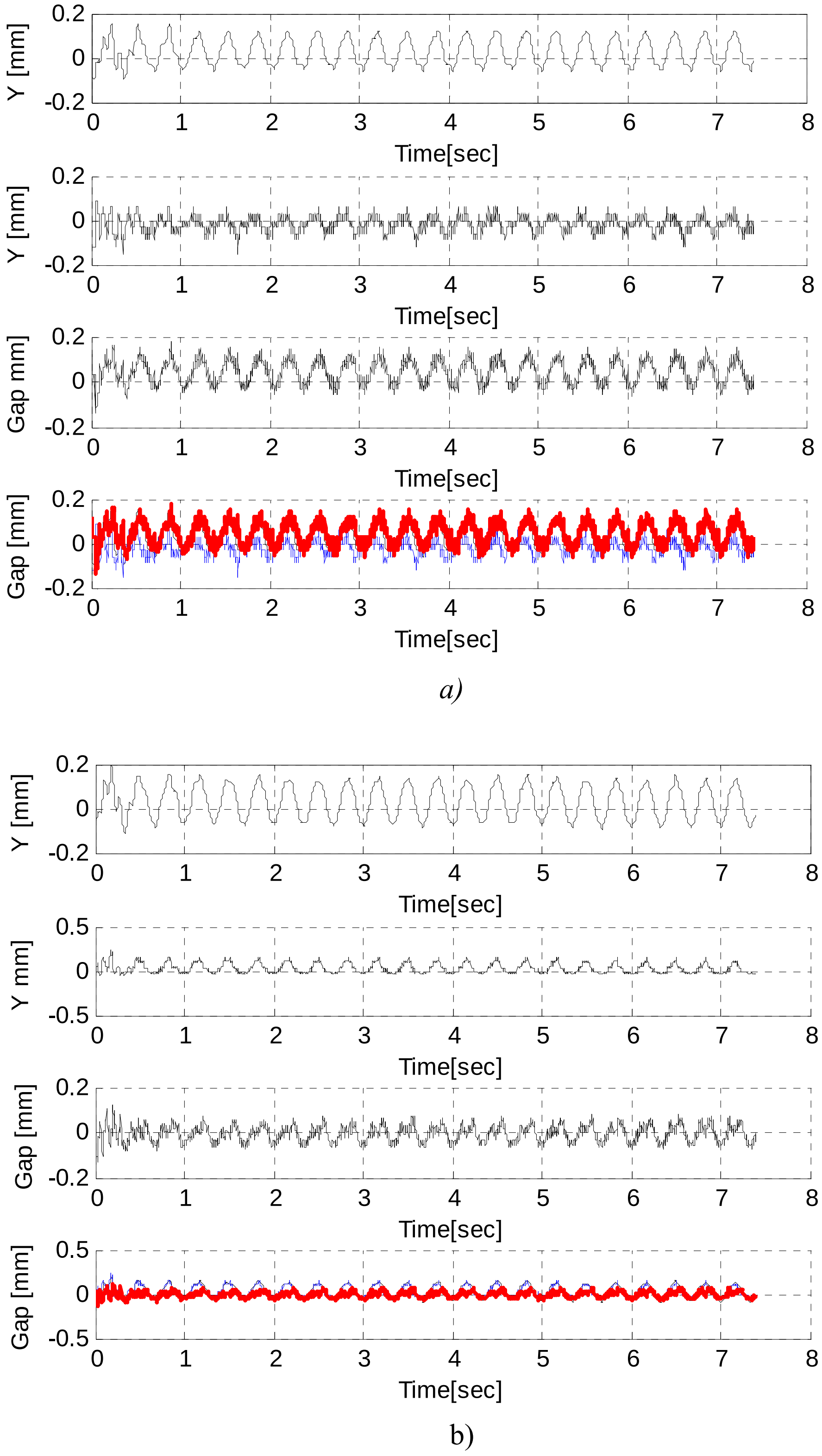

3.31 *Figure – Gap opening between the firs and the second segment of pin deck connection a) and fully fixed deck connection test-run b)*

The charts above represent the value of gap opening recorded during the test. As for the first test were the deck connection was without post-tension even for the pin and fully fix deck connection the focus for the gap opening is on the section between the first and the second segment. As is easy to understand due to an increase of restrains on the deck there is a reduction of the gap opening.

The small scale of the bridge has a consequence of a small value of gap opening. The main problem of this experiment was the design of the solicitation. The entire system was widely influenced by the length of the pier post tension bar. The bar is just 550mm tall and the yielding stress is reached very quickly. Due to this the chose of the input was done with the idea to make visible the gap opening and at the same time have a wide margin against the yielding of the bar.

4

RUAUMOKO MODEL

4.1 Introduction

In this chapter is proposed the numerical model of the specimen with Ruaumoko program. The specimen analysed is the mono pier bridge solution with 40KN pier post-tension level and free connection between deck and abutment.

The numerical model was created to predict the dynamic behaviour of the specimen focused on the gap opening between the segments.

A variety of modelling techniques exists for the post-tensioned rocking systems ranging from simple lumped plasticity models to complex finite element models. In this chapter two different methodology of schematization of the system are explained. The first represent the rocking phase with a lumped plasticity model, the second with a multi-axial spring model. Nevertheless, in this chapter only the lumped plasticity model was developed and analysed.

4.2 Cycling Modelling Techniques for Post-Tensioned Rocking Connections

4.2.1 Lumped Plasticity Models

Lumped plasticity models, comprising rotational springs in parallel, have been extensively developed to model the moment-rotation response of post-tensioned rocking system [87-89]. The physical layout of such a model is illustrate in Figure 4.1 having two rotational springs in parallel of zero length located at the rocking interface. The column/beam/wall element is modelled as an elastic Giberson frame element with appropriate (effective/cracked) section properties. Macro model of this sort require a proper understanding of the physical problem to yield sensible results. To start with, a section analysis (described in the first chapter) must be carried out. In doing so, the various moment-rotation components of the section can be disaggregated in to the mild steel contribution and prestressed (and/or axial load) contribution. An appropriate non-linear hysteresis rule is calibrate to each of the moment components. Generally a bilinear or trilinear non-linear elastic hysteresis rule is used to model the tendon/bar or axial moment response. For the mild steel, the type of non-linear inelastic hysteresis model depends on the type of dissipation adopted. The non-linear rule showed, for example, in the Figure 4.1 is the Ramber-Osgood steel rule [90]. It is representative of a system with external dissipaters. Another example could be use for internally grouted reinforcement a Modify Takeda [91].

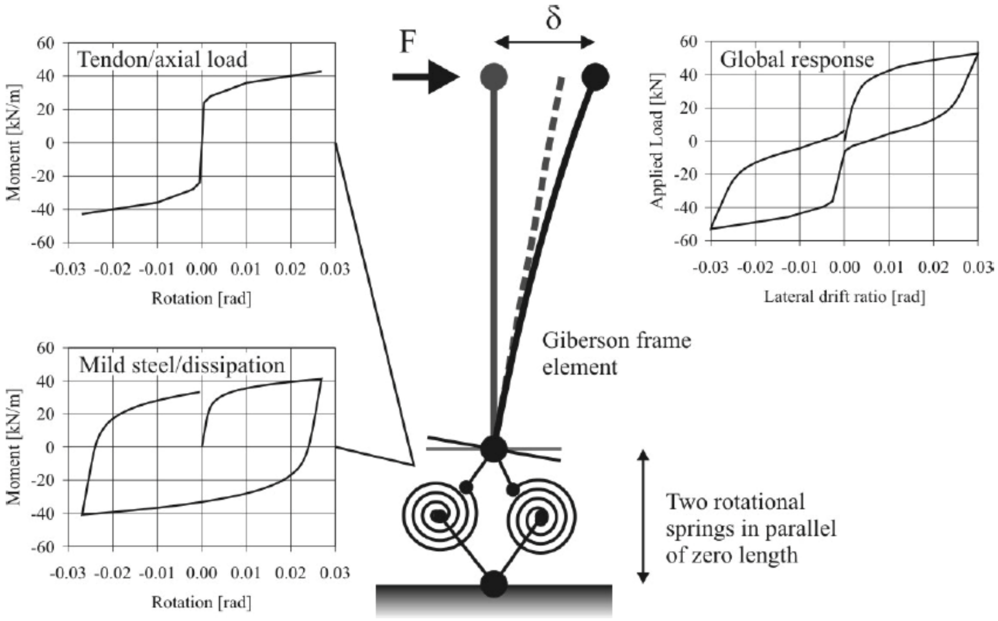

4.1 *Figure – Lumped plasticity model consisting of two rotational spring in parallel [92]*

4.2.2 Multi-Axial Spring Models

Detailed macro-models utilising multiple axial springs located along the rocking interface of a post-tensioned connection have been widely investigate by Kim [93], Spieth [94] and Palermo [95]. Kim implemented a multi-spring element that was available in the computer program DRAIN-2DX. This element had nine uniformly distributed spring elements of equal stiffness and strength located along the rocking interface. The axial springs can be modelled as compression only to simulate the contact behaviour and they are developed as elastic-perfectly plastic element having a yield displacement corresponding to a designed strain. The elongation of the mild steel, tendons/bars and beam elongation is inherently captured within such a model.

Spieth et. Al carried out a finite element analysis to determine the required length of the cantilever element that can be used to define the axial stiffness of the multi-spring element. The analysis studied the strain distribution within the element to determine the depth of the distributed strain region. A value of one quarter of the element depth was found to give a reliable results with the response being relatively insensitive to an increase in length of 200%. The multi-spring element was added in the finite element Ruaumoko program [96]; Figure 4.2. This element has the option of 2-10 individual springs in addition to various weighting options for spring stiffness and spring distribution within the element. This multi-spring model was also used to model post-tensioned concrete wall and beam column joint, providing further validation of the model, by Palermo in 2005.

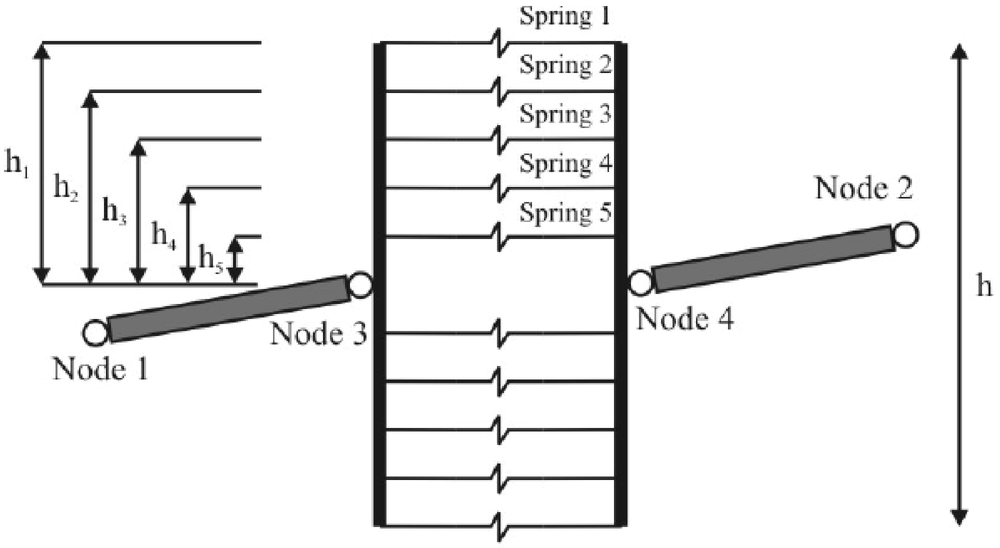

4.2 *Figure – Multi-spring element within Ruaumoko, [96]*

4.3 Numerical Model

The numerical model to predict the physical model behaviour is show in the Figure 4.3. The model was calibrated using the Lumped Plasticity Model. However to define the system a variation of the model described above was used. The change from the standard model consist in to using only one rotational spring instead of two. This is a consequence of the physical geometry of the specimen. The real specimen does not have any devices with the aim to dissipate energy, so only the rotational spring to represent the post-tensioned bar was used.

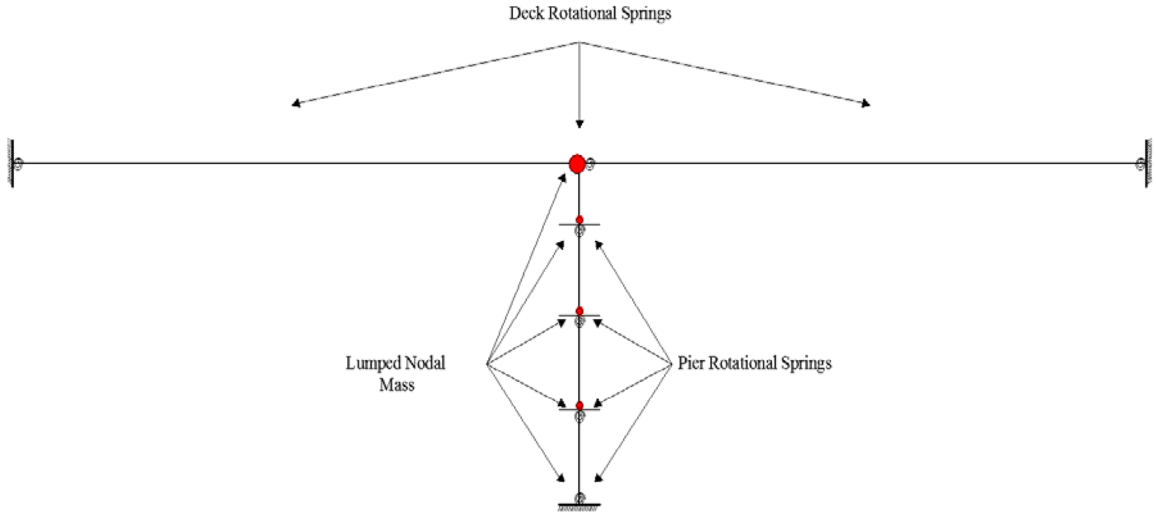

4.3 *Figure – Numerical Model schematization*

The simplified system is composed two different element type: the Giberson beam frame to describe the characteristic of the pier and deck and the rotational spring to describe the rocking system.

A beam member (Figure 4.4-a) is a general three dimensional member which may use almost any of the hysteresis rules governing the behaviour of the plastic hinges implemented in Ruaumoko program. In this specific case a linear hysteresis rule was adopted. A beam member may also have a bi-linear axial load axial-displacement hysteresis. However, there is no interaction between the axial yield and those associated with the moment curvature yield states. Rigid end-blocks may be incorporated within the length of any of the frame members (Figure 4.4-b). If there are joint flexibilities or shear deformation, the member stiffness is inverted to get the member flexibility, the joint and shear-flexibilities are added and the resulting matrix is again inverted to get the final stiffness of the beam member.

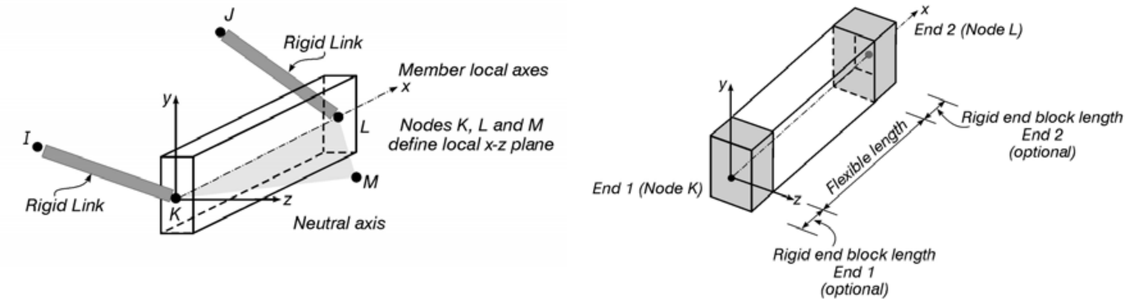

a) b)

4.4 *Figure – Beam member a), rigid end-members b)*

Spring members (Figure 4.5) may be used to model special effects in the structure like post tensioned tendon force or to describe the rocking phase. The spring member orientation is given by the axial orientation of the member but if the two end nodes coincide resulting in a zero length member then the longitudinal and transverse directions coincide with the structure, or global X,Y and Z axes respectively. The rotational spring moments are only proportional to the differences in the rotations at each end of the member. If the end nodes are coincident then the transverse rotational components behave like the torsional clock spring. This member may be thought of as a generalised Truss member which may follow any of the hysteresis rules. There is no interaction between the yield behaviour of the longitudinal, transverse and rotational actions. In this specific case to describe the behaviour of the rocking phase and thus calibrate the springs, a tri-linear hysteresis rule was adopted

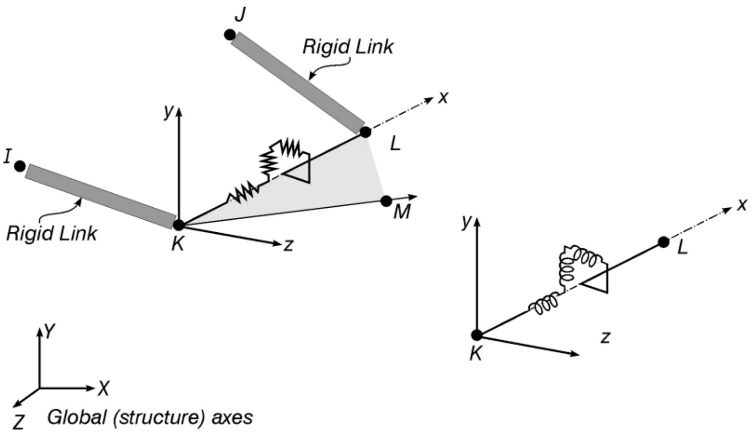

4.5 *Figure – Spring member*

4.3.1 Results

The Figure 4.6 below represent the horizontal displacement of each node placed on the top of each segment due to the rocking phase. A part the first segment which has the relative displacement compared to the foundation, the values of the subsequent nodes are composed by the relative displacement plus the displacement of the previous nodes.

By the using of the Lumped Plasticity Model with Rotational spring the gap opening and thus the vertical displacement is unreadable.

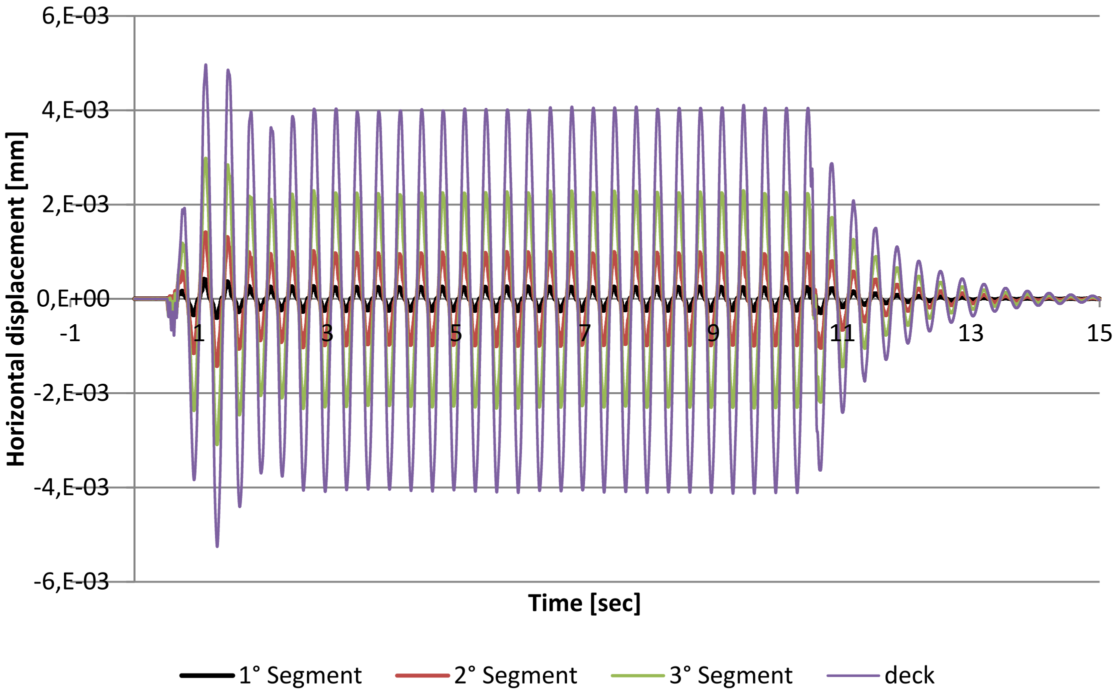

4.6 *Figure – Horizontal displacement on the top of each segment*

The following figure show the stress-strain chart and as it is possible to check the pier element remain always in to the elastic range. The real peer was composed by three concrete block covered by an Square Hollow section (SHS). In to Ruaumoko model this section was approximate to the real one using a normal concrete section, but the mechanical characteristic was incremented by the augment of the elastic modulus and by the setting of an higher values of concrete for yielding and cracking. The results reflect the elastic behaviour of the pier element found during the physical test on the shake-table.

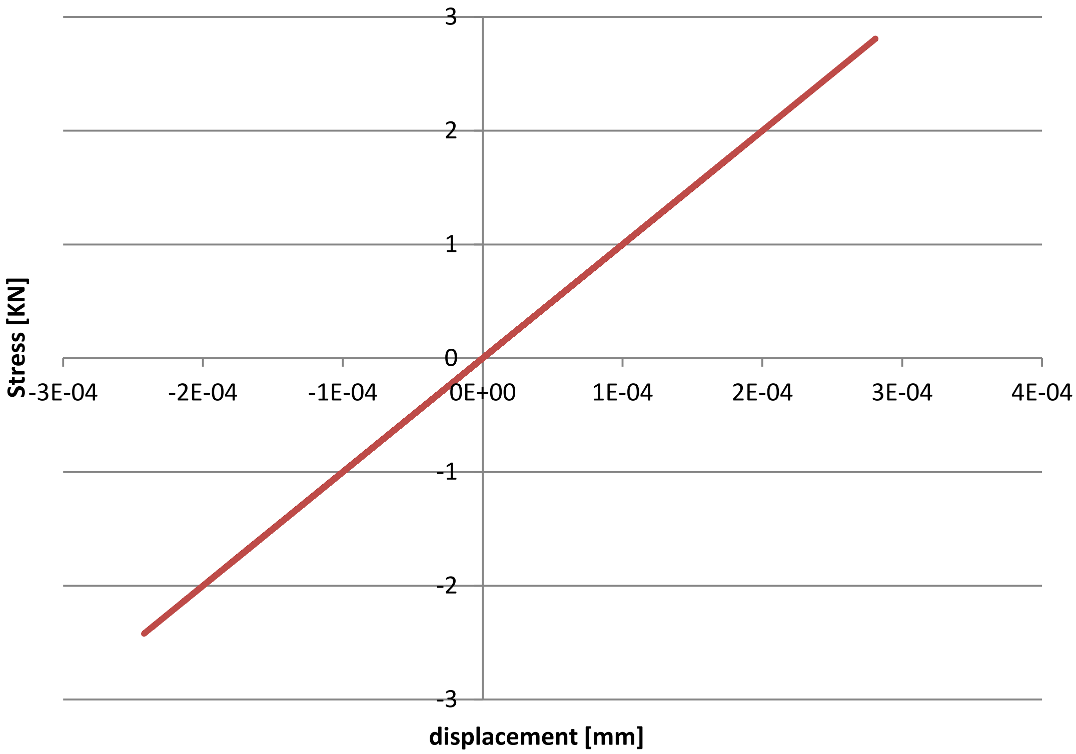

4.7 *Figure – Stress-Displacement curves of the first and second displacement*

The figure 4.8 below show the moment curvature charts of the multi-spring between the first and the second pier segment.

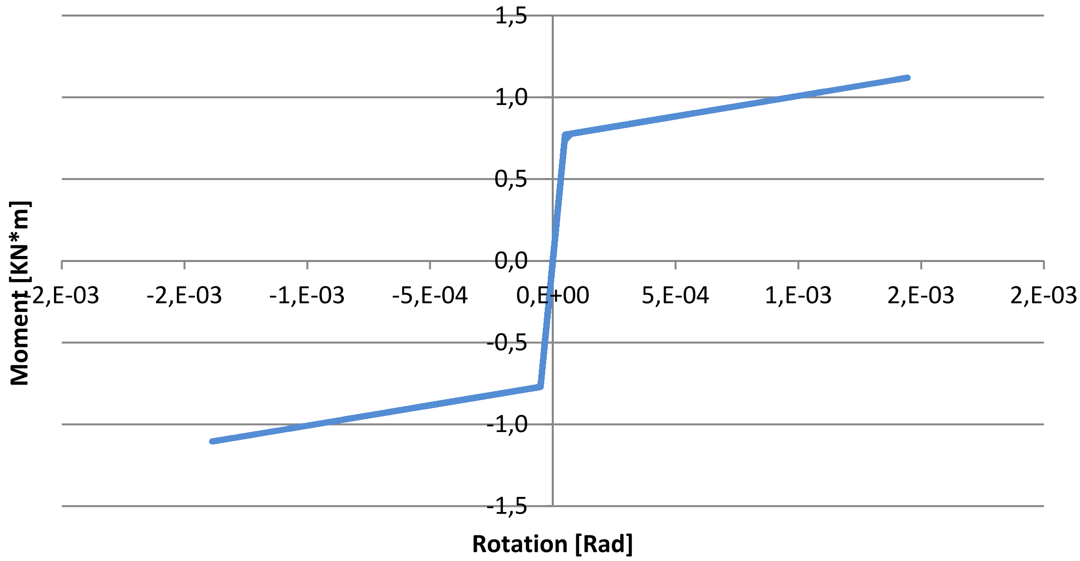

4.8 *Figure – Moment Rotation curve of the rotational spring*

In this chart as in the chart showed before it is possible note as due to the non-symmetry of the input the model response is non-symmetry as during the shake-table test run. In Figure 4.9 is show a comparison between the Ruaumoko model results with the mathematical results. The blue line describes the behaviour during the rocking phase of the numerical model, instead the red dots the behaviour of the mathematical prediction. At the moment value 0.4 KN*m there is reached the decompression moment and following this value the rocking phase starts.

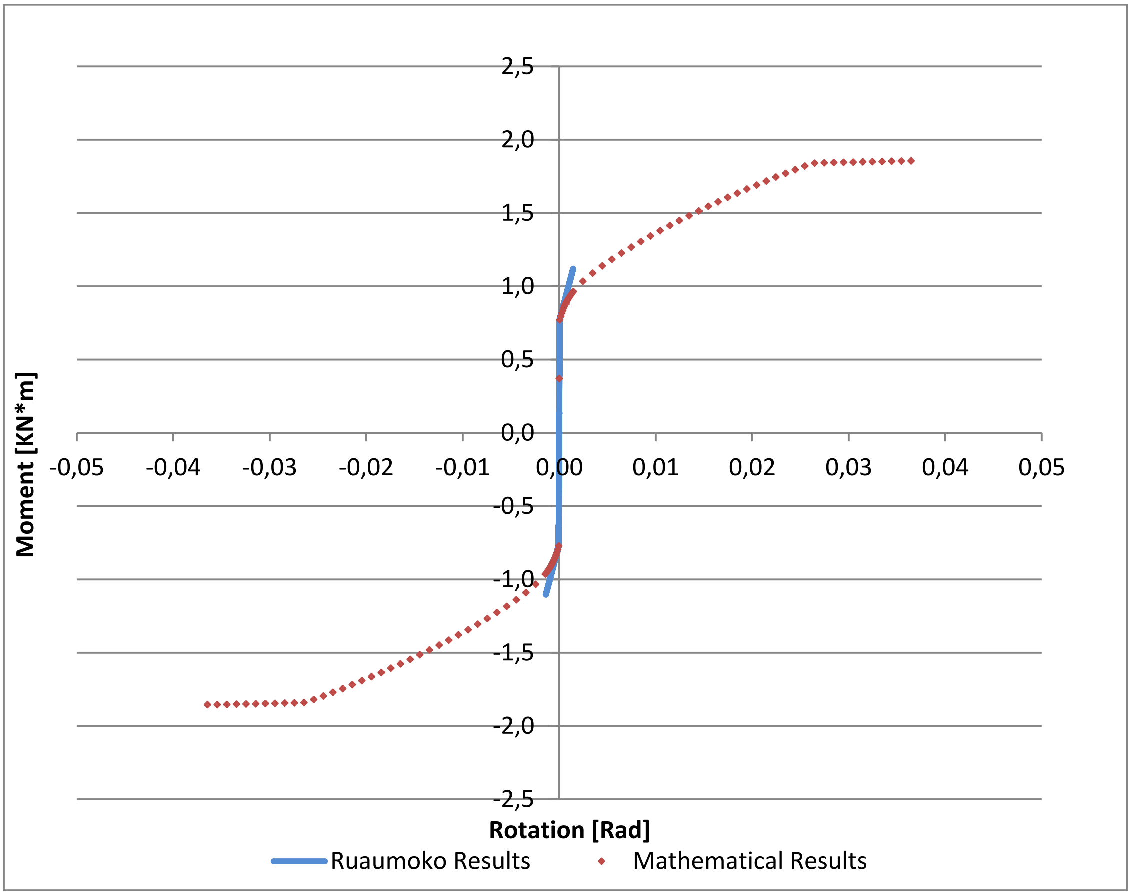

4.9 *Figure – Comparison between the Numerical and the Mathematical results*

Despite was difficult compare the results of the numerical with the physical model due to the nature of the shake-table test run, it is possible say that the Ruaumoko model approximate enough the real and the mathematical model.

Conclusion

In this research were analyzed different types of specimen. In the first part the focus was on the bridge pier configuration with different types of pier segments geometry and with variation of the friction coefficient . From the analysis both in free oscillation decay and quasi sinusoidal input the results obtained was that the pier composed by three rectangular parallelepiped has an high rocking phase, while the three cube segment pier has an high sliding phase. The using of one cube segment with two rectangular parallelepiped underline as the main rocking section is not anymore the between the bottom block but the intersection between the second last and last segment. Introducing the rubber pad the dynamic behavior of the specimens in radically changed. The sliding phase was prevented even in the 3Cu bridge configuration. However the prevention of sliding was not the only consequence because of the introducing of the rubber pad an unpredicted behavior was recorded.

During the second experiment the behavior of the scaled bridge has followed the predictions done. The main gap was recorded on the bottom interface between the last segment with the foundation surface. Moreover a second relevant gap opening was recorded between the bottom segment with the middle block. Due to the small scale even the gaps opening recorded were really small in order of 0.2-0.4 mm. As a consequence of small scale was the amplification of some effect like the torsion of the deck, which in a full scale are not the main consequence during a dynamic sollecitation.

The using of the High-Speed Camera to understand the dynamic behavior is a good compromise between velocity of data acquisition and data processing with the precision of the results. Nevertheless the High-Speed Camera were not designed for long term registration and because of this the time range in which is possible obtain satisfactory results is limited around the 8 second. An further compromise was taken between the precision and the time range for the data acquisition. Due to this in the analysis was always present a sort of background noise and in some test-run it make impossible the analyzing of the data acquired. In conclusion the High-Speed Camera for this types of works is not the best way to collect data; despite is more than enough for a preliminary analysis.

References

1. R. Park and T. Paulay, *Reinforced concrete structures.* 1975.
2. Quincy T. Ma and J.W. Butterworth, *Simplified expressions for modelling rigid rocking structures on two spring foundation.* Bulletin of New Zealand society for earhquake engineering, 2010.
3. I. N. Psycharis, D. Y. Papastamatiou, and A.P. Alexandris, *Parametric investigation of the stability of classical columns under harmonic and earthquake excitations.* Earthquake Engineering structural Dynamics, 2000.
4. Pampanin, S., *Controversial aspects in seismic assessment and retrofit of structures in modern times: understanding and implementing lessons from ancient heritage.* Bulletin of New Zealand society for earhquake engineering, 2006.
5. Ma, Q.T.M., *The mechanism of rocking structures subjected to ground motion* 2010.
6. Housner, G.W., *The behavior of inverted pendulum structures during earthquakes.* Bulletin of the seismological society of America,1963.
7. I. N. Psycharis, *Dynamic behavior of rocking structures allowed to uplift. California Institute of Technology,* 1981, California Institute of Technology: Pasadena, California.
8. Psycharis, I.N., *Effect of Base Uplift on Dynamic Response of SDOF Structures.* Journal of structural engineering (New York, N.Y.), 1991. 117(3): p. 733-754.
9. P. Pozzati, *Teoria e tecnica delle strutture.* Vol. second. 1977, Torino: Unione Tipografico-Editore Torinese.
10. E. Winkler, *Die Lehre von der elastizitat und festigkeit,* 1867: Praha.
11. Xu, C. and C.C. Spyrakos, *Seismic analysis of towers including foundation uplift.* Engineering Structures, 1996. 18(4): p. 271-278.
12. Song, Y.-H. and D.-G. Lee, *An improved two-spring model for foundation uplift analysis.* Computers & Structures, 1993. 46(5): p. 791-805.
13. I. N. Psycharis, *Investigation of the dynamic response of rigid footings on tensionless Winkler foundation.* Soil Dynamics and Earthquake Engineering, 2008. 28(7): p. 577-591.
14. Celep, Z. and K. Güler, *Dynamic response of a column with foundation uplift.* Journal of Sound and Vibration, 1991. 149(2): p. 285-296.
15. Allotey, N. and M. Hesham El Naggar, *Analytical moment–rotation curves for rigid foundations based on a Winkler model.* Soil Dynamics and Earthquake Engineering, 2003. 23(5): p. 367-381.
16. Prieto, F., P.B. Lourenço, and C.S. Oliveira, *Impulsive Dirac-delta forces in the rocking motion.* Earthquake Engineering & Structural Dynamics, 2004. 33(7): p. 839-857.
17. P. Dirac, *Principles of quantum mechanics.* 4th. ed1958, Oxford: Claredon Press.
18. Apostolou, M., G. Gazetas, and E. Garini, *Seismic response of slender rigid structures with foundation uplifting.* Soil Dynamics and Earthquake Engineering, 2007. 27(7): p. 642-654.

19. G. Gazetas, M.Apostolou, and J. Anastasopoulos, *Seismic uplifting of foundation on soft soil, with exaple from Adapazari.* 2003.
20. Acikgoz, S. and M.J. DeJong, *The interaction of elasticity and rocking in flexible structures allowed to uplift.* Earthquake Engineering & Structural Dynamics, 2012: p. 1-18.
21. Chopra, A.K., *Dynamic of structures, Theory and application to Earthquake Engineering*1995, University of california Berkeley: Prentice Hall.
22. Oliveto, G., I. Caliò, and A. Greco, *Large displacement behaviour of a structural model with foundation uplift under impulsive and earthquake excitations.* Earthquake Engineering & Structural Dynamics, 2003. 32(3): p. 369-393.
23. Spyrakos, C. and G. Nikolettos, *Overturning Stability Criteria for Flexible Structures to Earthquakes.* Journal of Engineering Mechanics, 2005. 131(4): p. 349-358.
24. Makris, N., *The rocking spectrum and the shortcomings of design Guidlines*, 2001, Pacific Earthquake Engineering Research Center.
25. Makris, N. and D. Konstantinidis, *The rocking spectrum and the limitations of practical design methodologies.* Earthquake Engineering & Structural Dynamics, 2003. 32(2): p. 265-289.
26. Restrepo, J.I., *New generation of earthquake resisting systems*, in *FIB congres*2002.
27. M. Aslam, W. G. Godden, and D.T. Scalise, *Earthquake rocking response of rigid bodies.* Journal of Structural Division, ASCE, 1980. 106: p. 377-392.
28. Marriott, D., *The Development of High-Performance Post-Tensioned Rocking Systems for the Seismic Design of Structures*, in *Civil Engineering*2009, University of Canterbury.
29. N. Makris and j. Zhang, *Rocking Response and Overturning of Anchored Equipment under Seismic Excitations*, in *Peer report*1999: University of California, Berkeley.
30. Pampanin, S., M.J. Nigel Priestley, and S. Sritharan, *Analitycal modelling of the seismic behaviour of precast concrete frames designed with ductile connections.* Journal of Earthquake Engineering, 2001. 5(3): p. 329-367.
31. Pampanin, S., et al., *PRESS Design Handbook* First ed2010, New Zealand: NZ Concrete Society Inc.
32. Palermo, A., *The Use of Controlled Rocking In the Seismic Design of Bridges*, in *Dottorato di Ricerca in Ingegneria Sismica*2004, Tecnical university of Milan: Milan, Italy.
33. Palermo, A., S. Pampanin, and G. Calvi, *Concept and development of hybrid solutions for seismic resistant bridge systems.* Journal of earthquake engineering : JEE, 2005. 9(6): p. 899.
34. Priestly, M.j.N., *Overview of the PRESSS research programme.* PCI journal, 1991. 36.
35. Englerkirk, R.E., *Design-construction of The Paramount: a 39-story precast prestressed concrete apartment building.* PCI journal, 2002. 47(4).
36. A. Palermo and M. Mashal, *Accellerated bridge construction (ABC) and seismic damage resistant technology: A New Zealand challange.* 2012.
37. Pampanin, S., *Emerging solution for high seismic performance of precast/prestressed concrete building;*2005.

38. ASSHTO, *Strategic Highway Safety Plan.* 2005.
39. AASHTO Highway Subcommittee on Bridges and Structures, *Grand Challenges: A Strategic Plan for Bridge Engineering*, 2005: Washington, D.C., USA.
40. AASHTO Technology Implementation Group (TIG), *Prefabricated Bridges 2004*, Federal Highway Administration, Editor 2004.
41. AASHTO Technology Implementation Group (TIG), *Prefabricated Bridges: Get in, get out, stay out.*, in *American Association of State Highway and Transportation Officials*,2002: Chicago, USA.
42. Freyermuth, C.L., *Ten years of segmental achievements and projections for the next century.* American Industrial Hygiene Association journal, 1999. 44: p. 36.
43. Billington, S.L., R.W. Barnes, and J.E. Breen, *Alternate substructure systems for standard highway bridges.* Journal of Bridge Engineering, 2001. 6(Compendex): p. 87-94.
44. J. T. Hewes and M.J.N. Priestley*, Seismic design and performance of precast concrete segmental bridge columns.* 2001.
45. Kwan, W. and S. Billington, *Unbonded Posttensioned Concrete Bridge Piers. I: Monotonic and Cyclic Analyses.* . J. Bridge Eng, 2003. 8(2): p. 92-101.
46. Yu-Chen Ou, et al., *Cyclic Performance of Precast Concrete Segmental Bridge Columns: Simplified Analytical and Finite Element Studies* Transportation Research Record: Journal of the Transportation Research Board, 2007. Volume 1976 / 2006: p. 66-74.
47. Palermo, A. and S. Pampanin, *Enhanced seismic performance of hybrid bridge systems: Comparison with traditional monolithic solutions.* Journal of Earthquake Engineering, 2008. 12(Compendex): p. 1267-1295.
48. Marriott, A.P.S.P.a.D., <*Design, Modeling, and Experimental Response of Seismic Resistant Bridge Piers with Posttensioned Dissipating Connections.* 2007.
49. Wang, J.-C., et al., *Large-scale seismic tests of tall concrete bridge columns with precast segmental construction.* Earthquake Engineering & Structural Dynamics, 2008. 37(12): p. 1449-1465.
50. Sideris, P., et al., *Seismic performance of precast segmental bridges.* 9th US National and 10th Canedian Conference on Earthquake Engineering, 2010.
51. Mohamed ElGawady, M.A.A.J.B.a.H.M.D., S.M.ASCE, <*Seismic Behavior of Posttensioned Concrete-Filled Fiber Tubes*, 2010.
52. Mohamed A. ElGawady, H.M.D., <*Analysis of segmental piers consisted of concrete filled FRP tubes.* 2012.
53. Chen, C.-C.C.a.Y.-C., *Cyclic tests of post-tensioned precast CFT segmental bridge columns with unbonded strands.* 2006.

54. Demosthenous, G.C.M.M., *Models of ancient columns and colonnades subjected to horizontal base motions – Study of their dynamic and earthquake behavior*, in *11th European Conference Earthquake Engineering*1998: Rotterdam.
55. Demosthenous, G.C.M.M., *Study of the dynamic responce of models of ancient columns or colonnades subjected to horizontal base motions*, in *12th World Conference Earthquake Engineering*2000: Aukland, New Zealand.

56. G. C Manos, et al., *Study of thr dynamic and earthquake behavior of ancient columns and colonnades with and without the inclusion of wires with energy dissipation characteristics* in *12th World Conference Earthquake Engineering*2000: Auckland, New Zealand.
57. Pampanin, S., *Controversial aspects in seismic assessment and retrofit of structures in modern times: understanding and implementing lessons from ancient heritage.* Bulletin of New Zealand society for earhquake engineering, 2006.
58. Nelson_Pine, *NZ Laminated Veneer Lumber (LVL) 11, mechanical property*, 2011.
59. Zhou, X., et al., *A novel capacitive accelerometer with a highly symmetrical double-sided beam-mass structure.* Sensors and Actuators A: Physical, 2012.
60. Zhou, X., et al., *Low cross-axis sensitivity micro-gravity microelectromechanical system sandwich capacitance accelerometer.* Micro & Nano Letters, 2011. **6**(7): p. 510.
61. Morikawa, S.R.K., et al. *Triaxial Bragg grating accelerometer*. in *Optical Fiber Sensors Conference Technical Digest, 2002. Ofs 2002, 15th*. 2002.
62. Casio, *EX-F1 Users's Guide*, 2008.
63. Green, B. *Sensor artifacts and CMOS rolling shutter*. 2012.
64. Litwiller, D., *CMOS vs. CCD: Maturing technologies, maturing markets.* 2005.
65. Sutton, M.A., et al., *Determination of displacements using an improved digital correlation method.* Image and Vision Computing, 1983. **1**(3): p. 133-139.
66. Bruck, H.A., *Digital image correlation using Newton-Raphson method of partial differential correction.* Experimental mechanics, 1989. **29**(3): p. 261-267.
67. Luo, P.F., *Accurate measurement of three-dimensional deformations in deformable and rigid bodies using computer vision.* Experimental mechanics, 1993. **33**(2): p. 123-132.
68. Tao, G. and Z. Xia, *A non-contact real-time strain measurement and control system for multiaxial cyclic/fatigue tests of polymer materials by digital image correlation method.* Polymer Testing, 2005. **24**(7): p. 844-855.
69. Poncelet, M., et al., *Biaxial High Cycle Fatigue of a type 304L stainless steel: Cyclic strains and crack initiation detection by digital image correlation.* European Journal of Mechanics - A/Solids, 2010. **29**(5): p. 810-825.
70. Tiwari, V., et al., *Application of 3D image correlation for full-field transient plate deformation measurements during blast loading.* International Journal of Impact Engineering, 2009. **36**(6): p. 862-874.
71. Leclerc, H., et al., *Integrated Digital Image Correlation for the Identification of Mechanical PropertiesComputer Vision/Computer Graphics CollaborationTechniques*, A. Gagalowicz and W. Philips, Editors. 2009, Springer Berlin / Heidelberg. p. 161-171.
72. Eberl, C., et al., *Digital Image Correlation and Tracking with MatLab.* 2010.
73. Ma, Q.T.M., *The mechanism of rocking structures subjected to ground motion* 2010.
74. Chang, S.Y., *Numerical characteristics of constant average acceleration method in solution of nonlinear systems.* Journal of the Chinese Institute of Engineers, 2009. **32**(4): p. 519-529.

75. NZ_Transport_Agency, *Standard precast concrete bridge beams, research report 364.* 2008.
76. Transit_NZ, *NZS 1170.5,Structural desigh Actions, earthquake actions.* 2004.
77. Kowalsky, M.J. and L.A. Montejo, *Cumbia user manual* 2007: North Carolina State University.
78. Priestley, M.J.N., F. Seible, and G.M. Calvi, *Seismic design and retrofit of bridge structures*1996, New York: Jhon Wiley and Sons.
79. M. J. Kowalsky, M.J.N. Priestley, and F. Seible, *Dynamic Behavior of Lightweight Concrete Bridges.* Structural Journal 2000. **97**(4): p. 602-618.
80. Moyer, M.J. and M.J. Kowalsky, *Influence of Tension Strain on Buckling of Reinforcement in Concrete Columns.* Structural Journal, 2003. **100**(1): p. 75-85.
81. Berry, M. and M. Eberhard, *Practical Performance Model for Bar Buckling.* Journal of Structural Engineering, 2005. **131**: p. 1060-1070.
82. Mander, J., M.J. Priestley, and R. Park, *Theoretical Stress and Strain Model for Confined Concrete.* Journal of Structural Engineering, 1988. **114**.
83. Carvalho, E.C., *Seismic testing of the structures.* Earthquake Engineering & Structural Dynamics, 1999.
84. Pampanin, S., et al., *PRESS Design Handbook* First ed2010, New Zealand: NZ Concrete Society Inc.
85. Marriott, D., *The Development of High-Performance Post-Tensioned Rocking Systems for the Seismic Design of Structures*, in *Civil Engineering*2009, University of Canterbury.
86. RedLake, *MotionPro X3 user guide.* 2004.
87. Pampanin, S., M.J. Nigel Priestley, and S. Sritharan, *Analitycal modelling of the seismic behaviour of precast concrete frames designed with ductile connections.* Journal of Earthquake Engineering, 2001. **5**(3): p. 329-367.
88. Priestley, M.J.N., F. Seible, and G.M. Calvi, *Seismic design and retrofit of bridge structures*. 1996, New York: Jhon Wiley and Sons.
89. Palermo, A., S. Pampanin, and G. Calvi, *Concept and development of hybrid solutions for seismic resistant bridge systems.* Journal of earthquake engineering : JEE, 2005. **9**(6): p. 899.
90. Ramberg, W. and W.R. Osgood, *Description of stress-Strain Curves by Three Parameters.* National Advisory and Commitee on Areonautics, 1943.
91. Otani, S., *A computer program for inelastic responce of R/C frames to earthquakes.* , 1974: University of Illinois
92. Marriott, D., *The Development of High-Performance Post-Tensioned Rocking Systems for the Seismic Design of Structures*, in *Civil Engineering*2009, University of Canterbury.
93. Kim, J., *Behaviour of hybrid frames under seismic loading*, 2002: Univerity of Washington
94. Spieth, H.A., et al., *Modelling of precast prestressed concrete frame structures with rocking beam column connections*, 2004: University of Canterbury.
95. Palermo, A., S. Pampanin, and A.J. Carr, *Efficiency of simplified alternative modelling approaches to predict the seismic responce of precast concrete hybrid system.*, in *Fib*2005: Budapest.
96. Carr, A.J., *Ruaumoko user manual.* 2005.

Appendix A

Results of Timber Segments Tests Run

A-1 1+2 Spring 3.5N in Free Oscillation

A-1.1 Bottom Block

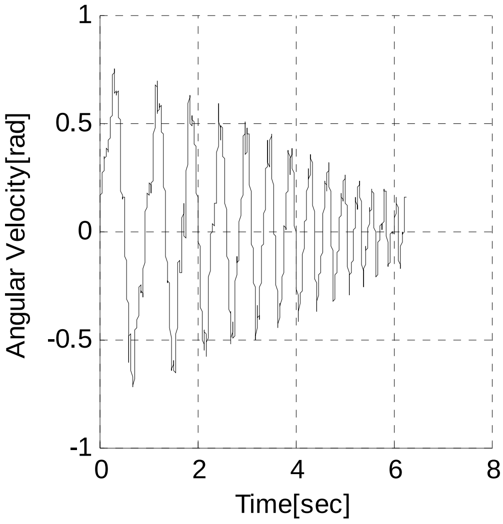

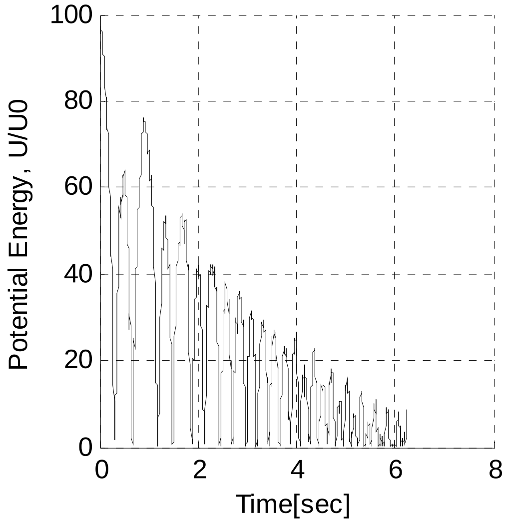

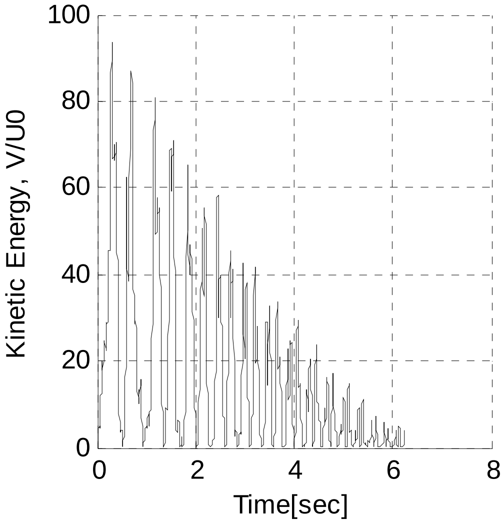

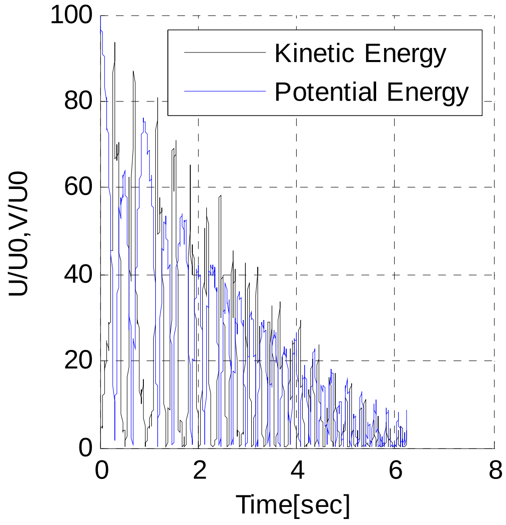

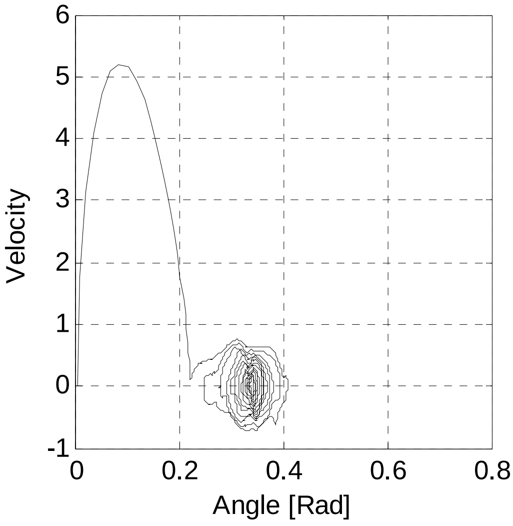

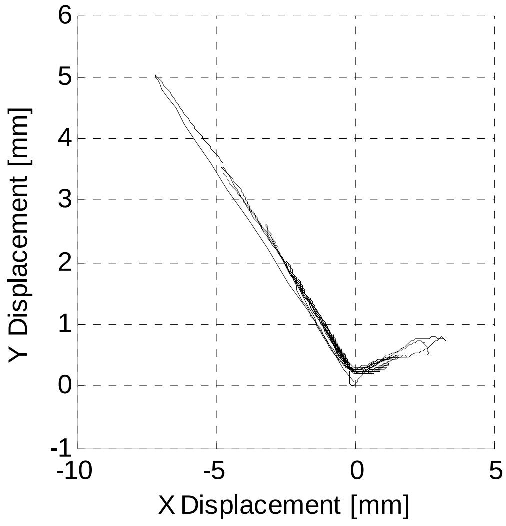

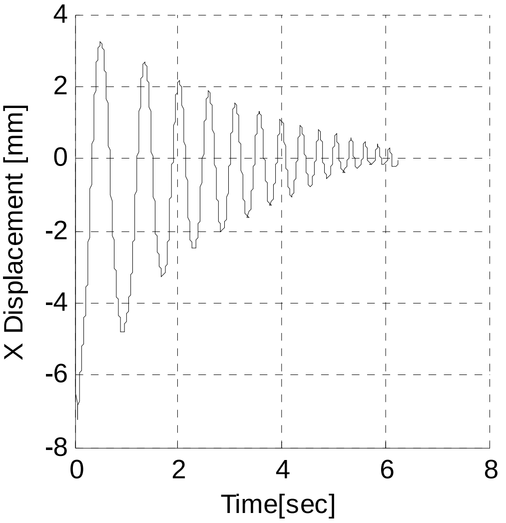
X Displacement [mm]
Time[sec]
4
2
0
-2
-4
-6
-8
0
2
4
6
8

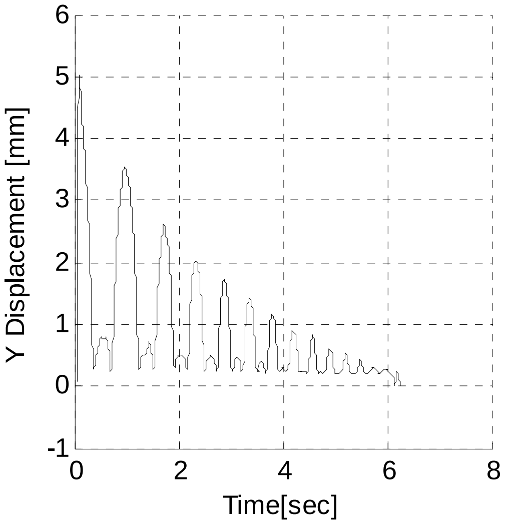
Y Displacement [mm]
Time[sec]
6
5
4
3
2
1
0
-1
0
2
4
6
8

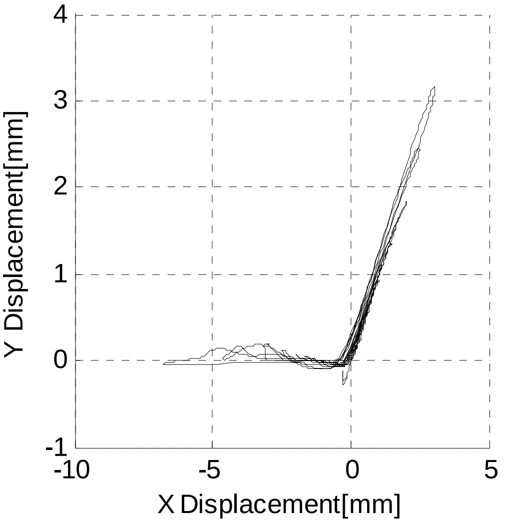
Y Displacement[mm]
X Displacement[mm]
4
3
2
1
0
-1
-10
-5
0
5

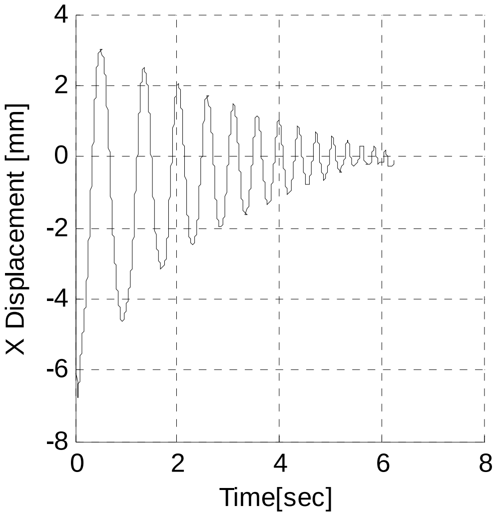
X Displacement [mm]
Time[sec]
4
2
0
-2
-4
-6
-8
0
2
4
6
8

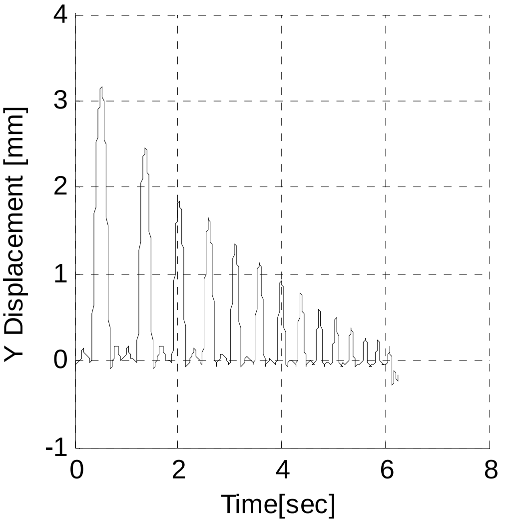
Y Displacement [mm]
Time[sec]
4
3
2
1
0
-1
0
2
4
6
8

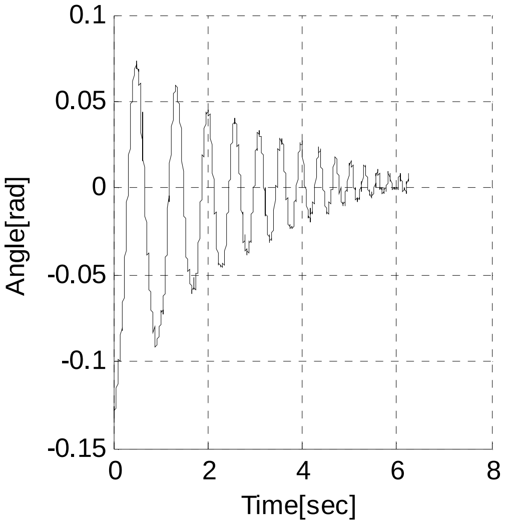
Angle[rad]
Time[sec]
0.1
0.05
0
-0.05
-0.1
-0.15
0
2
4
6
8

A-2 1+2 Spring 3.5N in Quasi-Sinusoidal Input 3Hz

A-2.1 Bottom Block

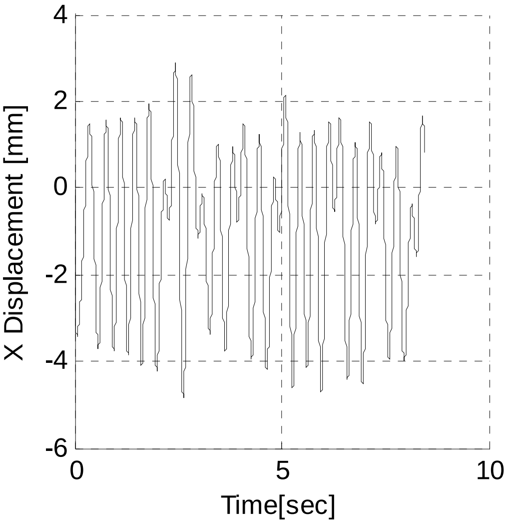

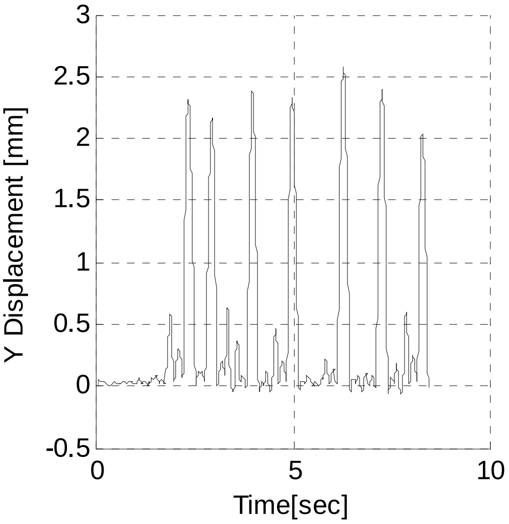

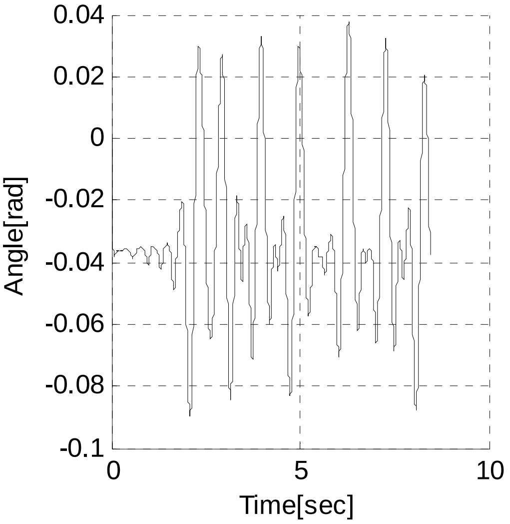

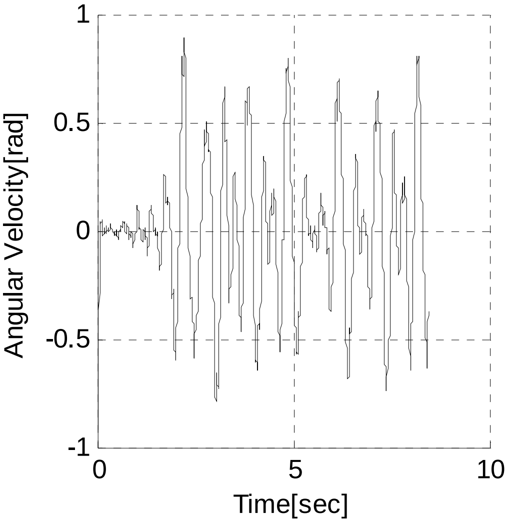

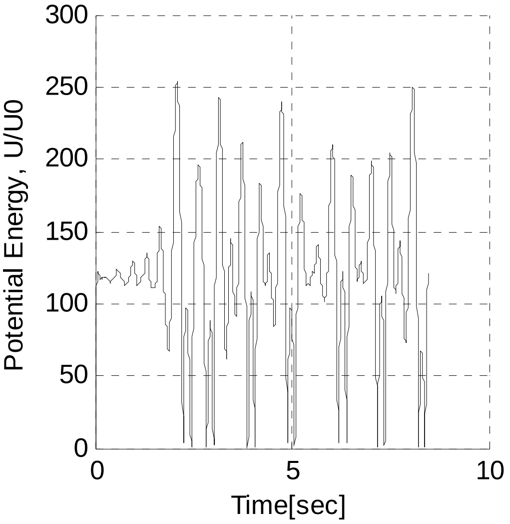

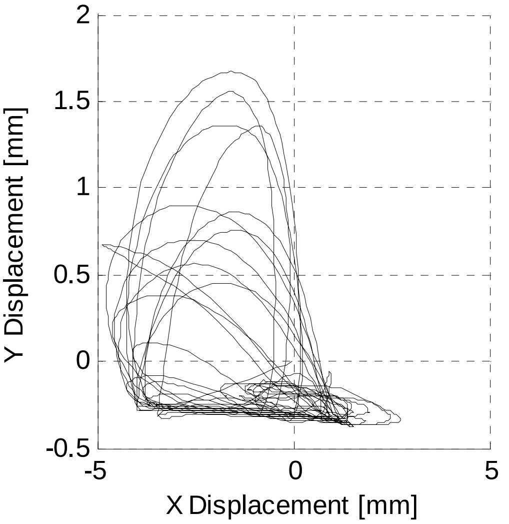

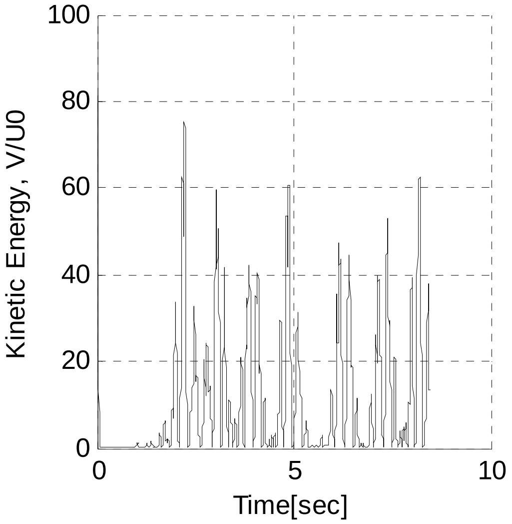
Kinetic Energy, V/U0
100
80
60
40
20
0
0
5
10
Time[sec]

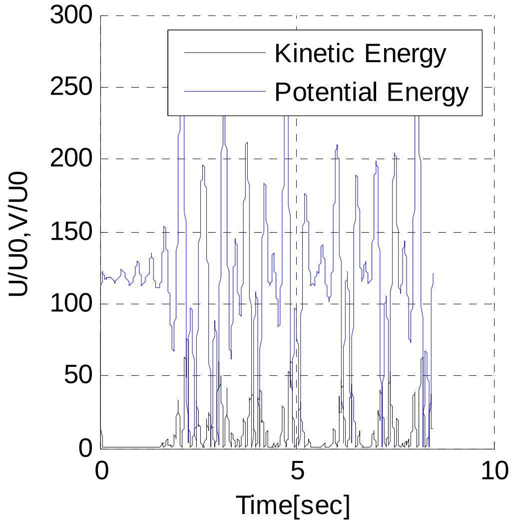
U/U0,V/U0
300
250
200
150
100
50
0
0
5
10
Time[sec]
Kinetic Energy
Potential Energy

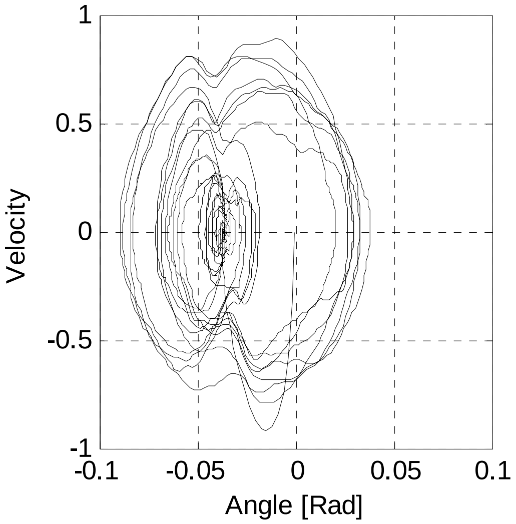
Velocity
1
0.5
0
-0.5
-1
-0.1
-0.05
0
0.05
0.1
Angle [Rad]

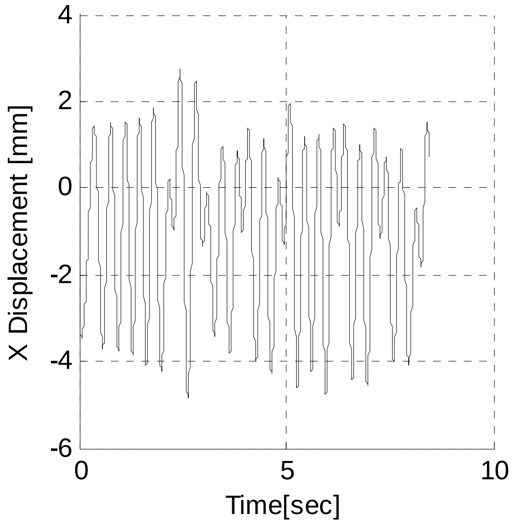
X Displacement [mm]
4
2
0
-2
-4
-6
0
5
10
Time[sec]

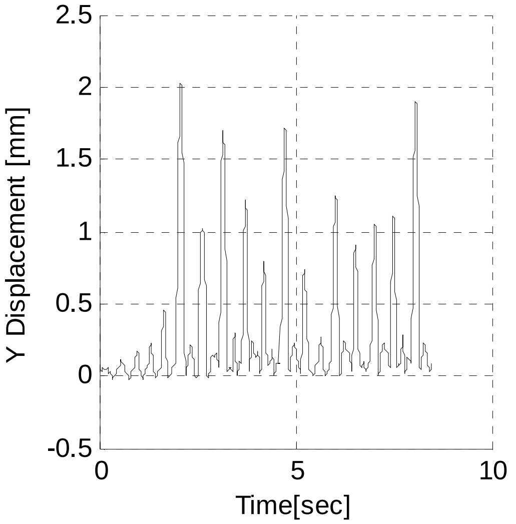
Y Displacement [mm]
2.5
2
1.5
1
0.5
0
-0.5
0
5
10
Time[sec]

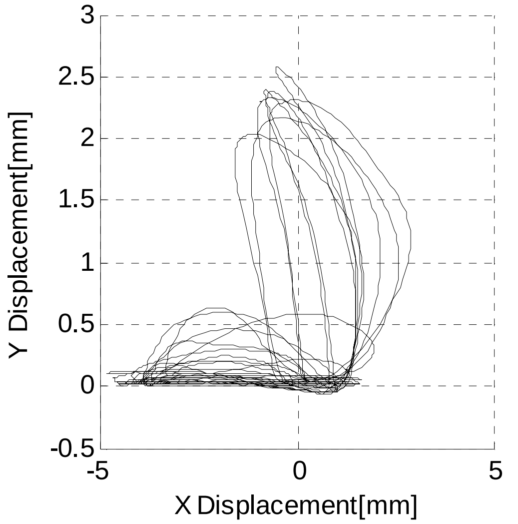
Y Displacement[mm]
3
2.5
2
1.5
1
0.5
0
-0.5
-5
0
5
X Displacement[mm]

A-3 1+2 Spring 3.5N in Quasi-Sinusoidal Input 4Hz

A-3.1 Bottom Block

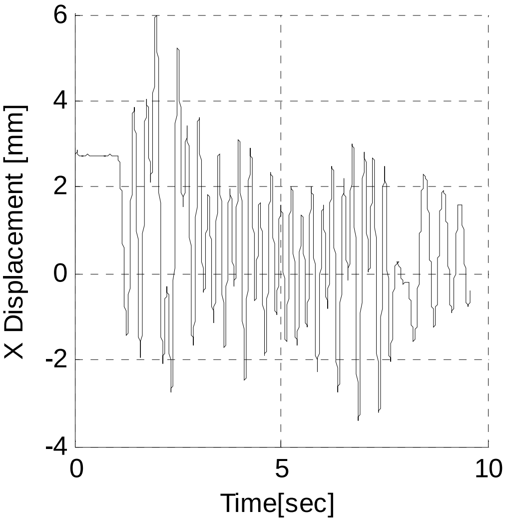

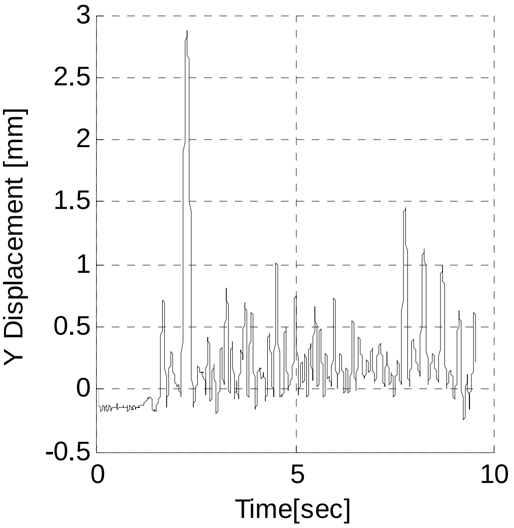

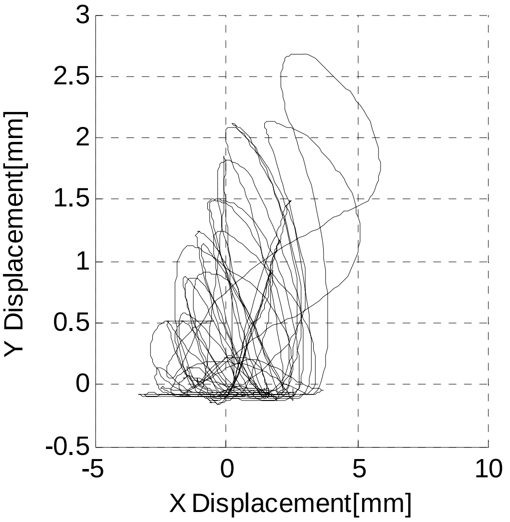

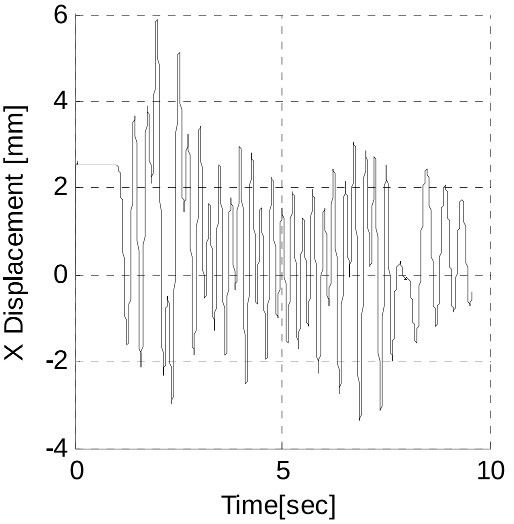

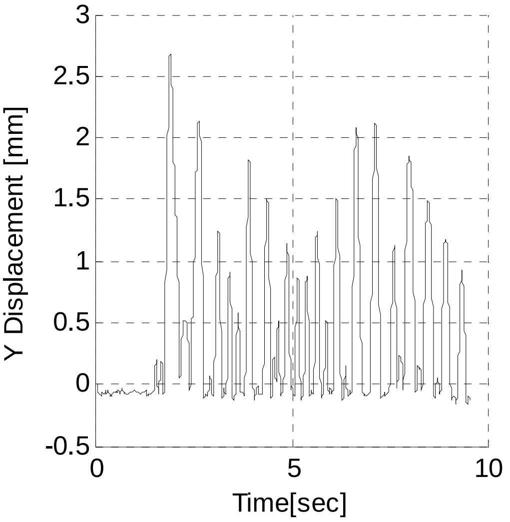

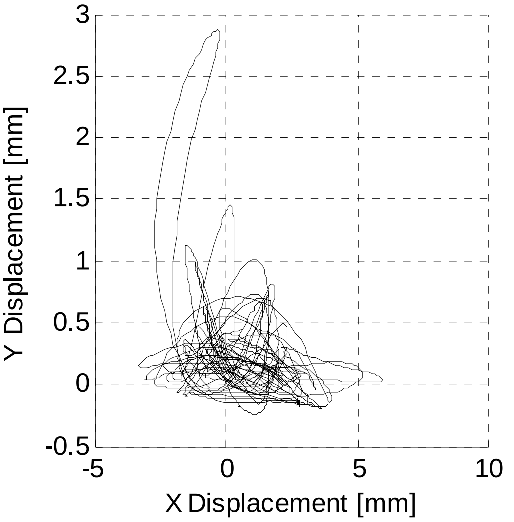

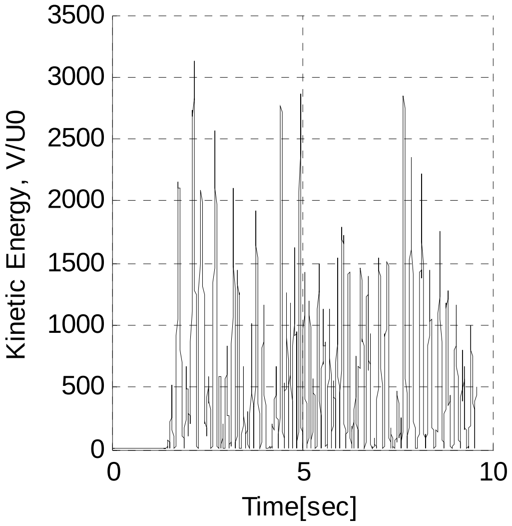
Kinetic Energy, V/U0
3500
3000
2500
2000
1500
1000
500
0
0
5
10
Time[sec]

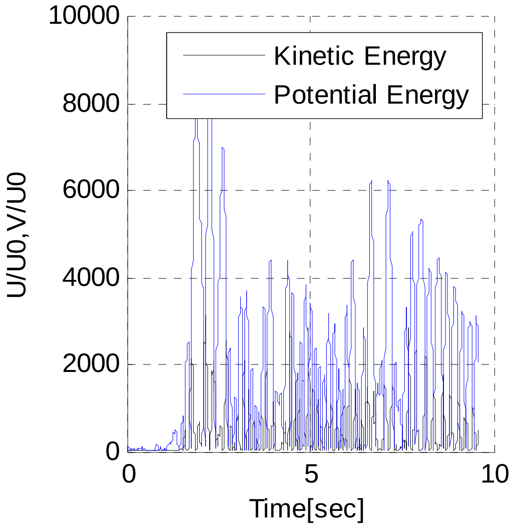
U/U0,V/U0
10000
8000
6000
4000
2000
0
0
5
10
Time[sec]
Kinetic Energy
Potential Energy

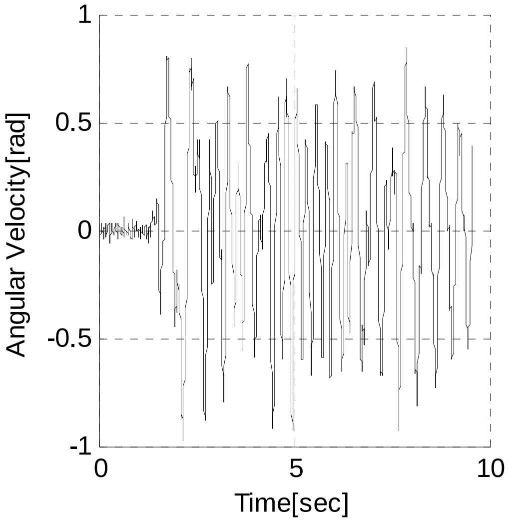
Angular Velocity[rad]
1
0.5
0
-0.5
-1
0
5
10
Time[sec]

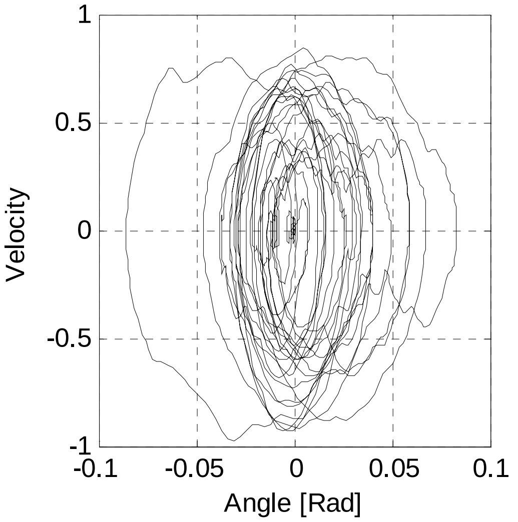
Velocity
1
0.5
0
-0.5
-1
-0.1
-0.05
0
0.05
0.1
Angle [Rad]

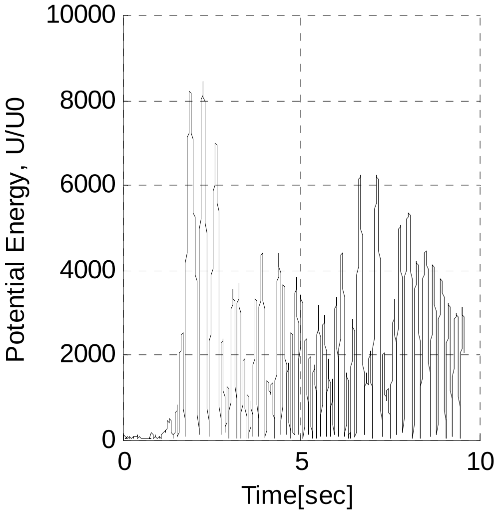
Potential Energy, U/U0
10000
8000
6000
4000
2000
0
0
5
10
Time[sec]

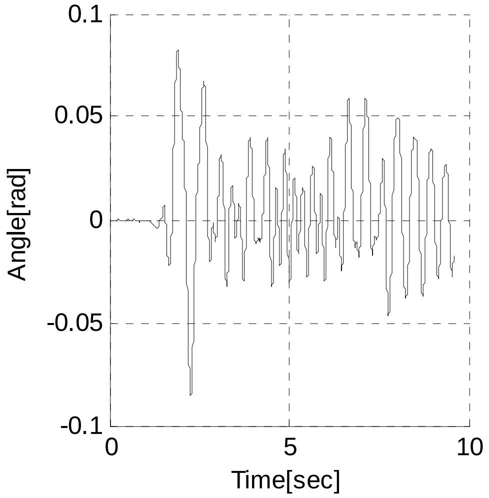
Angle[rad]
0.1
0.05
0
-0.05
-0.1
0
5
10
Time[sec]

A-4 1+2 Spring 3.5N in Quasi-Sinusoidal Input 5Hz

A-4.1 Bottom Block

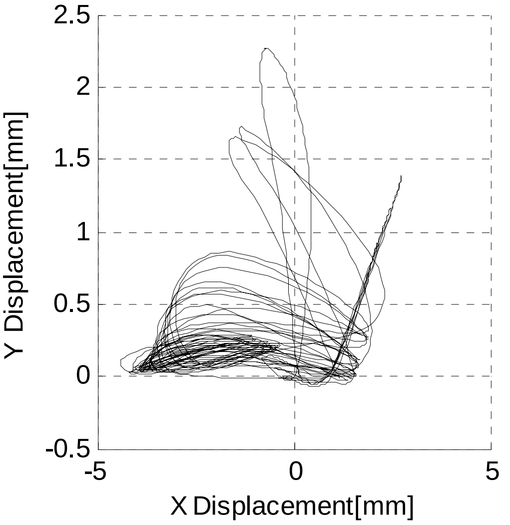

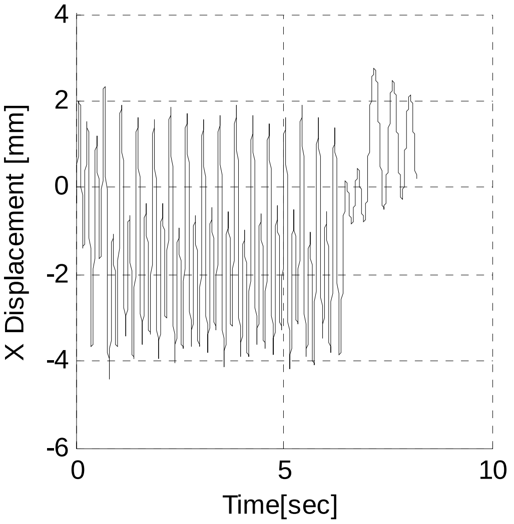

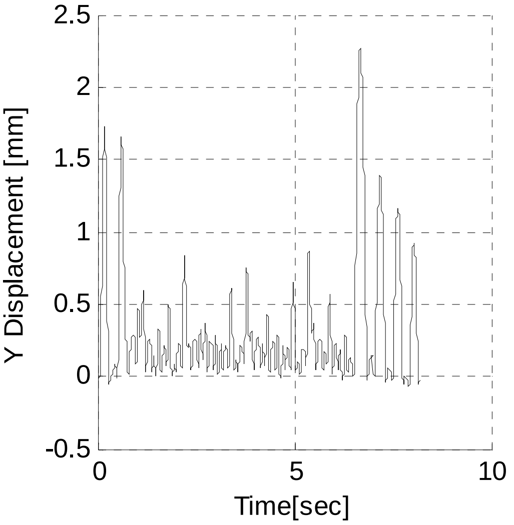

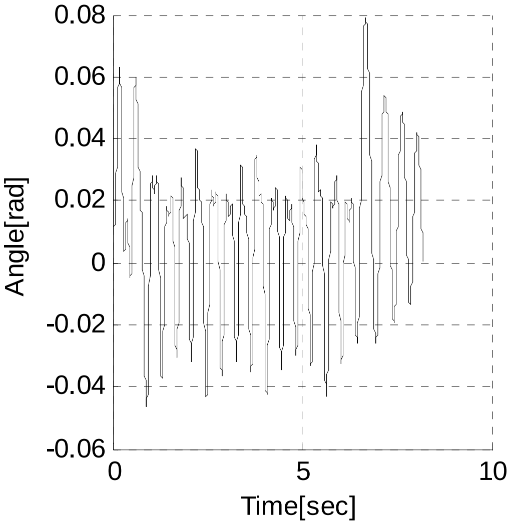

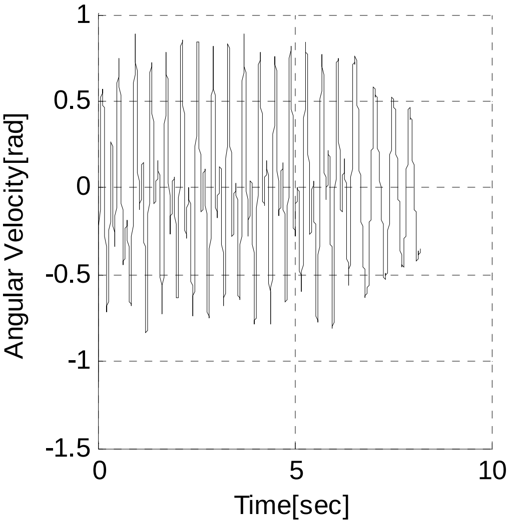

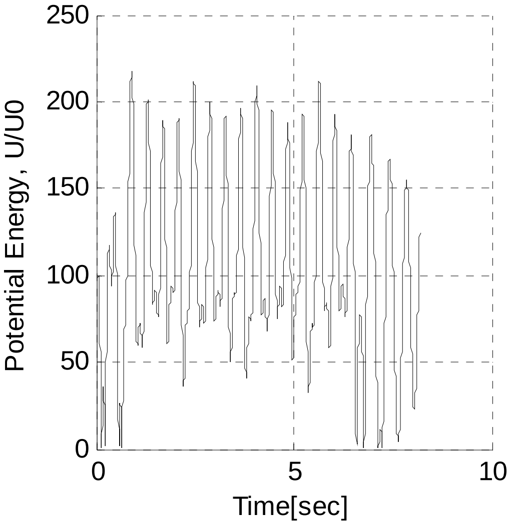

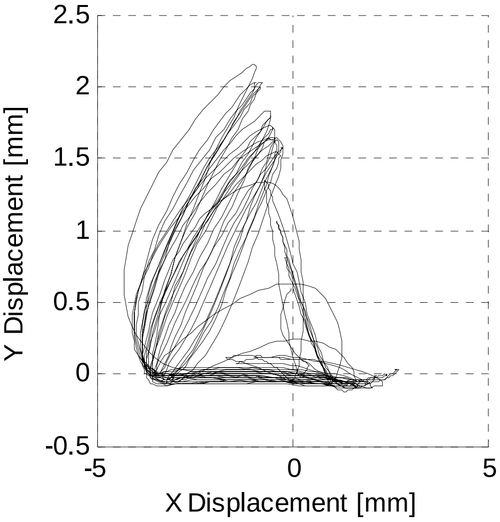
Y Displacement [mm]
X Displacement [mm]
2.5
2
1.5
1
0.5
0
-0.5
-5
0
5

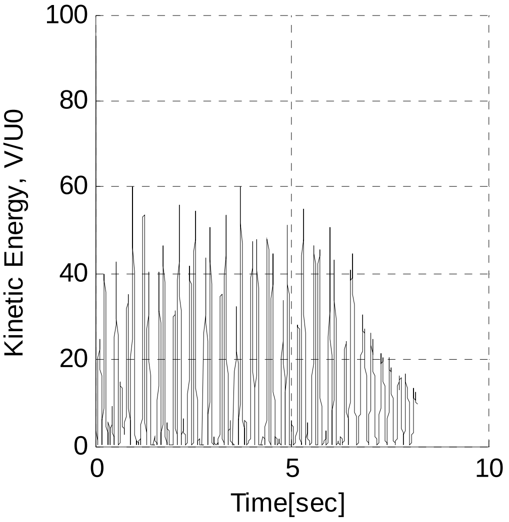
Kinetic Energy, V/U0
Time[sec]
100
80
60
40
20
0
0
5
10

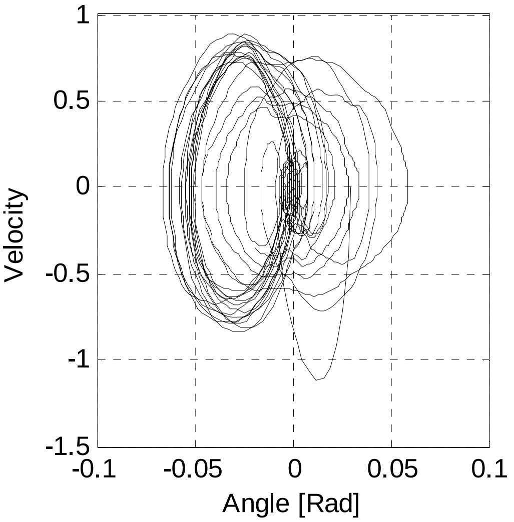
Velocity
Angle [Rad]
1
0.5
0
-0.5
-1
-1.5
-0.1
-0.05
0
0.05
0.1

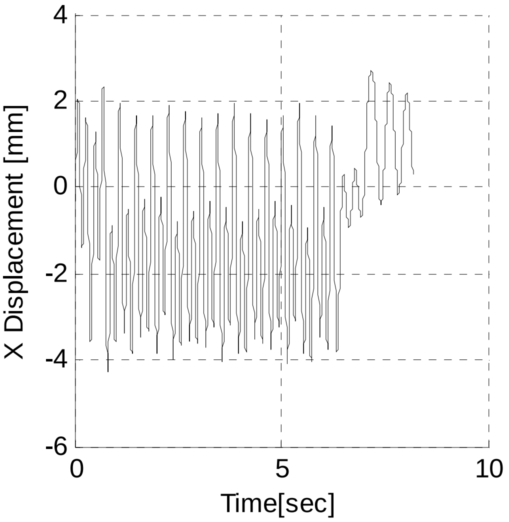
X Displacement [mm]
Time[sec]
4
2
0
-2
-4
-6
0
5
10

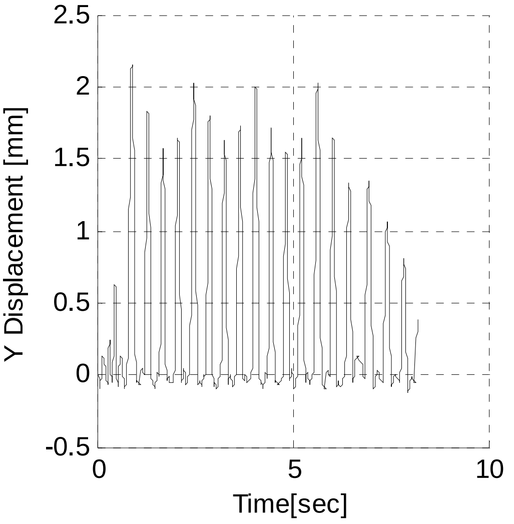
Y Displacement [mm]
Time[sec]
2.5
2
1.5
1
0.5
0
-0.5
0
5
10

A-5 3Cu Spring 3.5N in Quasi-Sinusoidal Input 3.5Hz

A-5.1 Bottom Block

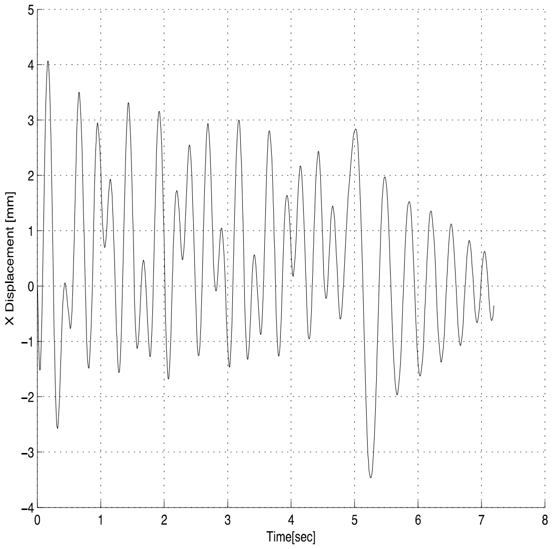

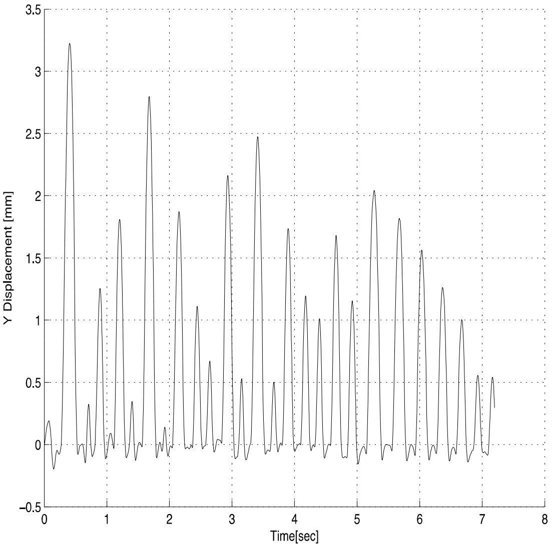

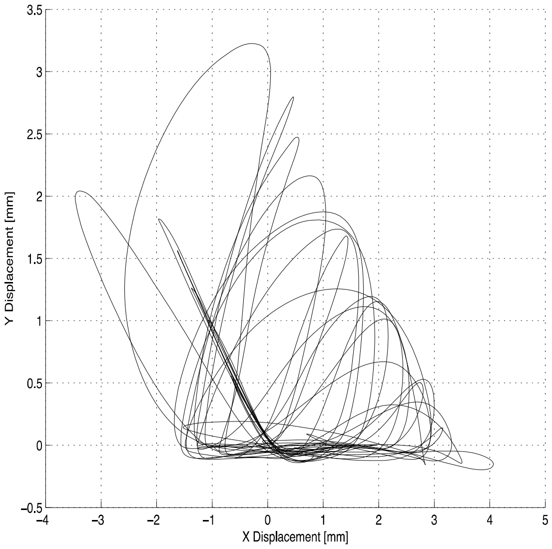

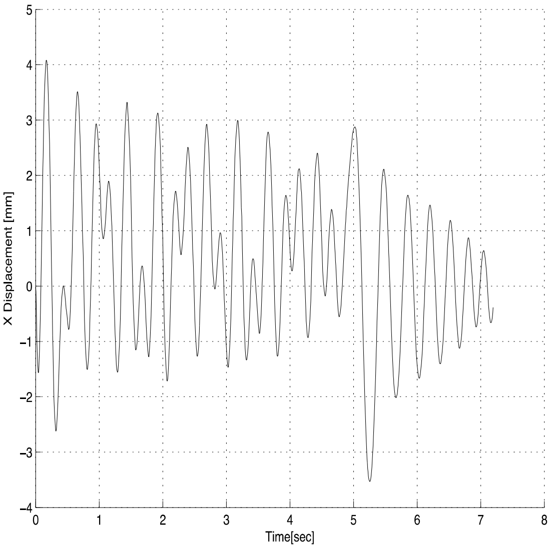

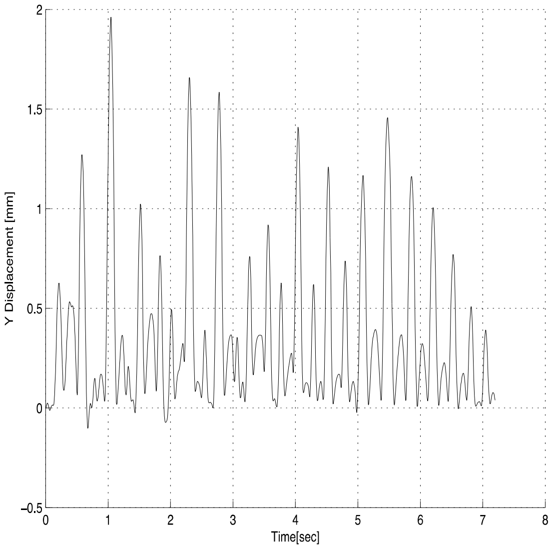

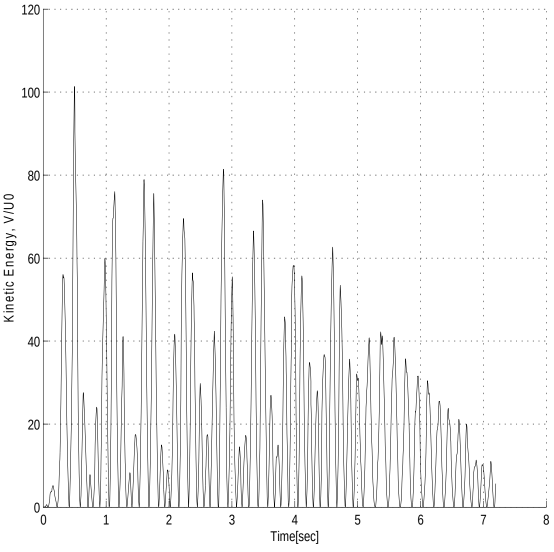

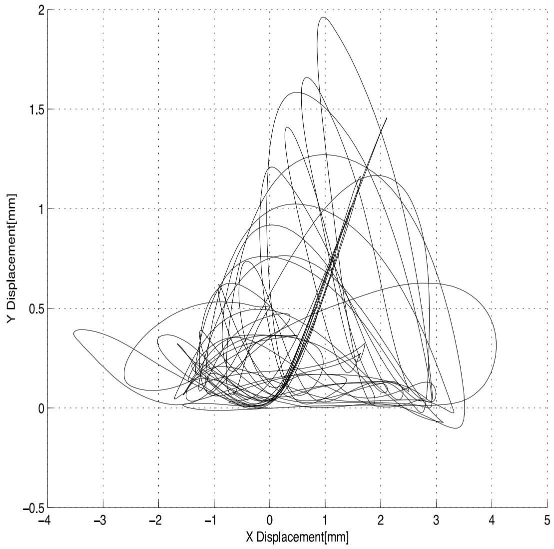

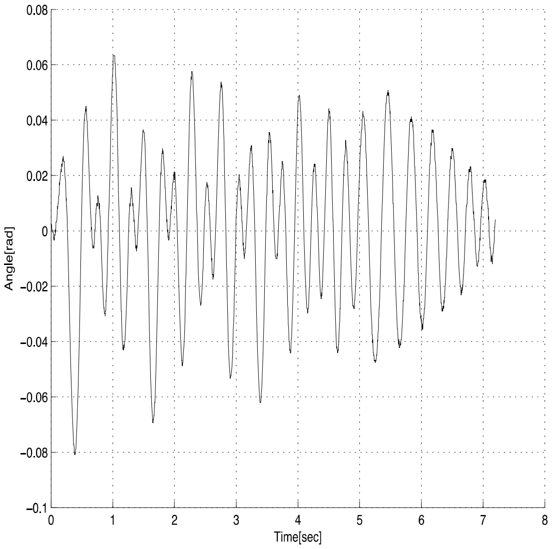

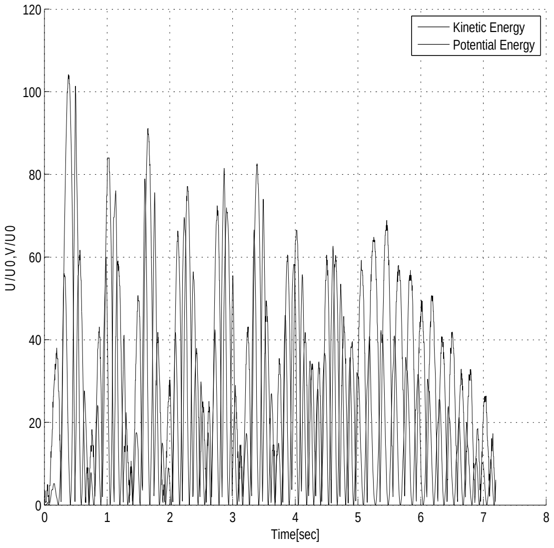

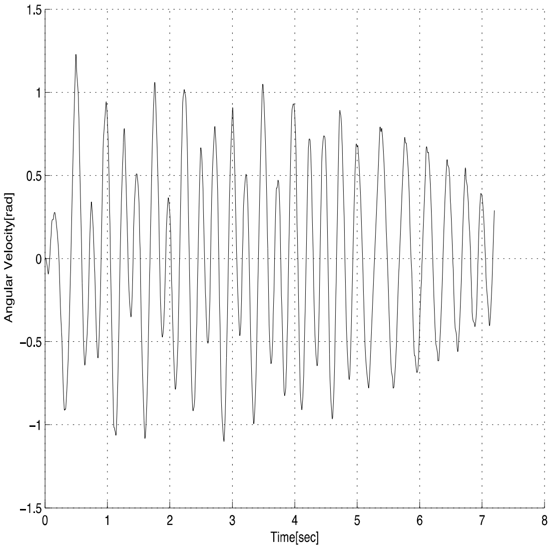

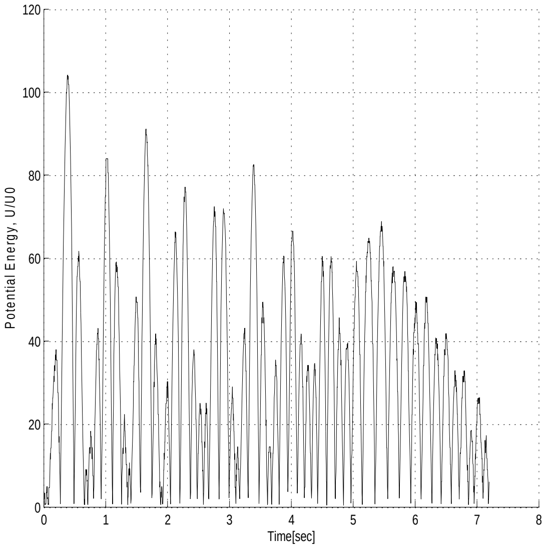

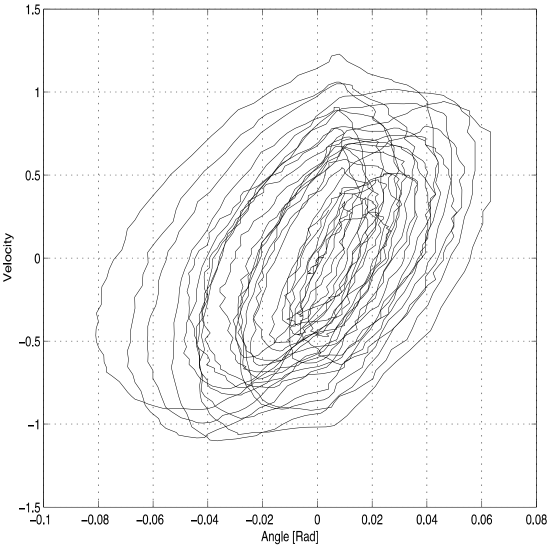

middle block

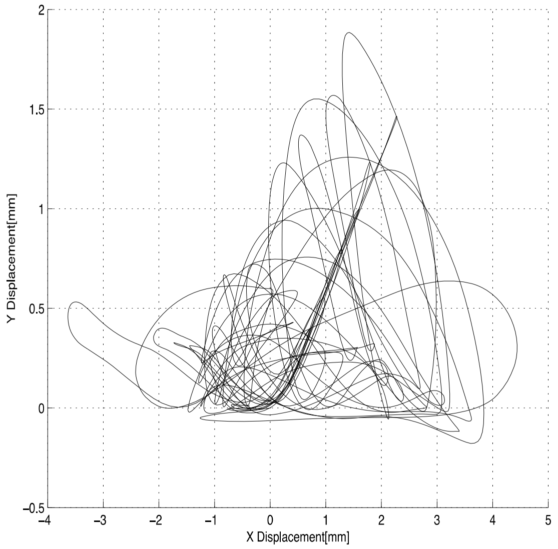
Y Displacement[mm]
X Displacement[mm]
2
1.5
1
0.5
0
−0.5
−4
−3
−2
−1
0
1
2
3
4
5

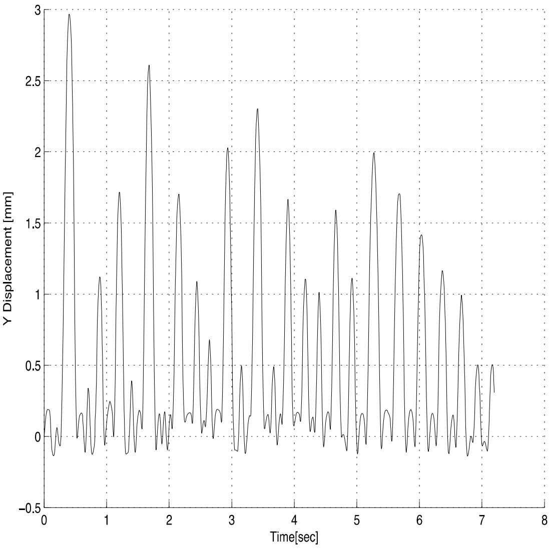
Y Displacement [mm]
Time[sec]
3
2.5
2
1.5
1
0.5
0
−0.5
0
1
2
3
4
5
6
7
8

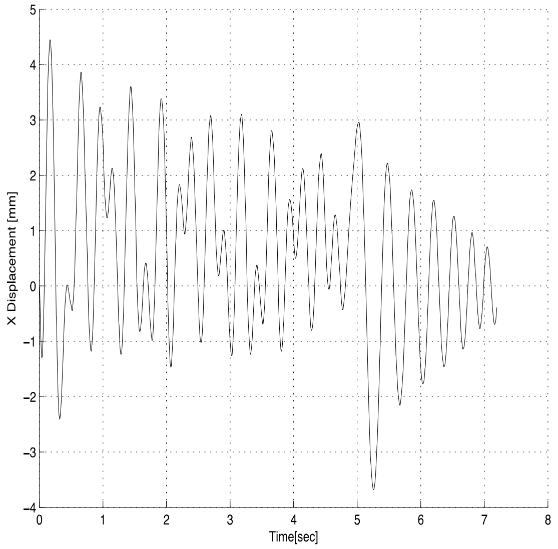
X Displacement [mm]
Time[sec]
5
4
3
2
1
0
−1
−2
−3
−4
0
1
2
3
4
5
6
7
8

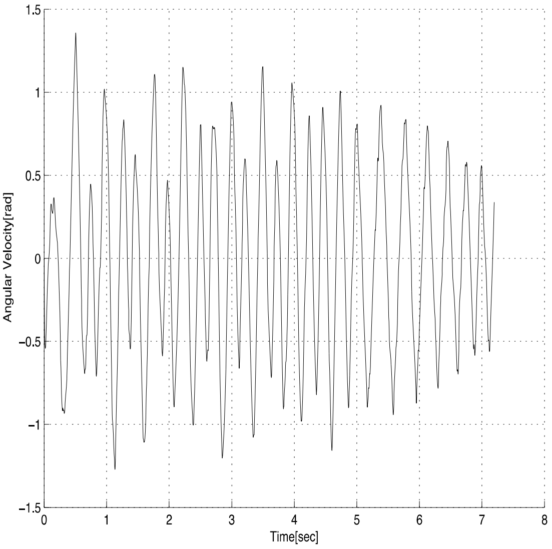
Angular Velocity[rad]
Time[sec]
1.5
1
0.5
0
−0.5
−1
−1.5
0
1
2
3
4
5
6
7
8

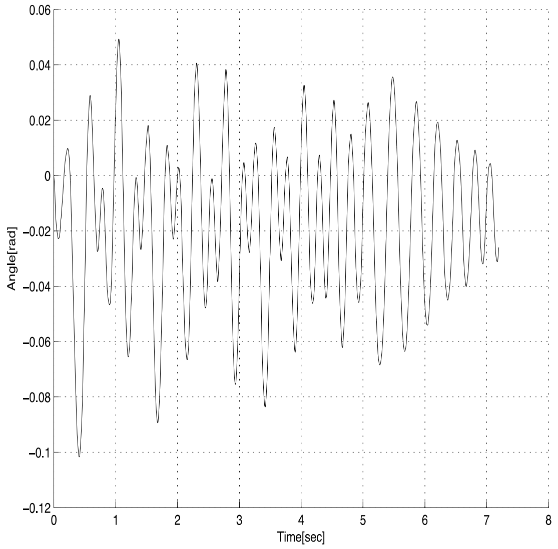
Angle[rad]
Time[sec]
0.06
0.04
0.02
0
−0.02
−0.04
−0.06
−0.08
−0.1
−0.12
0
1
2
3
4
5
6
7
8

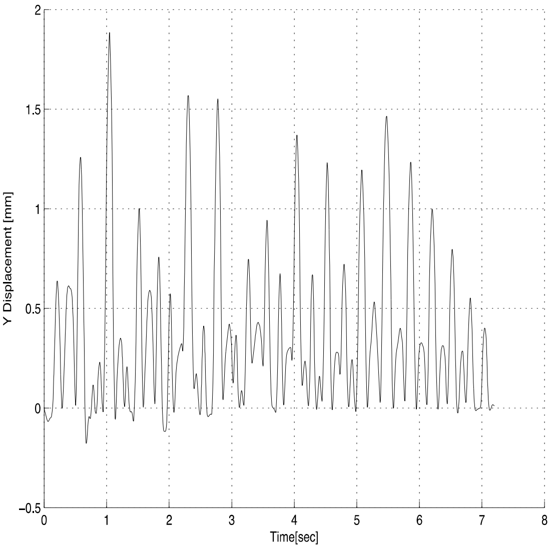
Y Displacement [mm]
Time[sec]
2
1.5
1
0.5
0
−0.5
0
1
2
3
4
5
6
7
8

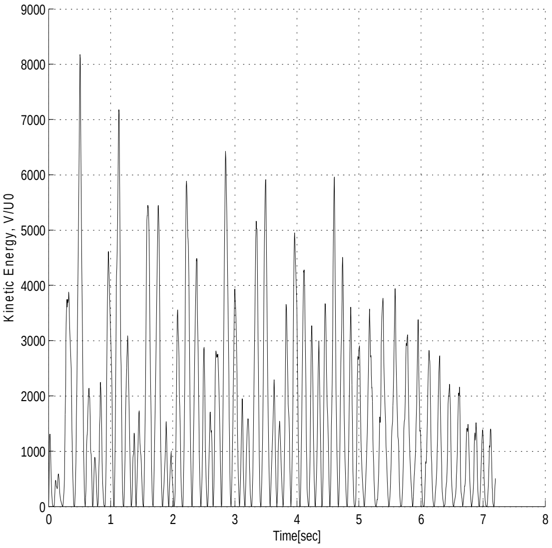
Kinetic Energy, V/U0
9000
8000
7000
6000
5000
4000
3000
2000
1000
0
0
1
2
3
4
5
6
7
8
Time[sec]

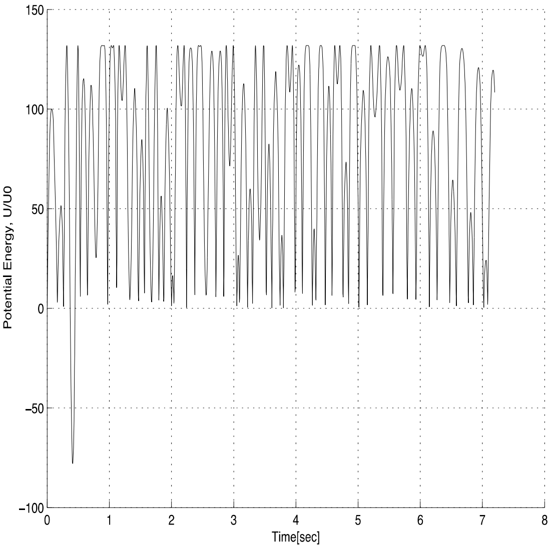
Potential Energy, U/U0
150
100
50
0
−50
−100
0
1
2
3
4
5
6
7
8
Time[sec]

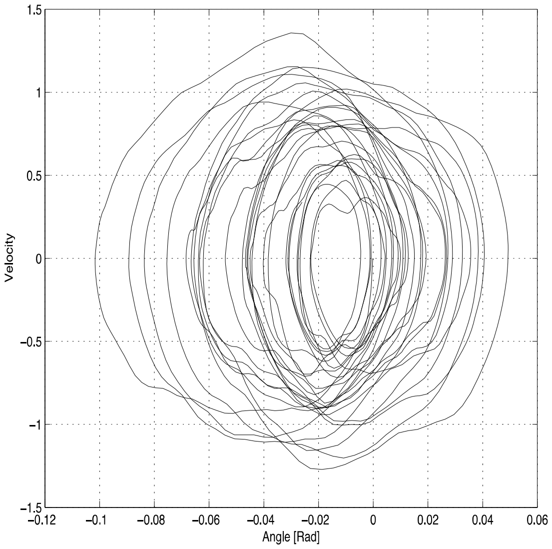
Velocity
1.5
1
0.5
0
−0.5
−1
−1.5
−0.12
−0.1
−0.08
−0.06
−0.04
−0.02
0
0.02
0.04
0.06
Angle [Rad]

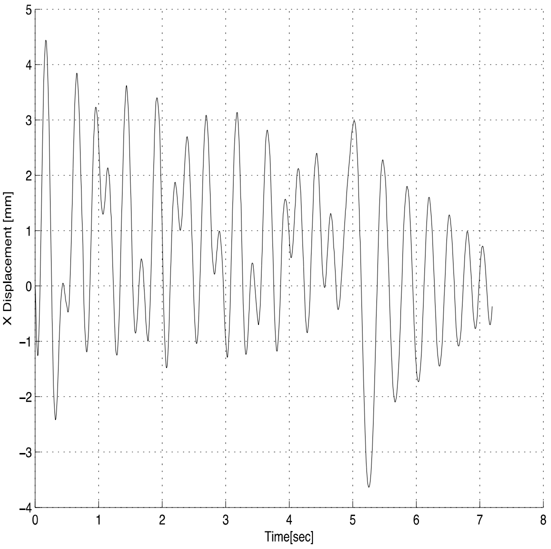
X Displacement [mm]
5
4
3
2
1
0
−1
−2
−3
−4
0
1
2
3
4
5
6
7
8
Time[sec]

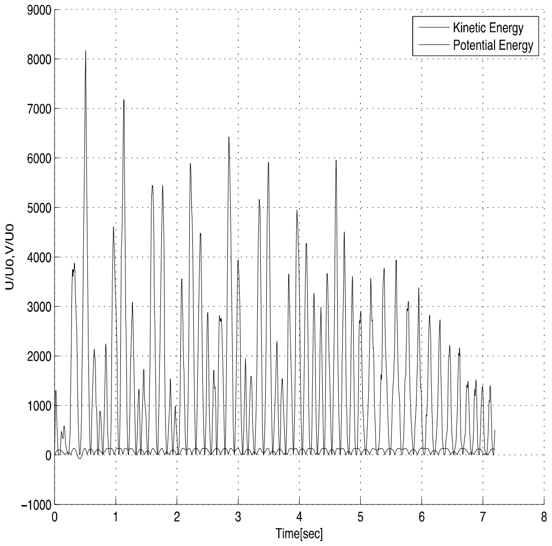
U/U0,V/U0
Kinetic Energy
Potential Energy
9000
8000
7000
6000
5000
4000
3000
2000
1000
0
−1000
0
1
2
3
4
5
6
7
8
Time[sec]

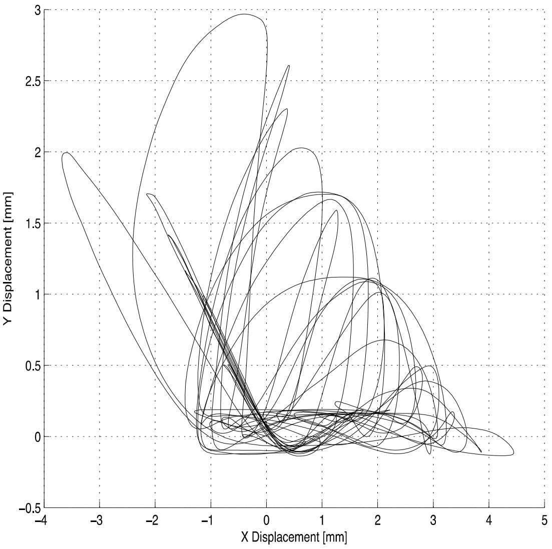
Y Displacement [mm]
3
2.5
2
1.5
1
0.5
0
−0.5
−4
−3
−2
−1
0
1
2
3
4
5
X Displacement [mm]

A-6 3Cu Spring 3.5N in Quasi-Sinusoidal Input 5Hz

A-6.1 Bottom Block

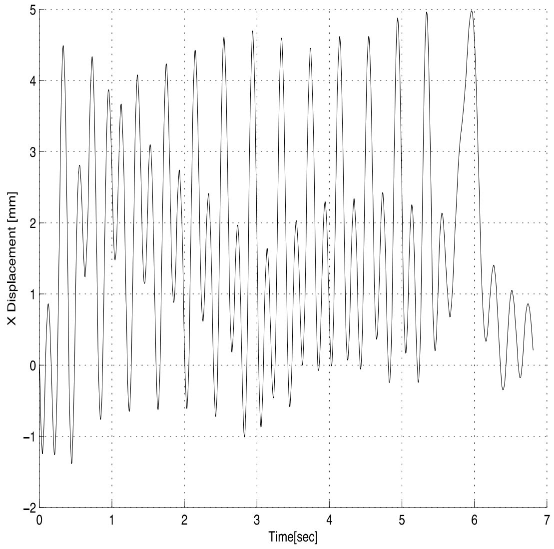

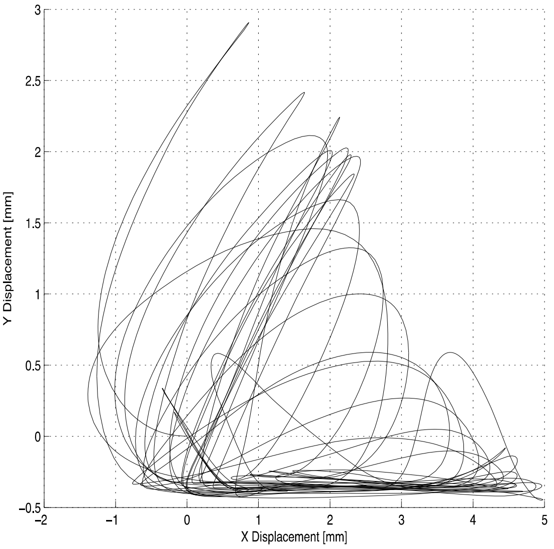

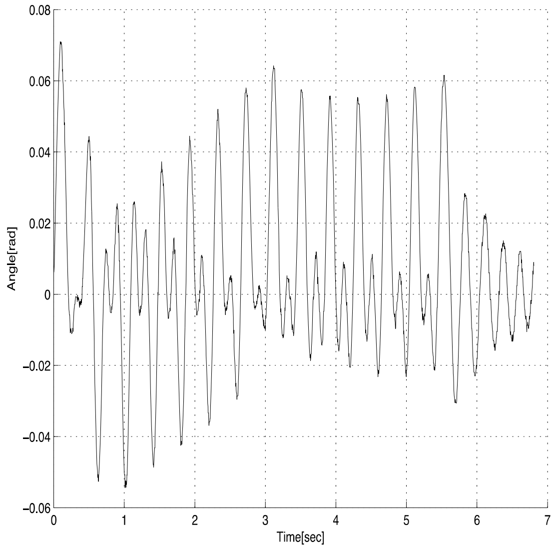

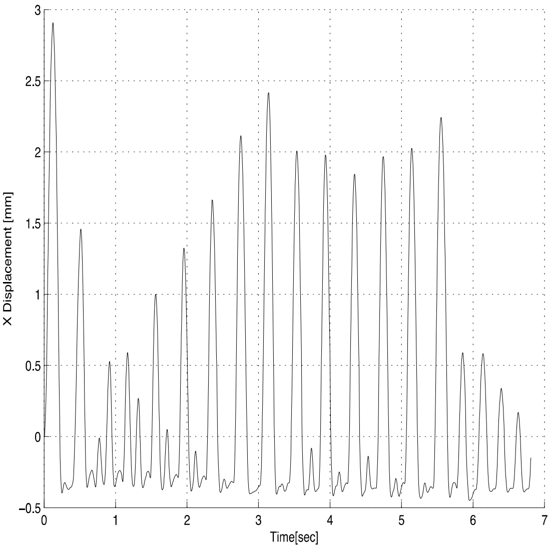

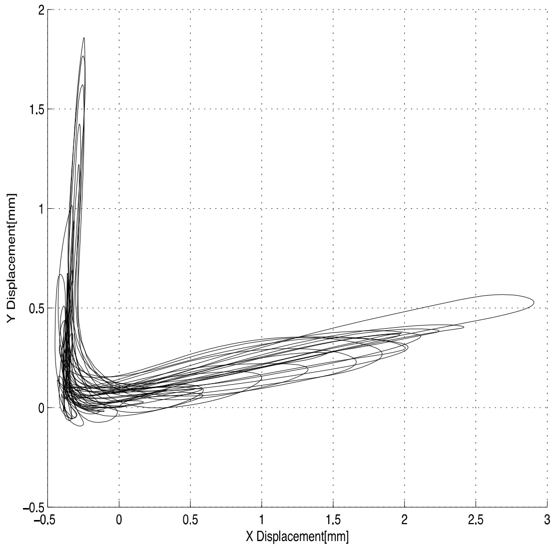

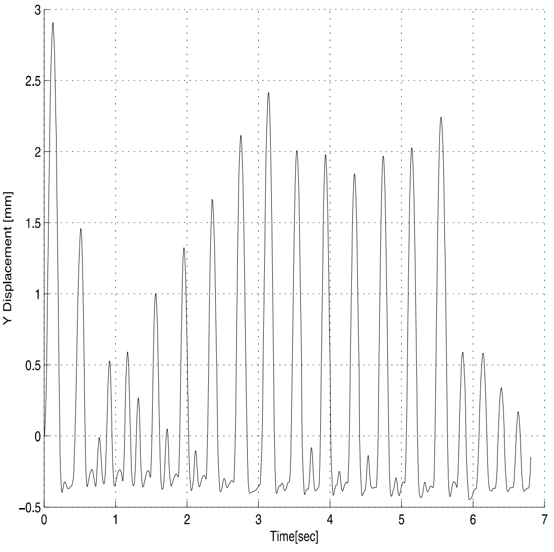

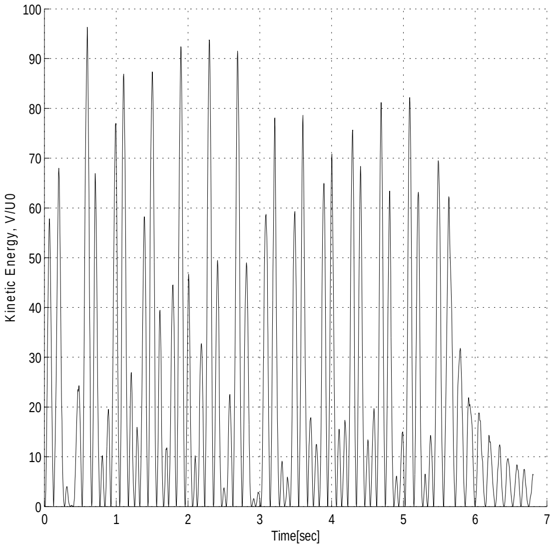
Kinetic Energy, V/U0
0
10
20
30
40
50
60
70
80
90
100
Time[sec]
0
1
2
3
4
5
6
7

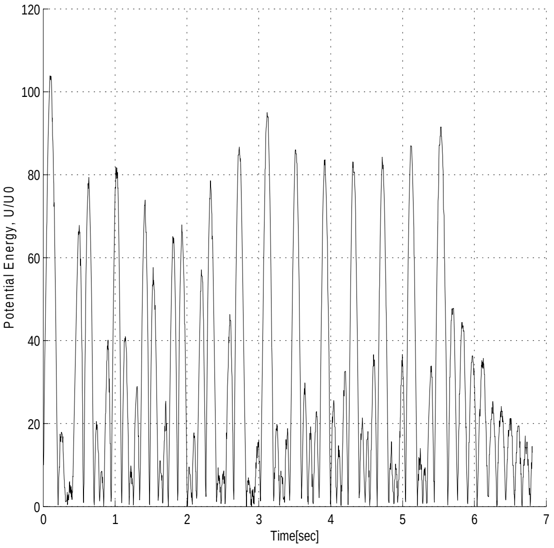
Potential Energy, U/U0
0
20
40
60
80
100
120
Time[sec]
0
1
2
3
4
5
6
7

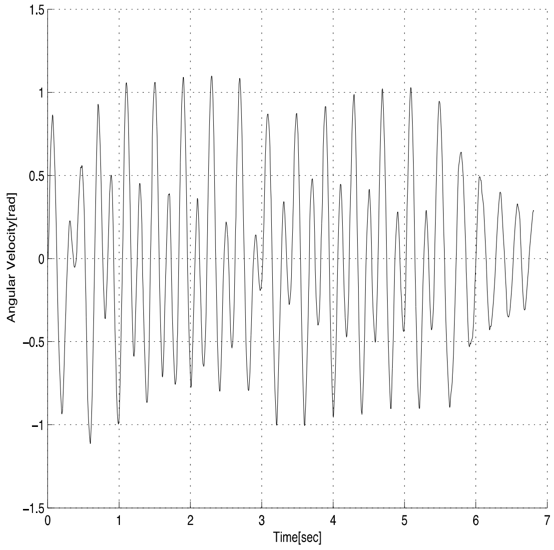
Angular Velocity[rad]
−1.5
−1
−0.5
0
0.5
1
1.5
Time[sec]
0
1
2
3
4
5
6
7

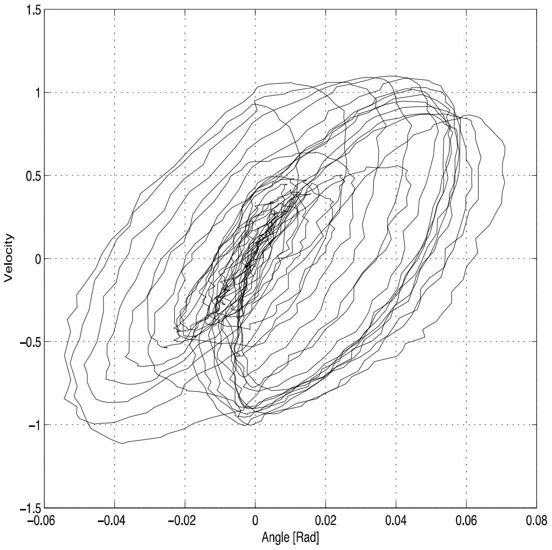
Velocity
−1.5
−1
−0.5
0
0.5
1
1.5
Angle [Rad]
−0.06
−0.04
−0.02
0
0.02
0.04
0.06
0.08

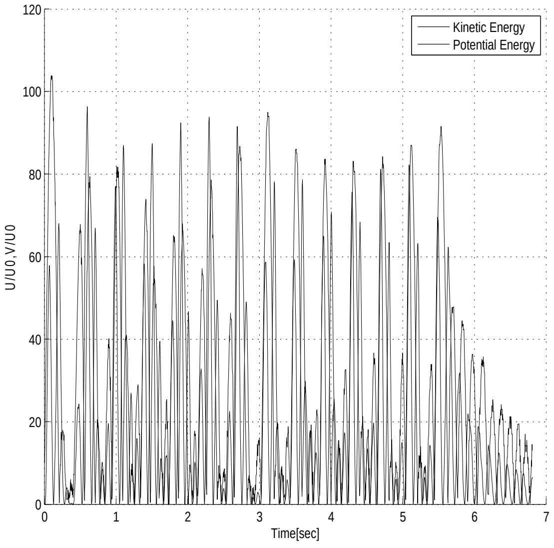
U/U0, V/U0
Kinetic Energy
Potential Energy
0
20
40
60
80
100
120
Time[sec]
0
1
2
3
4
5
6
7

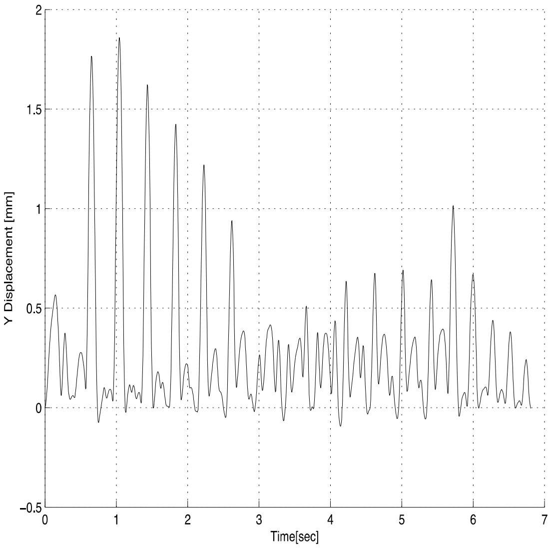
Y Displacement [mm]
−0.5
0
0.5
1
1.5
2
Time[sec]
0
1
2
3
4
5
6
7

A-6.2 Middle Block

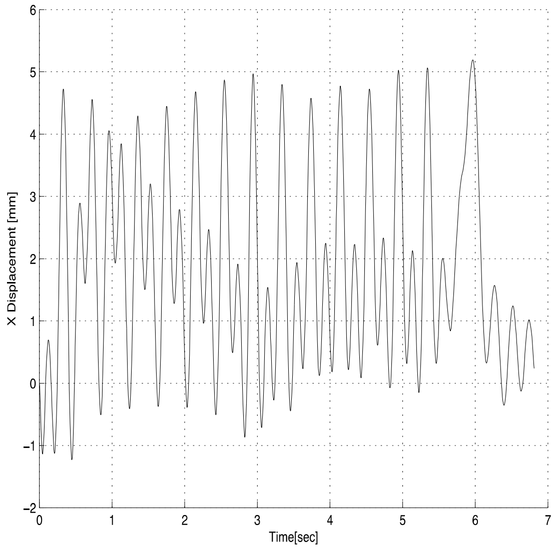

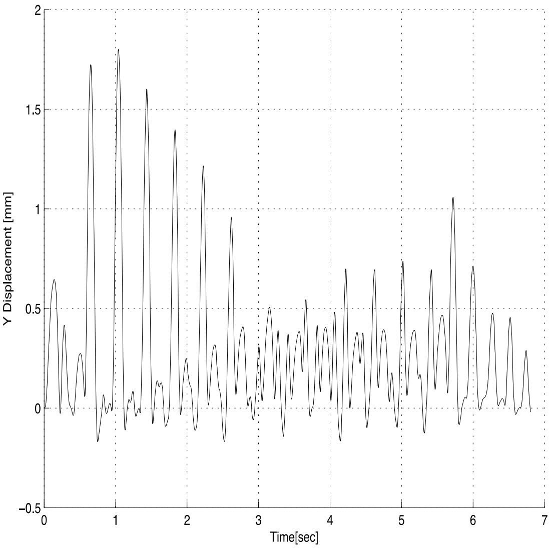

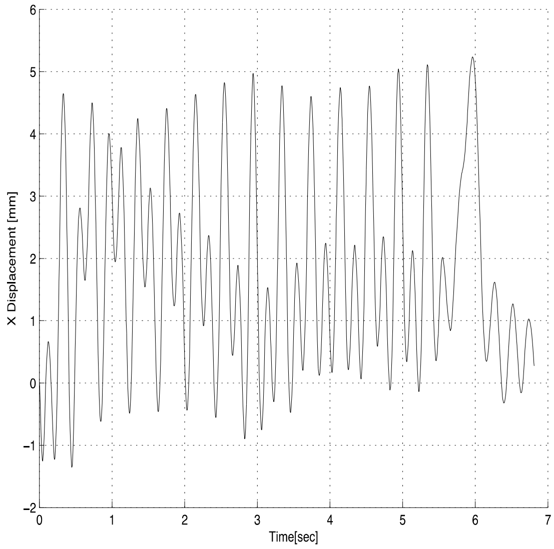

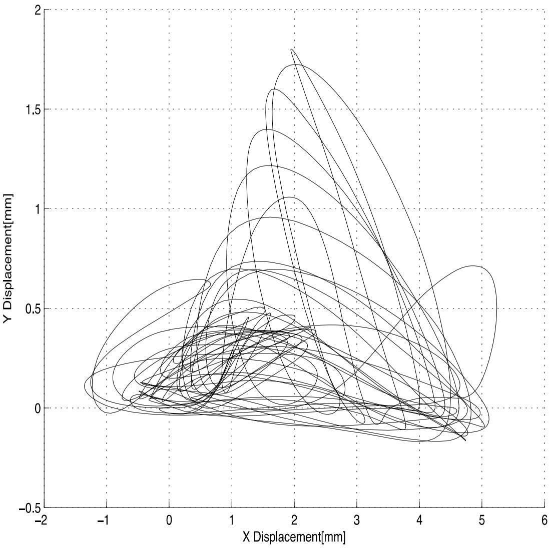

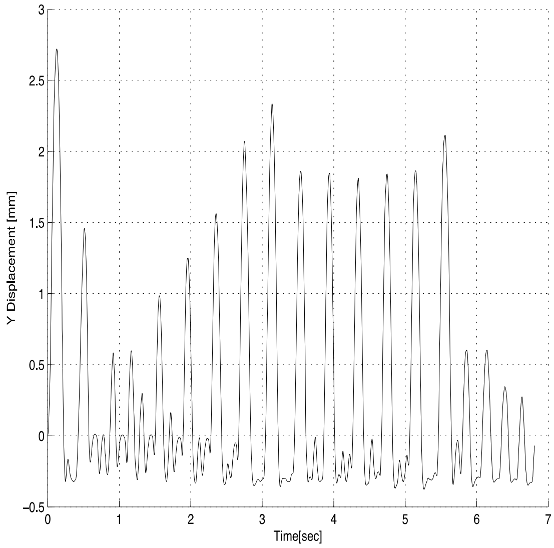

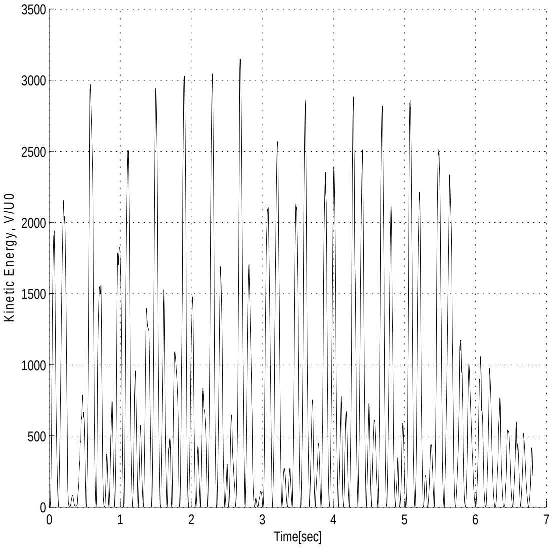

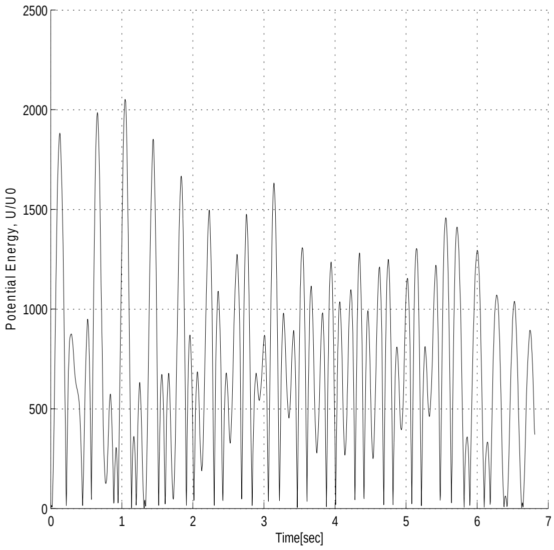
Potential Energy, U/U0
Time[sec]
0
500
1000
1500
2000
2500
0
1
2
3
4
5
6
7

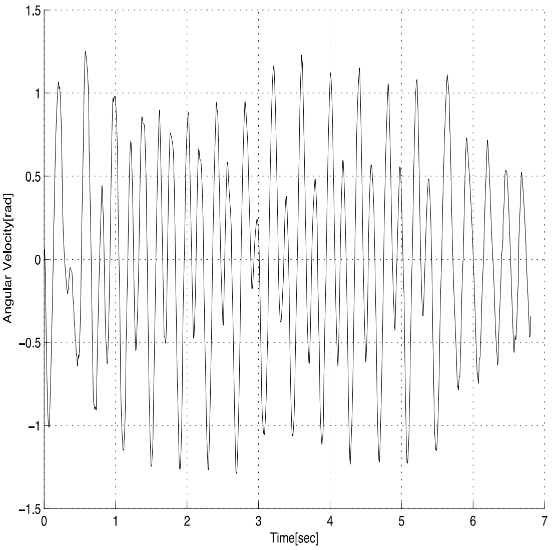
Angular Velocity[rad]
Time[sec]
1.5
1
0.5
0
−0.5
−1
−1.5
0
1
2
3
4
5
6
7

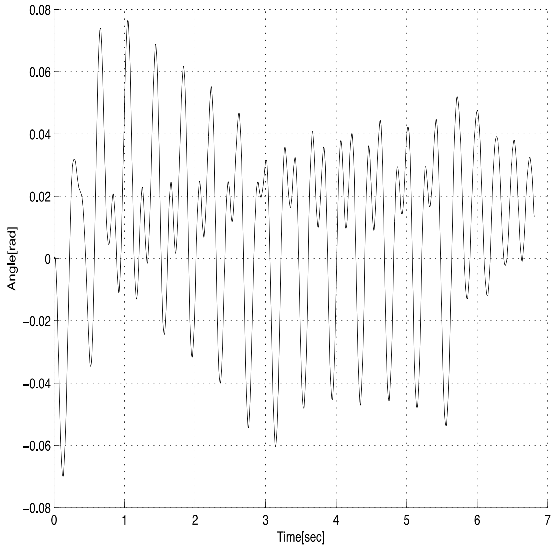
Angle[rad]
Time[sec]
0.08
0.06
0.04
0.02
0
−0.02
−0.04
−0.06
−0.08
0
1
2
3
4
5
6
7

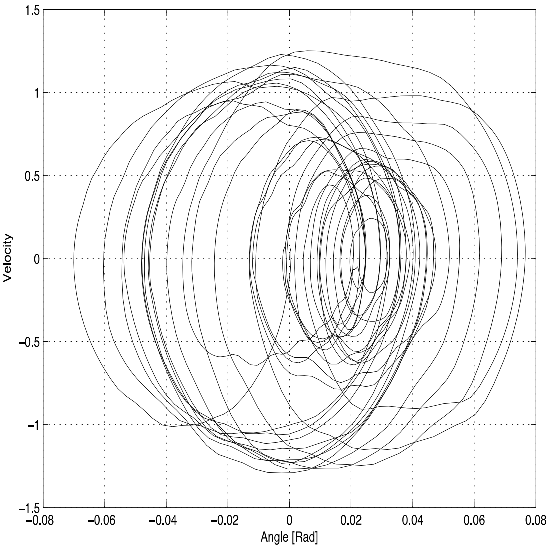
Velocity
Angle [Rad]
1.5
1
0.5
0
−0.5
−1
−1.5
−0.08
−0.06
−0.04
−0.02
0
0.02
0.04
0.06
0.08

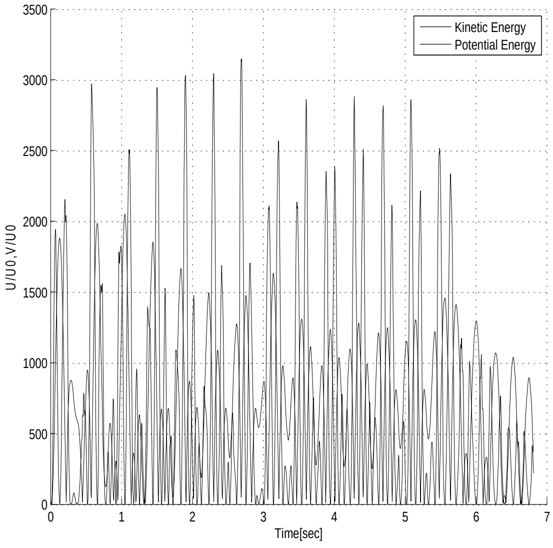
U/U0,V/U0
Time[sec]
Kinetic Energy
Potential Energy
3500
3000
2500
2000
1500
1000
500
0
0
1
2
3
4
5
6
7

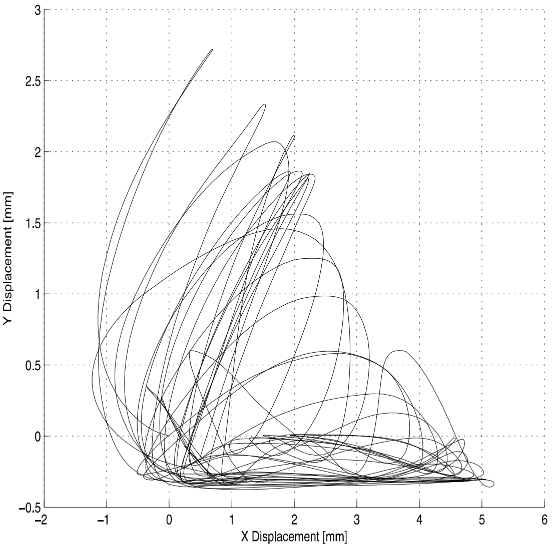
Y Displacement [mm]
X Displacement [mm]
3
2.5
2
1.5
1
0.5
0
−0.5
−2
−1
0
1
2
3
4
5
6

A-7 3Cu Spring 3.5N in Quasi-Sinusoidal Input 6Hz

A-7.1 Bottom Block

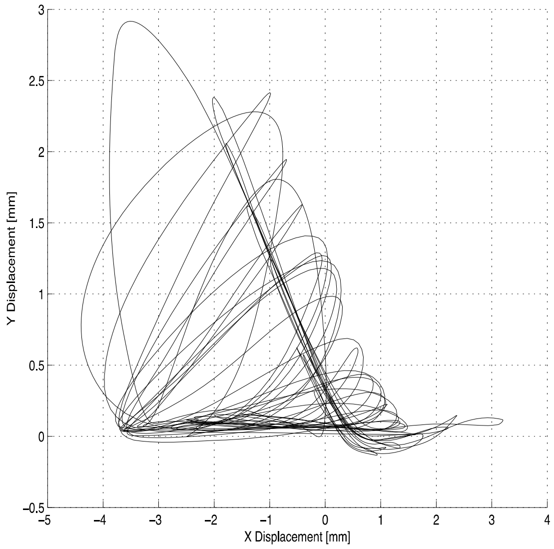

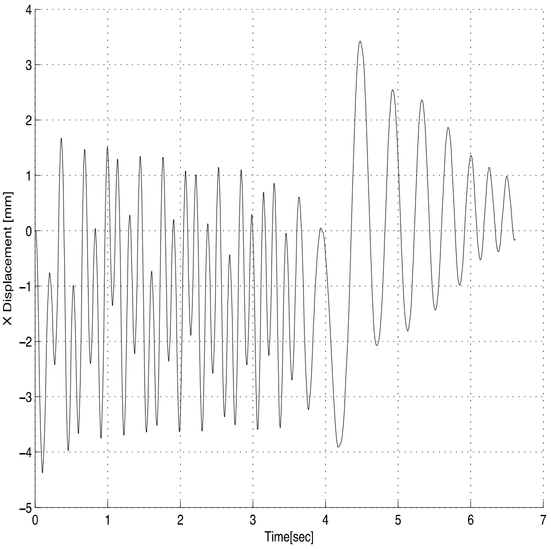

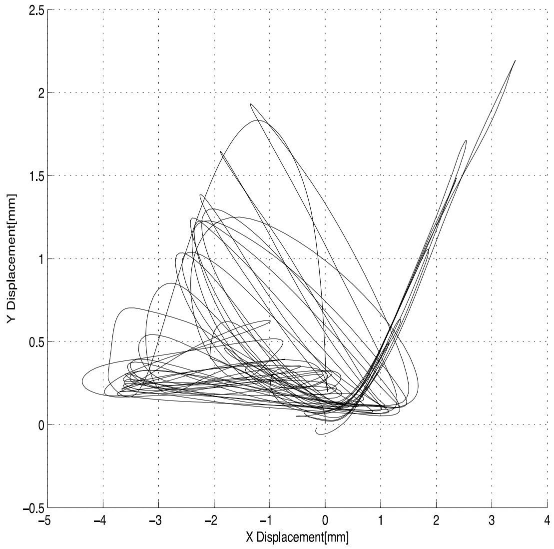

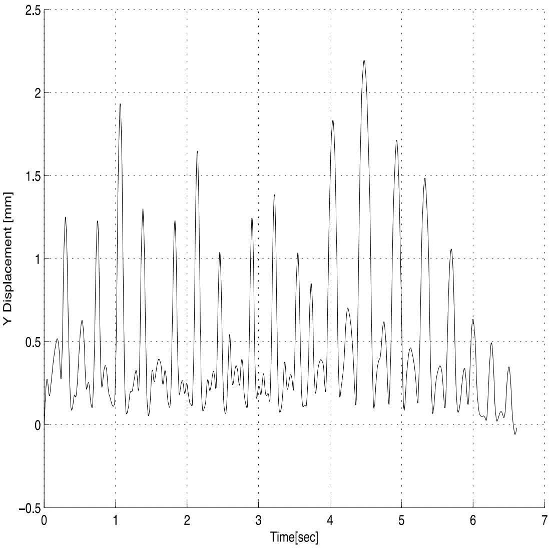

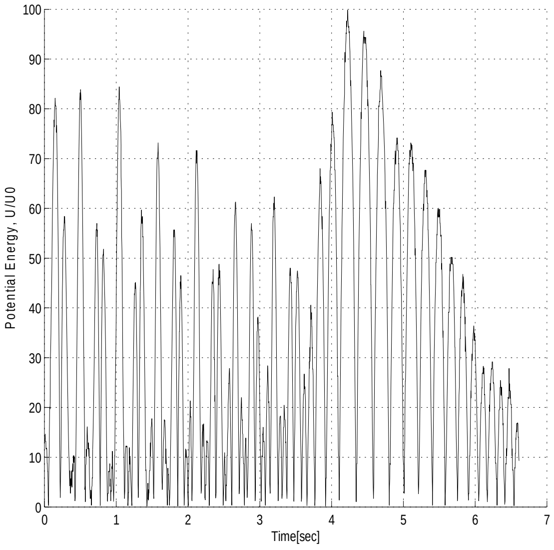

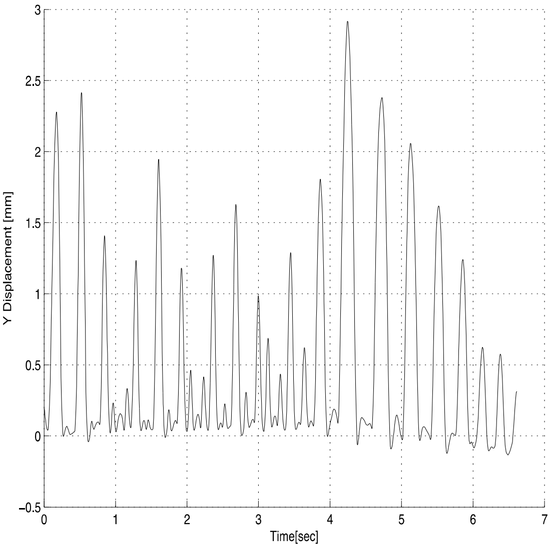

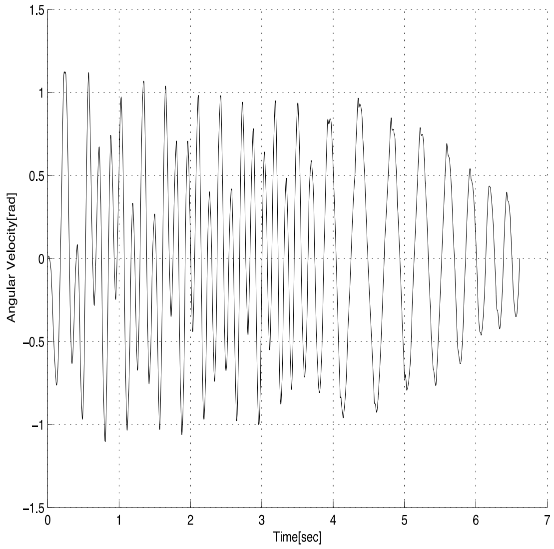
Angular Velocity[rad]
1.5
1
0.5
0
−0.5
−1
−1.5
0
1
2
3
4
5
6
7
Time[sec]

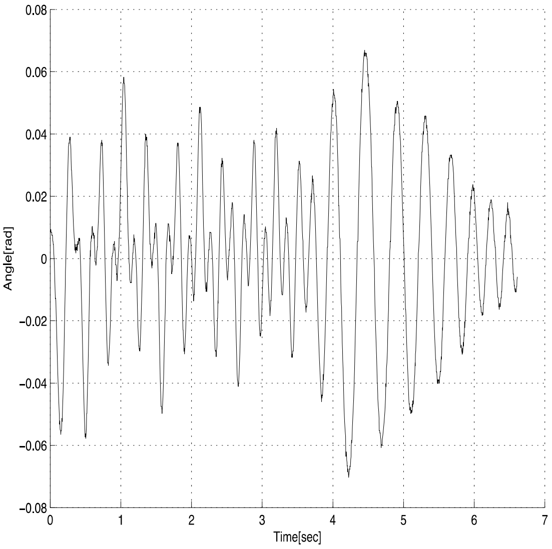
Angle[rad]
0.08
0.06
0.04
0.02
0
−0.02
−0.04
−0.06
−0.08
0
1
2
3
4
5
6
7
Time[sec]

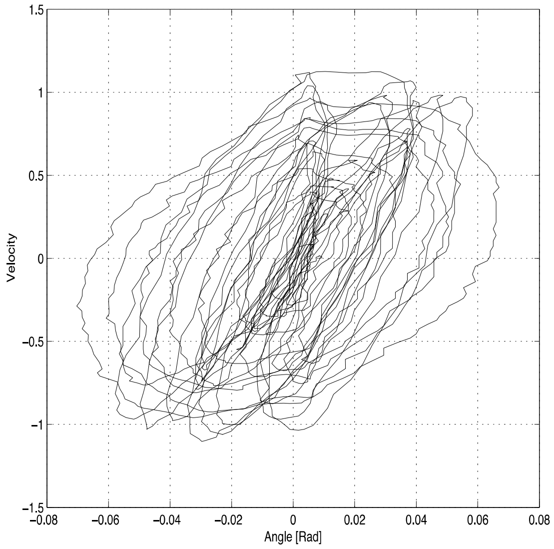
Velocity
1.5
1
0.5
0
−0.5
−1
−1.5
−0.08
−0.06
−0.04
−0.02
0
0.02
0.04
0.06
0.08
Angle [Rad]

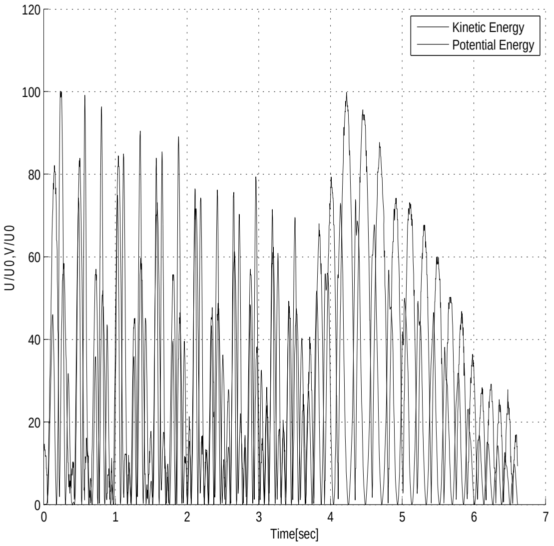
Kinetic Energy
Potential Energy
U/U0,V/U0
120
100
80
60
40
20
0
0
1
2
3
4
5
6
7
Time[sec]

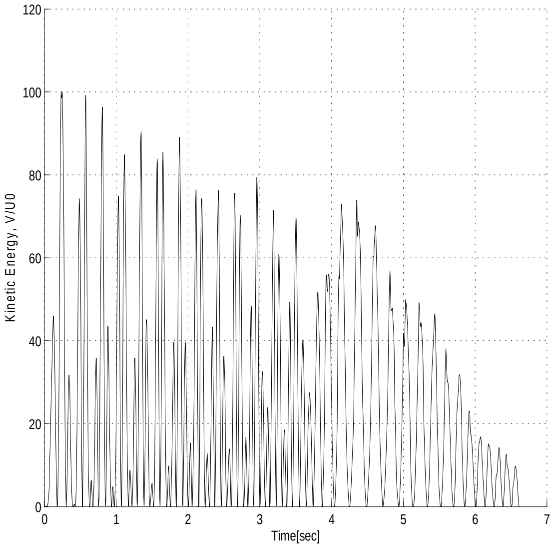
Kinetic Energy, V/U0
120
100
80
60
40
20
0
0
1
2
3
4
5
6
7
Time[sec]

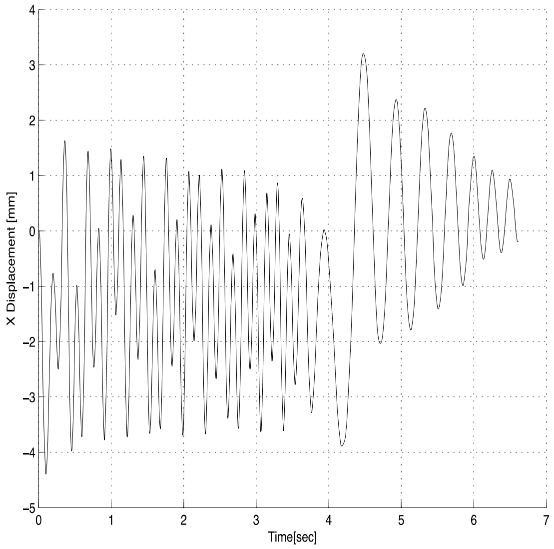
X Displacement [mm]
4
3
2
1
0
−1
−2
−3
−4
−5
0
1
2
3
4
5
6
7
Time[sec]

A-7.2 Middle Block

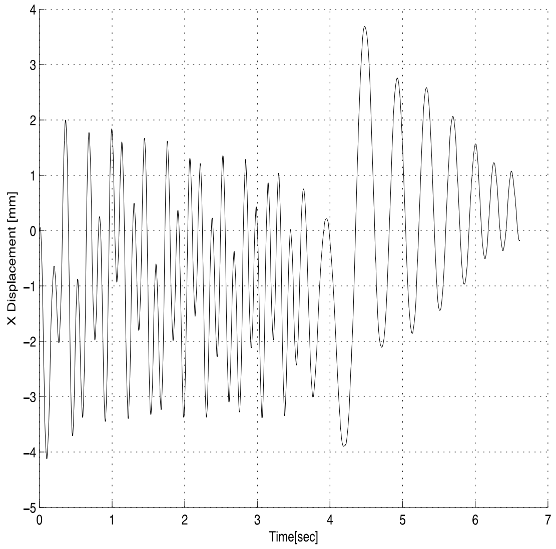

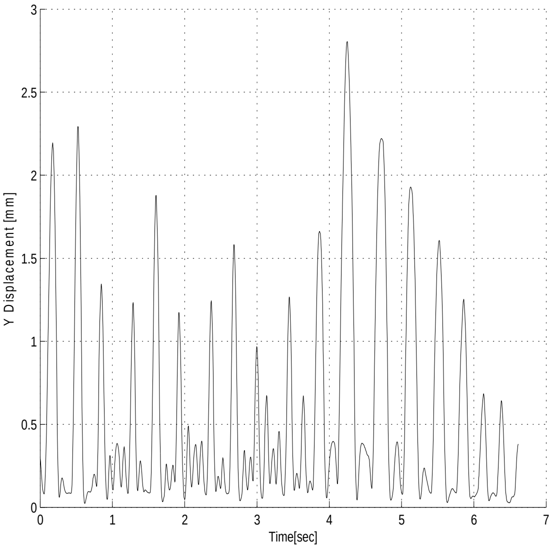

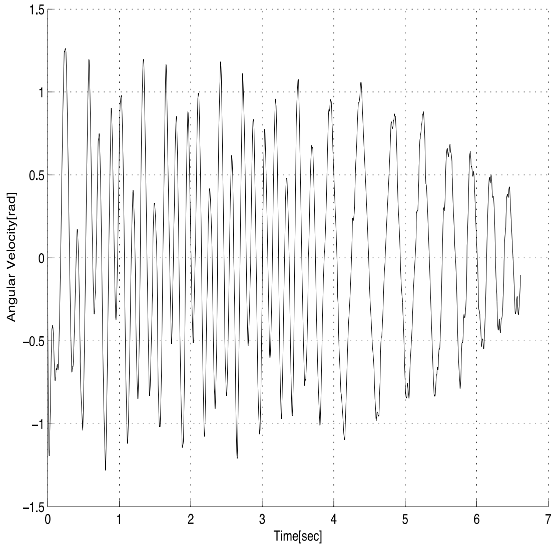

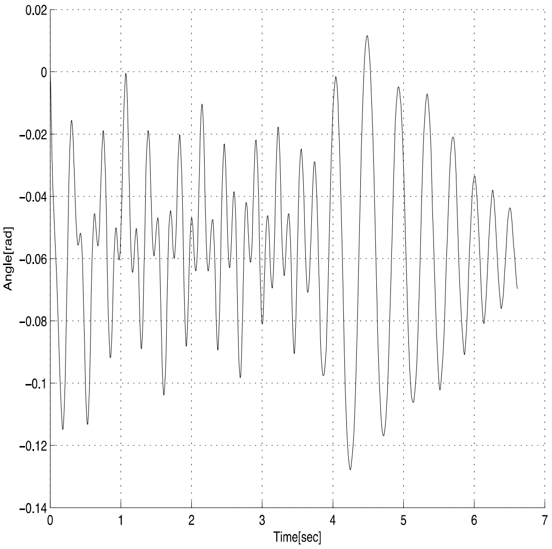

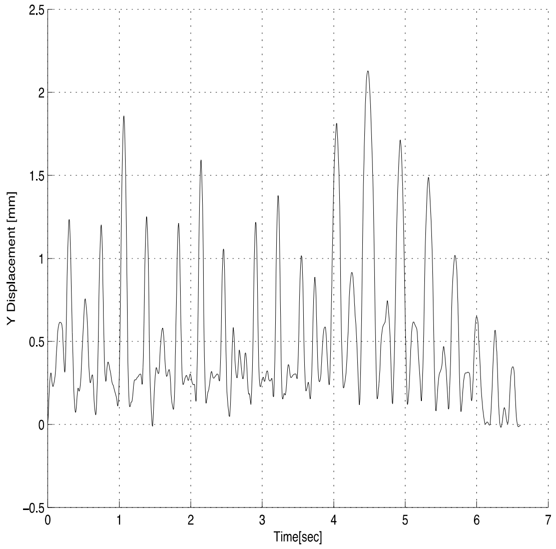

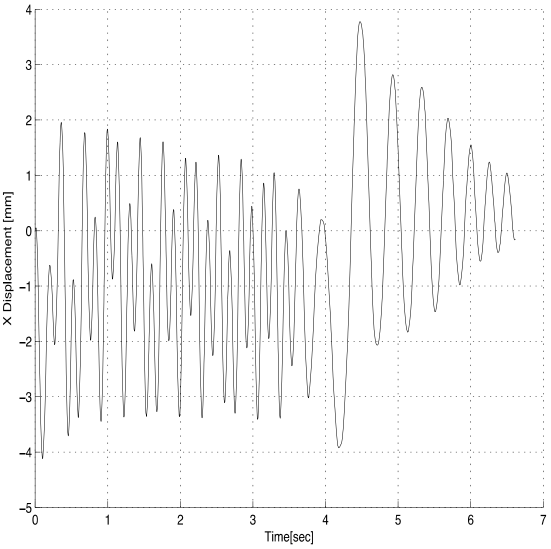

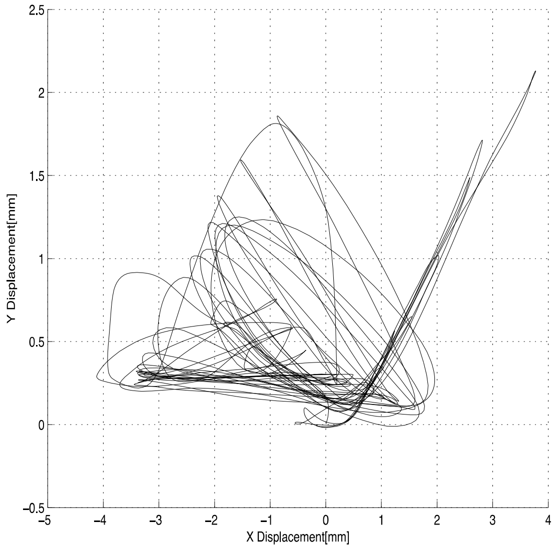
Y Displacement[mm]
X Displacement[mm]
2.5
2
1.5
1
0.5
0
−0.5
−5
−4
−3
−2
−1
0
1
2
3
4

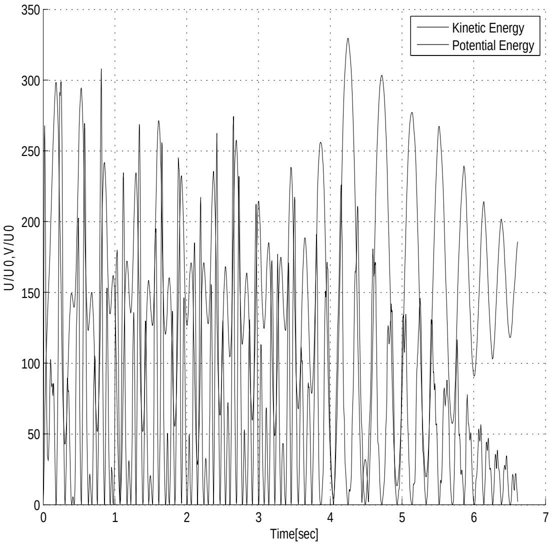
U/U0,V/U0
Time[sec]
Kinetic Energy
Potential Energy
350
300
250
200
150
100
50
0
0
1
2
3
4
5
6
7

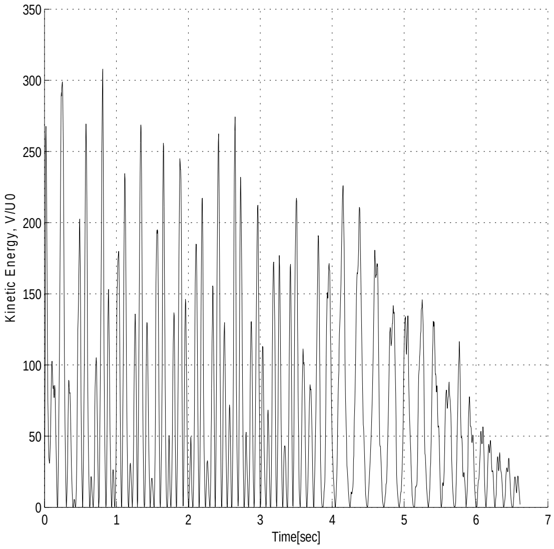
Kinetic Energy, V/U0
Time[sec]
350
300
250
200
150
100
50
0
0
1
2
3
4
5
6
7

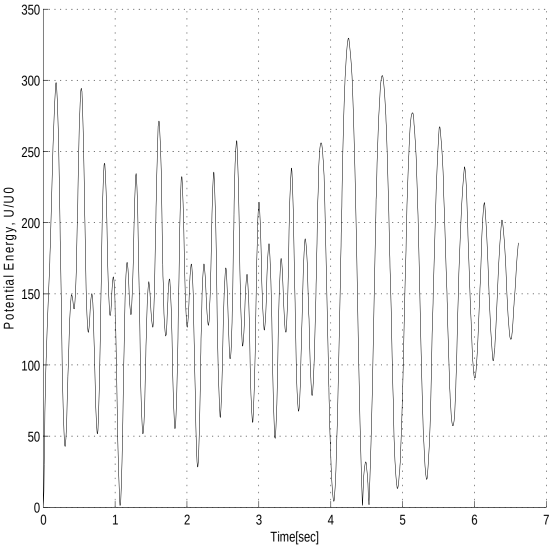
Potential Energy, U/U0
Time[sec]
350
300
250
200
150
100
50
0
0
1
2
3
4
5
6
7

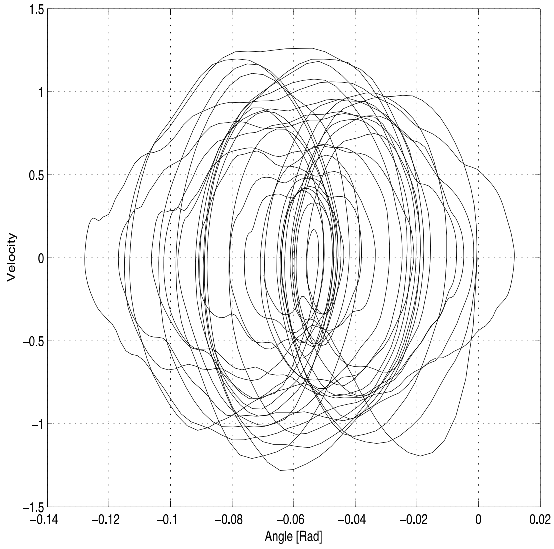
Velocity
Angle [Rad]
1.5
1
0.5
0
−0.5
−1
−1.5
−0.14
−0.12
−0.1
−0.08
−0.06
−0.04
−0.02
0
0.02

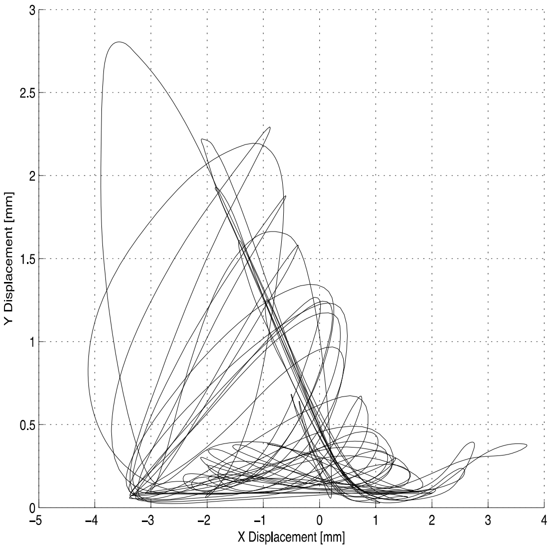
Y Displacement [mm]
X Displacement [mm]
3
2.5
2
1.5
1
0.5
0
−5
−4
−3
−2
−1
0
1
2
3
4

A-8 3Cu Spring 6N in Quasi-Sinusoidal Input 6Hz

A-8.1 Bottom Block

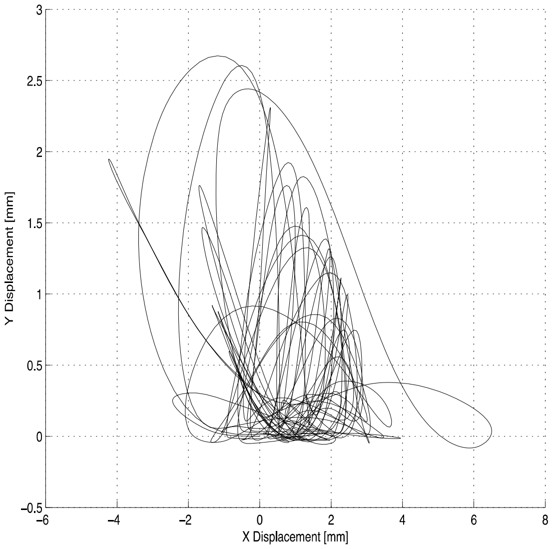

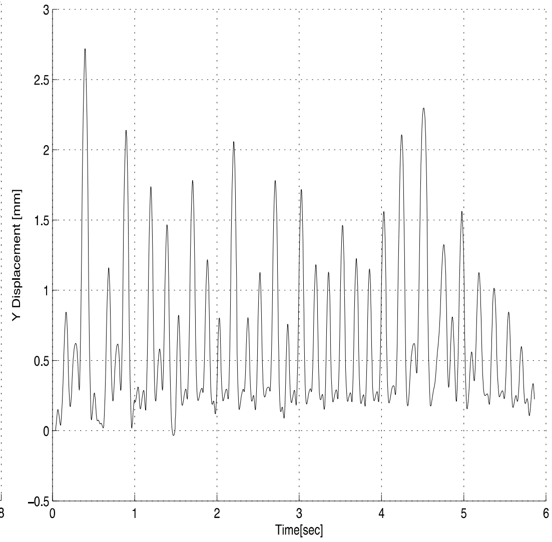

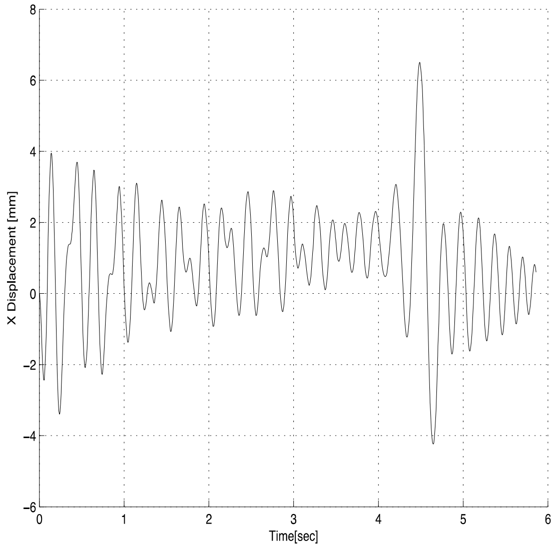

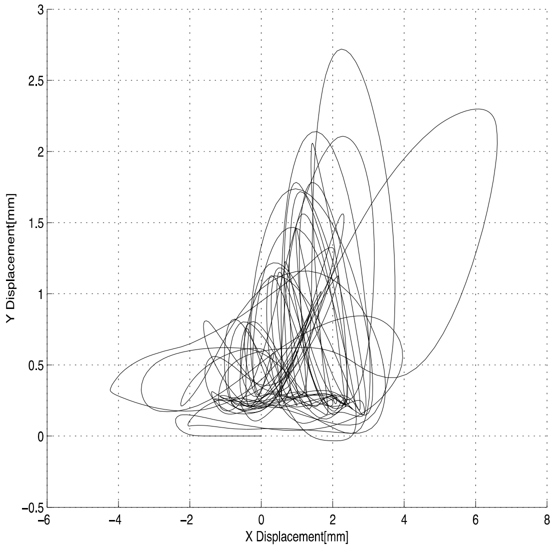

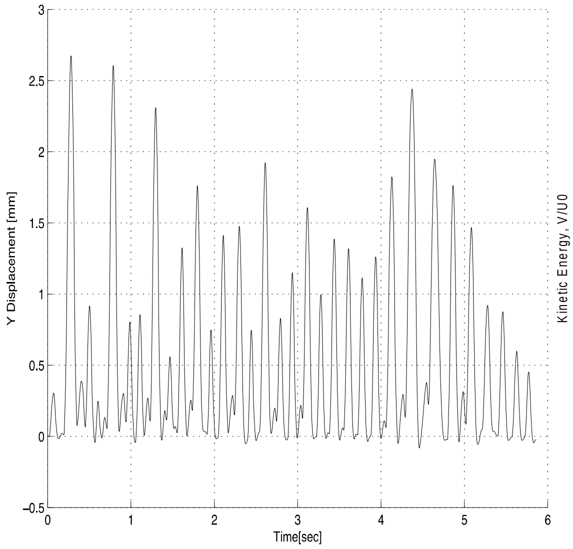

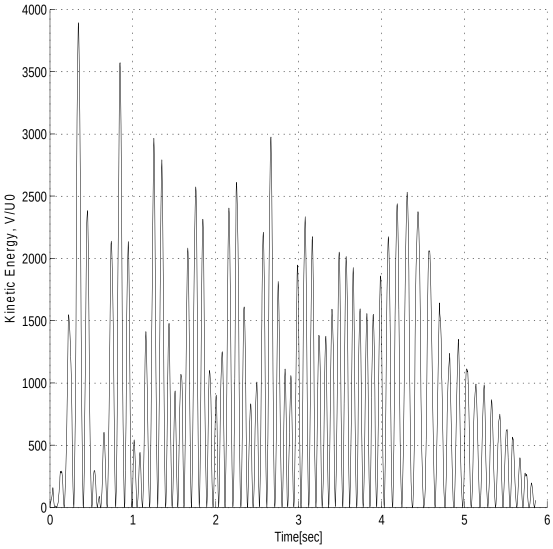

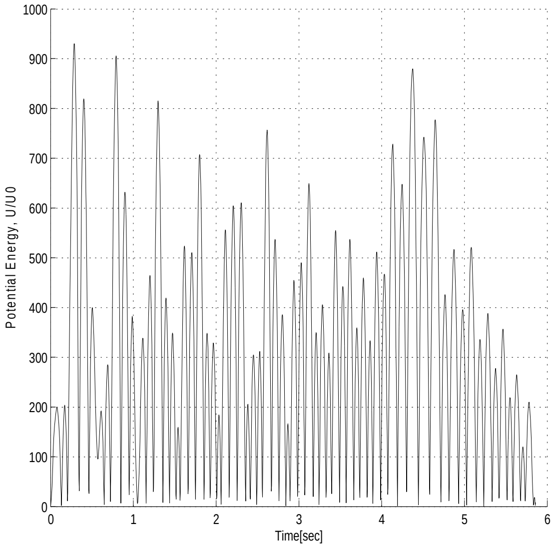
Potential Energy, U/U0
0
100
200
300
400
500
600
700
800
900
1000
Time[sec]
0
1
2
3
4
5
6

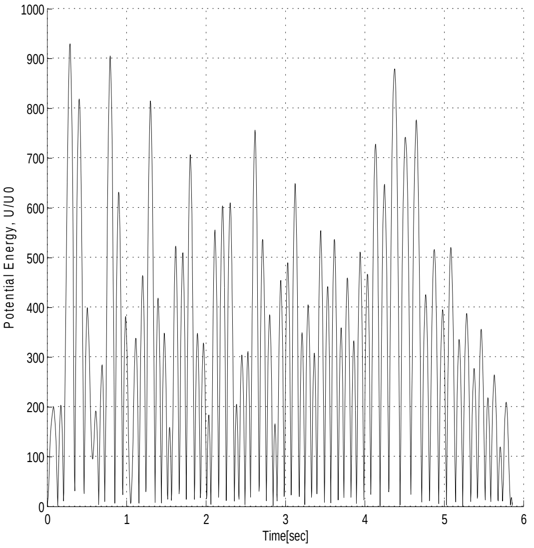
Potential Energy, U/U0
0
100
200
300
400
500
600
700
800
900
1000
Time[sec]
0
1
2
3
4
5
6

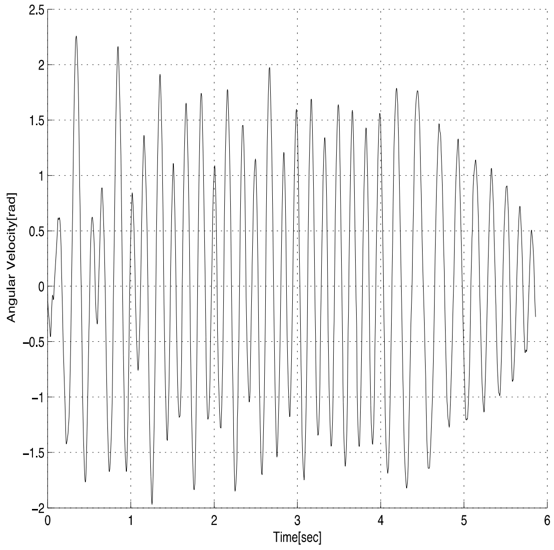
Angular Velocity[rad]
−2
−1.5
−1
−0.5
0
0.5
1
1.5
2
2.5
Time[sec]
0
1
2
3
4
5
6

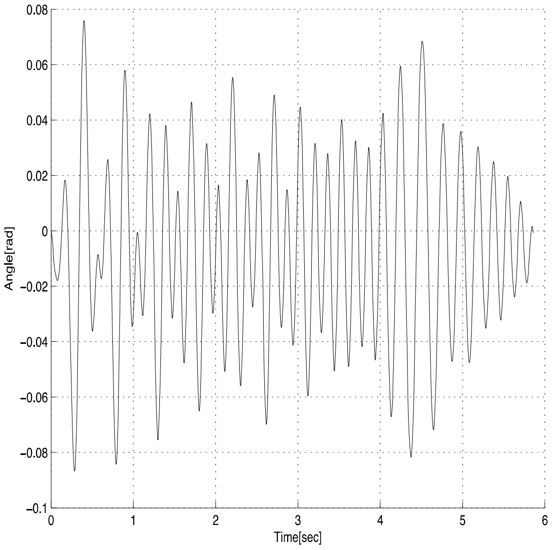
Angle[rad]
−0.1
−0.08
−0.06
−0.04
−0.02
0
0.02
0.04
0.06
0.08
Time[sec]
0
1
2
3
4
5
6

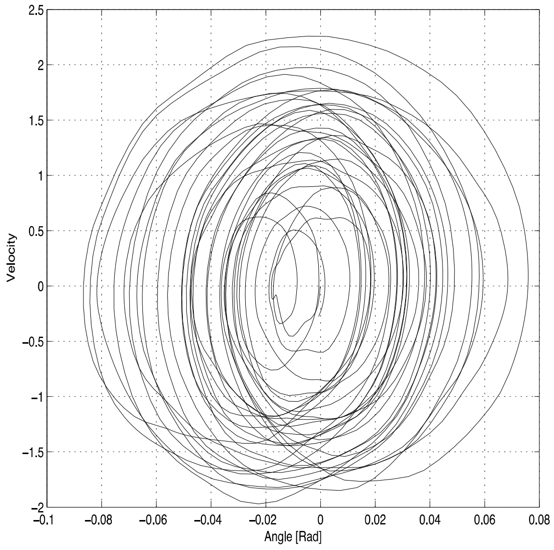
Velocity
−2
−1.5
−1
−0.5
0
0.5
1
1.5
2
2.5
Angle [Rad]
−0.1
−0.08
−0.06
−0.04
−0.02
0
0.02
0.04
0.06
0.08

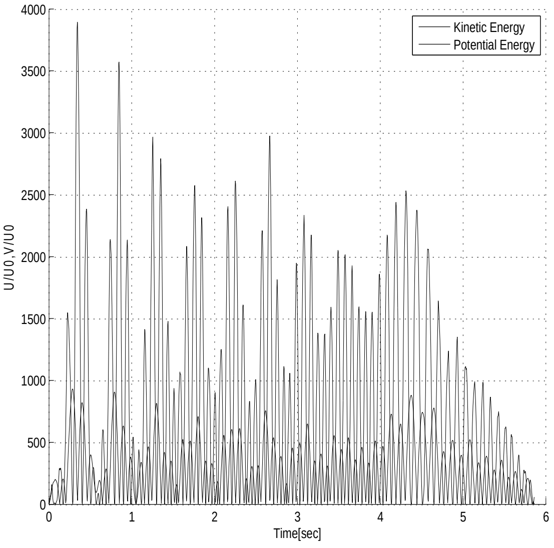
Kinetic Energy
Potential Energy
U/U0, V/U0
0
500
1000
1500
2000
2500
3000
3500
4000
Time[sec]
0
1
2
3
4
5
6

A-9 3Rect Spring 6N in Quasi-Sinusoidal Input 3.5Hz

A-9.1 Bottom Block

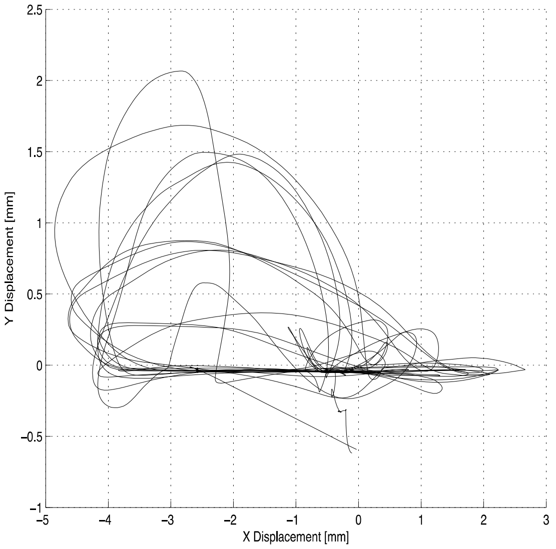

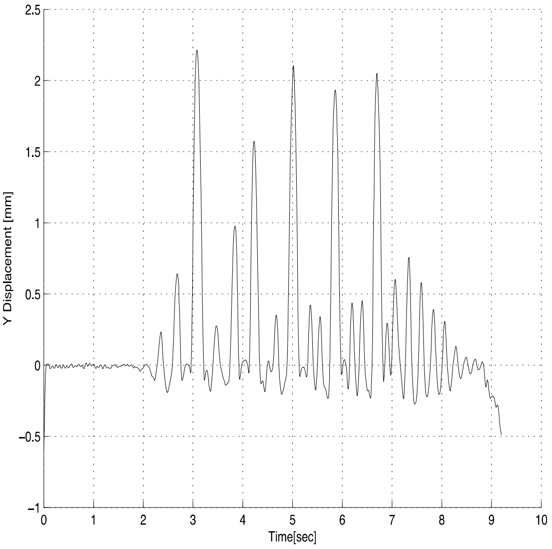

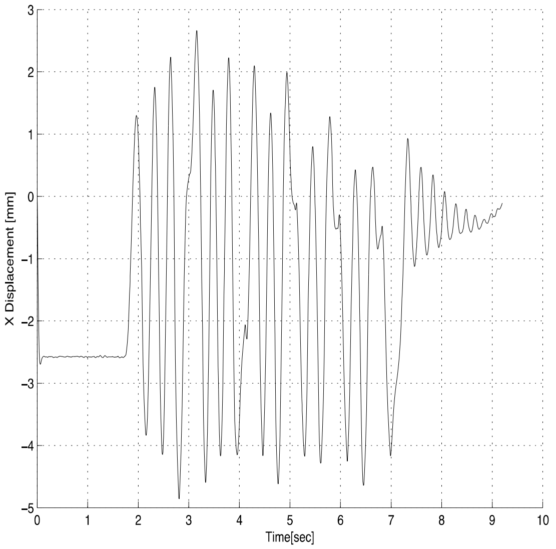

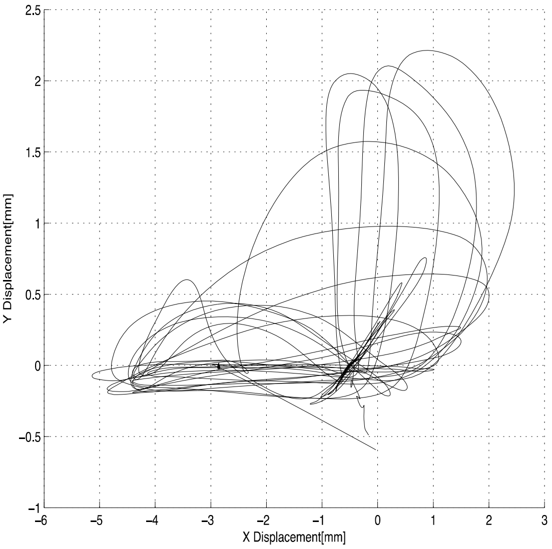

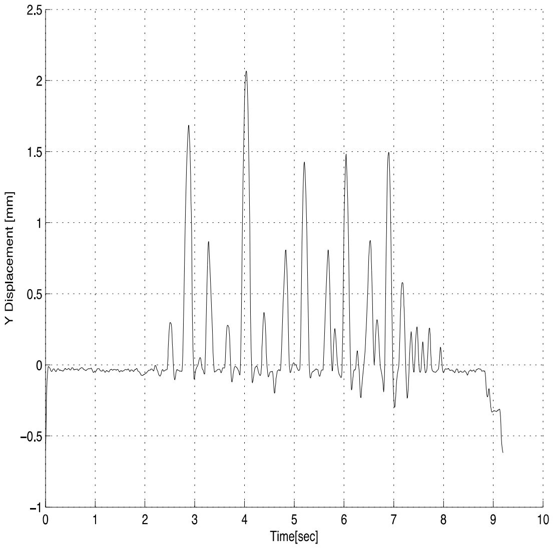

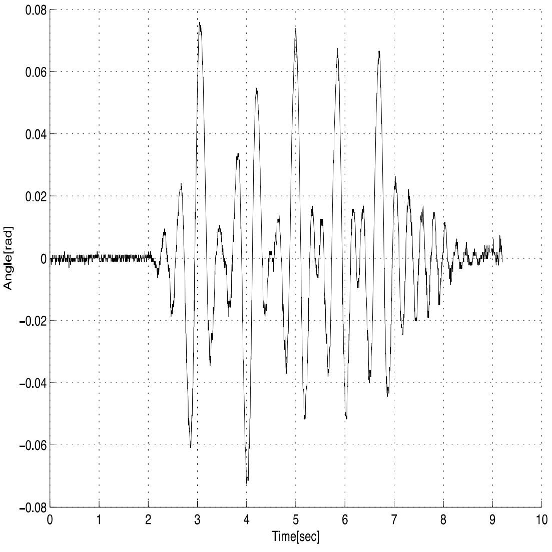

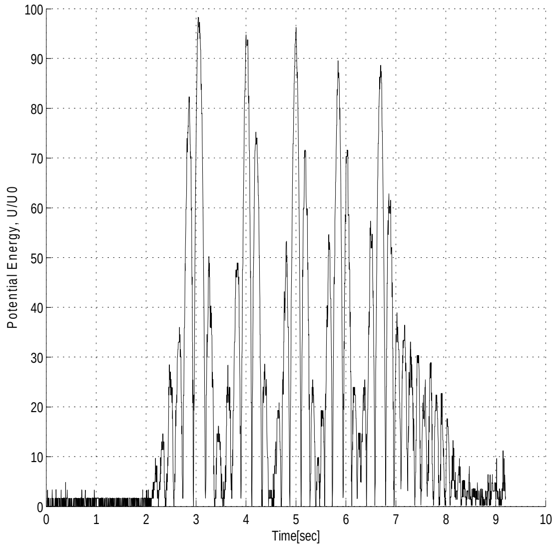
Potential Energy, U/U0
Time[sec]
0
10
20
30
40
50
60
70
80
90
100
0
1
2
3
4
5
6
7
8
9
10

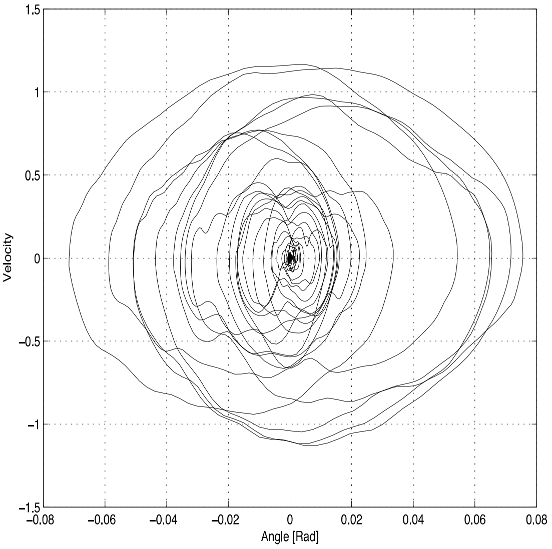
Velocity
Angle [Rad]
1.5
1
0.5
0
−0.5
−1
−1.5
−0.08
−0.06
−0.04
−0.02
0
0.02
0.04
0.06
0.08

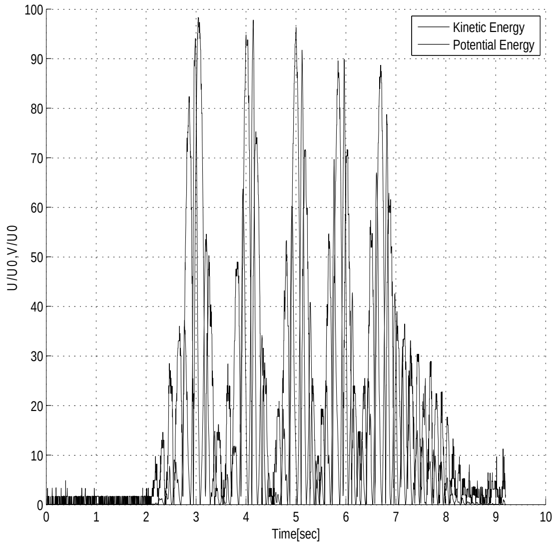
U/U0,V/U0
Time[sec]
Kinetic Energy
Potential Energy
0
10
20
30
40
50
60
70
80
90
100
0
1
2
3
4
5
6
7
8
9
10

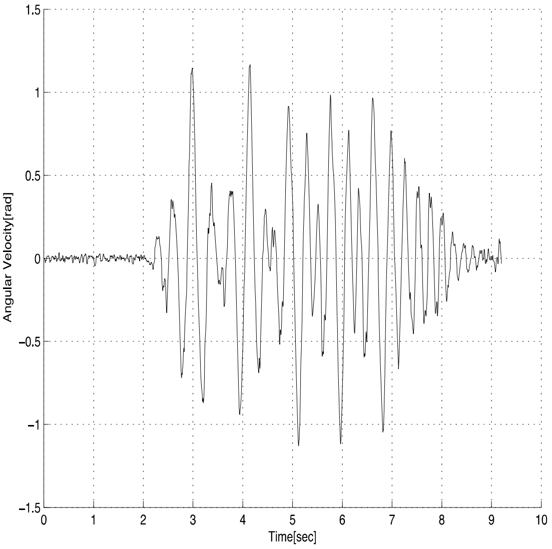
Angular Velocity[rad]
Time[sec]
1.5
1
0.5
0
−0.5
−1
−1.5
0
1
2
3
4
5
6
7
8
9
10

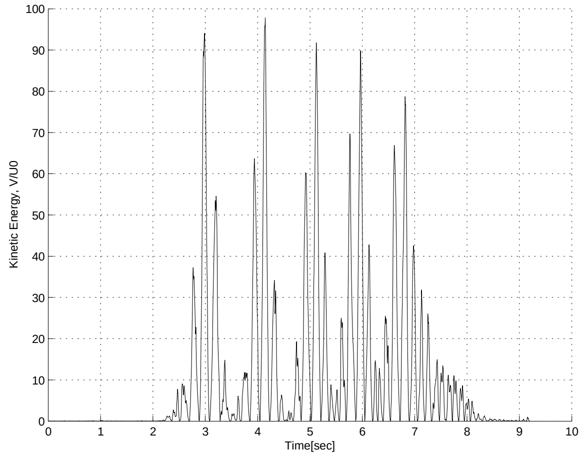
Kinetic Energy, V/U0
Time[sec]
0
10
20
30
40
50
60
70
80
90
100
0
1
2
3
4
5
6
7
8
9
10

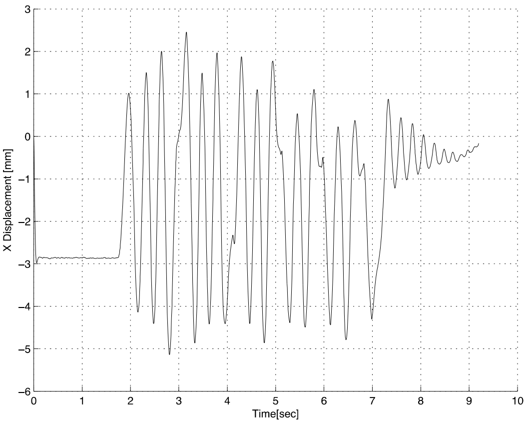
X Displacement [mm]
Time[sec]
3
2
1
0
−1
−2
−3
−4
−5
−6
0
1
2
3
4
5
6
7
8
9
10

A-9.2 Middle Block

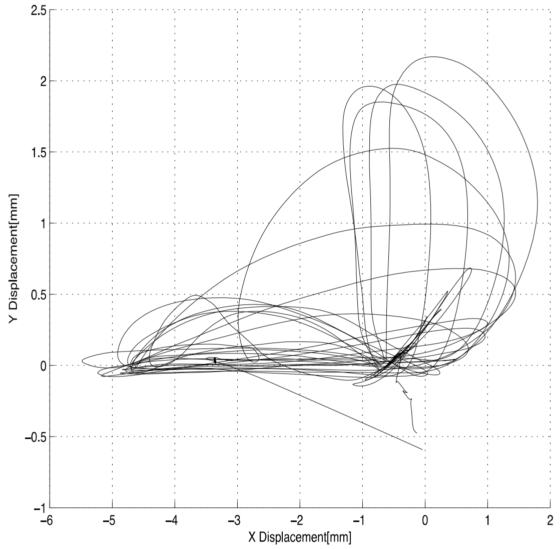

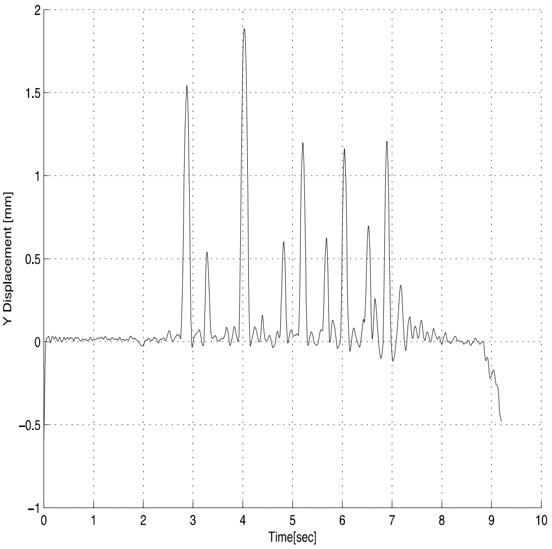

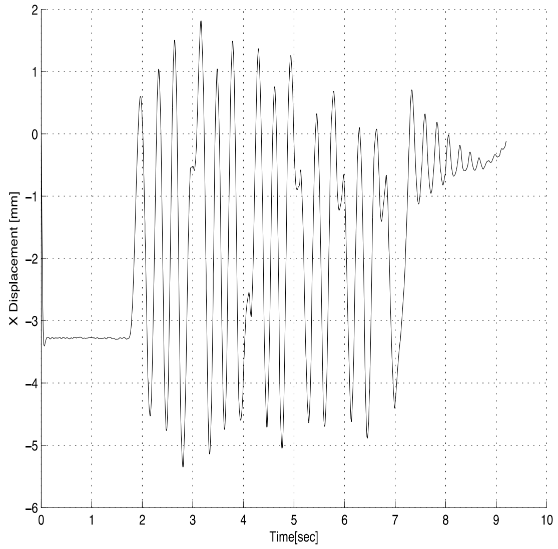

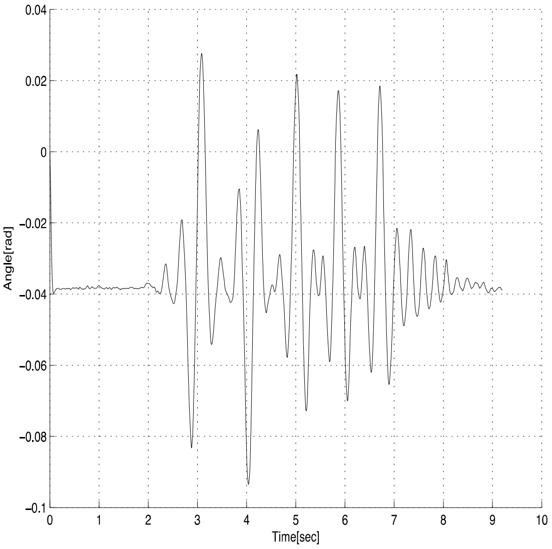

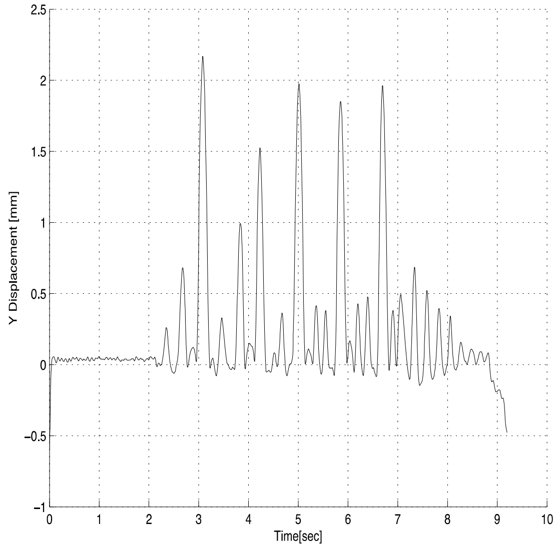

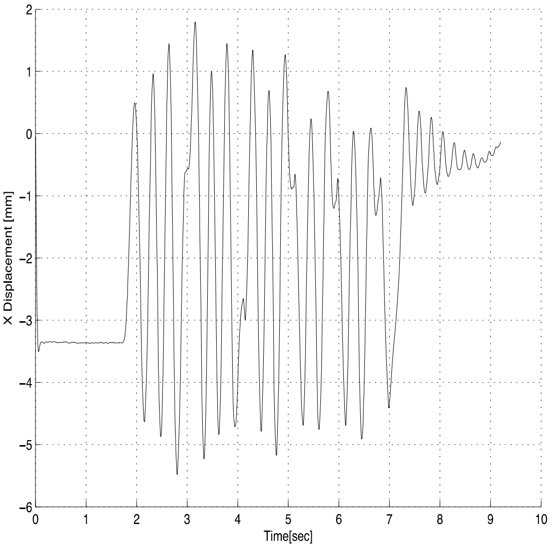

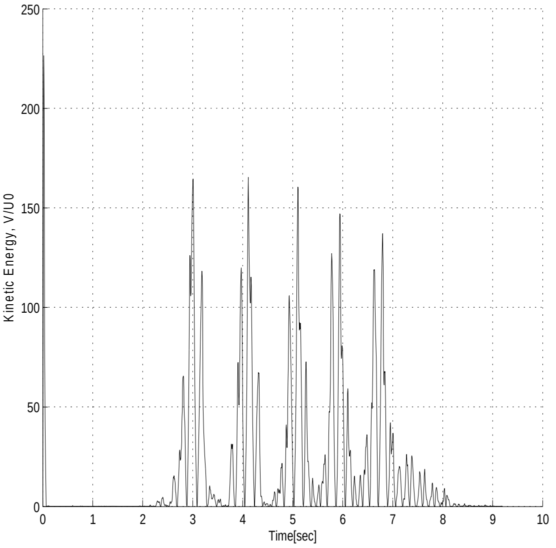
Kinetic Energy, V/U0
250
200
150
100
50
0
0
1
2
3
4
5
6
7
8
9
10
Time[sec]

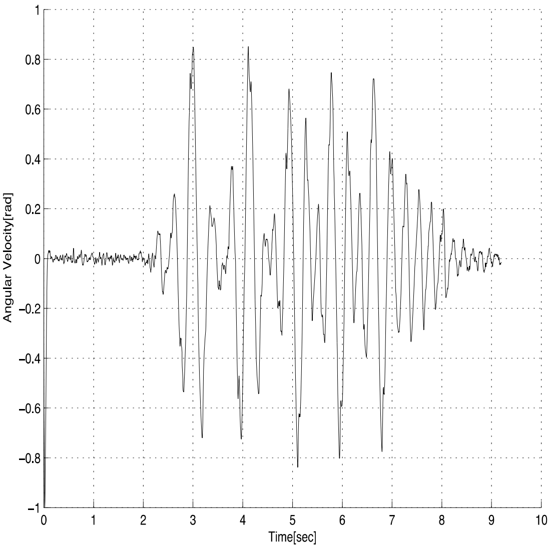
Angular Velocity[rad]
1
0.8
0.6
0.4
0.2
0
−0.2
−0.4
−0.6
−0.8
−1
0
1
2
3
4
5
6
7
8
9
10
Time[sec]

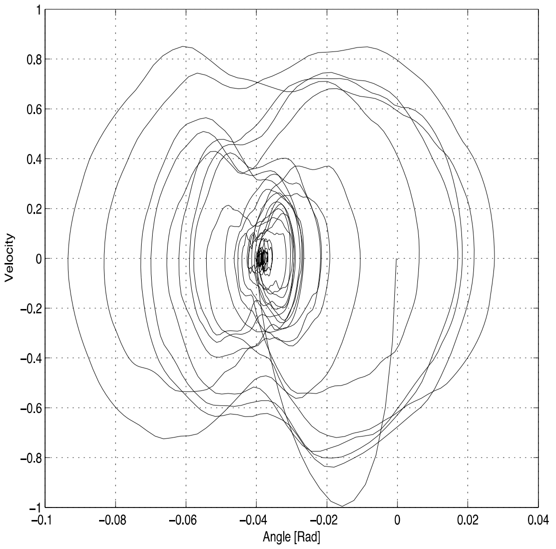
Velocity
1
0.8
0.6
0.4
0.2
0
−0.2
−0.4
−0.6
−0.8
−1
−0.1
−0.08
−0.06
−0.04
−0.02
0
0.02
0.04
Angle [Rad]

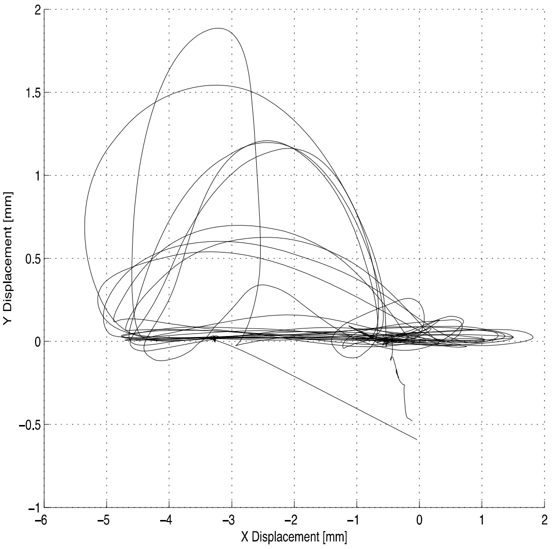
Y Displacement [mm]
2
1.5
1
0.5
0
−0.5
−1
−6
−5
−4
−3
−2
−1
0
1
2
X Displacement [mm]

A-10 3Rect Spring 6N in Quasi-Sinusoidal Input 4Hz

A-10.1 Bottom Block

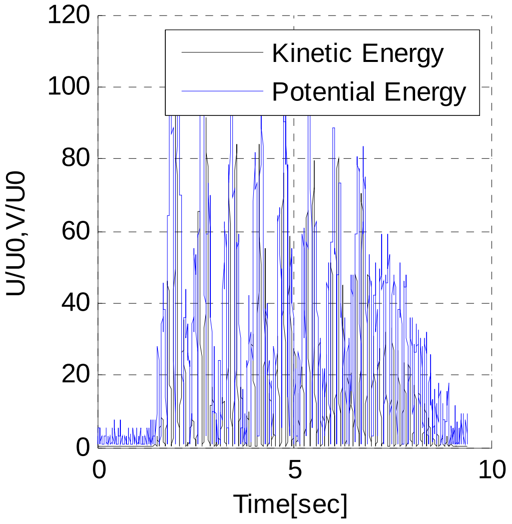

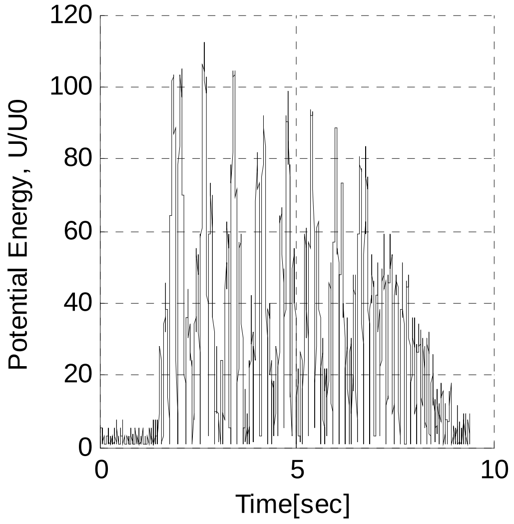

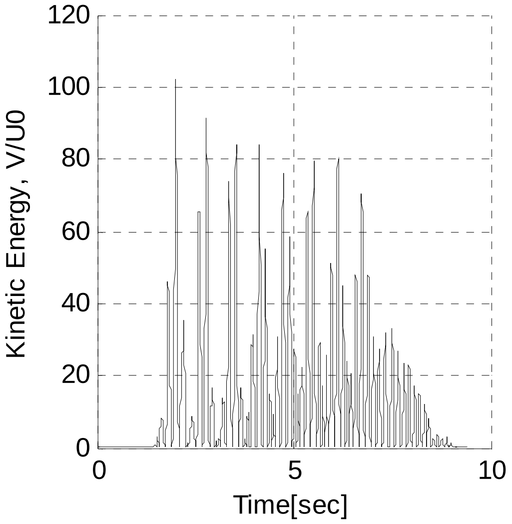

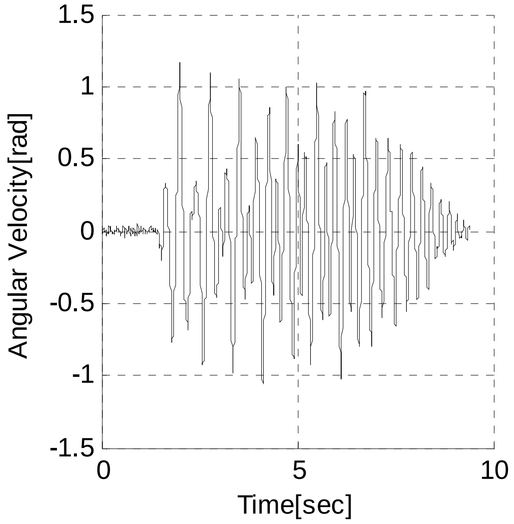

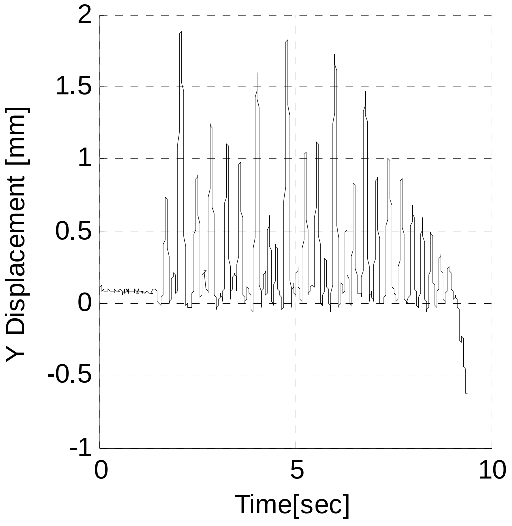

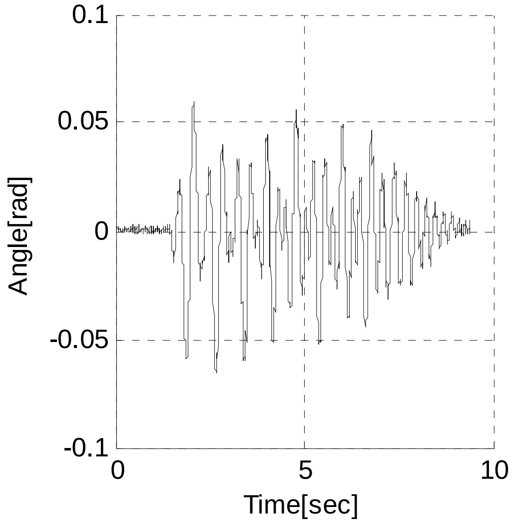

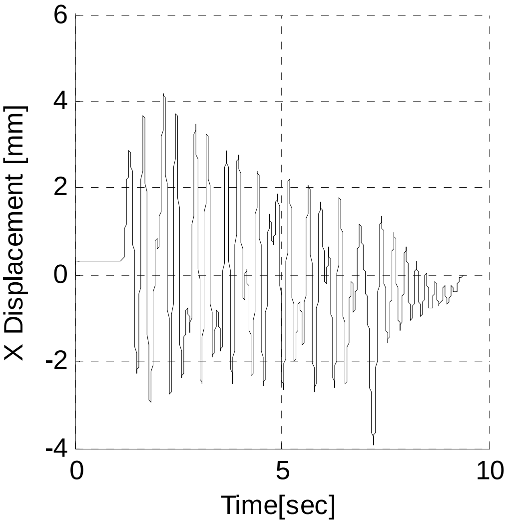
X Displacement [mm]
6
4
2
0
-2
-4
0
5
10
Time[sec]

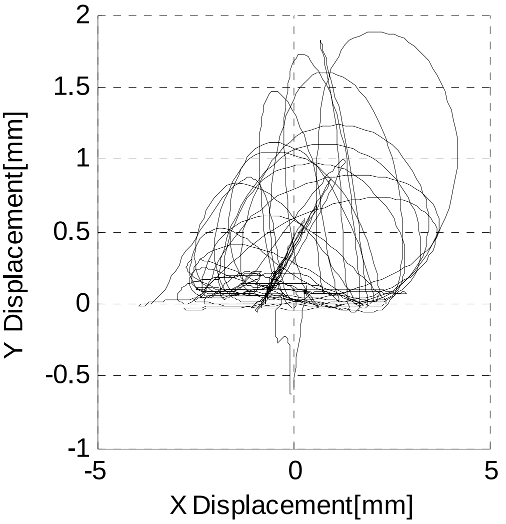
Y Displacement[mm]
2
1.5
1
0.5
0
-0.5
-1
-5
0
5
X Displacement[mm]

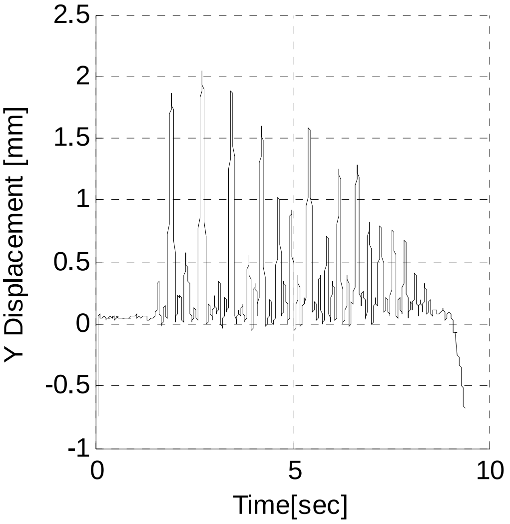
Y Displacement [mm]
2.5
2
1.5
1
0.5
0
-0.5
-1
0
5
10
Time[sec]

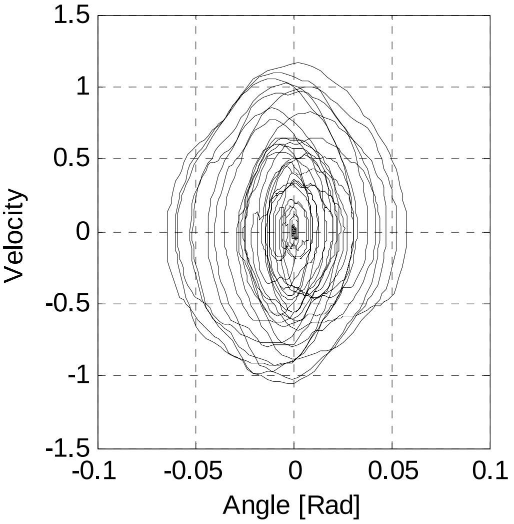
Velocity
1.5
1
0.5
0
-0.5
-1
-1.5
-0.1
-0.05
0
0.05
0.1
Angle [Rad]

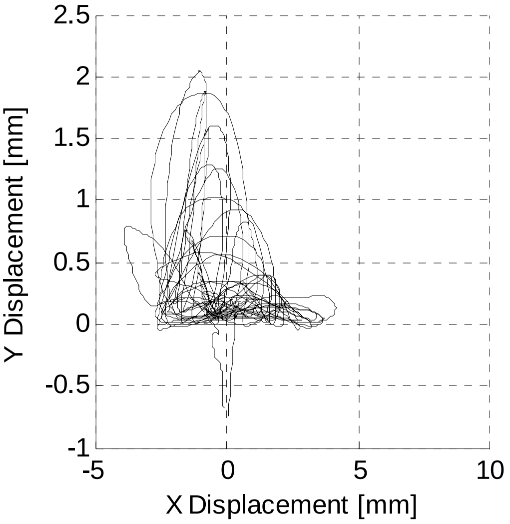
Y Displacement [mm]
2.5
2
1.5
1
0.5
0
-0.5
-1
-5
0
5
10
X Displacement [mm]

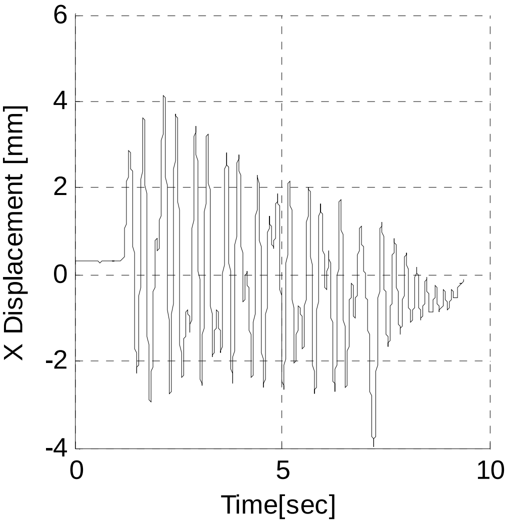
X Displacement [mm]
6
4
2
0
-2
-4
0
5
10
Time[sec]

A-10.2 Middle Block

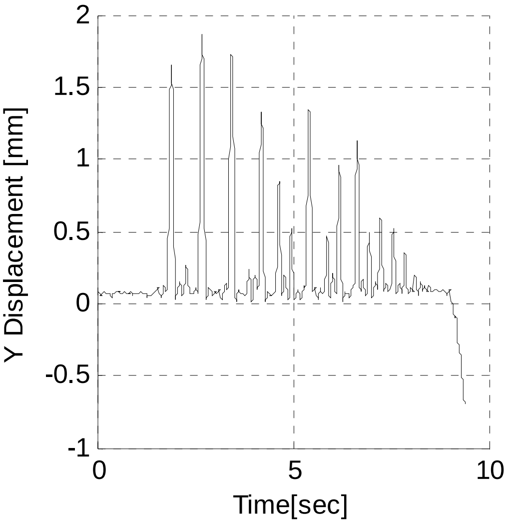

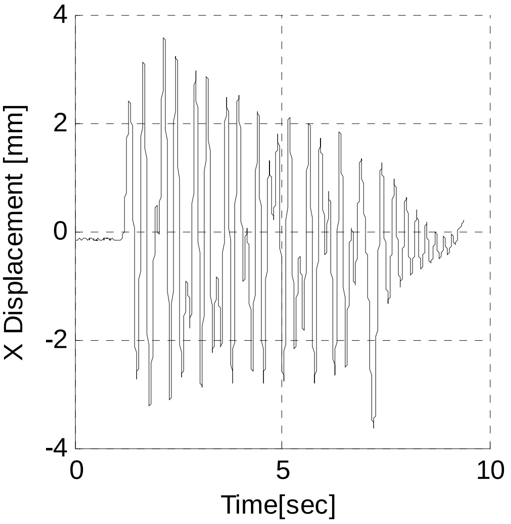

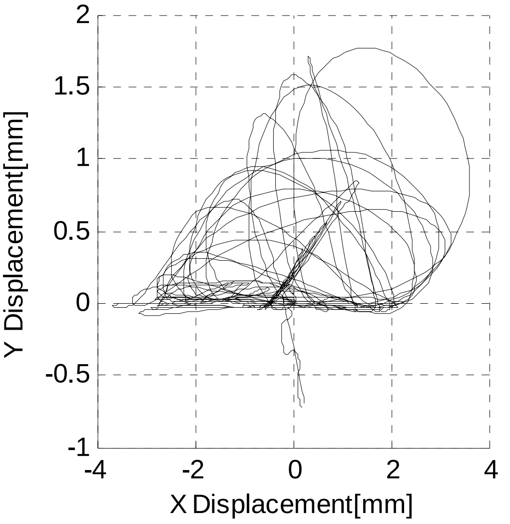

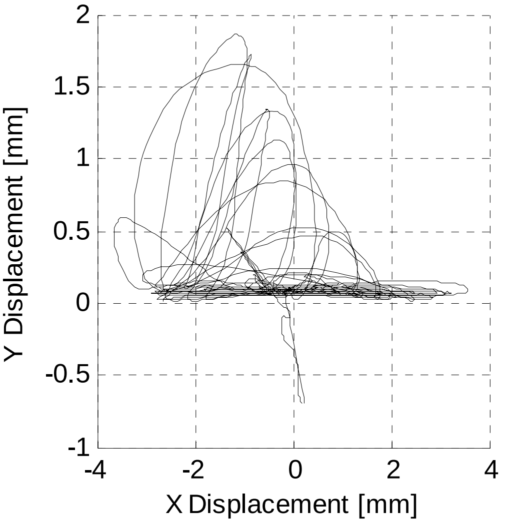

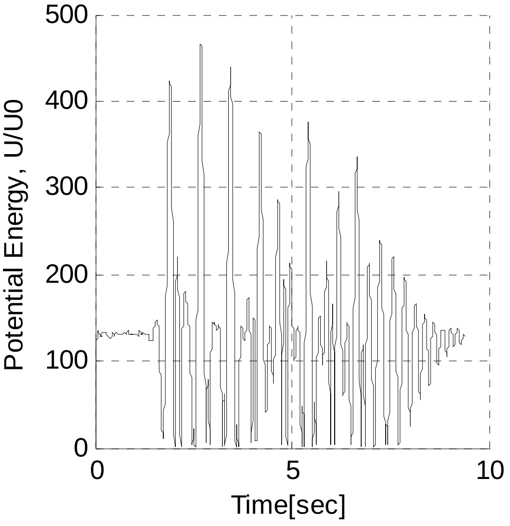

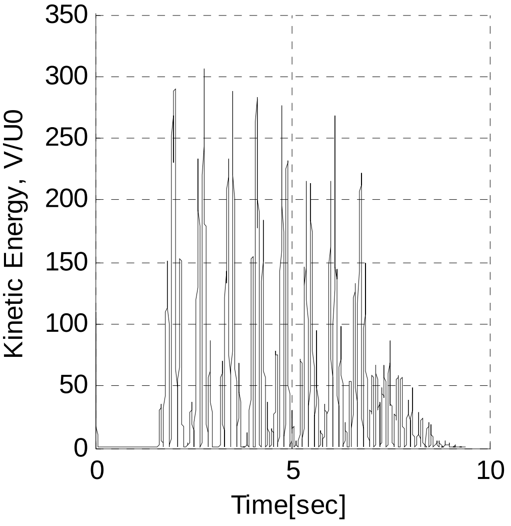

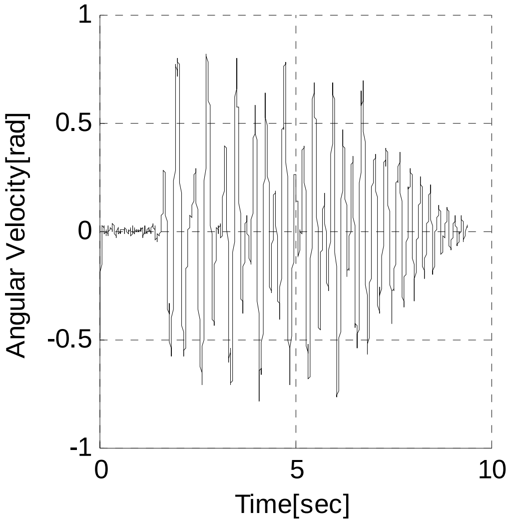
Angular Velocity[rad]
Time[sec]
1
0.5
0
-0.5
-1
0
5
10

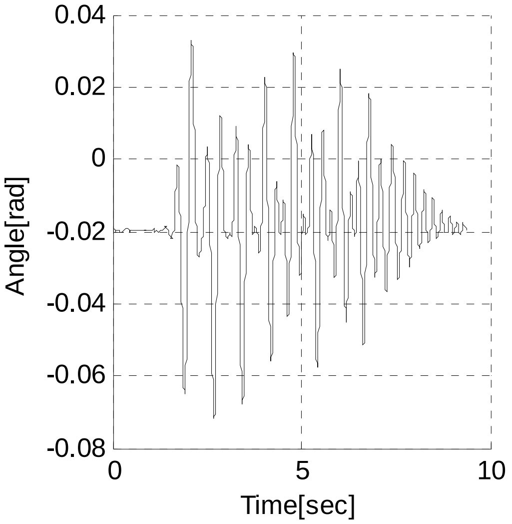
Angle[rad]
Time[sec]
0.04
0.02
0
-0.02
-0.04
-0.06
-0.08
0
5
10

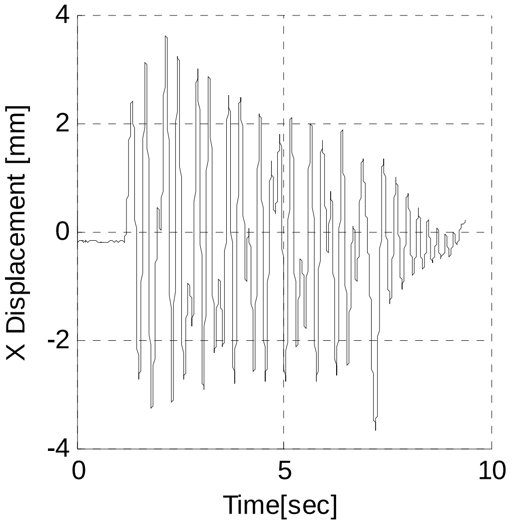
X Displacement [mm]
Time[sec]
4
2
0
-2
-4
0
5
10

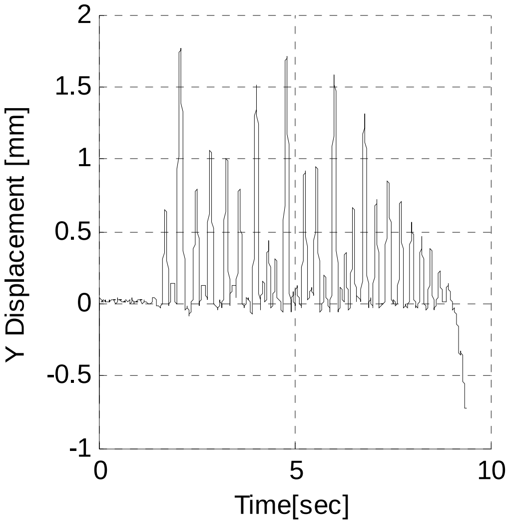
Y Displacement [mm]
Time[sec]
2
1.5
1
0.5
0
-0.5
-1
0
5
10

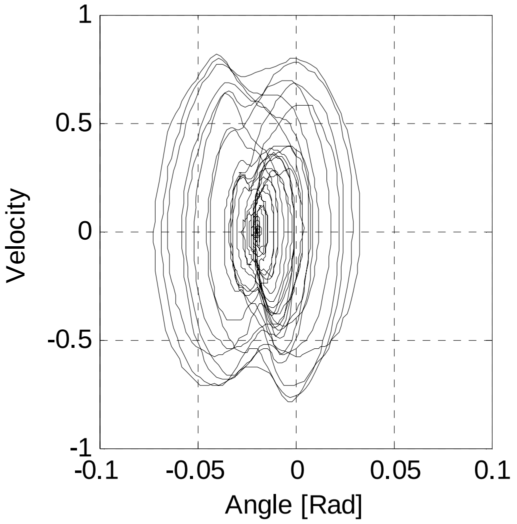
Velocity
Angle [Rad]
1
0.5
0
-0.5
-1
-0.1
-0.05
0
0.05
0.1

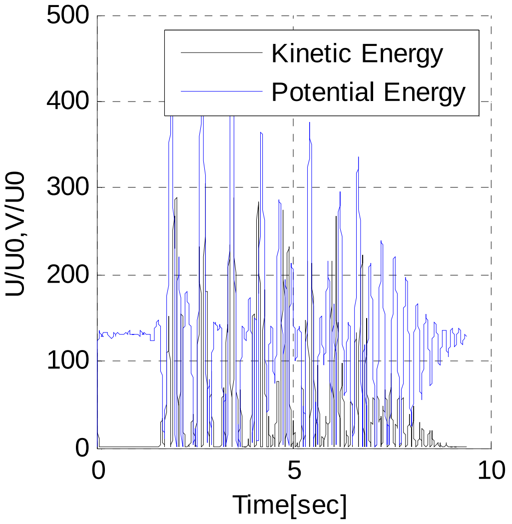
U/U0,V/U0
Time[sec]
Kinetic Energy
Potential Energy
500
400
300
200
100
0
0
5
10

A-11 3Rect Spring 6N in Quasi-Sinusoidal Input 5Hz

A-11.1 Bottom Block

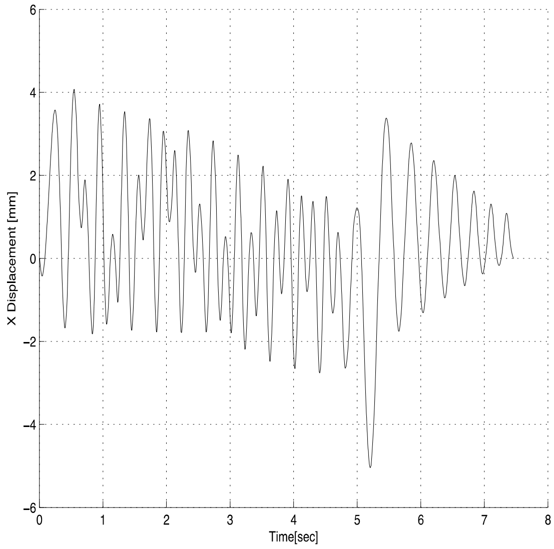

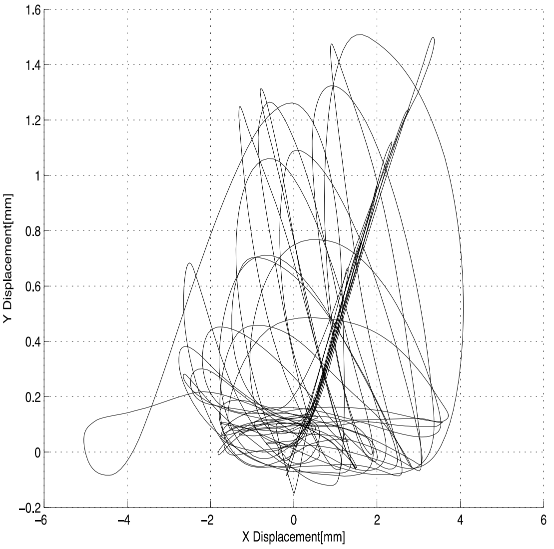

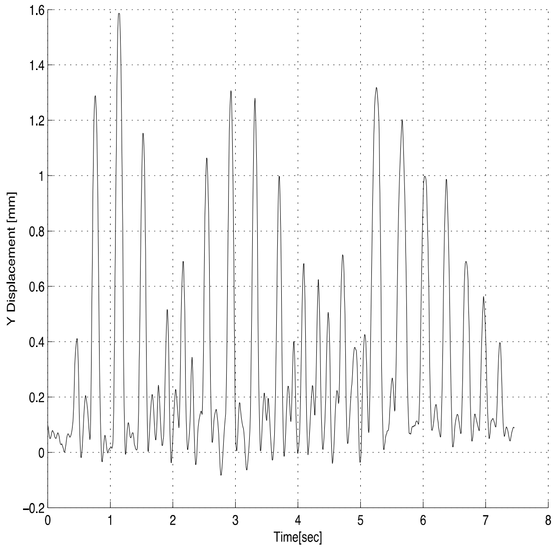

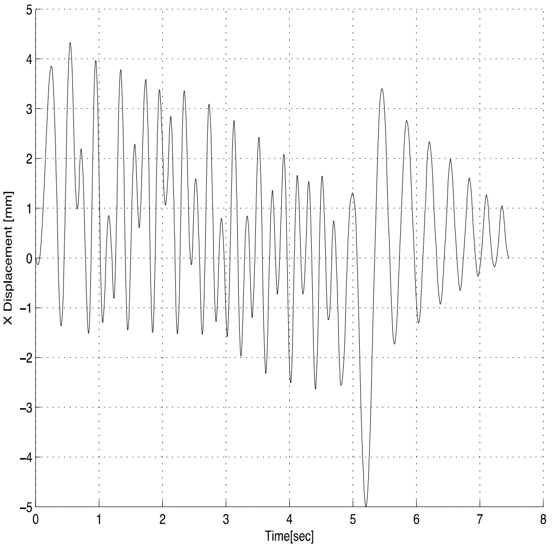

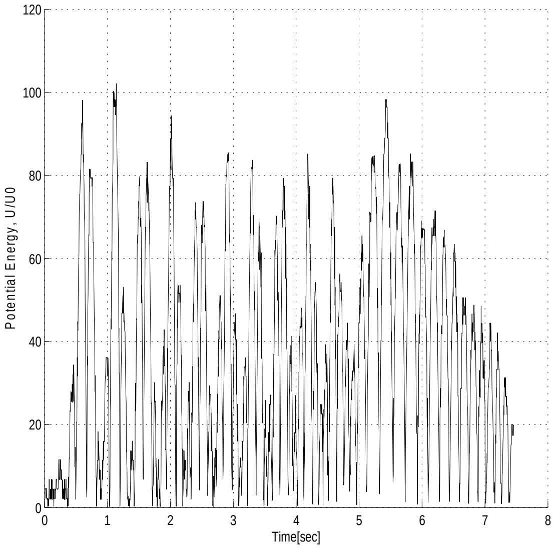

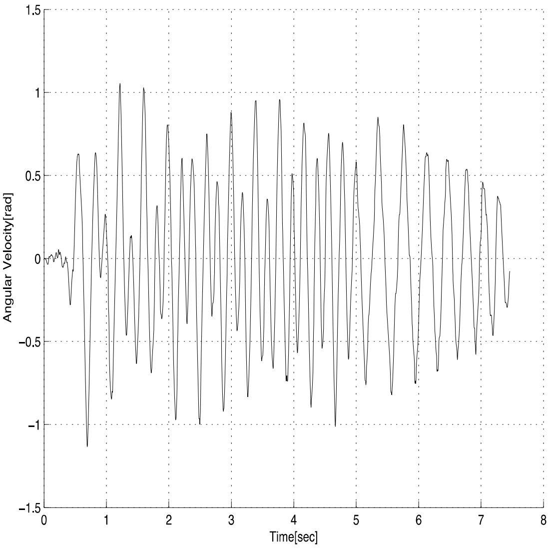

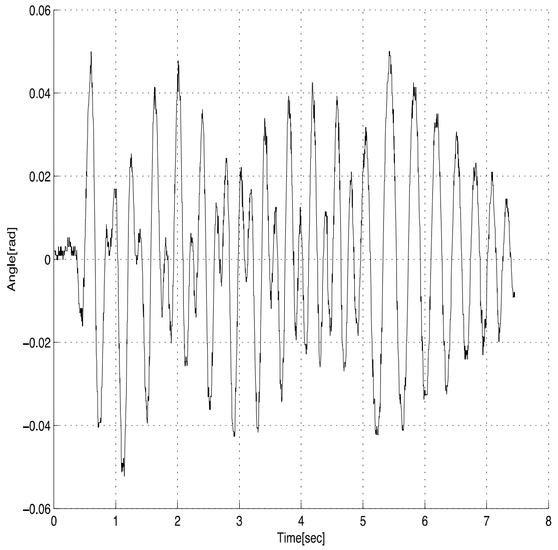
Angle[rad]
Time[sec]
0.06
0.04
0.02
0
−0.02
−0.04
−0.06
0 1 2 3 4 5 6 7 8

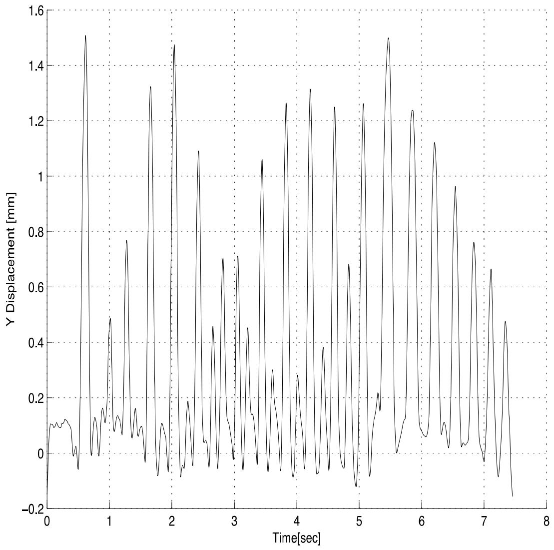
Y Displacement [mm]
Time[sec]
1.6
1.4
1.2
1
0.8
0.6
0.4
0.2
0
−0.2
0 1 2 3 4 5 6 7 8

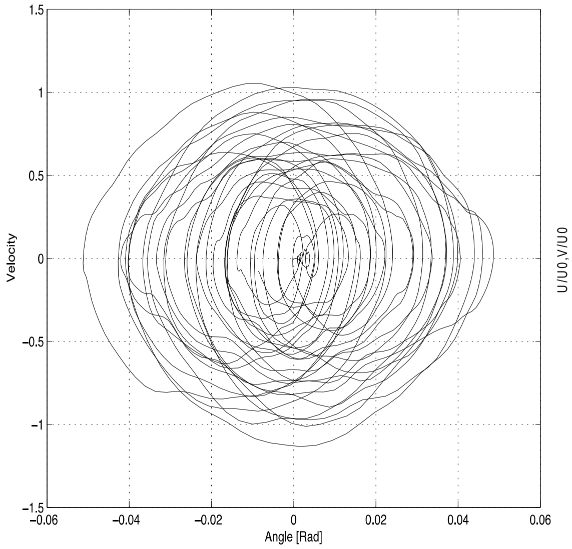
Velocity
Angle [Rad]
1.5
1
0.5
0
−0.5
−1
−1.5
−0.06 −0.04 −0.02 0 0.02 0.04 0.06

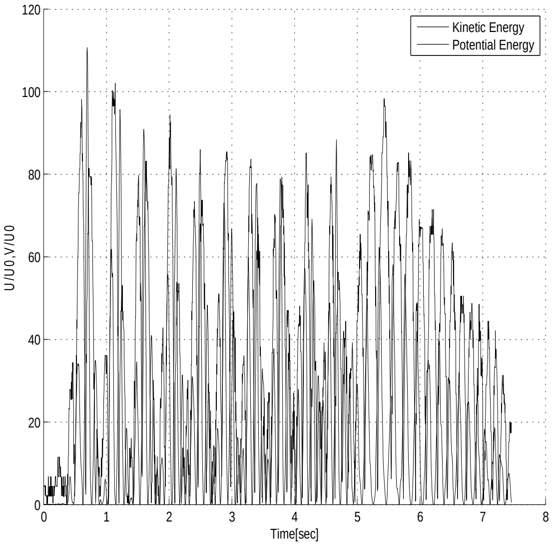
Kinetic Energy
Potential Energy
U/U0,V/U0
Time[sec]
120
100
80
60
40
20
0
0 1 2 3 4 5 6 7 8

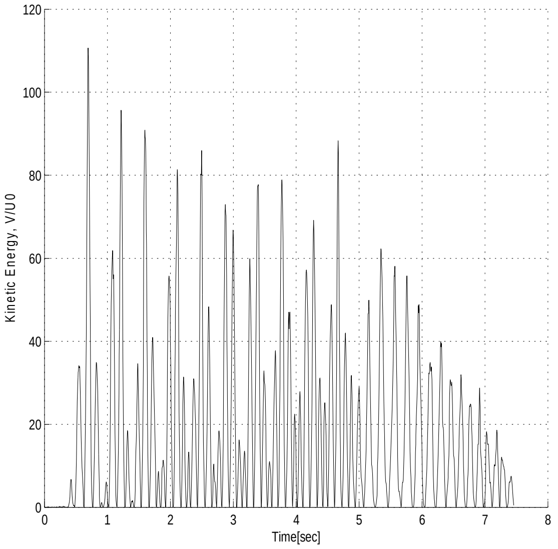
Kinetic Energy, V/U0
Time[sec]
120
100
80
60
40
20
0
0 1 2 3 4 5 6 7 8

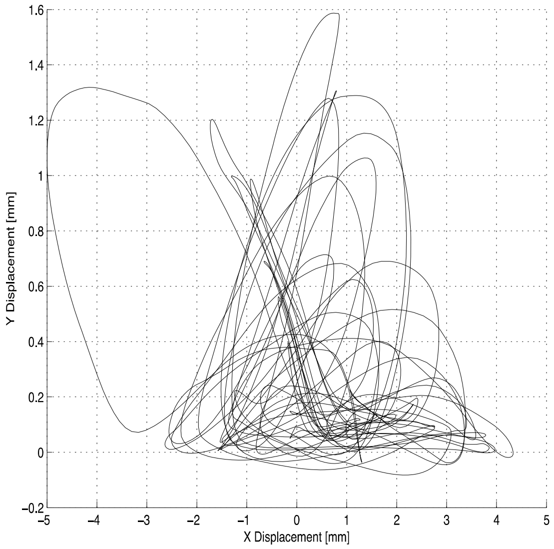
Y Displacement [mm]
X Displacement [mm]
1.6
1.4
1.2
1
0.8
0.6
0.4
0.2
0
−0.2
−5 −4 −3 −2 −1 0 1 2 3 4 5

A-11.2 Middle Block

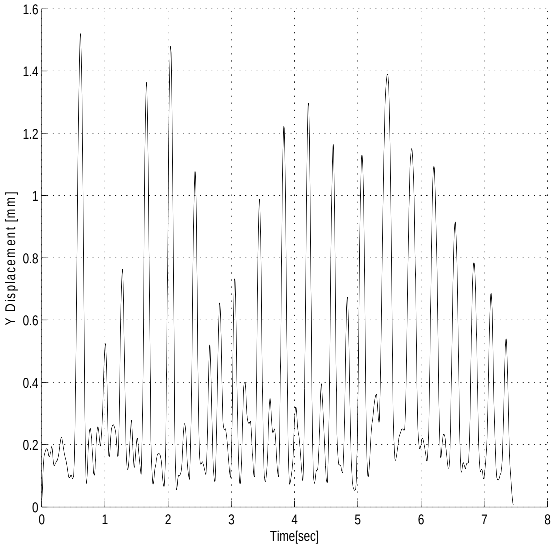

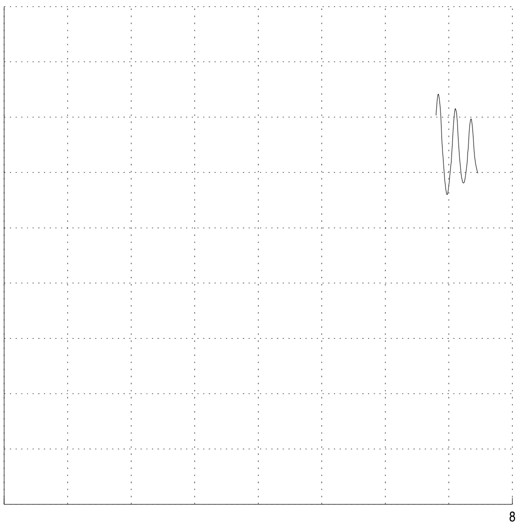

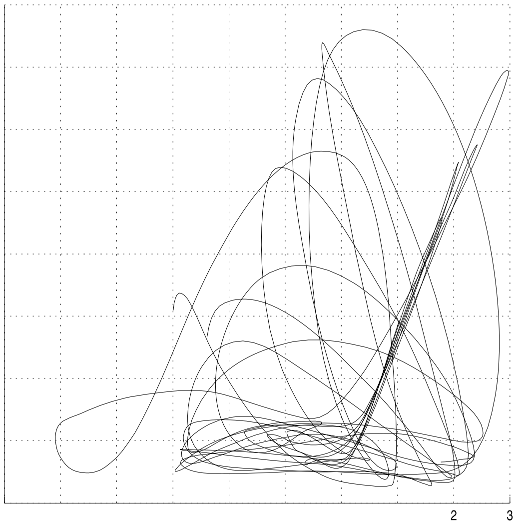

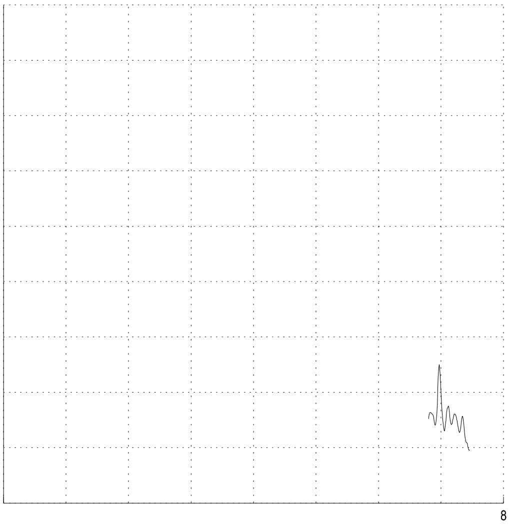

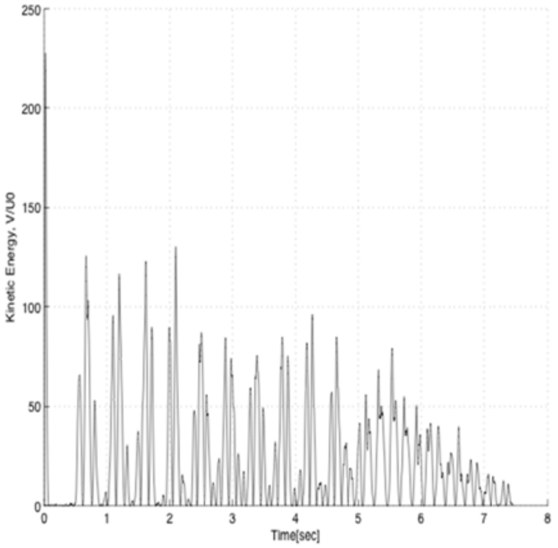

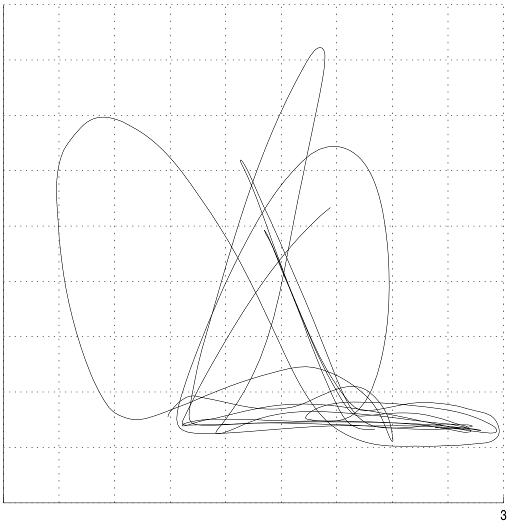

Appendix B

Technical Drawings

SIDE VIEW

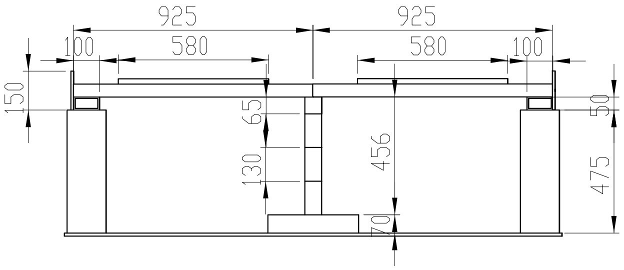

TOP VIEW

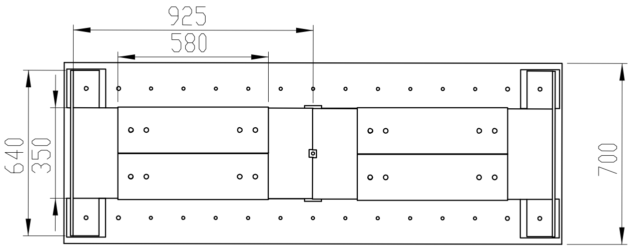

FRONT VIEW

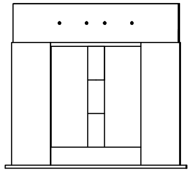

ISOMETRIC VIEW

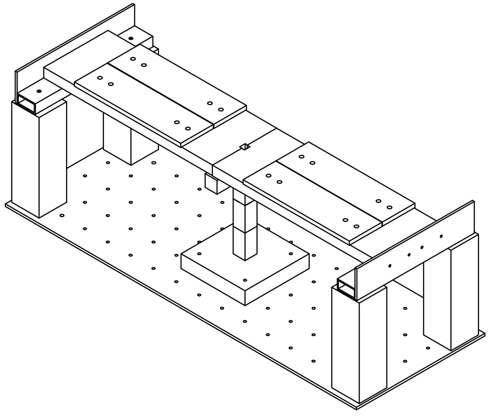

UNLESS OTHERWISE SPECIFIED:
DIMENSIONS ARE IN MILLIMETERS
SURFACE FINISH:
TOLERANCES:
LINEAR:
ANGULAR:

FINISH:

DEBUR AND
BREAK SHARP
EDGES

DO NOT SCALE DRAWING

REVISION

	NAME	SIGNATURE	DATE
DRAWN			
CHK'D			
APPV'D			
MFG			
Q.A			

MATERIAL:

WEIGHT:

TITLE:

SCALE 1:20

DWG NO.

3D

A3

SCALE:1:20

SHEET 1 OF 1

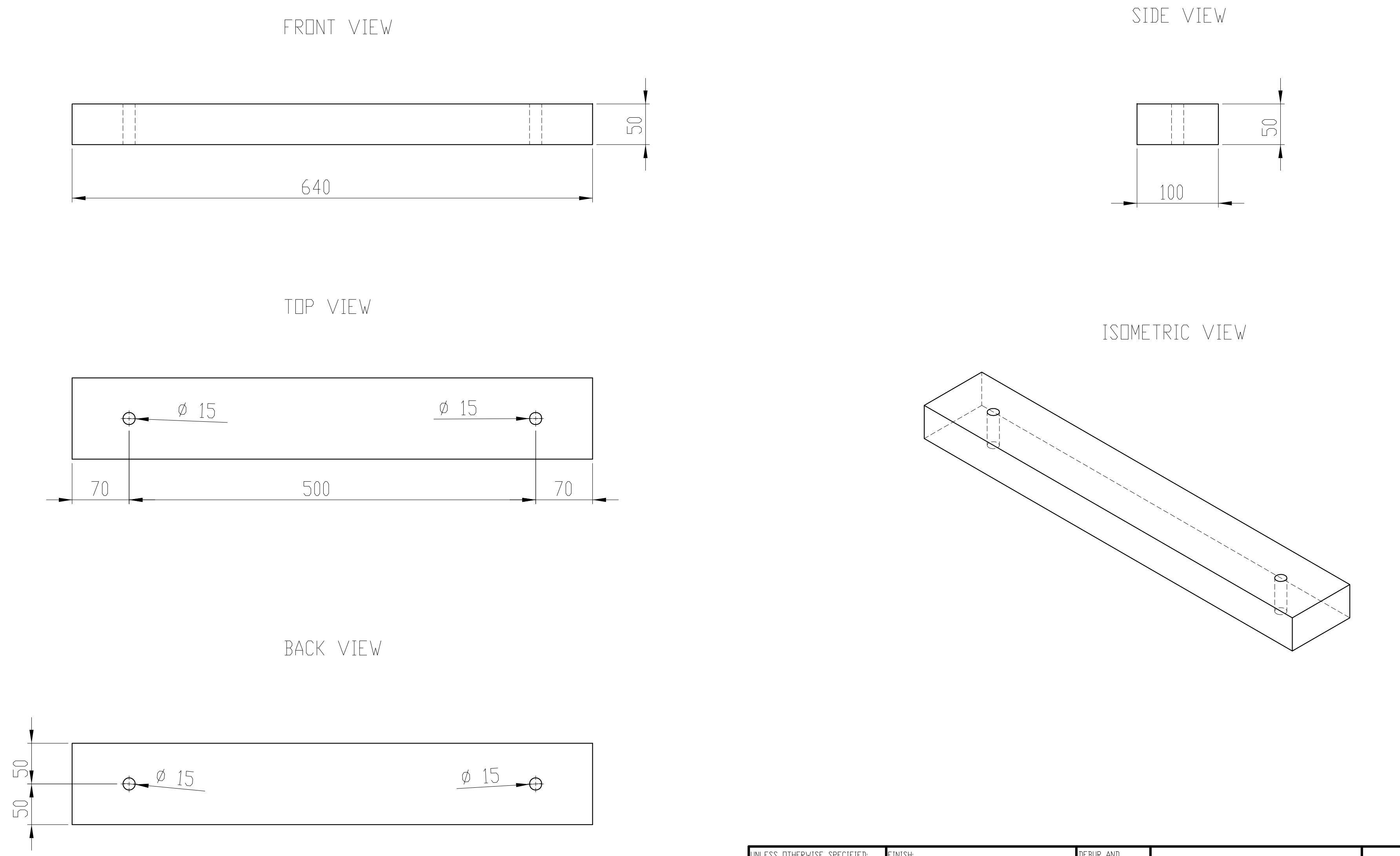

UNLESS OTHERWISE SPECIFIED:
DIMENSIONS ARE IN MILLIMETERS
SURFACE FINISH:
TOLERANCES:
LINEAR:
ANGULAR:

FINISH:

DEBUR AND
BREAK SHARP
EDGES

DO NOT SCALE DRAWING

REVISION

	NAME	SIGNATURE	DATE
DRAWN			
CHK'D			
APPV'D			
MFG			
Q.A			

TITLE:
SCALE 1:5

MATERIAL:

DWG NO.
beam_100x50x6_09-07

A3

WEIGHT:

SCALE:1:5

SHEET 1 OF 1

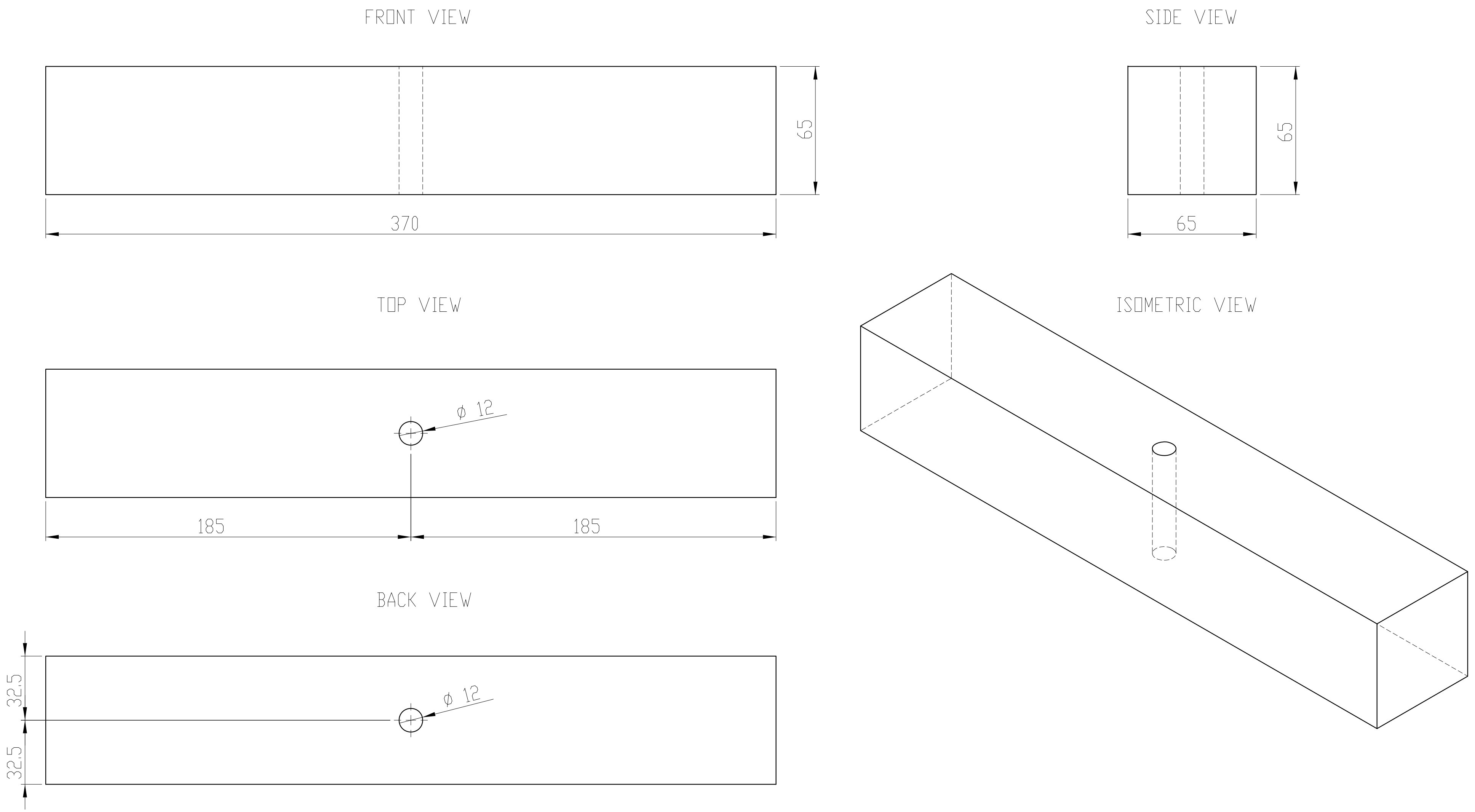

UNLESS OTHERWISE SPECIFIED:
DIMENSIONS ARE IN MILLIMETERS
SURFACE FINISH:
TOLERANCES:
LINEAR:
ANGULAR:

FINISH:

DEBUR AND
BREAK SHARP
EDGES

DO NOT SCALE DRAWING

REVISION

	NAME	SIGNATURE	DATE
DRAWN			
CHK'D			
APPV'D			
MFG			
Q.A			

TITLE: SCALE 1:2

MATERIAL:

DWG NO. Cap_65x65x370_10-07_

A3

WEIGHT:

SCALE:1:2

SHEET 1 OF 1

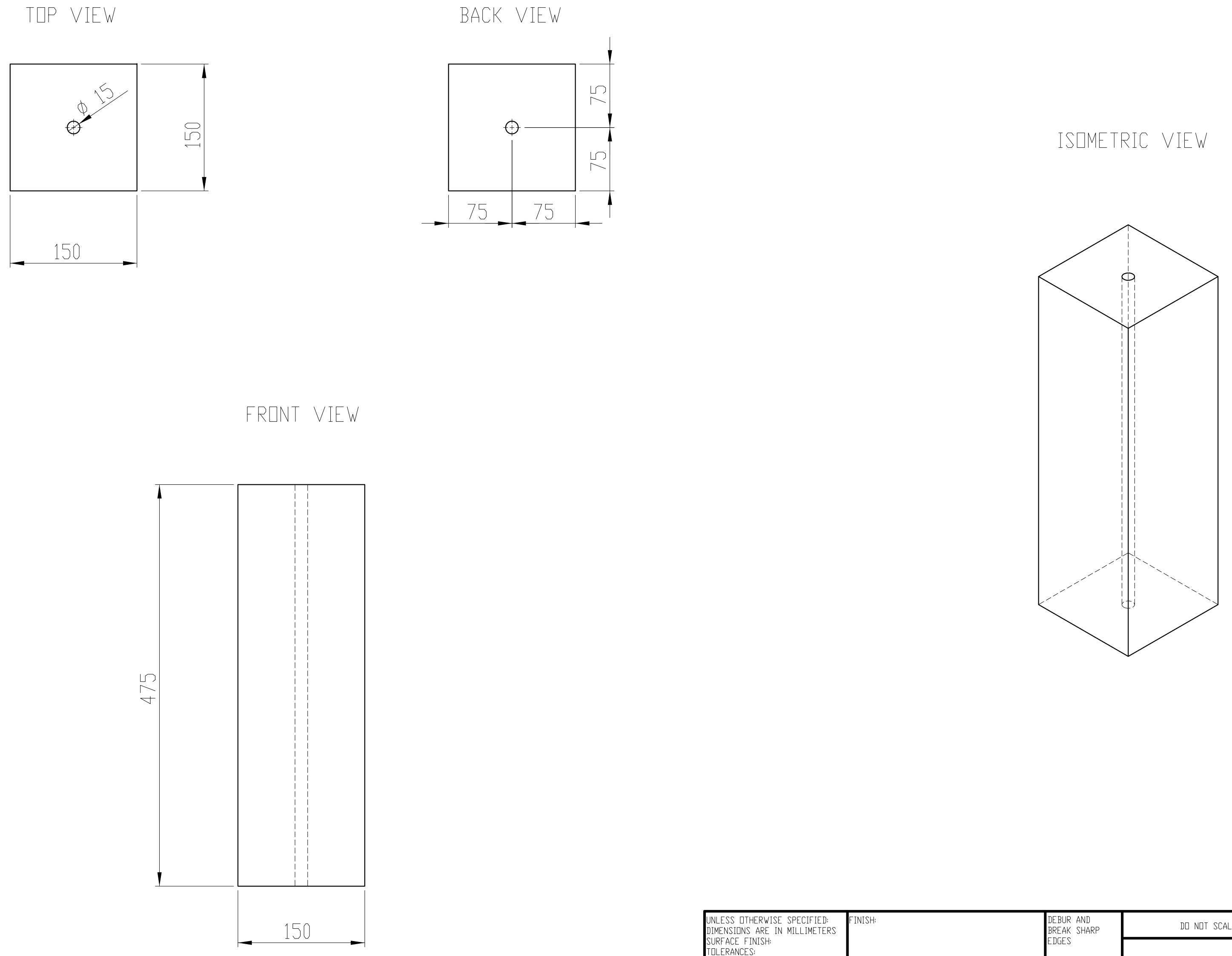

UNLESS OTHERWISE SPECIFIED:
DIMENSIONS ARE IN MILLIMETERS
SURFACE FINISH:
TOLERANCES:
LINEAR:
ANGULAR:

FINISH:

DEBUR AND
BREAK SHARP
EDGES

DO NOT SCALE DRAWING

REVISION

	NAME	SIGNATURE	DATE
DRAWN			
CHK'D			
APPV'D			
MFG			
Q.A			

TITLE:

SCALE 1:5

MATERIAL:

DWG NO.

concrete support_150x150x475_09-07

A3

WEIGHT:

SCALE:1:5

SHEET 1 OF 1

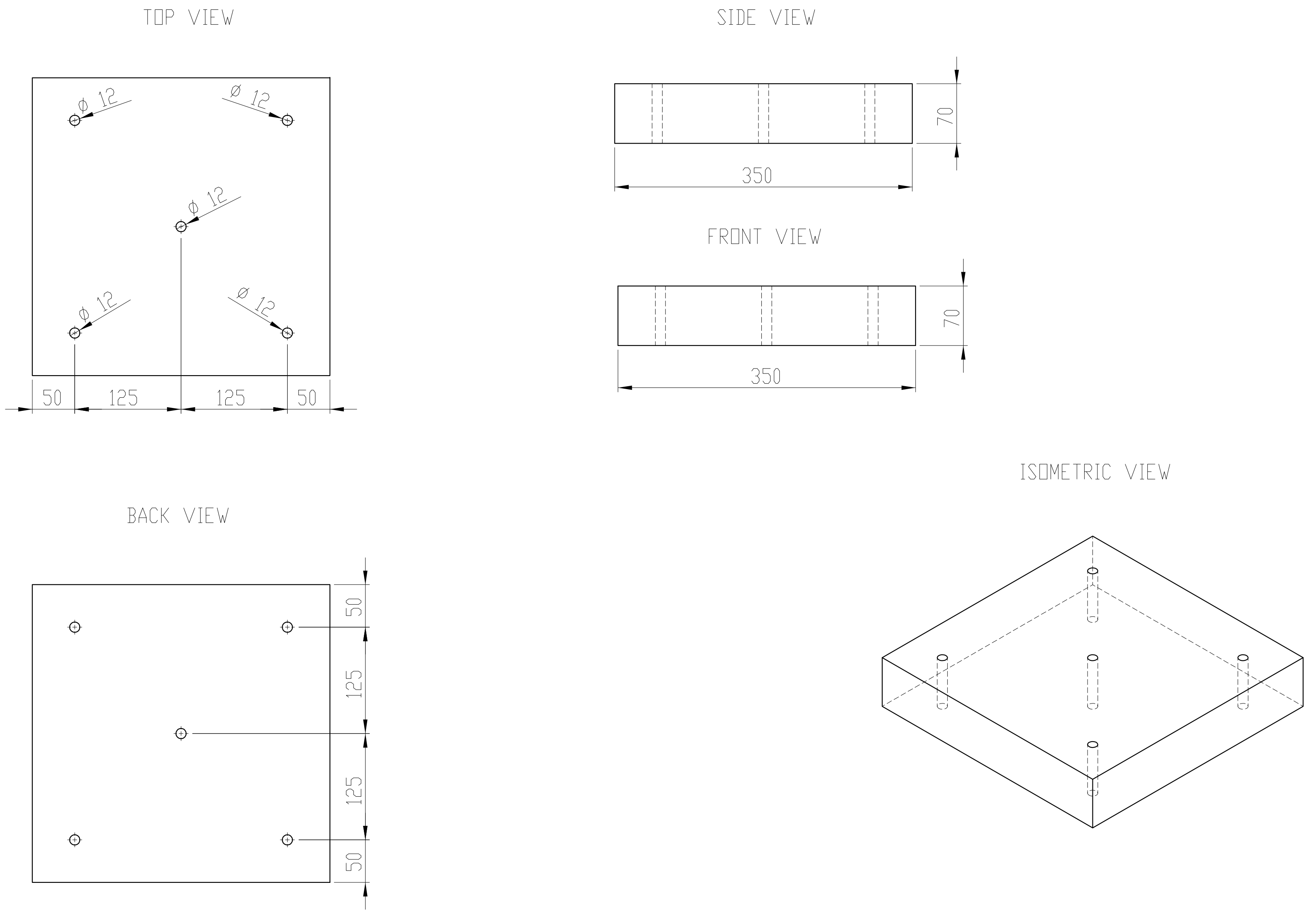

UNLESS OTHERWISE SPECIFIED:
DIMENSIONS ARE IN MILLIMETERS
SURFACE FINISH:
TOLERANCES:
LINEAR:
ANGULAR:

FINISH:

DEBUR AND
BREAK SHARP
EDGES

DO NOT SCALE DRAWING

REVISION

	NAME	SIGNATURE	DATE
DRAWN			
CHK'D			
APPV'D			
MFG			
Q.A			

MATERIAL:

WEIGHT:

TITLE: SCALE 1:5

DWG NO. Foundation_09-07

A3

SCALE:1:5

SHEET 1 OF 1

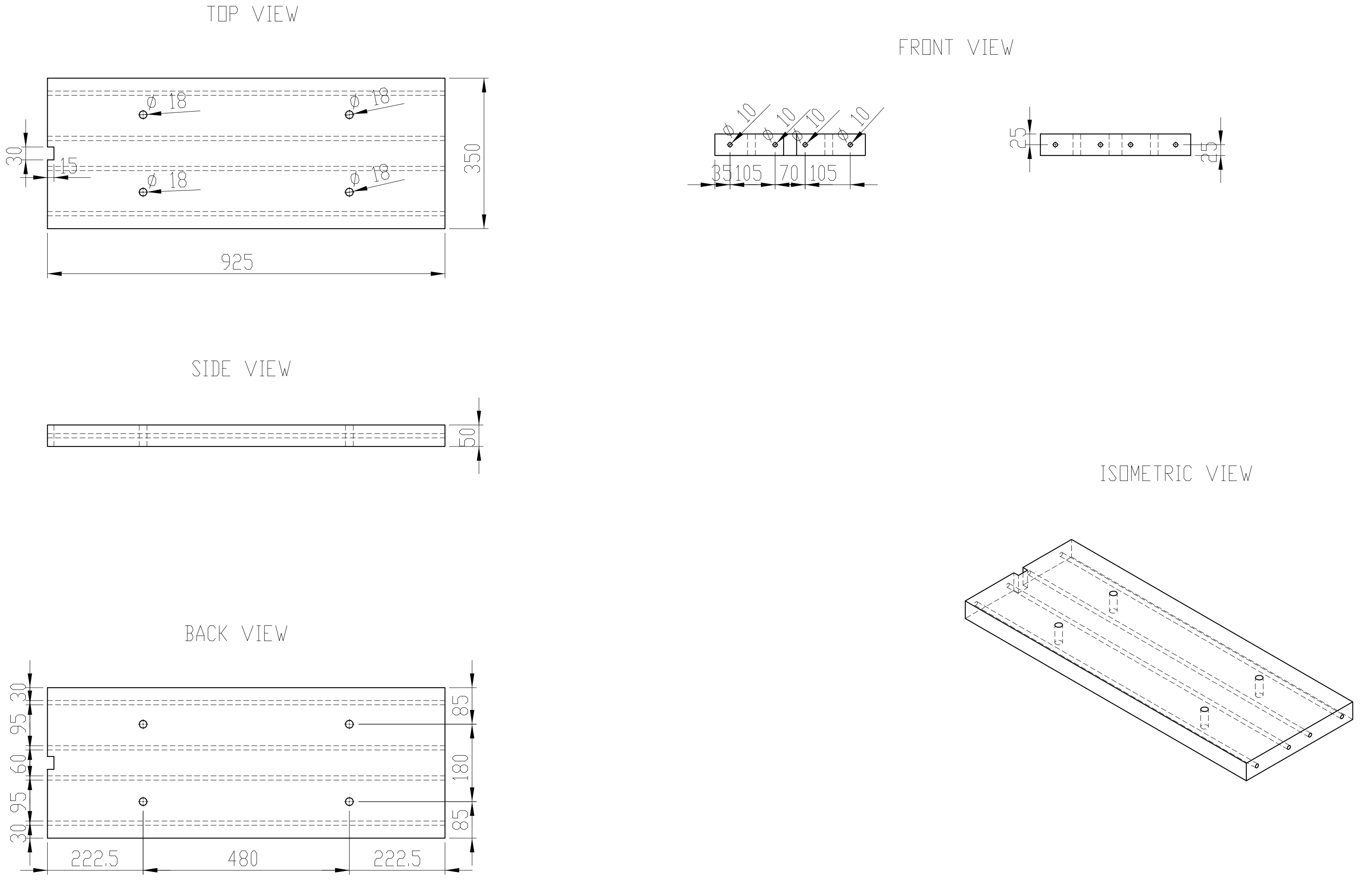

UNLESS OTHERWISE SPECIFIED:
DIMENSIONS ARE IN MILLIMETERS
SURFACE FINISH:
TOLERANCES:
LINEAR:
ANGULAR:

FINISH:

DEBUR AND
BREAK SHARP
EDGES

DO NOT SCALE DRAWING

REVISION

	NAME	SIGNATURE	DATE
DRAWN			
CHK'D			
APPV'D			
MFG			
Q.A			

MATERIAL:

WEIGHT:

TITLE:

SCALE 1:10

DWG NO.
Half Deck_925_10-07

A3

SCALE:1:10

SHEET 1 OF 1

TOP VIEW

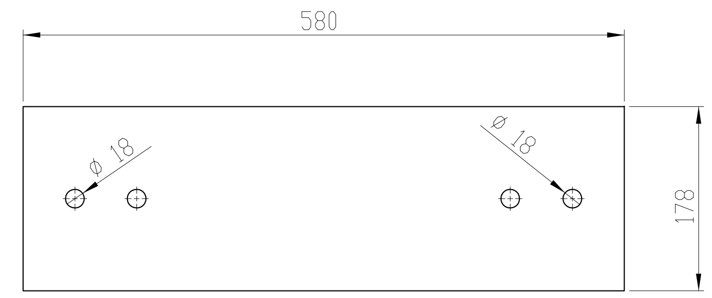

FRONT VIEW

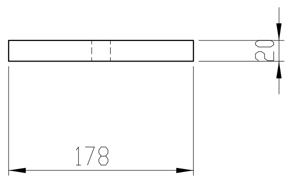

SIDE VIEW

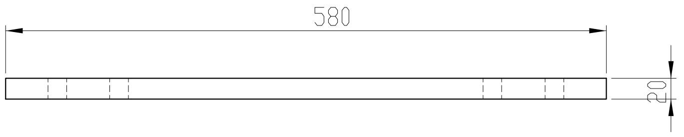

ISOMETRIC VIEW

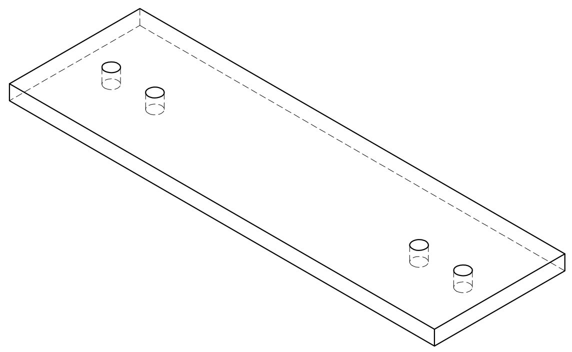

BACK VIEW

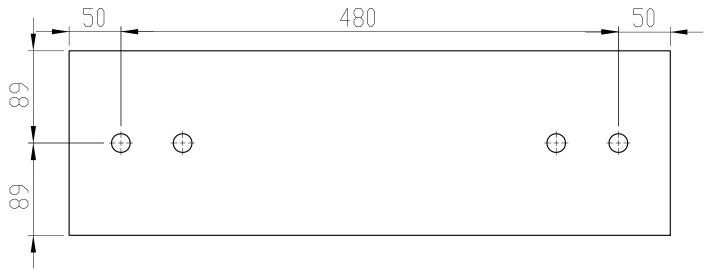

UNLESS OTHERWISE SPECIFIED:
DIMENSIONS ARE IN MILLIMETERS
SURFACE FINISH:
TOLERANCES:
LINEAR:
ANGULAR:

FINISH:

DEBUR AND
BREAK SHARP
EDGES

DO NOT SCALE DRAWING

REVISION

	NAME	SIGNATURE	DATE
DRAWN			
CHK'D			
APPV'D			
MFG			
Q.A			

MATERIAL:

WEIGHT:

TITLE:

SCALE 1:5

DWG NO. load plate_10-07

A3

SCALE:1:5

SHEET 1 OF 1

TOP VIEW

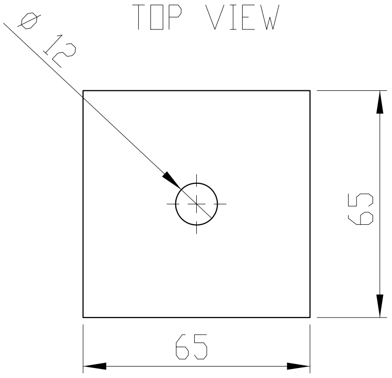

BACK VIEW

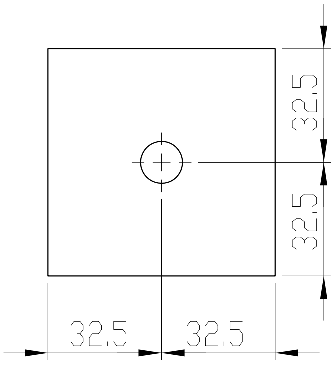

SIDE VIEW

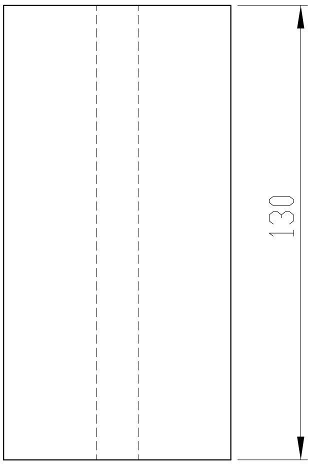

ISOMETRIC VIEW

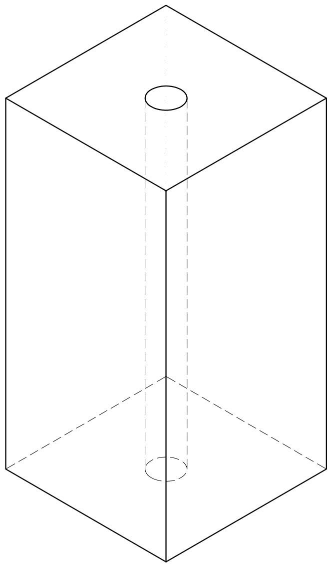

UNLESS OTHERWISE SPECIFIED: DIMENSIONS ARE IN MILLIMETERS SURFACE FINISH: TOLERANCES: LINEAR: ANGULAR:	FINISH:				DEBUR AND BREAK SHARP EDGES	DO NOT SCALE DRAWING · REVISION
	NAME	SIGNATURE	DATE			TITLE:
DRAWN						SCALE 1:2
CHK'D						
APPV'D						
MFG						
Q.A				MATERIAL:		DWG NO. pier_segment_65x65x130_09-07 · A4
				WEIGHT:		SCALE:1:2 · SHEET 1 OF 1

TOP VIEW

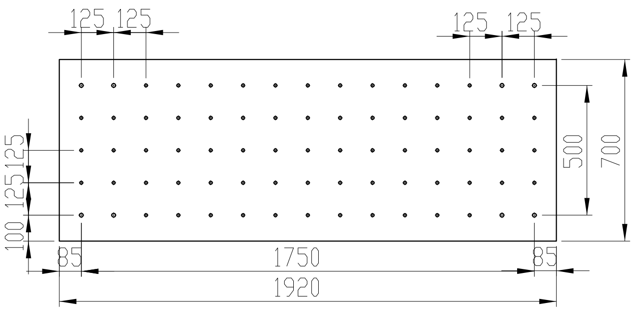

FRONT VIEW

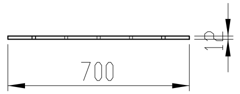

BACK VIEW

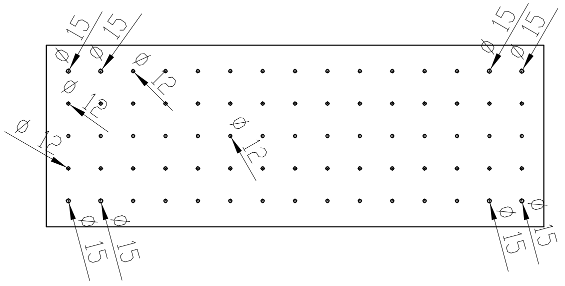

ISOMETRIC VIEW

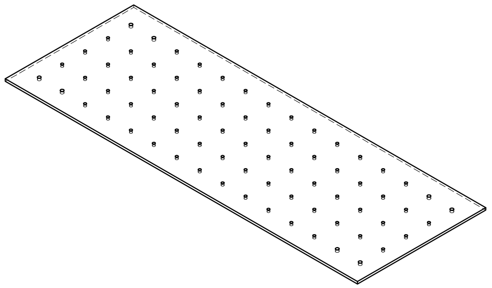

SIDE VIEW

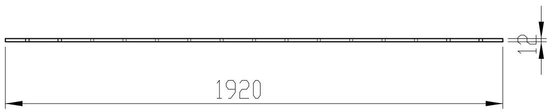

UNLESS OTHERWISE SPECIFIED:
DIMENSIONS ARE IN MILLIMETERS
SURFACE FINISH:
TOLERANCES:
LINEAR:
ANGULAR:

FINISH:

DEBUR AND
BREAK SHARP
EDGES

DO NOT SCALE DRAWING

REVISION

	NAME	SIGNATURE	DATE		
DRAWN					
CHK'D					
APPV'D					
MFG					
Q.A					

MATERIAL:

WEIGHT:

TITLE:

SCALE 1:20

DWG NO.

Steel plate_10-07

A3

SCALE:1:20

SHEET 1 OF 1

FRONT VIEW

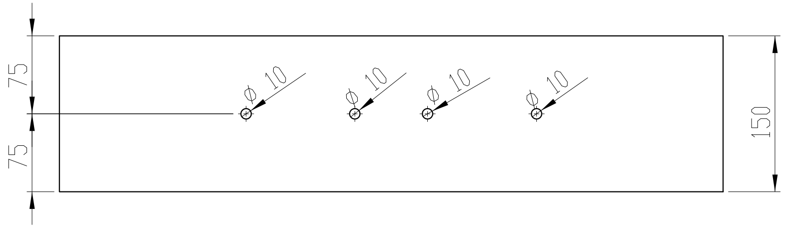

BACK VIEW

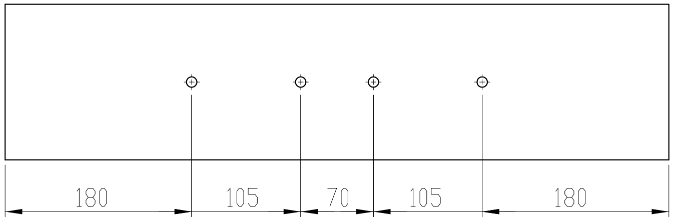

TOP VIEW

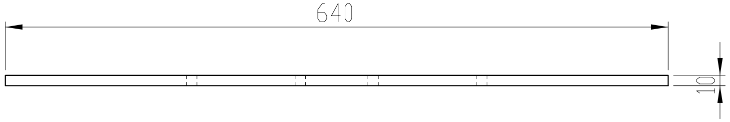

ISOMETRIC VIEW

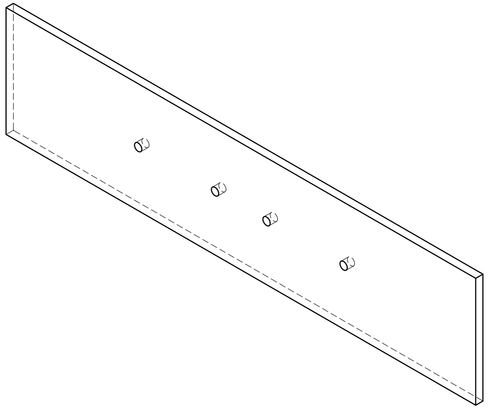

SIDE VIEW

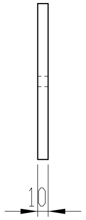

UNLESS OTHERWISE SPECIFIED: DIMENSIONS ARE IN MILLIMETERS SURFACE FINISH: TOLERANCES: LINEAR: ANGULAR:	FINISH:		DEBUR AND BREAK SHARP EDGES	DO NOT SCALE DRAWING	REVISION	
	NAME	SIGNATURE	DATE	TITLE: SCALE 1:5		
DRAWN						
CHK'D						
APPV'D						
MFG						
Q.A			MATERIAL:	DWG NO. steel support_10-07		A3
			WEIGHT:	SCALE:1:5	SHEET 1 OF 1	

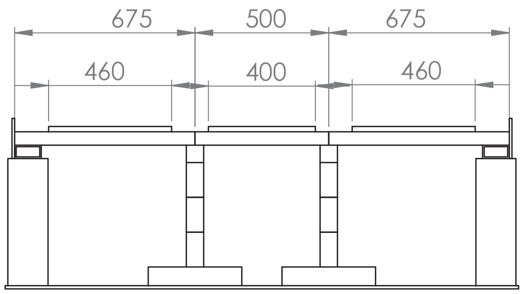

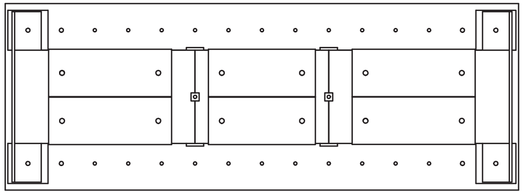

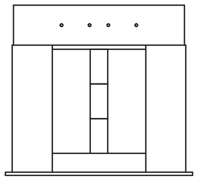

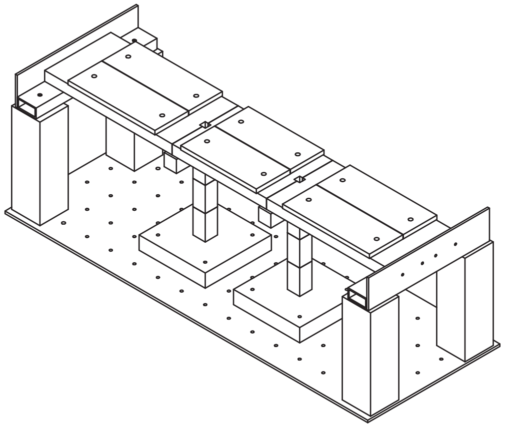

UNLESS OTHERWISE SPECIFIED:
DIMENSIONS ARE IN MILLIMETERS
SURFACE FINISH:
TOLERANCES:
LINEAR:
ANGULAR:

FINISH:

DEBUR AND BREAK SHARP EDGES

DO NOT SCALE DRAWING

REVISION

10/07/2012

Rodolfo Mazza

	NAME	SIGNATURE	DATE
DRAWN			
CHK'D			
APPV'D			
MFG			
Q.A			

MATERIAL:

WEIGHT:

TITLE:

SCALE 1:20
UNITS: mm

DWG NO.

3D 1

A3

SCALE:1:20

SHEET 1 OF 1

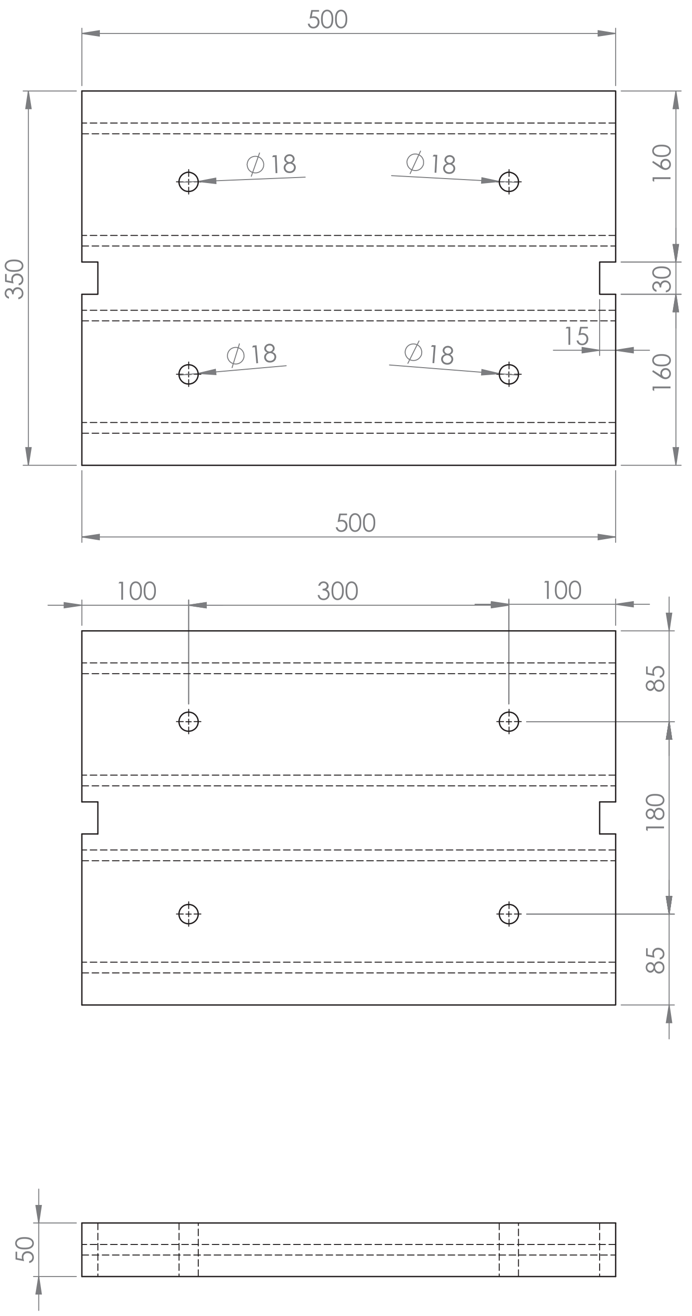

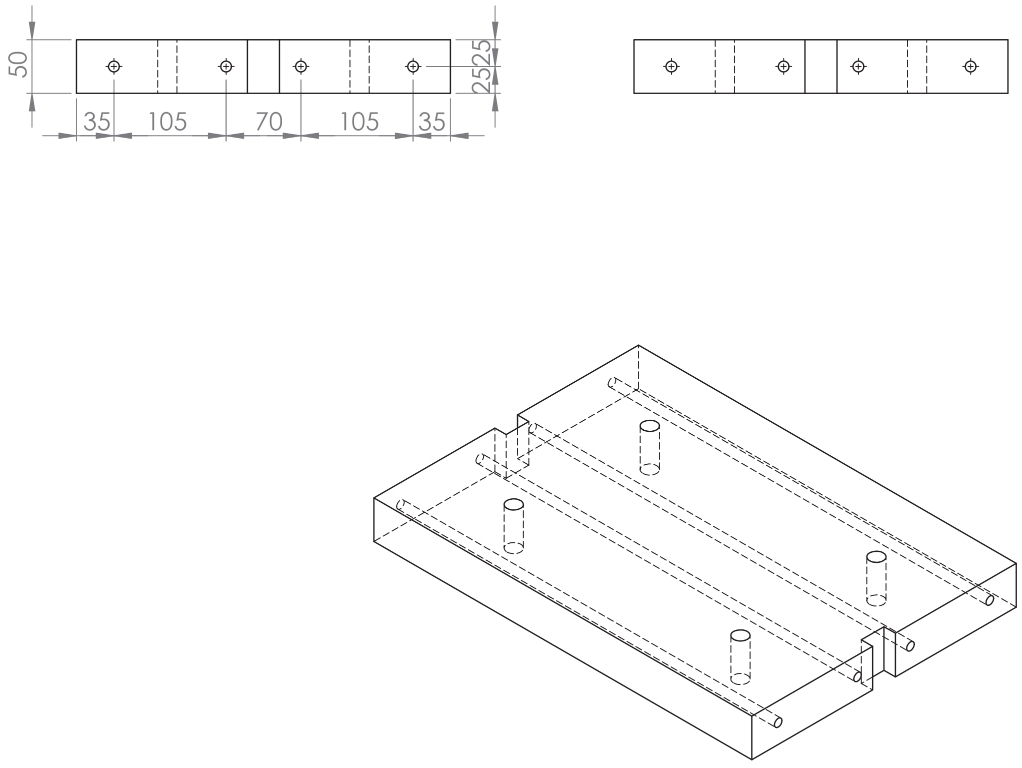

UNLESS OTHERWISE SPECIFIED: DIMENSIONS ARE IN MILLIMETERS SURFACE FINISH: TOLERANCES: LINEAR: ANGULAR:	FINISH:	DEBUR AND BREAK SHARP EDGES	DO NOT SCALE DRAWING	REVISION	
			10/07/2012	Rodolfo Mazza	
	NAME	SIGNATURE	DATE	TITLE: SCALE 1:5 UNITS: mm	
DRAWN					
CHK'D					
APPV'D					
MFG					
Q.A			MATERIAL:	DWG NO. Half Deck_500	A3
			WEIGHT:	SCALE:1:5	SHEET 1 OF 1

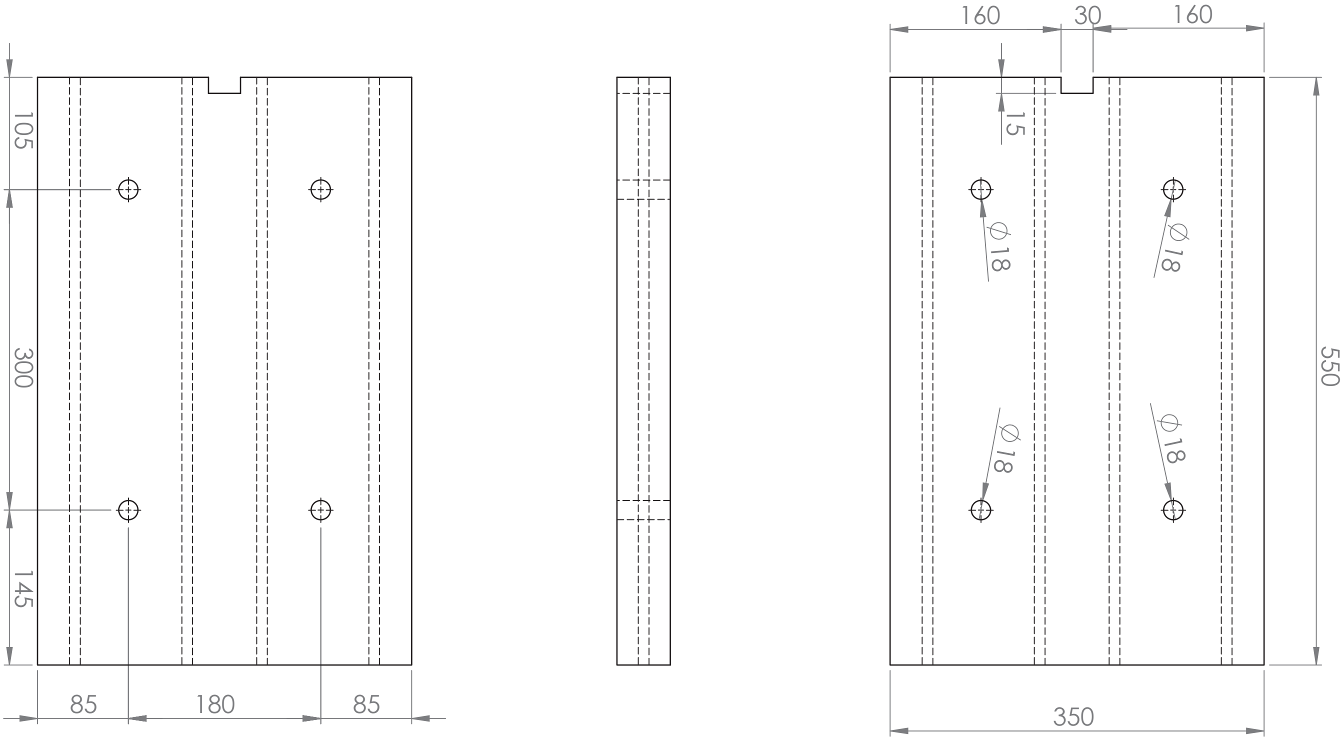

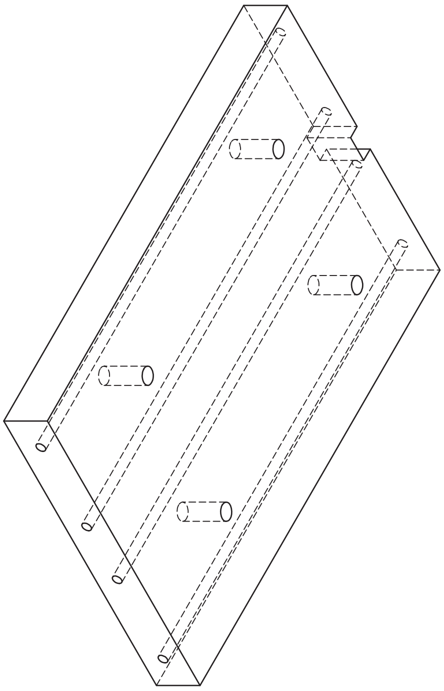

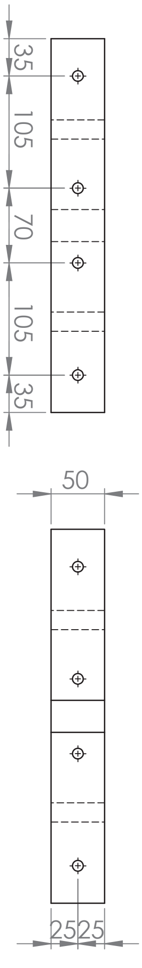

UNLESS OTHERWISE SPECIFIED:
DIMENSIONS ARE IN MILLIMETERS
SURFACE FINISH:
TOLERANCES:
LINEAR:
ANGULAR:

FINISH:

DEBUR AND
BREAK SHARP
EDGES

DO NOT SCALE DRAWING

REVISION

	NAME	SIGNATURE	DATE
DRAWN			
CHK'D			
APPV'D			
MFG			
Q.A			

MATERIAL:

WEIGHT:

10/07/2012
SCALE :5
UNITS: mm

TITLE:
Rodolfo Mazza

DWG NO.
Half Deck_550

A3

SCALE:1:5

SHEET 1 OF 1

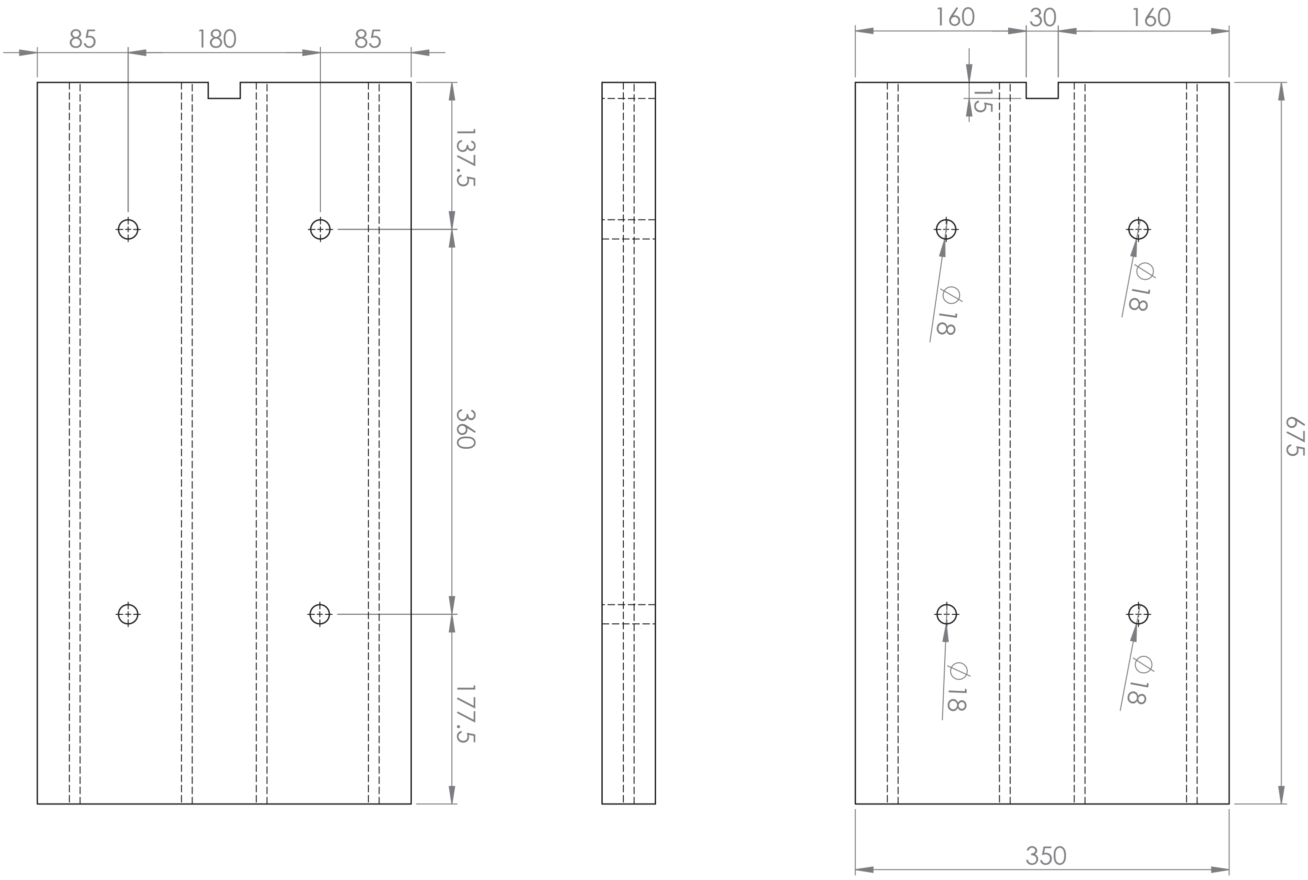

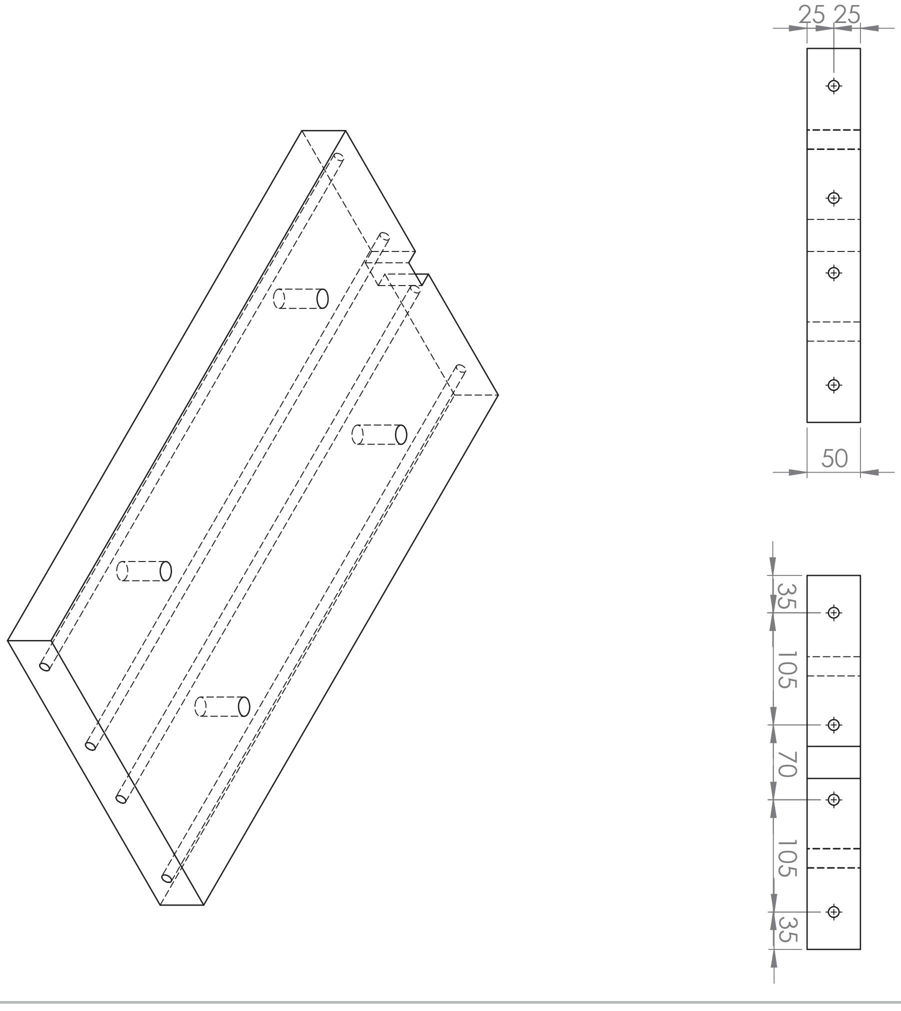

UNLESS OTHERWISE SPECIFIED:
DIMENSIONS ARE IN MILLIMETERS
SURFACE FINISH:
TOLERANCES:
LINEAR:
ANGULAR:

FINISH:

DEBUR AND
BREAK SHARP
EDGES

DO NOT SCALE DRAWING

REVISION

	NAME	SIGNATURE	DATE
DRAWN			
CHK'D			
APPV'D			
MFG			
Q.A			

MATERIAL:

WEIGHT:

TITLE:

10/07/2012

Rodolfo Mazza

SCALE 1:5
UNITS: mm

DWG NO.

Half Deck_675

A3

SCALE:1:5

SHEET 1 OF 1

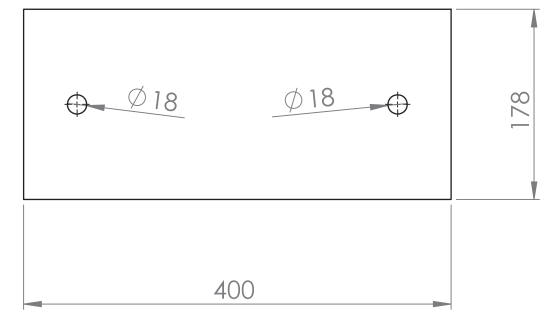

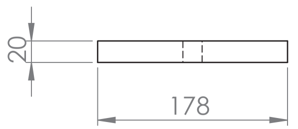

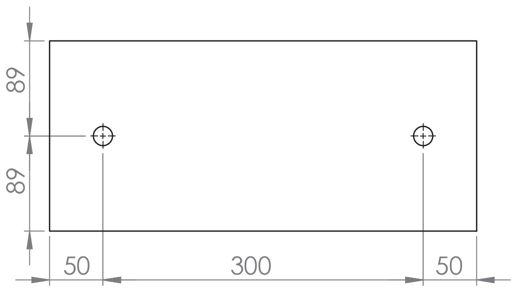

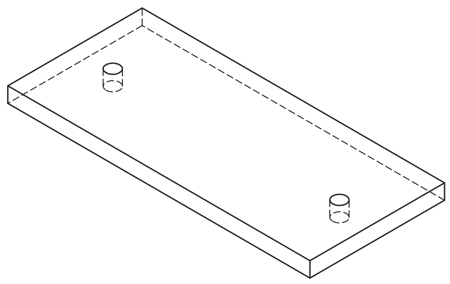

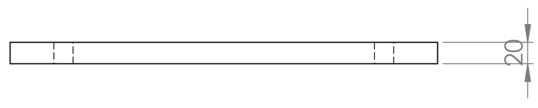

UNLESS OTHERWISE SPECIFIED: DIMENSIONS ARE IN MILLIMETERS SURFACE FINISH: TOLERANCES: LINEAR: ANGULAR:	FINISH:	DEBUR AND BREAK SHARP EDGES	DO NOT SCALE DRAWING	REVISION	
			10/07/2012	Rodolfo Mazza	
	NAME	SIGNATURE	DATE	TITLE:	
DRAWN				SCALE 1:5 UNITS: mm	
CHK'D					
APPV'D					
MFG					
Q.A			MATERIAL:	DWG NO. load plate 400	A3
			WEIGHT:	SCALE:1:5	SHEET 1 OF 1

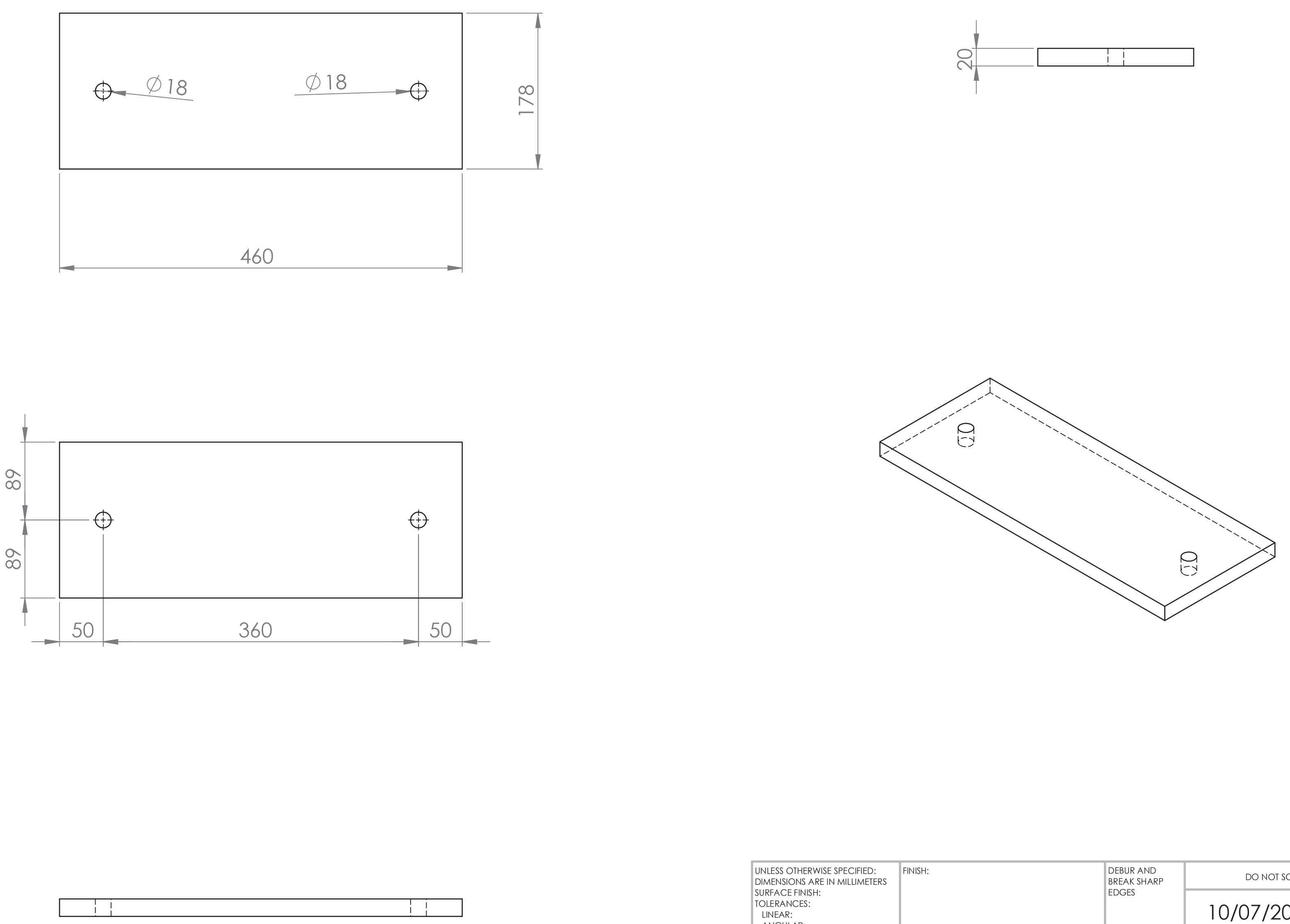

UNLESS OTHERWISE SPECIFIED:
DIMENSIONS ARE IN MILLIMETERS
SURFACE FINISH:
TOLERANCES:
LINEAR:
ANGULAR:

FINISH:

DEBUR AND
BREAK SHARP
EDGES

DO NOT SCALE DRAWING

REVISION

10/07/2012

Rodolfo Mazza

	NAME	SIGNATURE	DATE
DRAWN			
CHK'D			
APPV'D			
MFG			
Q.A			

MATERIAL:

WEIGHT:

TITLE:
UNITS: mm
SCALE 1:5

DWG NO. load plate 460

A3

SCALE:1:5

SHEET 1 OF 1